Experimental Characterization and Finite Element Modeling of Composites to Support a Generalized Orthotropic Elasto-Plastic Damage Material Model for Impact Analysis

by

Bilal Khaled

A Dissertation Presented in Partial Fulfillment
of the Requirements for the Degree
Doctor of Philosophy

Approved April 2019 by the
Graduate Supervisory Committee:

Subramaniam Rajan, Chair
Robert Goldberg
Yongming Liu
Barzin Mobasher
Narayanan Neithalath

ARIZONA STATE UNIVERSITY

August 2019

ABSTRACT

An orthotropic elasto-plastic damage material model (OEPDMM) suitable for impact simulations has been developed through a joint research project funded by the Federal Aviation Administration (FAA) and the National Aeronautics and Space Administration (NASA). Development of the model includes derivation of the theoretical details, implementation of the theory into LS-DYNA®, a commercially available nonlinear transient dynamic finite element code, as material model MAT 213, and verification and validation of the model. The material model is comprised of three major components: deformation, damage, and failure. The deformation sub-model is used to capture both linear and nonlinear deformations through a classical plasticity formulation. The damage sub-model is used to account for the reduction of elastic stiffness of the material as the degree of plastic strain is increased. Finally, the failure sub-model is used to predict the onset of loss of load carrying capacity in the material. OEPDMM is driven completely by tabulated experimental data obtained through physically meaningful material characterization tests, through high fidelity virtual tests, or both. The tabulated data includes stress-strain curves at different temperatures and strain rates to drive the deformation sub-model, damage parameter-total strain curves to drive the damage sub-model, and the failure sub-model can be driven by the data required for different failure theories implemented in the computer code. The work presented herein focuses on the experiments used to obtain the data necessary to drive as well as validate the material model, development and implementation of the damage model, verification of the deformation and damage models through single element (SE) and multi-element (ME) finite element simulations, development and implementation of experimental procedure for modeling delamination, and finally

validation of the material model through low speed impact simulations and high speed impact simulations.

DEDICATION

To my parents, Marwan and Layla, and my brother, Ahmed, who have always been there when I needed them. I would not have made it through this chapter of my life without their support.

ACKNOWLEDGMENTS

I would like to acknowledge my research advisor, Dr. Rajan, for his patience, wisdom, and mentorship which kept me steady while I stumbled through this process. I would also like to thank my committee members, Dr. Neithalath, Dr. Mobasher, Dr. Goldberg, and Dr. Liu for their guidance and meaningful discussions.

A special thank you goes out to Peter Goguen and Jeff Long both of whom I pestered endlessly for help in the labs. I would also like to thank my friends and colleagues, past and present, from here at ASU as well as George Mason University, Ohio State University, NASA, and the FAA.

This work would not be possible without research funding, and I would like to gratefully acknowledge the support of (a) the Federal Aviation Administration through Grant #17-G-001 titled "Composite Material Model for Impact Analysis" and Grant #17-G-005 "Enhancing the Capabilities of MAT213 for Impact Analysis", William Emmerling and Dan Cordasco, Technical Monitors, and (b) The National Aeronautics and Space Administration (NASA) through Contract Number: NN15CA32C titled "Development and Implementation of an Orthotropic Plasticity Progressive Damage Model for Transient Dynamic/Impact Finite Element Analysis of Composite Structures", Robert Goldberg, Contracting Officer Representative.

TABLE OF CONTENTS

Page

LIST OF TABLES

Table Page

LIST OF FIGURES

Figure Page

Figure Page

Figure Page

Figure Page

Figure Page

Figure Page

Figure Page

Figure Page

1 INTRODUCTION

Composite materials are increasingly becoming ubiquitous in the design of structural systems used in aerospace, automotive, and other industries (Khaled et al. 2019a). These structural systems are often subjected to a variety of environmental and loading conditions. For some applications, impact events are among the most critical of loading conditions. Predicting the behavior of the system requires powerful numerical tools, such as finite elements. Under impact loads, composite structures typically experience deformation, damage, and failure. All three behavioral components influence the future response of the composite. Obtaining high-fidelity experimental data for use in a comprehensive finite element model is challenging but necessary to drive increasingly refined models.

In the United States, several governmental agencies (including National Aeronautics and Space Administration, NASA and the Federal Aviation Administration, FAA) have recognized the importance of building a framework for composites system by forming a public–private consortium. A press release (Clark 2015) states that "NASA formed the consortium in support of the Advanced Composites Project, which is part of the Advanced Air Vehicles Program in the agency's Aeronautics Research Mission Directorate. The project's goal is to reduce product development and certification timelines by 30 percent for composites infused into aeronautics applications." A major reason for these challenges is the lack of mature material models that should be able to predict, with some degree of certainty, the deformation, damage and failure of composite systems (Hoffarth et al. 2017). Under a joint effort started by the FAA and then joined by NASA, George Mason University, GMU and Livermore Software Technology Corporation, LSTC, a new

orthotropic composite material model is being developed, which is driven entirely by experimental data and is suitable for impact analysis. The new model offers users more flexibility in defining how the material behaves since many of the input parameters are given as tabular input. The material model has provisions for representing strain-rate and temperature dependent deformation, quasi-static and room temperature (QS-RT) damaged behavior, and QS-RT failure. The three sub-models - deformation, damage, and failure, are driven completely by unique sets of tabulated experimental data. As such, high fidelity experimental data is paramount for properly verifying and validating the material model.

One of the more popular commercial programs for impact modeling is LS-DYNA® (LSTC 2018a), a nonlinear transient dynamic finite element package. The software package supports numerous material models for representing composites. Many of these material models require only linear elastic properties to predict deformation since the assumption is that the composite would fail in a sudden, brittle manner. Some require plasticity and fracture properties, presumably to compute damage-related parameters. Finally, there are a number of strength-related material values that are used with built-in failure models and element erosion.

In this dissertation, the primary focus is on providing the theoretical and implementation details of the deformation and damage sub-models as well as the experimental techniques used to obtain data for the two sub-models. The theory and algorithm are implemented in LS-DYNA as MAT 213. Finite element verification studies are presented to provide the expected behavior of the material. Experimental techniques used for deriving cohesive

zone model parameters are presented with the intention of providing additional experimental data to enhance the predictive capabilities of OEPDMM. Finally, simulations of low/high velocity impact tests are compared with experimental data to highlight the efficacy of the proposed approach.

1.1 Deformation Modeling Literature Review

There has been extensive research dedicated to predicting the manner in which composite materials behave. Several approaches have been proposed ranging from mechanistic to phenomenological. The mechanistic models typically utilize a micromechanical approach (Aboudi et al. 2013; Paley and Aboudi 1992; Sun and Chen 1991; Sun and Vaidya 1996) where the investigative focus is understanding how the individual composite constituents contribute to the overall response of the composite material. OEPDMM utilizes more of a phenomenological approach wherein the behavior of each constituent material is not considered, but rather, the homogenized response of the composite is utilized. Both approaches have advantages and disadvantages. Mechanistic models may offer a better understanding of how the composite behaves at the micro-level but phenomenological models are typically more computationally efficient. OEPDMM is being developed with the intention of simulating large scale impact and crush events efficiently while providing enough freedom in the input to remain physically accurate.

Several methodologies have been proposed for macroscale modeling of composite materials. The techniques can usually be separated into two categories: plasticity and continuum damage mechanics (CDM). The difference is in the way that nonlinear behavior

is handled at the element level within the context of finite element analysis (FEA). Plasticity based models attribute all nonlinear behavior to plastic flow of the material. Xie and Adams (Xie and Adams 1995) utilize a plasticity-based model to predict the behavior of unidirectional composites. Vaziri and co-workers (Vaziri et al. 1991) formulate a plasticity-based model for both unidirectional and woven composites. CDM based models assume the material behaves in a linear elastic fashion until failure at which time the material properties begin to degrade resulting in a softening. The element level softening would lead to global nonlinear behavior of the material. However, there are typically no provisions that handle permanent deformations that may be induced in the material. Liu and Zheng (Liu and Zheng 2008) use a CDM based approach in modeling unidirectional composites. There are models that utilize a combination of both plasticity and damage to some extent. Oller and co-workers (Oller et al. 1996) propose a model wherein each constituent in a composite is treated as developing both plasticity and damage and a mixing theory is used to amalgamate the response to produce the overall composite behavior. Donadon and co-workers (Donadon et al. 2008) propose a model where the response in the normal principal material directions are treated using a CDM approach while the shear behavior is treated as developing plasticity before failure and damage after a failure criterion has been satisfied. While the models listed have been shown to successfully simulate the behavior of a limited number of composite architectures, they currently are not available within commercial finite element packages. LS-DYNA offers various material models which are used to predict composite behavior. Table 1 presents a summary of the major composite material models in LS-DYNA.

Table 1. Composite Material Models Available in LS-DYNA

Material Model	Input Required to Drive the Model
MAT22 (Chang and Chang 1987a, 1987b)	Orthotropic elastic material properties (E,ν,G), tensile, compressive and shear strengths.
MAT58	Orthotropic elastic planar stress-strain (E,G) curve that can be rate dependent, ν, damage, tensile, compressive and shear strength values.
MAT158	Orthotropic elastic material properties (E,ν,G), tensile, compressive and shear strengths, bulk modulus for viscoelastic behavior, shear relaxation modulus and shear decay constant, rate dependency.
MAT161/162 (Yen 2012)	Orthotropic elastic material properties (E,ν,G), tensile, compressive and shear strengths, rate dependency.
MAT219 (Forghani et al. 2013)	Orthotropic elastic material properties (E,ν,G), damage-related strain values.
MAT261 (Pinho et al. 2006)	Orthotropic elastic material properties (E,ν,G), fracture toughness values, tensile, compressive and shear strengths.
MAT262 (Maimí et al. 2007a, 2007b)	Orthotropic elastic material properties (E,ν,G), fracture toughness values, tensile, compressive and shear strengths, plasticity-related data for in-plane shear plasticity.

In addition to the material models listed in Table 1, there are other material models, available in LS-DYNA, that enhance the modeling capabilities in small ways. MAT23 is similar to MAT22 but supports temperature dependency. Similarly, MAT54/55 are

enhanced versions of MAT22 with support for damage characterization and several failure criteria. MAT59 is similar to MAT22 but defines the failure modes that are a function of the element type. While the material models currently available in LS-DYNA each have attractive features, they also have deficiencies. Some of the models are limited to damage without plasticity being considered. Those which do include some form of nonlinearity, consider it only in the shear behavior. MAT261 allows for in-plane tabulated shear behavior to be provided and the data is used in an elasto-plastic formulation. MAT262 allows for a shear yield stress and tangent modulus to be defined which is used for pre-failure elasto-plastic analysis. The yield strain and tangent modulus may be defined as a function of shear strain rate. Composite materials have been shown to exhibit dependence on temperature (Cao et al. 2011; Skourlis and McCullough 1993; Thomason and Yang 2011) and strain rate (Gilat et al. 2002; Hsiao and Daniel 1998; Jacob et al. 2004; Shokrieh and Omidi 2009; Thiruppukuzhi and Sun 1998; Welsh and Harding 1985). Under impact events, composites have been shown to exhibit a localized rise in temperature (Johnston et al. 2017). The temperature rise leads to thermal softening of the composite. However, none of the models support both temperature and strain rate dependence. Many of the models utilize point wise input to drive predefined deformation behavior irrespective of the true behavior of the particular composite. Additionally, a subset of the models utilizes failure criteria that trigger softening and are tied to a particular composite architecture. MAT261 and MAT262 are applicable only to unidirectional composites, MAT58 is applicable for both unidirectional composites and fabrics. MAT161/162 has provisions for both unidirectional and woven composites.

MAT_213 is being developed as a general orthotropic elasto-plastic damage failure material model. No assumptions about material behavior or architecture are made *a priori* as the input to the model is provided in the form of tabulated data. The deformation sub-model that captures evolution of stress/strain, is governed by a classical plasticity formulation with stress-strain curves defined at various strain rate and temperature combinations. Both tension and compression stress-strain curves are provided independently for each of the orthogonal principal material directions (PMD), herein referred to as the 1, 2, and 3-directions respectively; shear stress-tensorial shear strain curves are provided for the orthogonal principal material planes (PMP), herein referred to as the 1-2, 2-3, and 1-3 planes respectively; and off-axis tension or compression stress-strain curves defined in the 1-2, 2-3, and 1-3 PMP. Poisson's ratio in all three PMP as well as coefficients used for plastic strain evolution are provided as point wise data. All of the required input is obtained directly from physically meaningful, coupon level testing or virtual testing. Theoretical details are provided in Chapter 2.

In order to verify and validate the proposed model, high fidelity experimental data must be obtained. The T800S/F3900 carbon fiber/epoxy resin unidirectional composite system, manufactured by Toray Composite Materials America[1] (Toray), was used to illustrate how the required input data is obtained for quasi-static, room temperature (QS-RT) behavior. This material was selected since FAA had data from previous research (Raju and Acosta 2010) and it is close to tape used in the design of aircraft fuselage. Toray describes the

[1] https://www.toraycma.com/

composite as one with an intermediate modulus, high tensile strength fiber, developed as a cost-effective alternative to T800H. Obtaining reliable experimental data offers a new set of challenges apart from the theoretical derivation. Many of the difficulties in testing unidirectional composites (Fig. 1) have been well documented. Performing a simple tension test on a unidirectional (UD) composite along the direction of the fibers (1-direction) is difficult as these composites are very strong and brittle with large stiffness and failure stress values (Adams 2013). Applying a proper gripping force to the test specimen becomes a challenge. If the gripping force is too high, the specimen may be crushed, and damage will be induced in the specimen even before the experiment begins. If the gripping force is not high enough, the specimen may slip during the experiment. There are many ways of mitigating this issue including proper specimen tabbing using a more compliant material (Adams and Adams 2002) or through thickness tapering of the specimen (Adams 2013) as a means of reducing the required force to induce proper failure in the specimen. Similarly, obtaining consistent results from 1-direction compression tests poses challenges due to the various modes of failure that the composite may experience (Schultheisz and Waas 1996; Waas and Schultheisz 1996). Obtaining experimental data in the through-thickness direction (3-direction) of the composite is often limited by the available composite panels but is extremely important in the context of impact applications. Composite laminates are typically thin providing little material for the through-thickness tests. Often, transverse isotropy of the composite can be used as the in-plane transverse (2-direction) and the out of plane transverse (3-direction) properties may be assumed to be identical. However, the reality is that experimental results show that the material behavior does not satisfy the assumptions of transverse isotropy that is consistent with the actual

fiber packing in the lamina (Fig. 2). The process of manufacturing the composite laminate leads to inherent weaknesses present at the lamina boundary. The failure may be caused by interlaminar delamination in the 3-direction (Kachanov 1977; Luo and Tong 2009; Wilkins et al. 1982) while the failure mode in the 2-direction may be caused by a different mechanism such as the formation of shear bands in the matrix parallel to the plane of the fibers (González and LLorca 2007) or failure of the fiber-matrix interface. The differing properties along material directions may influence the results when performing validation testing as the effect of the ply boundary properties may or may not be properly captured in finite element models.

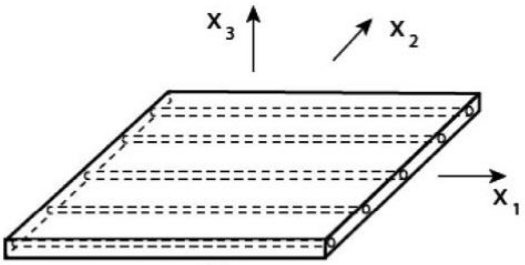

Fig. 1. Principal Material Directions (PMD) for a Unidirectional Composite

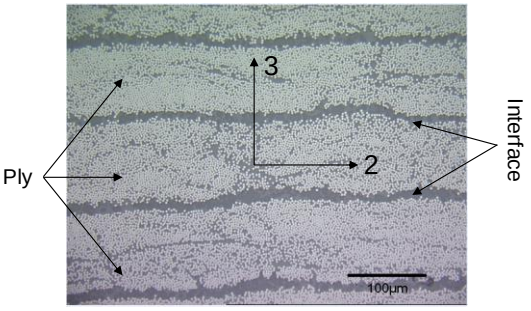

Fig. 2. Principal Material Directions Shown in the Optical Microscopy Image for the T800S/F3900 Composite (the Unidirectional Fibers Are Oriented in the 1-direction)

The transverse isotropy assumptions are not sufficient to build a proper model and through-thickness tests must be carried out since they are needed to complete most finite element models (Broughton and Sims 1994). Many finite element models for composites are shell

element based since the composites are thin and are only subjected to in-plane loads locally. However, in impact applications, the composites are typically thicker and in general the through-thickness response is important. Little research has been done on developing proper methods to obtain through thickness properties of UD composites. Broughton and co-workers (Broughton et al. 1990) performed a suite of tests on a variety of composites including a UD carbon-fiber reinforced polymer. The test suite included tension, compression, and shear tests. Tension and compression tests were performed using a variety of block geometries including the DERA waisted specimen (Ferguson et al. 1998) and parallel sided block specimens. While the results obtained by the block specimens were promising, the advantages provided by waisted specimens are difficult to estimate since the specimens are expensive and difficult to machine. If machining is not done properly, eccentricities may be induced in the specimen and the results obtained may not be indicative of the material properties. Parallel sided block specimens are easier to machine. However, difficulties may arise when aligning the specimen in the testing frame. Broughton and co-workers (Broughton et al. 1990) also used a variety of test specimens to obtain the through thickness shear properties, including the Iosipescu V-notched specimen and the double notched shear specimen presented in ASTM D3846 (D20 Committee 2015a). The double notched shear specimen may lead to unwanted transverse stresses and does not always yield a state of pure shear.

The development of test and analysis methods to obtain the in-plane shear properties of UD composites has been the subject of an extensive amount of research. Amongst competing techniques, the Iosipescu test is the most popular since it has been shown to

induce a state of pure shear in the test specimen. Walrath and Adams (Walrath and Adams 1983) adapted the Iosipescu shear test to measure the in-plane shear properties of UD composites. However, the V-notched test specimen is prone to cracks emanating from the notch roots as well as specimen sliding, bending, and out of plane twisting. Research has been done in an attempt to modify the Iosipescu shear fixture to reduce the effects of the unwanted deformations (Hawong et al. 2004; Melin and Neumeister 2006). Research has also been done to improve the specimen geometry, specifically the notch geometry (Neumeister and Melin 2003). The conclusion is typically that the notch geometry is dependent on the degree of the in-plane isotropy of the composite. The Iosipescu shear test is also not effective at yielding a shear failure stress, when the stress is computed based on the cross-sectional area between the notch tips. Research has been done where the finite element method (FEM) and traditional failure theories have been used to perform an inverse analysis in order to determine the shear strength of the composite (Odegard and Kumosa 2000; Pierron and Vautrin 1998). Typically, the point where the cracks initiate at the notch root is used as the failure point in the finite element simulations. Others have compared the torsion tube test and Iosipescu shear test (Broughton et al. 1990; Swanson et al. 1985) and have shown that the point of failure in the torsion tube test and the point where cracks initiate at the notch roots of the Iosipescu shear specimens coincide. There are alternate shear test procedures. The two and three rail shear tests (D30 Committee 2015b) are also used to determine the in-plane shear properties of UD composites. The two-rail shear test is similar to the Iosipescu test in that it attempts to induce a state of pure shear in a single central region of the specimen through either opposing tensile or compressive forces. The major difference is the manner in which the opposing forces are

applied. The standard Iosipescu test applies forces directly to the top and bottom edges of the specimen whereas the two-rail shear test clamps the face of the specimen using a fastening system and the tensile or compressive forces are applied through a shear load transfer. There has also been extensive research on the optimal specimen geometry for the two-rail shear test (Adams et al. 2003; Hussain and Adams 2004). The three-rail shear test loads the specimen through a series of fasteners similar to the two-rail shear test. However, the test apparatus induces two zones of pure shear in the specimen. Additionally, there has been comparatively less work done on the specimen geometries and a rectangular specimen is typically used to conduct the three-rail shear test experiments.

1.2 Damage Modeling Literature Review

As previously stated, under impact loads, composite structures experience deformation, damage, and failure at both the micro and macro scales. All three components influence the future response of the composite. Damage typically effects the residual stiffness of the composite. Though damage is an important factor when attempting to predict the response of composites under impact, there is often a lack of available damage-related experimental data for a given composite and analysts rely on empirical damage evolution models to predict the response.

Damage in fiber reinforced-polymer matrix composites (FRP) is typically a phenomenon observed at the microscale which manifests itself as a degradation of macroscopic properties. Typically, damage does not result in a complete loss of load carrying capacity in the composite. Rather, it results in a reduction of load-carrying properties as the effective

load transfer mechanisms are altered. Damage can be realized in various ways in composite materials including fiber fracture, matrix cracking, and fiber-matrix debonding (Ogin et al. 2016). Damage is often quantified as a reduction of apparent elastic stiffness of the material.

This phenomenon is especially important when simulating impact events as parts of the structure may undergo loading/reloading and unloading multiple times during the event. Extensive research has been performed investigating the effect of impact on the residual structure and properties of composite laminates (Choi et al. 1991; Joshi and Sun 1987; Masters 1987; Uyaner and Kara 2007; Wu and Springer 1988; Yashiro et al. 2013). After being impacted, structural components begin to vibrate. The residual stiffness of the material dictates the way stress waves propagate after the structure is impacted. Shim and Yang (Shim and Yang 2005) and Kim and co-workers (Kim et al. 1993) have investigated the effects of impact damage on the residual properties of the structure, including stiffness and strength, and have found that the macroscopic properties degrade more rapidly as higher impact energies are imparted on the composite material.

Often, continuum damage models are used in conjunction with failure theories to predict the nonlinear response of composite materials. The continuum damage approach is based on the work of Kachanov (1958) wherein he considers an undamaged material state which carries an “effective stress” and compares this configuration with the damaged material state which carries the “true stress”. Anisotropic damage behavior, where different components of the compliance/stiffness tensor are degraded by their own independent

variables, is typically considered for use in composite models (Maire and Chaboche 1997; Matzenmiller et al. 1995). A common feature of these models is that all of the nonlinearity is attributed to damage and plasticity is typically ignored. Additionally, nonlinear composite models often utilize empirical damage evolution laws to predict how damage will grow as a function of a chosen state variable (stress, plastic strain, crack density etc.). Currently, many of the composite models available in commercial programs, such as LS-DYNA, employ this approach including some of the models presented in Table 1. Chang and Chang (Chang and Chang 1987a, 1987b) use a model in which both fiber and matrix failure criteria are used to reduce elastic properties for nonlinear progressive failure modeling. Yen (2012) presents a model wherein a damage surface is generated by utilizing different failure modes. The elastic stiffness tensor is degraded based on the damage surface which allows for the nonlinear response to be captured. This model also allows for prescribed coupling between certain damage parameters. Forghani and co-workers (Forghani et al. 2013) define equivalent strains for the initiation of fiber and matrix damage modes respectively and compare the values against a damage initiation strain. Damage parameters are calculated based on equivalent strain, initiation strain, and saturation strain utilizing a predefined damage evolution law. The damage parameters are then used to scale down the stress. Maimi and co-workers (Maimí et al. 2007a, 2007b) define four damage activation functions, based on separate failure criteria for fiber and matrix mechanisms, which define an initial elastic domain. The damage evolution functions are then constrained by the Karush-Kuhn-Tucker (KKT) optimality conditions (Karush 1939; Kuhn and Tucker 1951), similar to a plasticity model.

Damage may be characterized through a series of cyclic loading experiments. This is not to be mistaken with fatigue, where the specimen is cyclically loaded to a single pre-specified level of load or deformation and stiffness reduction is caused by a different mechanism (Philippidis and Vassilopoulos 2001). The stiffness reduction being measured, in this research, is caused by monotonic loading. Extensive research has been done on this subject including identifying damage mechanisms, developing experimental techniques, and processing the resulting experimental data. Daniel and Lee (Daniel and Lee 1990) investigate damage growth in composites under monotonic loading by measuring crack density in cross-ply laminates at various applied stress levels. Mirzaali and co-workers (Mirzaali et al. 2015) utilize an experimental procedure involving conditioning cycles to investigate damage in osteonal bone. Medina and co-workers (Medina et al. 2014) have experimentally investigated damage evolution during in-plane shear tests as a function of the composite architecture, including unidirectional laminates. The cyclic shear tests showed that the shear modulus reduces as much as 50% as plastic strain increases. Additionally, the stress-strain curves exhibit large hysteretic loops which are also indicative of increasing damage. Walter and co-workers (Walter et al. 2010) performed cyclic loading tests of short beams and observed that the loading and unloading cycles had minimal effect on the monotonic response of the material implying that the monotonic stress-strain curve envelopes the cyclic loading curve.

The framework of OEPDMM considers both stiffness reduction, through the damage sub-model, and plastic deformation, through the deformation sub-model. Consistent with the deformation sub-model, the damage sub-model is driven completely by tabulated

experimental data. The damage law allows for both uncoupled and coupled damage parameters to be defined. Uncoupled damage signifies that damage is induced in a PMD or PMP and the elastic stiffness is reduced in the same PMD or PMP. On the other hand, coupled damage indicates that when damage is induced in a PMD or PMP, the elastic stiffness is reduced in a different PMD or PMP. This is true for both shear and normal loading. The damage parameters are obtained through a series of cyclic loading experiments designed to induce damage in a given PMD or PMP and then interrogate the effects on the same or different PMD or PMP. Allowing full uncoupled and coupled damage yields a general formulation that can be tailored for any composite. The damage parameters are denoted as d_{ij}^{kl} indicating damage has been induced in direction *ij* and the reduction of stiffness has manifested in direction *kl*. In addition, the model does not assume that the tensile and compressive behaviors are the same and accounts for tension-compression asymmetry. Since the model is driven by tabulated data in the form of damage-total strain curves, arbitrary damage evolution laws are permitted offering more flexibility than the previously discussed approaches.

1.3 Failure Modeling Literature Review

Though the failure sub-model within OEPDMM is not presented in detail within this document, for the purpose of completeness, failure modeling is briefly discussed. Often, the terms damage and failure are used interchangeably within the context of finite element analysis. Within OEPDMM, *damage* refers to degradation of elastic properties, while *failure* refers to complete loss of load carrying capacity and results in the numerical deletion or erosion of an element from the model. Failure of composites has been

investigated at both the microscale and the macroscale. At the microscale, the failure of a composite structure is attributed to a particular failure mechanism of one of the constituents. Jelf and Fleck (Jelf and Fleck 1992) have examined various composite failure mechanisms that are prominent in composites. The mechanisms include fiber failure, elastic microbuckling, matrix failure, and plastic microbuckling. Ha and coworkers (Ha et al. 2008) have developed a micromechanical failure model which is capable of predicting specific failure modes for a variety of composite systems and loading conditions. At the macroscale, failure is typically predicted using strain and stress ratios. The Tsai-Wu failure criterion (Tsai and Wu 1971) is a quadratic failure criterion which utilizes stress to strength ratios with full stress interaction to predict the failure of composites. Recently, there has been a concerted effort to identify strengths and weaknesses of various proposed methods of predicting failure in polymer matrix composites. The effort is known formally as the World-Wide Failure Exercise and has recently completed its third iteration (Hinton et al. 2004; Hinton and Kaddour 2012; Kaddour et al. 2013). While the exercise has helped refine some of the failure models thought to be completely mature, it has also shown that there is much to be done in the field of composite failure.

Within OEPDMM, multiple failure theories are currently being implemented including a tabulated failure approach wherein a stress based failure surface can be supplied by the user (Goldberg et al. 2018). In the tabulated approach, no assumptions are made as to the shape of the surface or architecture of the composite. The tabulated input may be derived directly from physical experimentation, however, this process may prove to be cumbersome. Thus virtual testing can be employed as a means by which the required data

is obtained (Harrington et al. 2017). To date, the required physical/virtual testing to generate the failure surface has not been performed. The proposed approach is currently in its infancy and is a focus of future work (Shyamsunder et al. 2019).

1.4 Cohesive Zone Modeling Literature Review

While composites are often referred to as materials, they are in fact complex structures. Being comprised of individual constituents and interfaces makes prediction of where and how failure occurs, a difficult task. Several failure theories which attempt to describe possible failure modes in composite laminae have been proposed, a subset of which have been outlined in Section 1.3. The researchers often use stress, strain, or energy relations to predict how a lamina will fail. Often, these failure models do not account for the laminated nature of some composite structures, e.g. unidirectional composites. Reiner and Vaziri (2017) provide an overview of popular techniques used in modeling composite behavior including damage and failure. They discuss techniques to predict damage initiation and evolution at various spatial scales using both continuum and discrete modeling approaches. The third worldwide failure exercise (WWFE3) (Kaddour et al. 2013) has recently been completed and was focused on predicting and analyzing damage mechanisms, including delamination, in composites. Composite materials are most often used as laminates in practice to compensate for intrinsic weaknesses in the composite architecture, e.g. large degrees of anisotropy present in unidirectional composites. The interface where two composite laminae are bonded is inherently weaker than the rest of the composite structure making delamination a critical failure mode since the overall load carrying capacity of the structure is affected while the laminae may remain fully intact.

Delamination damage may develop in composite laminates involved in impact events without any external signs being exhibited. Research conducted by Choi and co-workers (Choi et al. 1991) showed that there exists an energy threshold above which damage is likely to occur. Their forensic imaging technique indicated that the damage threshold does not necessarily coincide with observable exterior damage. Cantwell and Morton (1989) performed both low and high velocity impacts on carbon fiber reinforced polymer laminates of varying stacking sequences and thicknesses and provided micrographs showing significant delamination without complete perforation of the laminate. They also showed that the specimens subjected to low velocity impact, and subsequently tested in tension, exhibited a strength reduction of up to 30% prior to perforation. Research conducted by Finn and co-workers (Finn et al. 1993) showed delamination of various composite laminates under relatively low impact energies. Sun and Hallett (2017) investigated the delamination of single-ply laminates and blocked-ply laminates subjected to low velocity impact. Their results showed delamination developing between all ply interfaces at impact energies between 10 J and 16 J. Sun and Hallett (2018) performed compression after impact (CAI) experiments on two types of composite laminates and the results showed a reduction in strength of up to 70%. In addition to strength reduction under static, monotonic loading, Clark (1989) and Jones and co-workers (Jones et al. 1988) also showed the strength continues to reduce under fatigue loading. Aircraft structures experience a wide variety of fatigue loading conditions throughout their lifetime including pressurizing and depressurizing that affect the fuselage, wings, etc. The wide array of

experimental results indicate that delamination must be accounted for in predictive models of composite structures.

Since delamination is essentially the propagation of a crack through a medium, fracture mechanics becomes an attractive approach to describe the phenomena. While the assumptions governing linear elastic fracture mechanics (LEFM) (Griffith 1920; Irwin 1957) are easily violated by many loading conditions and materials, the concept of cohesive fracture mechanics, first introduced by Dugdale (1960) and Barenblatt (1962) separately, is more easily adapted to delamination since it allows for nonlinear and progressive failure of the material. The concepts of cohesive fracture mechanics have been widely used in modeling the interfaces present in composite materials within the framework of finite element (FE) analysis using cohesive zone models (CZM) (Caner et al. 2011; Chandra 2002; Šmilauer et al. 2011). CZM allow the analyst to represent the interface as a component within the composite laminate. The constitutive relation governing the CZM is in the form of a traction-separation law shown in Fig. 3 where $\sigma_{\max}$ is the maximum allowable traction, δ_0 is the separation when softening begins, δ_f is the separation when the material ultimately fails, and *k* is the initial penalty stiffness.

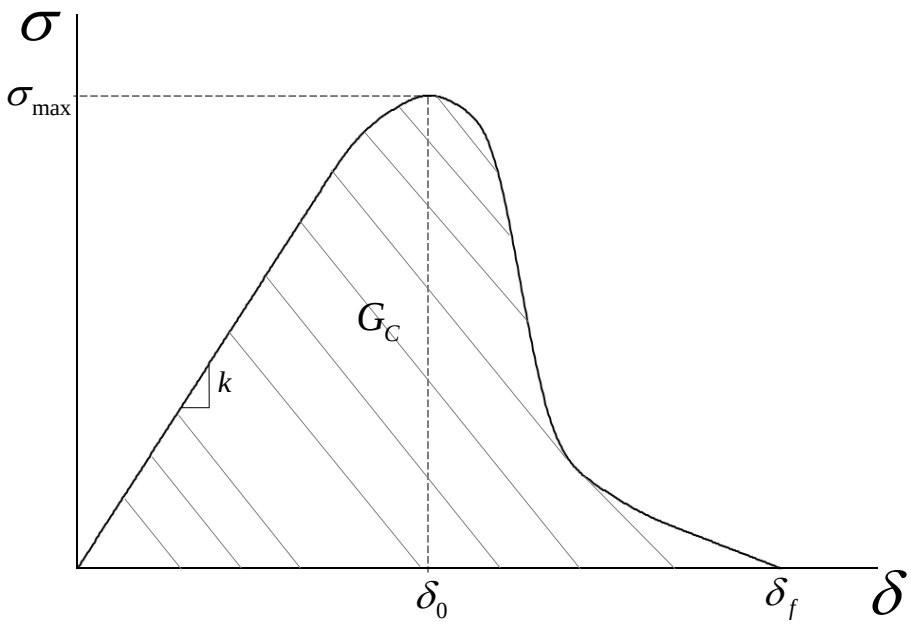

Fig. 3. General Traction Separation Law Used in CZM

Extensive research has been performed on devising new cohesive zone laws and as well as incorporating CZM in the analysis of composites. One major advantage of utilizing CZM to model delamination instead of other techniques like virtual crack closure technique (VCCT), is that no initial flaw is required. In other words, no knowledge of where delamination is initiated is required *a priori* (Elices et al. 2002; Krueger et al. 2013). However, the locations where delamination may potentially occur, must be modeled using cohesive zone elements (CZE). Borg and co-workers (Borg et al. 2004) devised a delamination model for shell elements that utilizes a penalty contact formulation for tying shells together and a cohesive zone model which accounts for degradation of adhesive forces. The degradation model utilizes both force and energy measures. Camanho and co-workers (Camanho et al. 2003) developed a decohesion element enhancing the modeling of mixed mode delamination where a quadratic traction interaction law is used to predict

when softening of the interface would start under mixed mode fracture conditions. Elmarakbi and co-workers (Elmarakbi et al. 2009) devised an adaptive CZM scheme in which a bilinear traction separation law was utilized that changes depending on the state of the deformed cohesive zone element (CZE). The adaptive nature resulted in a more stable response and avoided the elastic snapback phenomenon often encountered in simulations using CZM. While a bilinear traction-separation law is often used to describe the cohesive zone behavior because of its simplicity, trilinear laws are also employed because these laws can better capture the effects of fiber bridging that show an increase in critical energy release rate as the crack propagates (Heidari-Rarani et al. 2013; Li et al. 2005). One shortcoming of many of the traction-separation laws is that they use a pre-determined shape of the constitutive behavior despite how the material may actually behave (Li et al. 2005; Tsouvalis and Anyfantis 2011).

Under impact events, delamination rarely falls into a pure fracture mode (i.e. Mode I or Mode II). Rather, the delamination is likely caused by some combination of the two (Benzeggagh and Kenane 1996). The mixed mode interaction theories are driven by a set of Mode I and Mode II CZM parameters. The double cantilever beam (DCB) test has been employed by many researchers to characterize Mode I behavior (Gillespie Jr. et al. 1986a; Johnson and Mangalgiri 1987; Martin and Murri 1988; Prel et al. 1989; Wilkins 1981) while the end notched flexure (ENF) test has been used to characterize Mode II behavior (Gillespie Jr. et al. 1986b; Martin and Murri 1988; Prel et al. 1989; Russell and Street 1985). Obtaining parameters to drive CZM can be achieved through experimental techniques, numerical calibration, or a combination of both. While the Mode I and Mode

II critical energy release rates (G_C) can typically be computed directly from the experimental results of the DCB and ENF tests using elastic beam theory (Hashemi et al. 1990), the remaining parameters shown in Fig. 3 are more difficult to obtain analytically and are typically determined by calibration of FE models with experimental data. Some researchers have streamlined the process of obtaining CZM parameters either through novel analytical techniques (Arrese et al. 2017), through design of experiments and optimization methods (Lee et al. 2010), or through inverse solution techniques (Ortega et al. 2016). However, numerical calibration of the CZM model may lead to a non-unique set of parameters that may need to be retuned depending on the loading conditions the composite is subjected to. While researchers have used experimental data to completely derive the Traction Separation Law (TSL) for a given composite system or interface (Fuchs and Major 2011; van der Vossen and Makeev 2018; Zhu et al. 2009), the developed relationship is used in verification rather than validation simulations.

1.5 Dissertation Objectives

OEPDMM is currently being developed as a generalized orthotropic composite tabulated plasticity damage material model. The genesis of OEPDMM comes from a need for a robust model that can be used for simulating a wide array of loading conditions common in aerospace structures, such as impact and crush. OEPDMM offers flexibility to the analyst as all of the required input is provided in the form of tabulated data. This input data can be generated via laboratory experiments or via virtual testing (Harrington et al. 2017). OEPDMM is also versatile since it allows for the analyst to include many effects which drive composite behavior in the simulation, e.g. plasticity, damage, failure, tension-

compression asymmetry, strain rate dependent deformation, and temperature dependent deformation. This dissertation focuses on the continuing development of MAT 213. The primary objectives are presented below.

1. Use on the T800S/F3900 unidirectional carbon fiber/epoxy resin composite system to illustrate OEPDMM features. The detailed study includes characterizing the material under quasi-static and room temperature conditions to obtain the necessary data required to drive the deformation, damage and failure sub-models. Monotonic tension, compression, and shear tests are performed to obtain the required data for the deformation and failure models while cyclic loading tests are performed illustrating how both uncoupled and coupled damage parameters are obtained for the semi-coupled damage model.
2. Provide the techniques used to extract the input from the experimental data necessary to run the material model.
3. Provide theoretical and implementation details for the orthotropic, semi-coupled damage model and illustrate how the damage model is incorporated into MAT 213.
4. Experimentally characterize the fracture behavior of the T800/F3900 composite and utilize cohesive zone modeling in conjunction with MAT 213 to enhance the predictive capabilities of the material model.
5. Perform verification testing with real experimental data to verify the accuracy of the implemented material model.
6. Perform validation testing in the form of plate low and high-velocity impact analysis to highlight the predictive capabilities of the developed approach.

2 DEFORMATION SUB-MODEL

Within OEPDMM, the deformation sub-model handles the evolution of stresses and strains in both the elastic and inelastic regimes. The material behavior is captured through a classical plasticity formulation with non-associative flow which utilizes fully tabulated stress-strain data in the principal material directions (PMD) and principal material planes (PMP) of the material to drive hardening behavior. This section provides theoretical details of the deformation sub-model, the experimental techniques used to derive the required input, and the results of a case study using the T800S/F3900 carbon fiber/epoxy resin unidirectional composite system manufactured by Toray.

2.1 Theoretical Details

In OEPDMM, stresses are assumed to be driven completely by elastic strains. The basic constitutive relationship can be written in rate form by linearly decomposing the total strain rate into elastic and plastic components as follows

$$\dot{\boldsymbol{\sigma}} = \mathbf{C} : \left(\dot{\boldsymbol{\varepsilon}}^{e} \right) = \mathbf{C} : \left(\dot{\boldsymbol{\varepsilon}}^{\mathbf{t}} - \dot{\boldsymbol{\varepsilon}}^{\mathbf{p}} \right) \tag{2.1}$$

where $\dot{\boldsymbol{\sigma}}$ is the Cauchy stress rate tensor, $\dot{\boldsymbol{\varepsilon}}^{\mathbf{t}}$ is the total strain rate tensor, $\dot{\boldsymbol{\varepsilon}}^{\mathbf{p}}$ is the plastic strain rate tensor, $\dot{\boldsymbol{\varepsilon}}^{e}$ is the elastic strain rate tensor, and $\mathbf{C}$ is the orthotropic elastic stiffness tensor shown below in Voigt notation.

$$\mathbf{C} = \mathbf{S}^{-1} = \begin{bmatrix} \frac{1}{E_{11}^{T/C}} & -\frac{v_{21}}{E_{22}^{T/C}} & -\frac{v_{31}}{E_{33}^{T/C}} & 0 & 0 & 0 \\ & \frac{1}{E_{22}^{T/C}} & -\frac{v_{32}}{E_{33}^{T/C}} & 0 & 0 & 0 \\ & & \frac{1}{E_{33}^{T/C}} & 0 & 0 & 0 \\ & & & \frac{1}{G_{23}} & 0 & 0 \\ & Sym & & & \frac{1}{G_{31}} & 0 \\ & & & & & \frac{1}{G_{12}} \end{bmatrix}^{-1} \qquad 2.2$$

where the subscripts 1-2-3 refer to the orthogonal PMD of the orthotropic material and the superscripts *T/C* indicate tension and compression respectively. Depending on the sign of the stress at the current instance of time during the simulation, the appropriate Young's modulus from the tabulated input curves are chosen for use in the analysis. The quadratic yield function takes a form similar to the Tsai-Wu failure criteria (Tsai and Wu 1971) and governs anisotropic yield stress evolution in the composite.

$$f(\sigma) = a + \begin{bmatrix} F_1 \\ F_2 \\ F_3 \\ 0 \\ 0 \\ 0 \end{bmatrix}^T \begin{bmatrix} \sigma_{11} \\ \sigma_{22} \\ \sigma_{33} \\ \sigma_{12} \\ \sigma_{23} \\ \sigma_{31} \end{bmatrix} + \begin{bmatrix} \sigma_{11} \\ \sigma_{22} \\ \sigma_{33} \\ \sigma_{12} \\ \sigma_{23} \\ \sigma_{31} \end{bmatrix}^T \begin{bmatrix} F_{11} & F_{12} & F_{13} & 0 & 0 & 0 \\ F_{12} & F_{22} & F_{23} & 0 & 0 & 0 \\ F_{13} & F_{23} & F_{33} & 0 & 0 & 0 \\ 0 & 0 & 0 & F_{44} & 0 & 0 \\ 0 & 0 & 0 & 0 & F_{55} & 0 \\ 0 & 0 & 0 & 0 & 0 & F_{66} \end{bmatrix} \begin{bmatrix} \sigma_{11} \\ \sigma_{22} \\ \sigma_{33} \\ \sigma_{12} \\ \sigma_{23} \\ \sigma_{31} \end{bmatrix} \qquad 2.3$$

where the value of a is taken as -1 such that a negative value of $f(\boldsymbol{\sigma})$ indicates an elastic state and a positive value indicates a plastic state. The yield function includes linear terms corresponding to the PMD resulting in the ability to distinguish between a tensile and compressive state of loading. The yield function coefficients corresponding to stresses solely in the PMD or PMP, F_{ii} and F_i, are a function of the yield stresses, the stress required to initiate plastic flow in the material at a given time instance, and are thus treated as variable due to hardening that may occur.

$$\begin{aligned}
F_1 &= \frac{1}{\sigma_{11}^T} - \frac{1}{\sigma_{11}^C} & F_{11} &= \frac{1}{\sigma_{11}^T \sigma_{11}^C} & F_{44} &= \frac{1}{\sigma_{12}^2} \\
F_2 &= \frac{1}{\sigma_{22}^T} - \frac{1}{\sigma_{22}^C} & F_{22} &= \frac{1}{\sigma_{22}^T \sigma_{22}^C} & F_{55} &= \frac{1}{\sigma_{23}^2} \\
F_3 &= \frac{1}{\sigma_{33}^T} - \frac{1}{\sigma_{33}^C} & F_{33} &= \frac{1}{\sigma_{33}^T \sigma_{33}^C} & F_{66} &= \frac{1}{\sigma_{31}^2}
\end{aligned} \qquad 2.4$$

where the superscripts T and C refer to tension and compression respectively allowing OEPDMM to handle asymmetric yield surface evolution (e.g. different behavior in tension and compression). The form of each of the coefficients is a result of assuming a state of uniaxial stress in a given PMD or PMP and solving for the unique set of values which satisfy the yield function. The full derivation can be found in Tsai and Wu's original paper (Tsai and Wu 1971). The ability to distinguish between tension and compression in the PMD is a desirable characteristic not found in other theories of plastic flow in anisotropic materials such as criterion proposed by Hill (1948) and later modified by Azzi and Tsai (1965). The interaction terms, F_{ij}, shown in Eq. 2.3, are derived from experimental data

wherein a multiaxial state of stress is induced in the material. While this process typically involves biaxial tension or compression tests, a similar effect can be achieved by performing uniaxial tension or compression experiments where the loading axis makes a non-zero angle with a given PMD, referred to as off-axis tension/compression tests. The following procedure shows how the values of F_{ij} are determined from off-axis tests. Fig. 4 shows a specimen where the PMD, shown in the 1-2 plane as an example, are rotated at an arbitrary angle from the longitudinal axis. A stress induced along the X-axis is denoted as σ_x.

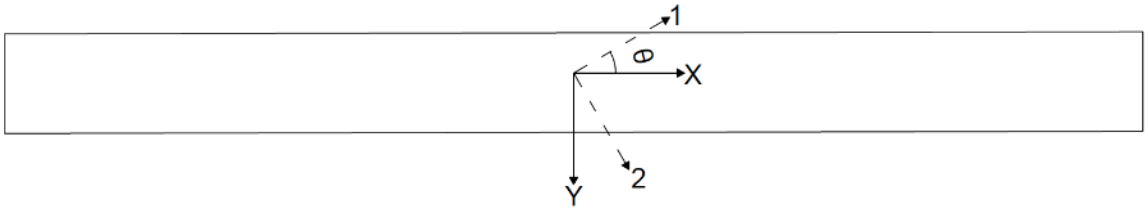

Fig. 4. Off-axis Tension/Compression Specimen in the 1-2 Plane

Assuming only tensile σ_x is induced in the material, the components of stress in the respective PMD can be obtained through a stress transformation

$$\begin{aligned} \sigma_{11} &= \sigma_x \cos^2(\theta) \\ \sigma_{22} &= \sigma_x \sin^2(\theta) \\ \sigma_{12} &= -\sigma_x \sin(\theta)\cos(\theta) \end{aligned} \qquad 2.5$$

The yield function can be rewritten in terms of the transformed stresses as

$$f(\boldsymbol{\sigma}) = a + F_1\sigma_{11} + F_2\sigma_{22} + F_3\sigma_{33} + F_{11}\sigma_{11}^2 + 2F_{12}\sigma_{11}\sigma_{22} + 2F_{13}\sigma_{11}\sigma_{33} + F_{22}\sigma_{22}^2 + 2F_{23}\sigma_{22}\sigma_{33} + F_{33}\sigma_{33}^2 + F_{44}\sigma_{12}^2 + F_{55}\sigma_{23}^2 + F_{66}\sigma_{31}^2$$

$$\begin{aligned} f(\boldsymbol{\sigma}) = -1 &+ F_1\left(\sigma_x\cos^2(\theta)\right) + F_2\left(\sigma_x\sin^2(\theta)\right) + F_{11}\left(\sigma_x\cos^2(\theta)\right)^2 \\ &+ 2F_{12}\left(\sigma_x\cos^2(\theta)\right)\left(\sigma_x\sin^2(\theta)\right) + F_{22}\left(\sigma_x\sin^2(\theta)\right)^2 \\ &+ F_{44}\left(-\sigma_x\sin(\theta)\cos(\theta)\right)^2 \end{aligned} \qquad 2.6$$

By assuming a state under which the material has yielded, the interaction term, F_{12}, can be solved for as

$$F_{12} = \frac{1 - \sigma_x\left[F_1\cos^2(\theta) + F_2\sin^2(\theta)\right] - \sigma_x^2\left[F_{11}\cos^4(\theta) + F_{22}\sin^4(\theta) + F_{44}\cos^2(\theta)\sin^2(\theta)\right]}{2\sigma_x^2\cos^2(\theta)\sin^2(\theta)} \qquad 2.7$$

For example, by assuming a compressive state of stress, the linear terms are affected, and the resulting expression takes the following form:

$$F_{12} = \frac{1 + \sigma_x\left[F_1\cos^2(\theta) + F_2\sin^2(\theta)\right] - \sigma_x^2\left[F_{11}\cos^4(\theta) + F_{22}\sin^4(\theta) + F_{44}\cos^2(\theta)\sin^2(\theta)\right]}{2\sigma_x^2\cos^2(\theta)\sin^2(\theta)} \qquad 2.8$$

A similar procedure can be followed to determine F_{13} and F_{23} respectively. Since the values of the interaction terms depend on the other coefficients, F_{ii} and F_i, they too are treated as variables. While the values of F_{ij} may be determined directly from experimental data, the values must also ensure convexity of the yield function. Tsai and Wu (1971)

proposed constraints on the values of the yield function coefficients, ensuring convexity and uniqueness of $f(\boldsymbol{\sigma})$, which take the following form

$$F_{ii}F_{jj} - F_{ij}^2 \geq 0 \tag{2.9}$$

where repeating indices do not imply a summation. Eq. 2.9 also implies

$$F_{ii} > 0 \tag{2.10}$$

By rearranging Eq. 2.9, the values of F_{ij} are restricted to

$$F_{ij} = \alpha\sqrt{F_{ii}F_{jj}} \quad \textit{where} \quad -1 \leq \alpha \leq 1 \tag{2.11}$$

Within the context of OEPDMM, if the experimental data, Eq. 2.7 and Eq. 2.8, do not satisfy the constraints set forth in Eq. 2.9, a *convex correction* is performed based on Eq. 2.11 to ensure numerical stability. In the current implementation, $\alpha = -1/2$ in Eq. 2.11.

Often, the yield function, $f(\boldsymbol{\sigma})$, is used not only to handle hardening of the material, but also the evolution of plastic strains. The plastic strain increment is typically assumed to be proportional to the stress gradient of the yield function for a given state of stress. The

resulting expression is known as an associated flow rule (Bland 1957; Drucker 1956; Ilyushin 1961; Prager 1947) and takes the following form

$$d\boldsymbol{\varepsilon}^p = d\lambda \frac{\partial f}{\partial \boldsymbol{\sigma}} \tag{2.12}$$

where $d\lambda$ is the scalar plastic multiplier increment and $\frac{\partial f}{\partial \boldsymbol{\sigma}}$ is the stress gradient of the yield function, a rank two tensor. Using an associated flow rule is not always desirable since the resulting equations may not be representative of the true behavior of the material (Hoffarth et al. 2017; Lubarda et al. 1996). Composites may exhibit varying degrees of plastic anisotropy, and more control over the plastic strain evolution is required, which may not be offered by the yield function. In such a case, a separate *plastic potential* function is introduced to separately handle the evolution of plastic strains. Eq. 2.13 shows a general quadratic function used as the plastic potential function in OEPDMM.

$$\begin{aligned} h^2 = {} & H_{11}\sigma_{11}^2 + H_{22}\sigma_{22}^2 + H_{33}\sigma_{33}^2 + 2H_{12}\sigma_{11}\sigma_{22} + 2H_{23}\sigma_{22}\sigma_{33} + 2H_{13}\sigma_{11}\sigma_{33} \\ & + \frac{1}{2}H_{44}\sigma_{12}^2 + \frac{1}{2}H_{44}\sigma_{21}^2 + \frac{1}{2}H_{55}\sigma_{23}^2 + \frac{1}{2}H_{55}\sigma_{32}^2 + \frac{1}{2}H_{66}\sigma_{13}^2 + \frac{1}{2}H_{66}\sigma_{31}^2 \end{aligned} \tag{2.13}$$

The non-associated flow rule used in OEPDMM is then written as

$$d\boldsymbol{\varepsilon}^p = d\lambda \frac{\partial h}{\partial \boldsymbol{\sigma}} \tag{2.14}$$

where $\frac{\partial h}{\partial \boldsymbol{\sigma}}$ is the stress gradient of the plastic potential function, a rank two tensor. The values of H_{ij}, herein referred to as the *flow rule coefficients*, in Eq. 2.13 must also conform to similar constraints governing the yield function coefficients. In order to ensure *h* is a convex function, necessary to ensure a unique solution to the problem, Eq. 2.13 must have a positive semi-definite Hessian matrix. This condition leads to the following set of constraints imposed on the elements of the coefficient matrix:

$$\begin{aligned} H_{ii}H_{jj} - H_{ij}^2 &\geq 0 \\ H_{ii} &\geq 0 \end{aligned} \qquad 2.15$$

where repeating indices do not imply a summation. The yield function coefficients and the flow rule coefficients are derived from experimental data independently. Additionally, whereas the yield function coefficients evolve during loading, the flow rule coefficients are assumed to remain constant.

The evolution of the yield stresses in the yield function, Eq. 2.4, is governed by tabulated input provided in the form of stress-total strain curves in the PMD and PMP. Specifically, tension and compression curves in the 1, 2, and 3 directions respectively; shear curves in the 1-2, 2-3, and 1-3 planes respectively; and off-axis tension or compression curves in the 1-2, 2-3, and 1-3 planes respectively. These curves can be supplied to MAT 213 at various total strain rates and temperatures. The curves are utilized in lieu of a predefined hardening law employed by other constitutive models to control yield surface evolution. Each of the

stress-total strain curves is internally converted to stress-effective plastic strain. This conversion offers a convenient means of tracking the individual yield stresses through a global scalar parameter. The conversion is done by utilizing the principle of equivalent plastic work (Berg 1972), shown below.

$$dW^p = \sigma_{ij} d\varepsilon_{ij}^p = \sigma_e d\varepsilon_e^p \tag{2.16}$$

The principle of equivalent plastic essentially states that there exists an equivalent scalar effective stress, σ_e, and scalar effective plastic strain increment, $d\varepsilon_e^p$, whose product is always equivalent to the scalar plastic work increment, dW^p, which is the result of fully contracting the stress tensor, $\boldsymbol{\sigma}$, with the incremental plastic strain tensor, $d\boldsymbol{\varepsilon}^p$. Using the flow rule, Eq. 2.14, the plastic work increment can be written as

$$\begin{aligned}
dW^p &= \sigma_{ij} d\varepsilon_{ij}^p \\
&= \sigma_{11}\left[\frac{d\lambda}{h}\left(H_{11}\sigma_{11} + H_{12}\sigma_{22} + H_{13}\sigma_{33}\right)\right] \\
&+ \sigma_{22}\left[\frac{d\lambda}{h}\left(H_{12}\sigma_{11} + H_{22}\sigma_{22} + H_{23}\sigma_{33}\right)\right] \\
&+ \sigma_{33}\left[\frac{d\lambda}{h}\left(H_{13}\sigma_{11} + H_{23}\sigma_{22} + H_{33}\sigma_{33}\right)\right] \\
&+ \sigma_{12}\left[\frac{d\lambda}{2h}\left(H_{44}\sigma_{12}\right)\right] + \sigma_{21}\left[\frac{d\lambda}{2h}\left(H_{44}\sigma_{21}\right)\right] \\
&+ \sigma_{23}\left[\frac{d\lambda}{2h}\left(H_{55}\sigma_{23}\right)\right] + \sigma_{32}\left[\frac{d\lambda}{2h}\left(H_{55}\sigma_{32}\right)\right] \\
&+ \sigma_{13}\left[\frac{d\lambda}{2h}\left(H_{66}\sigma_{13}\right)\right] + \sigma_{31}\left[\frac{d\lambda}{2h}\left(H_{66}\sigma_{31}\right)\right]
\end{aligned} \tag{2.17}$$

By utilizing the expanded form of the plastic potential function, Eq. 2.13, Eq. 2.17 can be reduced to

$$dW^p = \sigma_{ij} d\varepsilon_{ij}^p = h d\lambda \tag{2.18}$$

By assuming that the value of the plastic potential function, *h*, is the effective stress, the value of the incremental plastic multiplier, $d\lambda$, must then be equivalent to the effective plastic strain increment, $d\varepsilon_e^p$. The value of $d\lambda$ can then be written as follows

$$d\lambda = \frac{\sigma_{ij} d\varepsilon_{ij}^p}{h} \tag{2.19}$$

In the case of monotonic loading, Eq. 2.19 is integrable and results in

$$\lambda = \int \frac{\sigma_{ij} d\varepsilon_{ij}^p}{h} \tag{2.20}$$

Eq. 2.20 serves as the basis for converting input stress-total strain curves to stress-effective plastic strain which provide a convenient means of tracking the yield surface growth in all PMD based on a single global scalar value, λ. An example of how the 1-direction stress-total strain input curve is converted into stress-effective plastic strain is shown in Eq. 2.21

.

$$\lambda = \int \frac{\sigma_{ij} d\varepsilon_{ij}^{p}}{h} = \lambda = \int \frac{\sigma_{11} d\varepsilon_{11}^{p}}{\sqrt{H_{11}\sigma_{11}^{2}}} \tag{2.21}$$

Eq. 2.21 assumes the input stress-total strain curve in the 1-direction is the result of a uniaxial stress induced in the 1-direction, thereby reducing the effective stress, *h*, to include only terms related to uniaxial 1-direction stresses. The value of λ is the independent internal state variable which is solved for during plasticity calculations at a given integration point during a simulation. The Karush-Kuhn-Tucker complementarity conditions are enforced during loading/unloading events to ensure the yield surface does not shrink.

$$\dot{\lambda} \geq 0, \;\; f \leq 0, \;\; \dot{\lambda} f = 0 \tag{2.22}$$

The plastic multiplier increment is found by enforcing the consistency condition

$$\dot{\lambda} \dot{f} = 0 \tag{2.23}$$

which ensures the state of stress remains on the yield surface during plastic flow, $\dot{\lambda} > 0$. By enforcing the consistency condition, the solution for the plastic multiplier increment is solved as

$$\dot{f} = \frac{\partial f}{\partial \boldsymbol{\sigma}} \dot{\boldsymbol{\sigma}} + \frac{\partial f}{\partial \mathbf{q}} \dot{\mathbf{q}} = 0$$
$$\dot{f} = \frac{\partial f}{\partial \boldsymbol{\sigma}} \mathbf{C} : \left(\dot{\boldsymbol{\varepsilon}}^t - \dot{\lambda} \frac{\partial h}{\partial \boldsymbol{\sigma}} \right) + \frac{\partial f}{\partial \mathbf{q}} \dot{\lambda} \frac{d\mathbf{q}}{d\lambda} \qquad 2.24$$
$$\dot{\lambda} = \frac{\frac{\partial f}{\partial \boldsymbol{\sigma}} \mathbf{C} : \dot{\boldsymbol{\varepsilon}}^t}{\frac{\partial f}{\partial \boldsymbol{\sigma}} \mathbf{C} : \frac{\partial h}{\partial \boldsymbol{\sigma}} + \frac{\partial f}{\partial \mathbf{q}} \frac{d\mathbf{q}}{d\lambda}}$$

where $\mathbf{q}$ is the vector of the twelve yield stress values at the current instance of time. The plastic multiplier increment is solved for using a secant iteration root finding algorithm in conjunction with the radial return method (Simo and Taylor 1986). The increment is used to sequentially update the value of λ which is used to compute the updated yield function coefficients, i.e. $F_{ij}(\lambda)$ and $F_i(\lambda)$. Full implementation details are provided in an earlier work (Hoffarth et al. 2016). Fig. 5 illustrates the internal conversion of the input stress-total strain curves into stress-effective plastic strain curves for a PMD exhibiting plastic behavior.

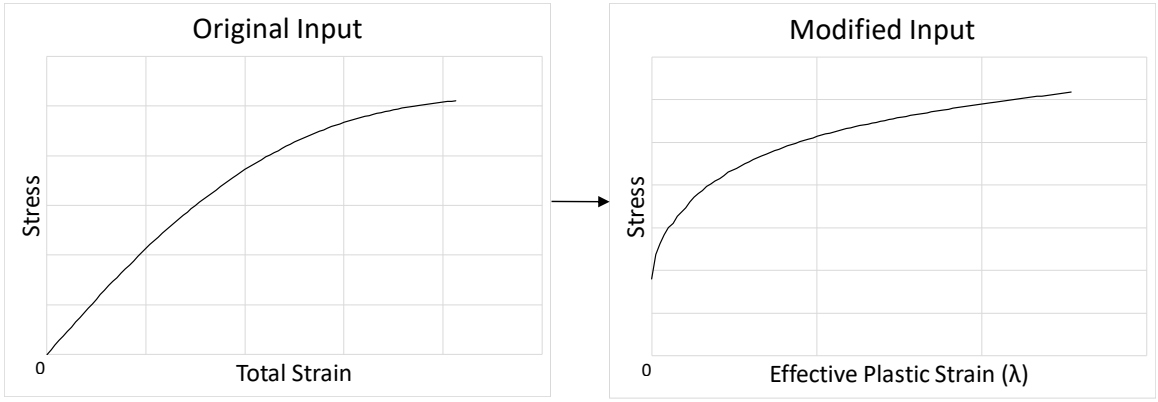

Fig. 5. Illustration of the Conversion of Tabulated Input Curves from Stress-Total Strain to Stress-Effective Plastic Strain

Prior to a non-zero value of λ being computed, the material is assumed to behave linear elastically.

The constant flow rule coefficients are computed from the same set of input stress-total strain curves and are meant to be a measure of the plastic anisotropy in the material. Being constant, the values of the coefficients are independent of the temperature and strain rate during the simulation. This implies the plastic flow relationship between each of the PMD remains constant. Using the non-associated flow rule, Eq. 2.14, the plastic strain rate components are written as

$$
\begin{aligned}
d\boldsymbol{\varepsilon}^p &= d\lambda \frac{\partial h}{\partial \boldsymbol{\sigma}} \\
d\varepsilon_{11}^p &= \frac{d\lambda}{h}\left(H_{11}\sigma_{11} + H_{12}\sigma_{22} + H_{13}\sigma_{33}\right) \\
d\varepsilon_{22}^p &= \frac{d\lambda}{h}\left(H_{12}\sigma_{11} + H_{22}\sigma_{22} + H_{23}\sigma_{33}\right) \\
d\varepsilon_{33}^p &= \frac{d\lambda}{h}\left(H_{13}\sigma_{11} + H_{23}\sigma_{22} + H_{33}\sigma_{33}\right) \\
d\varepsilon_{12}^p &= \frac{d\lambda}{2h} H_{44}\sigma_{12} \quad d\varepsilon_{21}^p = \frac{d\lambda}{2h} H_{44}\sigma_{12} \\
d\varepsilon_{23}^p &= \frac{d\lambda}{2h} H_{55}\sigma_{23} \quad d\varepsilon_{32}^p = \frac{d\lambda}{2h} H_{55}\sigma_{32} \\
d\varepsilon_{13}^p &= \frac{d\lambda}{2h} H_{66}\sigma_{13} \quad d\varepsilon_{31}^p = \frac{d\lambda}{2h} H_{66}\sigma_{31}
\end{aligned}
\tag{2.25}
$$

It is now convenient to introduce the plastic Poisson's ratio, ν_{ij}^p, which provides a numerical means of relating the plastic strain evolution between two PMD. However, this value is not necessarily a material constant. The plastic Poisson's ratio is defined as

$$\nu_{xy}^{p} = -\frac{d\varepsilon_{yy}^{p}}{d\varepsilon_{xx}^{p}} \tag{2.26}$$

where repeating indices do not imply a summation. The values of ν_{xy}^{p} may be determined experimentally from uniaxial tension or compression tests in a given plane. For example, using the 1-2 plane as an example and referencing Fig. 4, a uniaxial stress applied along the X-axis, at an arbitrary angle θ from the PMD, induces stresses in the PMD given by Eq. 2.5 The plastic strain components in the 1-2 plane are then obtained by substituting Eq. 2.5 into Eq. 2.25 resulting in

$$\begin{aligned} d\varepsilon_{11}^{p} &= \frac{d\lambda}{h}\left(H_{11}\sigma_x \cos^2(\theta) + H_{12}\sigma_x \sin^2(\theta)\right) \\ d\varepsilon_{22}^{p} &= \frac{d\lambda}{h}\left(H_{12}\sigma_x \cos^2(\theta) + H_{22}\sigma_x \sin^2(\theta)\right) \\ d\varepsilon_{12}^{p} &= -\frac{d\lambda}{2h} H_{44}\sigma_x \sin(\theta)\cos(\theta) \end{aligned} \tag{2.27}$$

The plastic strains along the X and Y axes can then be obtained by transforming the plastic strains in Eq. 2.27 into the global coordinate system as

$$
\begin{aligned}
d\varepsilon_{xx}^{p} &= d\varepsilon_{11}^{p}\cos^{2}(\theta)+d\varepsilon_{22}^{p}\sin^{2}(\theta)-2d\varepsilon_{12}^{p}\sin(\theta)\cos(\theta) \\
&= \sigma_{x}\frac{d\lambda}{h}\left[H_{11}\cos^{4}(\theta)+H_{22}\sin^{4}(\theta)+(2H_{12}+H_{44})\sin^{2}(\theta)\cos^{2}(\theta)\right] \\
d\varepsilon_{yy}^{p} &= d\varepsilon_{11}^{p}\sin^{2}(\theta)+d\varepsilon_{22}^{p}\cos^{2}(\theta)+2d\varepsilon_{12}^{p}\sin(\theta)\cos(\theta) \\
&= \sigma_{x}\frac{d\lambda}{h}\left[H_{12}\left(\sin^{4}(\theta)+\cos^{4}(\theta)\right)+(H_{11}+H_{22}-H_{44})\sin^{2}(\theta)\cos^{2}(\theta)\right]
\end{aligned}
\qquad 2.28
$$

Substituting Eq. 2.28 into Eq. 2.26 yields the expanded expression for plastic Poisson's ratio as

$$
\nu_{xy}^{p} = -\frac{d\varepsilon_{yy}^{p}}{d\varepsilon_{xx}^{p}} = -\frac{H_{12}\left(\sin^{4}(\theta)+\cos^{4}(\theta)\right)+(H_{11}+H_{22}-H_{44})\sin^{2}(\theta)\cos^{2}(\theta)}{H_{11}\cos^{4}(\theta)+H_{22}\sin^{4}(\theta)+(2H_{12}+H_{44})\sin^{2}(\theta)\cos^{2}(\theta)} \qquad 2.29
$$

By assuming $\theta = 0^{\circ}$, since the 1-direction is oriented along the global X-axis, the value of ν_{12}^{p} can be determined. Similarly, by assuming $\theta = 90^{\circ}$, since the 2-direction is oriented along the global X-axis, the value of ν_{21}^{p} can be determined. Using the same approach in the other two PMP, 2-3 and 1-3, the six plastic Poisson's ratios can be related to a subset of the flow rule coefficients as

$$
\begin{array}{ccc}
1-2\,Plane & 2-3\,Plane & 1-3\,Plane \\
\nu_{xy}^{p}\big|_{\theta=0^{\circ}} = \nu_{12}^{p} = -\dfrac{d\varepsilon_{22}^{p}}{d\varepsilon_{11}^{p}} = -\dfrac{H_{12}}{H_{11}} & \nu_{xy}^{p}\big|_{\theta=0^{\circ}} = \nu_{23}^{p} = -\dfrac{d\varepsilon_{33}^{p}}{d\varepsilon_{22}^{p}} = -\dfrac{H_{23}}{H_{22}} & \nu_{xy}^{p}\big|_{\theta=0^{\circ}} = \nu_{13}^{p} = -\dfrac{d\varepsilon_{33}^{p}}{d\varepsilon_{11}^{p}} = -\dfrac{H_{13}}{H_{11}} \\
\nu_{xy}^{p}\big|_{\theta=90^{\circ}} = \nu_{21}^{p} = -\dfrac{d\varepsilon_{11}^{p}}{d\varepsilon_{22}^{p}} = -\dfrac{H_{12}}{H_{22}} & \nu_{xy}^{p}\big|_{\theta=90^{\circ}} = \nu_{32}^{p} = -\dfrac{d\varepsilon_{22}^{p}}{d\varepsilon_{33}^{p}} = -\dfrac{H_{23}}{H_{33}} & \nu_{xy}^{p}\big|_{\theta=90^{\circ}} = \nu_{31}^{p} = -\dfrac{d\varepsilon_{11}^{p}}{d\varepsilon_{33}^{p}} = -\dfrac{H_{13}}{H_{33}}
\end{array}
\qquad 2.30
$$

An example of how the values are computed is shown later in Section 2.3.2. The system of equations given by Eq. 2.30 is rank deficient and cannot uniquely be solved with the plastic Poisson's ratios alone. However, if one of the flow rule coefficient values is known, the remainder can be solved for using Eq. 2.30. At least one of the unknown flow rule coefficient values in Eq. 2.30 can be solved for by obtaining the effective stress-effective plastic strain curve which governs the material. The effective stress-effective plastic strain curve can be thought of as a property of the composite architecture and layup. The curve governs the plastic behavior of the composite and its invariance can be related back to the postulate of equivalence of plastic work. As previously discussed, the effective stress, under an arbitrary state of stress, is assumed to be equivalent to the value of the plastic potential function given by Eq. 2.13 while the effective plastic strain is equivalent to the plastic multiplier given by Eq. 2.20. For any composite architecture, the curves can be obtained by first making assumptions based on the observed physical behavior of the material system. For example, unidirectional composites often exhibit linear elastic behavior along the material direction aligned with the fibers. Thus, with reference to Fig. 1, the plastic strain rate in the 1-direction is taken as zero.

$$d\varepsilon_{11}^{p} = \frac{d\lambda}{h}\left(H_{11}\sigma_{11} + H_{12}\sigma_{22} + H_{13}\sigma_{33}\right) = 0 \qquad 2.31$$

For Eq. 2.31 to hold true for an arbitrary state of stress, all three coefficients appearing in the equation must be zero, i.e. $H_{11} = H_{12} = H_{13} = 0$. The plastic potential function, Eq. 2.13 , reduces to

$$h^2 = H_{22}\sigma_{22}^2 + H_{33}\sigma_{33}^2 + 2H_{23}\sigma_{22}\sigma_{33} + H_{44}\sigma_{12}^2 + H_{55}\sigma_{23}^2 + H_{66}\sigma_{13}^2 \qquad 2.32$$

Note that symmetry of the Cauchy stress tensor has been enforced by appropriately combining the shear terms. At the lamina level, unidirectional composites exhibit an isotropic structure in the 2-3 plane as shown in Fig. 2. Eq. 2.32 can then be further reduced to

$$h^2 = H_{22}\left(\sigma_{22}^2 + \sigma_{33}^2\right) + 2H_{23}\sigma_{22}\sigma_{33} + H_{44}\left(\sigma_{12}^2 + \sigma_{13}^2\right) + H_{55}\sigma_{23}^2 \qquad 2.33$$

Under a state of plane stress in the 1-2 plane, i.e. $\sigma_{33} = \sigma_{23} = \sigma_{13} = 0$, Eq. 2.33 reduces to

$$h^2 = H_{22}\sigma_{22}^2 + H_{44}\sigma_{12}^2 \qquad 2.34$$

Under an arbitrary off-axis loading condition (Fig. 4), using Eq. 2.5, Eq. 2.34 is given as

$$h^2 = H_{22}\sigma_x^2 \sin^4(\theta) + H_{44}\sigma_x^2 \sin^2(\theta)\cos^2(\theta) \qquad 2.35$$

The plastic potential function is then given by

$$h = \sigma_x g(\theta) \qquad 2.36$$

where

$$g(\theta)=\left[H_{22}\sin^4(\theta)+H_{44}\sin^2(\theta)\cos^2(\theta)\right]^{\frac{1}{2}} \tag{2.37}$$

Substituting Eq. 2.36 into Eq. 2.28, the effective plastic strain increment under off-axis loading in the 1-2 plane for a unidirectional composite can be written as

$$d\lambda=\frac{d\varepsilon_{xx}^{p}}{g(\theta)} \tag{2.38}$$

At this point, the value of H_{22} is set to 1 without loss of generality in the derivation (Sun and Chen 1989). This can be done since the plastic anisotropy is still accounted for through relationship between the remaining flow rule coefficients with H_{22}. Eq. 2.37 can be rewritten as

$$g(\theta)=\left[\sin^4(\theta)+H_{44}\sin^2(\theta)\cos^2(\theta)\right]^{\frac{1}{2}} \tag{2.39}$$

The remaining unknown coefficient, H_{44}, is then obtained through off-axis testing in the 1-2 plane. Since the effective stress-effective plastic strain curve is considered a constant for the composite, with the appropriate value of H_{44}, the curve should be independent of the off-axis loading angle, θ. Recognizing that when $\theta=90^{\circ}$, Eq. 2.39 becomes independent of θ, the *master* effective stress-effective plastic strain curve is equivalent to

the stress-plastic strain curve resulting from a 2-direction uniaxial tension or compression test. In addition to being mathematically convenient, this result is physically meaningful since the majority of the nonlinear material behavior in unidirectional composites can be attributed directly to the polymeric matrix. The 2-direction response is dominated by the properties of the matrix. Off-axis experiments at various loadings angles in the 1-2 can then be performed, and the curves then can be converted into effective stress-effective plastic strain curves using Eq. 2.36-2.39 with various values of H_{44}. The value of H_{44} which causes all off-axis effective stress-effective plastic strain curves to collapse onto the master curve, is then the optimal value. Eq. 2.33 shows that H_{23} and H_{55} remain unknown. However, knowing the value of H_{22} and the value of ν_{23}^{p} or ν_{32}^{p}, which are computed directly from experiments, the value of H_{23} can be computed directly from the relationships presented in Eq. 2.30 as

$$H_{23} = -\nu_{23}^{p} H_{22} = -\nu_{32}^{p} H_{33} = -\nu_{32}^{p} H_{22} \tag{2.40}$$

The second form of Eq. 2.40 comes from the previous assumption that H_{22} and H_{33} are equivalent. Finally, H_{55} can be determined from off-axis tension or compression testing in the 2-3 plane. The same procedure used to find the optimal value of H_{44} can be used to find H_{55} using the 2-direction tension or compression uniaxial stress-plastic strain curve as the *master* curve.

In the case of a plain weave composite, the same assumptions used for the unidirectional composite may not hold true for a general case. Assuming the warp and fill yarns used on the composite are the same, the plastic potential function, Eq. 2.13, can be written as follows

$$h^2 = H_{11}\left(\sigma_{11}^2 + \sigma_{22}^2\right) + H_{33}\sigma_{33}^2 + 2H_{12}\sigma_{11}\sigma_{22} + 2H_{23}\left(\sigma_{22}\sigma_{33} + \sigma_{11}\sigma_{33}\right) + H_{44}\sigma_{12}^2 + H_{55}\left(\sigma_{23}^2 + \sigma_{13}^2\right) \tag{2.41}$$

Eq. 2.41 assumes the 1-2 plane to exhibit transverse isotropy, similar to the 2-3 plane in the unidirectional case. Eq. 2.41 implies that linear elasticity is not assumed in the warp and fill directions. Experimental data shows that slight nonlinearity is observed under tension and compression loading (Karayaka and Kurath 1994; Lomov et al. 2009; Ogihara and Reifsnider 2002). Considering a state of plane stress in the 1-2 plane, Eq. 2.41 reduces to

$$h^2 = H_{11}\left(\sigma_{11}^2 + \sigma_{22}^2\right) + 2H_{12}\sigma_{11}\sigma_{22} + H_{44}\sigma_{12}^2 \tag{2.42}$$

Under an arbitrary off-axis state of stress, substituting Eq. 2.5 into Eq. 2.42 yields the following

$$h^2 = \sigma_x^2\left[H_{11}\left(\cos^4(\theta) + \sin^4(\theta)\right) + \left(2H_{12} + H_{44}\right)\sin^2(\theta)\cos^2(\theta)\right] \tag{2.43}$$

The plastic potential function is then given by

$$h = \sigma_x r(\theta) \tag{2.44}$$

where

$$r(\theta) = \left[H_{11}\left(\cos^4(\theta) + \sin^4(\theta)\right) + \left(2H_{12} + H_{44}\right)\sin^2(\theta)\cos^2(\theta) \right]^{\frac{1}{2}} \tag{2.45}$$

Substituting Eq. 2.45 into Eq. 2.28, the effective plastic strain increment under off-axis loading in the 1-2 plane for a woven composite can be written as

$$d\lambda = \frac{d\varepsilon_{xx}^{p}}{r(\theta)} \tag{2.46}$$

The value of H_{11} can be set to 1 without loss of generality in the derivation. A similar assumption has been shown to be valid for woven composites by Ogihara and Reifsnider (2002). Eq. 2.45 is then reduced to

$$r(\theta) = \left[\left(\cos^4(\theta) + \sin^4(\theta)\right) + \left(2H_{12} + H_{44}\right)\sin^2(\theta)\cos^2(\theta) \right]^{\frac{1}{2}} \tag{2.47}$$

At this point, the value of H_{12} is computed using Eq. 2.30 using the known value of ν_{12}^p or ν_{21}^p as

$$H_{12} = -H_{11}\nu_{12}^p = -H_{11}\nu_{21}^p \tag{2.48}$$

where ν_{21}^p can be used since $H_{11} = H_{22}$. The unknown value of H_{44} can be obtained using the results of off-axis testing at various angles from the PMD, in the same fashion that is described for unidirectional composites. Referencing Eq. 2.41, the values of H_{33}, H_{23}, and H_{55} remain unknown. However, Eq. 2.30 can be used to compute the following values

$$\begin{aligned} H_{23} &= -H_{11}\nu_{23}^p = -H_{11}\nu_{13}^p \\ H_{33} &= H_{11}\frac{\nu_{23}^p}{\nu_{32}^p} = H_{11}\frac{\nu_{13}^p}{\nu_{32}^p} = H_{11}\frac{\nu_{23}^p}{\nu_{31}^p} = H_{11}\frac{\nu_{13}^p}{\nu_{31}^p} \end{aligned} \tag{2.49}$$

The forms of H_{23} and H_{33} provided by Eq. 2.49 are the result of assuming the 1-direction and 2-direction behave the same followed by rearranging the values shown in Eq. 2.30. The final unknown, H_{55}, can finally be obtained from off-axis tension or compression testing in the 2-3 plane. The same procedure used to find the optimal value of H_{44} can be used to find H_{55} using the 1-direction or 2-direction tension or compression uniaxial stress-plastic strain curve as the master curve.

The techniques provided in this section for computing the flow rule coefficients represents a subset of the possible scenarios. Appropriate assumptions must be made and validated by experimental data to obtain a set of coefficients consistent with the observed behavior. An experimental case study using the T800S/F3900 carbon fiber/epoxy resin unidirectional composite is presented in the next section with the goal of illustrating how all of the data required to drive the deformation sub-model is obtained including a proposed generalized method for computing the flow rule coefficients.

2.2 Experimental Methods

The experimental data needed to drive the model in its simplest form is enumerated in

Table 2 where the subscripts 1, 2, 3 refer to the principal material directions (PMD), superscripts *T*, *C*, and *p* denote tension, compression, and plastic respectively, and subscript *y* denotes yielding.

Table 2. Required Tests and Resulting Input for OEPDMM

Test Description	Resulting Input for OEPDMM
1-direction Tension	σ_{11}^{T} vs ε_{11}^{T} , $(\varepsilon_{11})_y^{T}$, $(\sigma_{11})_y^{T}$, (ν_{12},ν_{13}), $(\nu_{12}^{p},\nu_{13}^{p})$
2-direction Tension	σ_{22}^{T} vs ε_{22}^{T} , $(\varepsilon_{22})_y^{T}$, $(\sigma_{22})_y^{T}$, (ν_{23},ν_{21}), $(\nu_{23}^{p},\nu_{21}^{p})$
3-direction Tension	σ_{33}^{T} vs ε_{33}^{T} , $(\varepsilon_{33})_y^{T}$, $(\sigma_{33})_y^{T}$, (ν_{32},ν_{31}), $(\nu_{32}^{p},\nu_{31}^{p})$
1-direction Compression	σ_{11}^{C} vs ε_{11}^{C} , $(\varepsilon_{11})_y^{C}$, $(\sigma_{11})_y^{C}$, (ν_{12},ν_{13}), $(\nu_{12}^{p},\nu_{13}^{p})$
2-direction Compression	σ_{22}^{C} vs ε_{22}^{C} , $(\varepsilon_{22})_y^{C}$, $(\sigma_{22})_y^{C}$, (ν_{23},ν_{21}), $(\nu_{23}^{p},\nu_{21}^{p})$
3-direction Compression	σ_{33}^{C} vs ε_{33}^{C} , $(\varepsilon_{33})_y^{C}$, $(\sigma_{33})_y^{C}$, (ν_{32},ν_{31}), $(\nu_{32}^{p},\nu_{31}^{p})$
1-2 Plane Shear	σ_{12} vs ε_{12} , $(\varepsilon_{12})_y$, $(\sigma_{12})_y$
2-3 Plane Shear	σ_{23} vs ε_{23} , $(\varepsilon_{23})_y$, $(\sigma_{23})_y$
1-3 Plane Shear	σ_{13} vs ε_{13} , $(\varepsilon_{13})_y$, $(\sigma_{13})_y$
1-2 Plane 45° Off-axis tension/compression	σ_{45}^{1-2} vs ε_{45}^{1-2} , $(\varepsilon_{45}^{1-2})_y$, $(\sigma_{45}^{1-2})_y$
2-3 Plane 45° Off-axis tension/compression	σ_{45}^{2-3} vs ε_{45}^{2-3} , $(\varepsilon_{45}^{2-3})_y$, $(\sigma_{45}^{2-3})_y$
1-3 Plane 45° Off-axis tension/compression	σ_{45}^{1-3} vs ε_{45}^{1-3} , $(\varepsilon_{45}^{1-3})_y$, $(\sigma_{45}^{1-3})_y$

In this section, the experimental methods to obtain the twelve stress-strain curves are discussed, and include specimen preparation, test fixtures, experimental procedures, and data processing.

Test coupons were cut from three types of panels manufactured by Toray details of which are listed in

Table 3. The panels were inspected prior to being used for creating test coupons for manufacturing defects using pulse echo ultrasonic scans at 5 MHz and data was collected at increments of 1 mm in each direction. The scan results showed no significant indication of flaws or damage.

Table 3. Panels Used for Tests

Panel Type	**Nominal Dimensions (length x width)**	**Nominal Thickness, mm (in) (# of plies)**
PT1	304.8 mm x 609.6 mm (12” x 24”)	3.1 (0.122) (16)
PT2	304.8 mm x 304.8 mm (12” x 12”)	4.7 (0.185) (24)
PT3	304.8 mm x 304.8 mm (12” x 12”)	18.4 (0.724) (96)

All test coupons were cut from the raw panels using a water jet. Investigative cuts were performed with each of the panel types, presented in

Table 3, to ensure minimal damage from the cutting process. The final water jet specifications, used to manufacture the test specimens, are shown in

Table 4.

Table 4. Water Jet Specifications

Parameter	PT1	PT2	PT3
Abrasive Size, grit	80 (US Std)	80 (US Std)	80 (US Std)
Nozzle Diameter, in (mm)	0.03 (0.762)	0.03 (0.762)	0.03 (0.762)
Nominal Minimum Nozzle Pressure, psi (MPa)	200	200	200
Nominal Maximum Nozzle Pressure, psi (MPa)	310	310	310
Nominal Cut Speed, in/min (mm/min)	73 (1854)	51 (1295)	12 (305)

Test specimens showed no significant damage, i.e. delamination or cracking, from water jetting aside from minor fraying of the carbon fibers where they terminate at the edge of the coupon. After cutting the samples out of the composite panel, a grinding wheel was used to polish the edges to reduce the surface roughness of the specimen. Optical microscopy was used to ensure the grinding process did not damage the specimens. Optical micrographs of one of the test coupons under various magnifications are shown in Fig. 6.

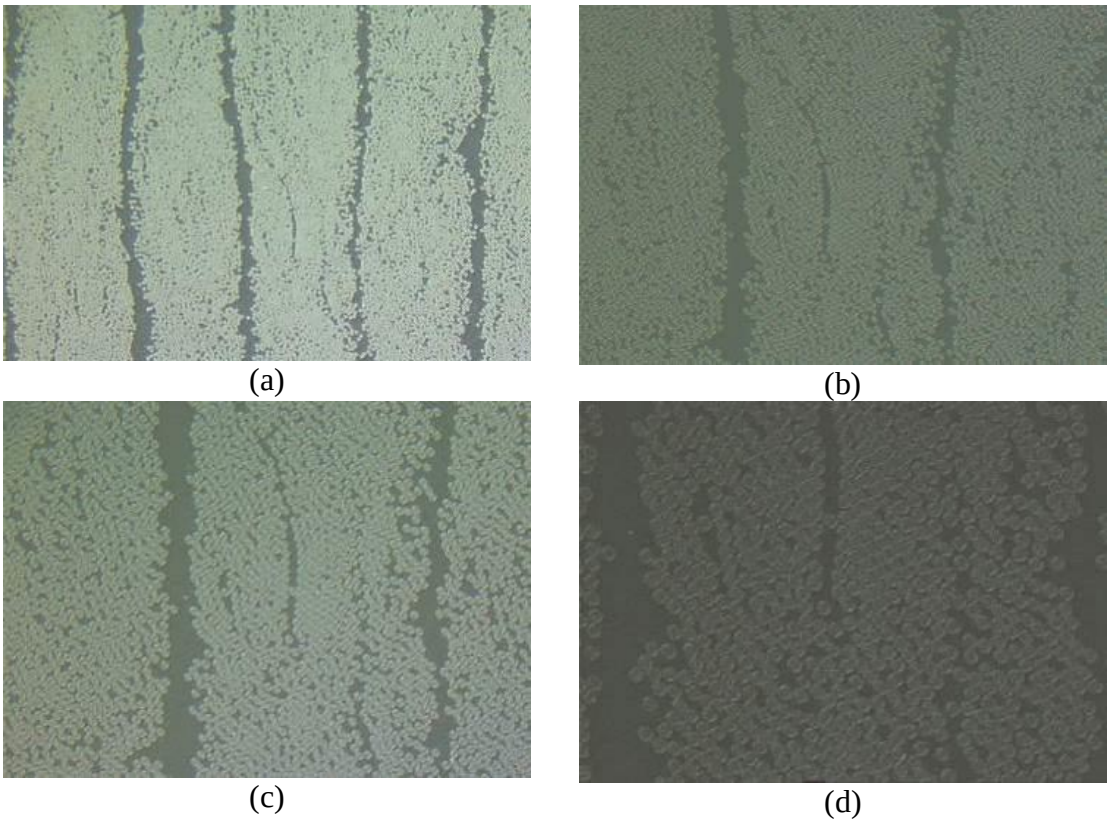

Fig. 6. Optical Micrographs of Finished Edges (after Grinding) (a) 200x, (b) 400x, (c) 500x, (d) 1000x

Each of the panel types shown in Table 3 was used to generate test coupons for different tests. The 16-ply panel (PT1) is used for 1 and 2-direction tension and compression tests, and the 1-2 plane off-axis tension tests; the 24-ply panel (PT2) is used for 1-2 plane shear tests; the 96-ply panel (PT3) is used for 3-direction tension and compression tests, the 1-3 plane and 2-3 plane shear tests, and the 1-3 plane and 2-3 plane off-axis compression tests. In addition to the mechanical testing, specific gravity tests were performed using all three panel types.

When required, G10 fiberglass tabs[2] are used with the sample. The fiberglass tabs act as compliant surfaces that prevent specimens from crushing when placed in the hydraulic grips. They also act as stiffening elements when conducting shear tests. The tabs are bonded to the specified specimen surfaces using 3M DP460 Scotch Weld toughened two-part epoxy[3]. All specimens are prepared in the same manner unless otherwise noted. The following list outlines the steps taken to fully prepare the specimens for testing.

1. The regions on a typical specimen where fiberglass tabs are bonded and the surfaces of the fiberglass tabs being bonded to the specimen, are lightly sanded using 120 grit sandpaper. Sanding the surfaces helps develop a complete bond between the specimen and the tabs.
2. The surfaces that were sanded are then cleaned using cotton swabs soaked with isopropyl alcohol. The surfaces are allowed to air dry until there is no visible moisture on the bonding surfaces.
3. The 3M epoxy is mixed in accordance to the manufacturer's recommendation. A thin layer of the mixed epoxy is applied to the prepared surface of the tabs using a wooden applicator.
4. The tabs are then placed on the specimen and positioned until the surfaces of the specimen and the tabs are in complete contact and aligned properly in the desired region.

---

[2] G10, FR4 Laminate Sheets 36"x 48", Epoxyglas™; NEMA Grade FR4, Mil-I-24768/27, http://www.acculam.com/

[3] http://multimedia.3m.com/mws/media/66122O/3mtm-scotch-weld-tm-epoxy-adhesive-dp460-ns-and-off-white.pdf

5. The specimens are allowed to cure at room temperature and atmospheric pressure for 48 hours as recommended by the manufacturer.

After the epoxy has finished curing, the specimen is then prepared to be used with digital image correlation (DIC) (Sutton et al. 2009). DIC is a non-contact optical technique which is used to compute full displacement fields on an object's surface. The DIC technique compares pixel subsets, an $n \times n$ array of pixels where n is the subset size, from an image of the deformed surface with the most similar pixel subset from an image of a reference surface. This is done by comparing grayscale values of individual pixels and solving a correlation function which determines the best match between the reference subset and the deformed subset. This procedure is done for all subsets in a given analysis region. For each pair of reference and deformed subsets, the location of the center of the subsets is compared and yields a displacement field. From the displacement field, the components of various strain tensors can be computed. Fig. 7 shows the correlation process schematically.

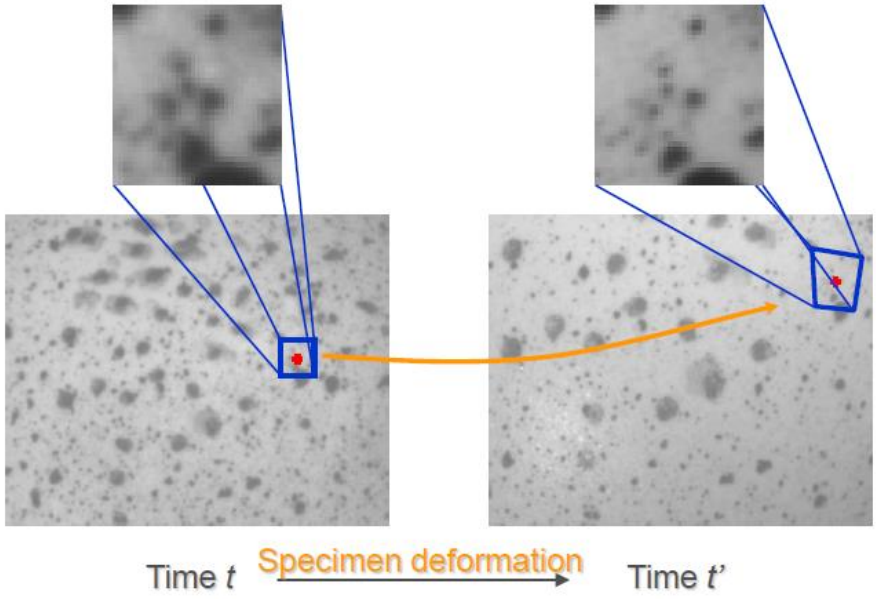

Fig. 7. Schematic Representation of DIC Principle (Correlated Solutions, Inc. 2009)

The black and white pattern shown in Fig. 7 provides contrast to the software so the pixel subsets can be defined uniquely. The pattern, referred to as the *speckle pattern*, can be provided either by the natural pigmentation of the specimen surface or through additional preparation of the surface. In this research work, contrast is provided by first spray painting the specimen surface with non-reflective white paint. After the white paint has dried completely, non-reflective black paint is used to apply speckles to the surface. Correlated Solutions has created a document outlining proper speckling protocol and the effects which improper speckling has on the solution (Correlated Solutions, Inc. 2018). Correlated Solutions provides two forms of DIC analysis software. The first is Vic-2D which performs two-dimensional (planar) analysis of the specimen surface and requires a single camera to capture images during the deformation process. The second is Vic-3D which performs three-dimensional analysis of the specimen surface and requires two cameras to generate

simultaneous images during the deformation process. The three-dimensional analysis provides out-of-plane displacements. However, it cannot provide out-of-plane strains. The additional out-of-plane information is useful in detecting and helping eliminate specimen and test frame misalignment during the experimental procedure. It also provides additional information for FE model validation. Three dimensional DIC analysis using Vic-3D v7 (*Vic-3D* 2016) was performed for all tests presented unless otherwise stated. Unless otherwise noted, all images during the experiments were captured using two Point Grey Grasshopper 3 cameras (FLIR Integrated Imaging Solutions, Inc. 2019). LED lamps are used to properly illuminate the specimen during the experimental procedure. The cameras and lights are fixed to the same rigid frame. The frame is leveled using a bubble level to ensure the cameras are properly oriented. In some instances, a Vision Research Phantom v7.3[4] high speed camera, recording at 5000 fps, is utilized to capture the failure event. Though the high speed camera is not used for DIC analysis in this instance, the images can provide a deeper insight into the failure mechanics of the material. Fig. 8 shows the optical equipment used for capturing the images.

[4] http://www.adept.net.au/cameras/visionresearch/pdf/PhantomV73.pdf

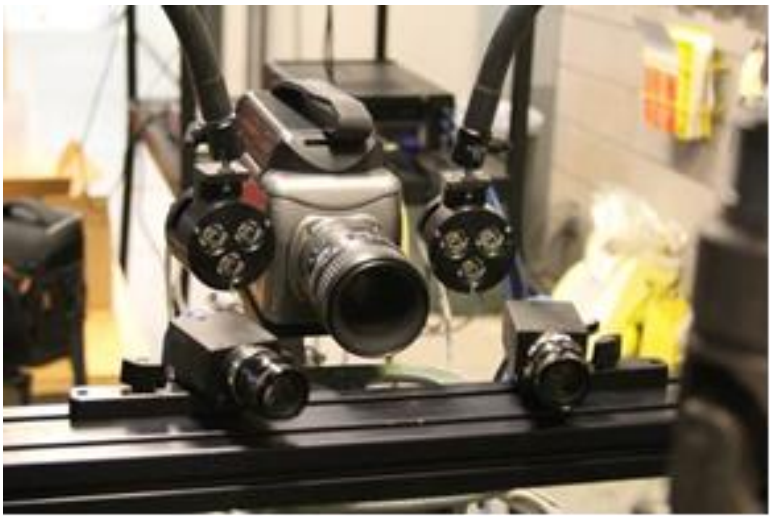

Fig. 8. Equipment Used to Capture Images During Experimental Procedures Showing Two DIC Cameras, One High Speed Camera, and Two LED Lamps

The two cameras used for capturing images must be calibrated such that the internal parameters are synchronized and the relative position of the cameras is provided. This is done by capturing a series of images of a calibration target with both cameras simultaneously. Fig. 9 shows an example of a glass calibration target.

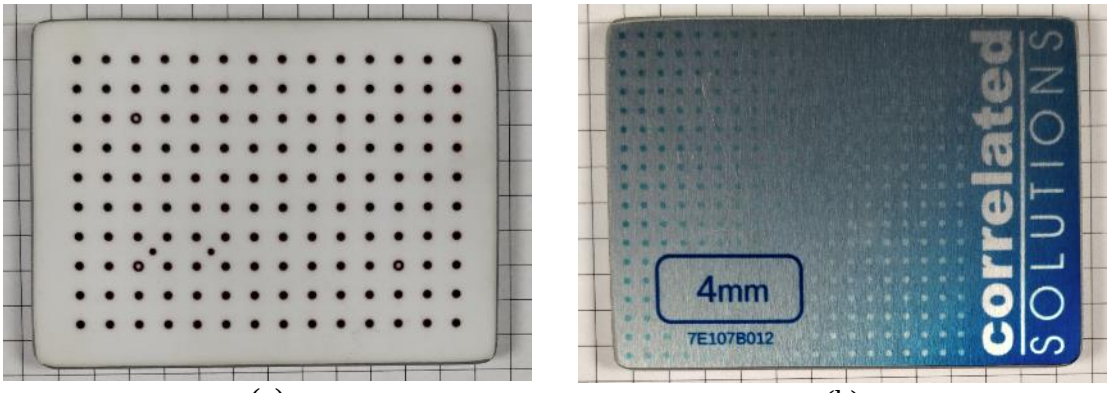

(a) (b)

Fig. 9. Calibration Target with 4 mm Dot Spacing (a) Front of Target and (b) Back of Target

The required synchronization information is gathered by capturing images of the calibration target at multiple orientations. All images, calibration and experimental, are captured using Vic-Snap 8 (*Vic-Snap* 2016).

All experimental procedures are performed using an MTS 810 hydraulic universal testing frame (Fig. 10a). Flat tension specimens are held in the frame with MTS 647.10A hydraulic grips (Fig. 10b). The hydraulic grips are aligned by clamping a rigid, flat steel plate and allowing the heads to freely rotate into position. After aligning the hydraulic grips, the specimen is placed into the test frame. For tension and compression tests, verticality of the specimen is ensured by using a laser alignment system (Fig. 10c). The specimen is gripped up to the end of the fiberglass tabs. Shear specimens are mounted in the test frame using an Iosipescu shear test fixture as shown in Fig. 10d. Compression cubes are bonded to custom fixtures (Fig. 10e), machined out of A2 tool steel, using Loctite liquid super glue. Alignment of the specimen is ensured using 0.2" deep square notches machined into the center of the fixtures as shown in Fig. 10f. Flat (in-plane) compression specimens were tested using a Wyoming Test Fixtures[5] combined loading compression fixture (CLC) as shown in Fig. 10g and Fig. 10h. The CLC fixture transfers load into the compression specimens through both shear load transfer and end load transfer thereby reducing the need for excessive clamping forces.

[5] https://www.wyomingtestfixtures.com/

(a)

(b)

(c)

(d)

(e)

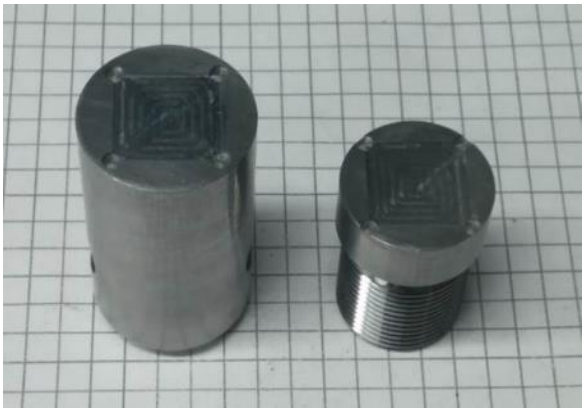

(f)

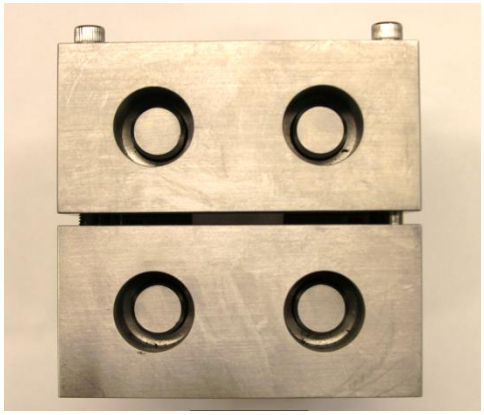

(g)

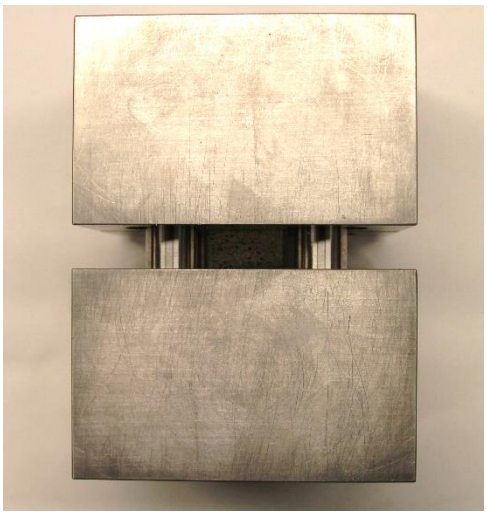

(h)

Fig. 10. Experimental Equipment (a) Test Frame, (b) Hydraulic Grips, (c) Specimen Alignment, (d) Iosipescu Shear Test Fixture, (e) Compression Cube Fixture, (f) Custom Fixture for Compression Tests, (g) CLC Compression Fixture (Top), and (h) CLC Fixture Front Showing C2 Specimen

Force data is gathered using an MTS 661.21A-03 load cell. All experiments are conducted under open loop displacement controlled conditions. The displacement rate refers to the stroke of the test frame actuator and is set using the MTS system controller. The displacement rates were chosen such that the resulting axial strain rate induced in the specimen was at a low quasi-static rate, approximately 10^{-4}/s.

Both the data from the load cell and the images during the experiment are initially processed separately and ultimately combined to generate the stress-strain response. The images captured during the experiment are processed for the purpose of obtaining a full strain field using Vic-3D v7. The Lagrangian strain tensor was used to perform the analysis.

As mentioned previously, Vic-3D v7 offers various options for computing finite strains on the specimen's surface. However, the strains observed during the experiments were small and the choice of finite strain tensor did not alter the results. For the initial processing, the entire speckled region of the specimen is analyzed. After the analysis is complete, several tools may be utilized to interrogate the response of a subset of the analyzed surface. For example, data from a single point may be obtained, the average data from within an area may be obtained, or virtual extensometers may be defined which yield the traditional engineering strain. The choice of the analysis tool depends on the observed response of the specimen. For all tension tests, in-plane compression tests, and all shear tests, the average area technique was used. The chosen area was assumed to be representative of the true response of the specimen under the prescribed loading. The area was chosen to be sufficiently away from the edges of the specimen such that the effects of strain concentrations caused by gripping and free edge effects did not influence the response. When analyzing all through thickness compression tests, the average area method provided inconsistent results. The manner in which the specimens were glued to the compression platens, Fig. 10f, likely over restricted the movement of the top and bottom surfaces. This caused the specimens to exhibit barreling, where much of the deformation takes place only in the center of the specimen while the top and bottom boundaries remain undeformed. With the short specimens, this leads to small zone where the strains are concentrated. To overcome this issue, virtual extensometers were placed along the length and width of the specimen with the average responses being used to compute the longitudinal and transverse strain. Sample images for the different strain reporting techniques are shown in Fig. 11.

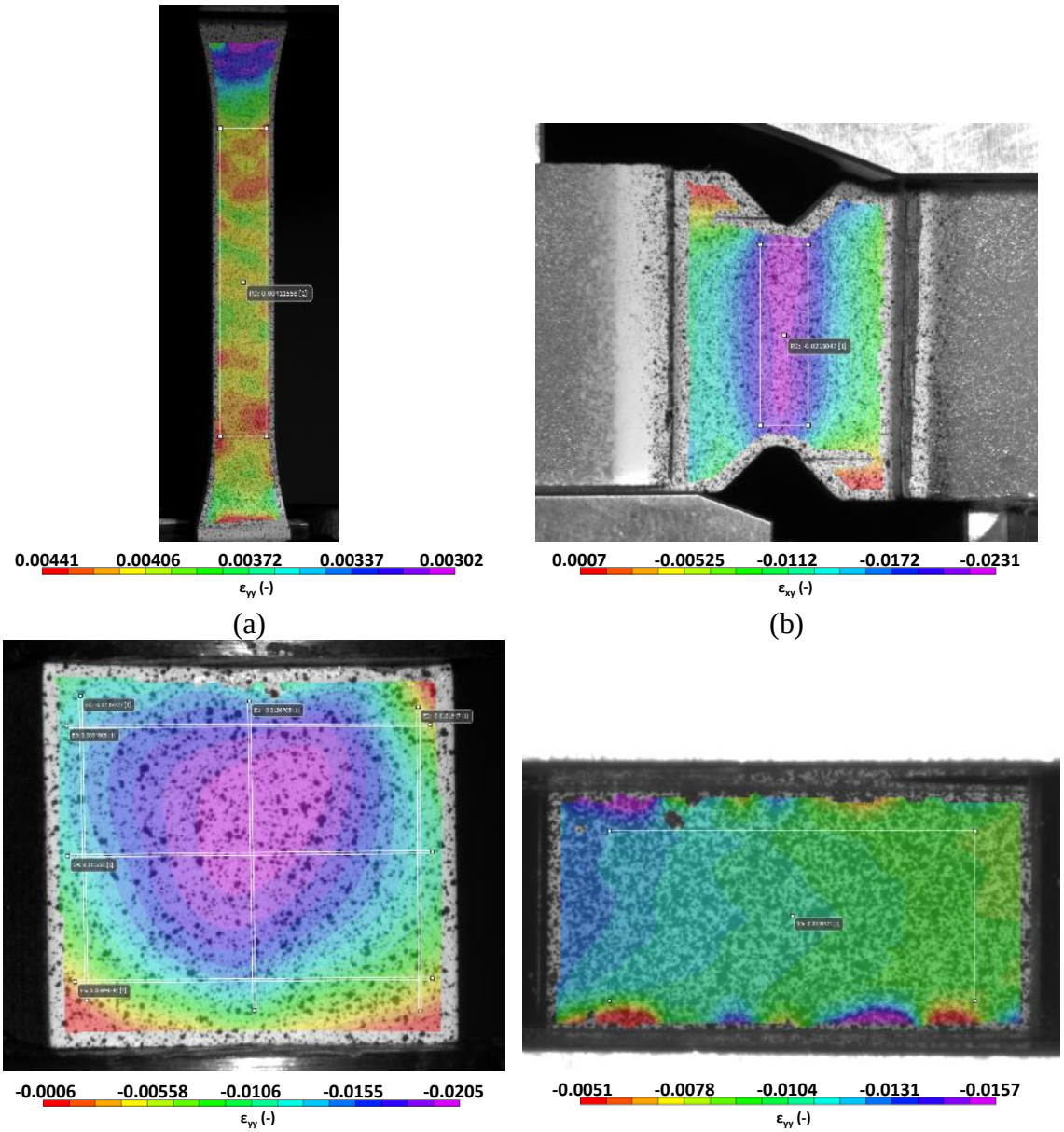

Fig. 11. Typical strain fields (a) In-Plane Tension Specimens (b) Shear Specimens (c) Through-Thickness Compression Specimens (d) In-Plane Compression Specimens

All strain measurements presented in this document are obtained from DIC using these techniques. Force data is obtained as a function of time from the load cell and is used to estimate the stress in the specimen which is computed using the average initial cross

sectional area of the specimen. For tension and compression specimens, the cross section perpendicular to the direction of loading is used to calculate the cross sectional area. The average normal stress is calculated as

$$\sigma = \frac{F}{A_0} \tag{2.50}$$

where F is the normal force reported by the load cell at a given instance of time and A_0 is the initial cross sectional area. For shear specimens, the surface between the notches, through the thickness of the specimen, is used to calculate the cross-sectional area. The average shear stress is calculated as

$$\tau = \frac{V}{A_0} \tag{2.51}$$

where V is the force reported by the load cell at the current time-step and A_0 is the initial cross sectional area. The strain reported from Vic 3D v7 in the region of interest is used in conjunction with the calculated stress to generate a stress-strain curve for any given specimen. After obtaining reliable and consistent data from a minimum of three replicates of each experiment, the results were used to generate the input data for the constitutive model (

Table 2). The (deterministic) constitutive model requires only one representative stress-strain curve for each of the experiments. This curve is referred to as the *model curve*. Each model curve is generated by carrying out a least-squares fit at each experimental strain value to obtain the model stress value, i.e. using the average stress value from all replicates for a given strain value, the model stress value is computed. The model curve ends at the average strain at failure from all replicates. Fig. 12 shows the resulting stress-strain curves using the described procedure for the 1-direction tension test.

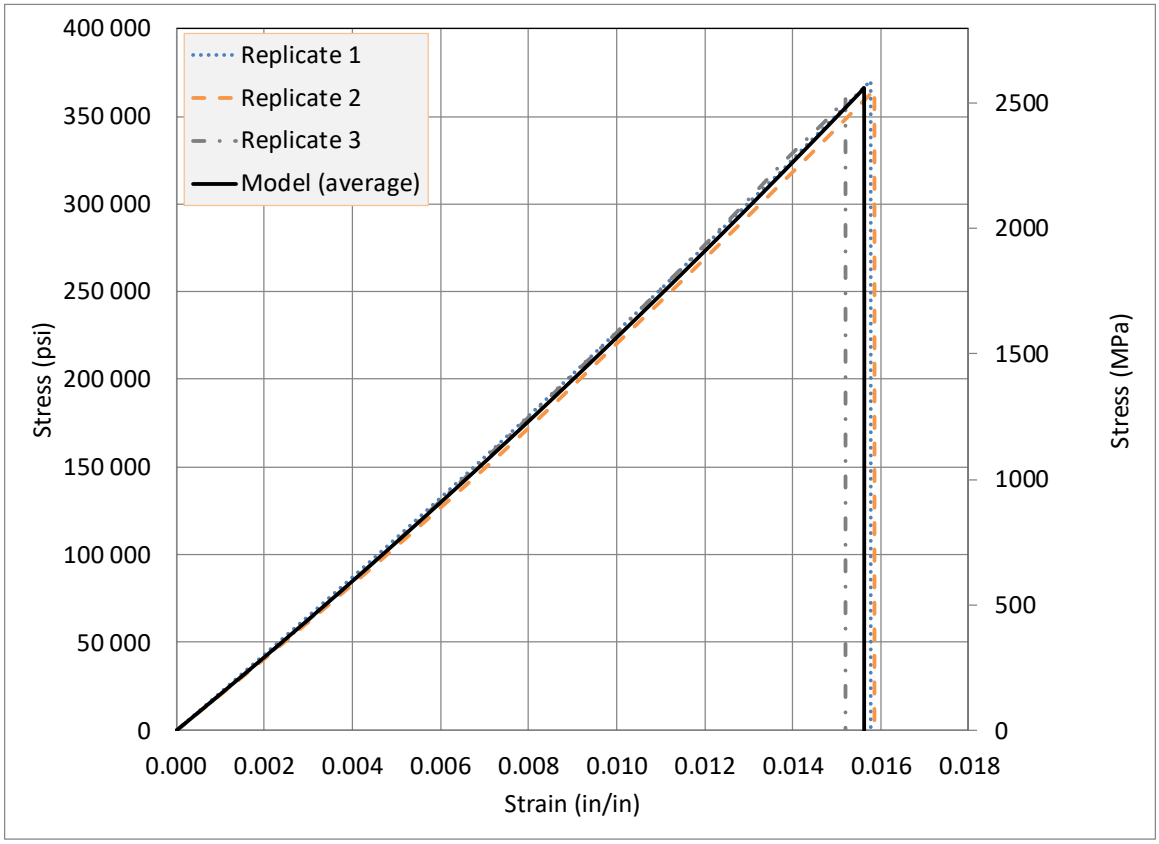

Fig. 12. Illustration of Stress-Strain Curve Averaging Technique

In addition to the model curve used as input for MAT 213, several parameters are obtained from the stress strain curves of each individual specimen for the purpose of determining how consistent the data is.
Table 5 describes each parameter and how they are obtained from the available data.

Table 5. Descriptions of the Nomenclature Used for Stress-Strain Curve Characteristics

Parameter	Definition	Method
Loading rate	Constant rate at which the actuator on the test frame is displaced.	Chosen by the experimenter as a fixed parameter at the beginning of the procedure. The rate is prescribed as a displacement over a certain period of time.
Strain rate	The rate at which strain is induced in the specimen during a given experiment.	The strain measure of interest is plotted as a function of time and the average strain rate during the experiment is obtained by performing a linear regression. The slope of the resulting best fit line is taken as the average strain rate.
Modulus	The slope of the initial linear region of the true stress-strain curve.	The analyst determines the region which is most linear in the initial portion of the curve and performs a linear regression on the data. The slope of the resulting best fit line is taken as the modulus.
Poisson's ratio	The negative ratio of transverse strain to longitudinal strain.	Both elastic and plastic Poisson's ratios may be

		obtained by plotting transverse strain as a function of normal strain. The elastic and plastic components of both the transverse and longitudinal strain are computed using the method described in a later section. A linear regression is performed on the elastic and plastic components, yielding the respective Poisson's ratio values.
Peak stress	Maximum stress achieved during a given experiment.	Selected from stress data obtained through scaling the force data reported by the load cell.
Ultimate strain	Strain measured at peak stress.	Selected as the largest strain when the specimen exhibits brittle failure with no post-peak strength.
Failure strain	Strain measured when the specimen fails.	Selected as the strain when there is a large drop in stress and the specimen no longer loads back up to that peak stress point. Typically this is when the test is terminated and used when specimen does not exhibit brittle failure.
Transverse strain	Strain induced in the specimen perpendicular to the direction of	Obtained through DIC measurements.

	loading in tension and compression tests. In shear tests it is defined as strain induced in specimen parallel to the movement of the actuator.	
Longitudinal strain	Strain induced in the specimen parallel to the direction of loading in tension and compression tests. In shear tests it is defined as strain induced in specimen perpendicular to the movement of the actuator.	Obtained through DIC measurements.
Shear strain	Tensorial shear strain induced in the principal plane being observed.	Obtained through DIC measurements.

The specimen geometries used were guided by the respective ASTM standard unless otherwise necessary.

1-direction Tension Test: During preliminary 1-direction tension testing, inducing failure in the specimen and obtaining consistent results proved to be challenging. Since a large tensile force is needed to induce failure, applying the proper gripping pressure so as to prevent slippage and not induce unwanted damage in the specimen was difficult. Finally, through trial-and-error, a modified form of the ASTM D3039/D3039M-17 (D30 Committee 2017a) specimen geometry (Fig. 13) was found that yielded consistent results. The shaded regions indicate the area where G10 fiberglass tabs were used.

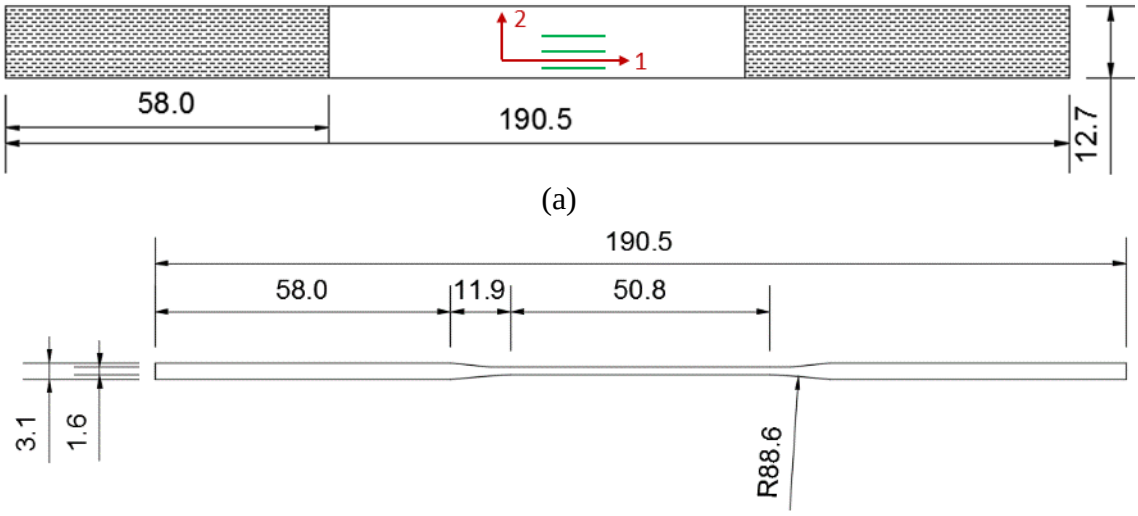

Fig. 13. Nominal 1-direction Tension Specimen Dimensions and Layout (a) Plan View and (b) Elevation View (All Dimensions in mm)

Note that Fig. 13b shows a (thickness) tapered gage section. Adams (Adams 2013) proposed using a tapered section though an actual experiment was never conducted with such a section. The specimens were machined using a CNC milling machine to grind away approximately one-quarter of the specimen thickness from each side. After grinding down one side of the specimen, a special fixture was created to match the contour of the specimen taper and was used to support the specimen as the other side was ground. The new specimen geometry test specimens consistently failed in the gage section using a gripping pressure that did not damage the specimen.

2-direction Tension Test: Two specimen geometries were used in the investigative studies. The first was the standard specimen geometry (Fig. 14a) recommended by ASTM

D3039/D3039M-17 (D30 Committee 2017a). The second uses a dog bone geometry (Fig. 14b). The straight sided specimens failed near the gripping region. Thus, the dog-bone geometry was used in an effort to mitigate the influence of stress concentrations that are induced in the specimen near the gripping region. The shaded regions indicate the area where G10 fiberglass tabs were used.

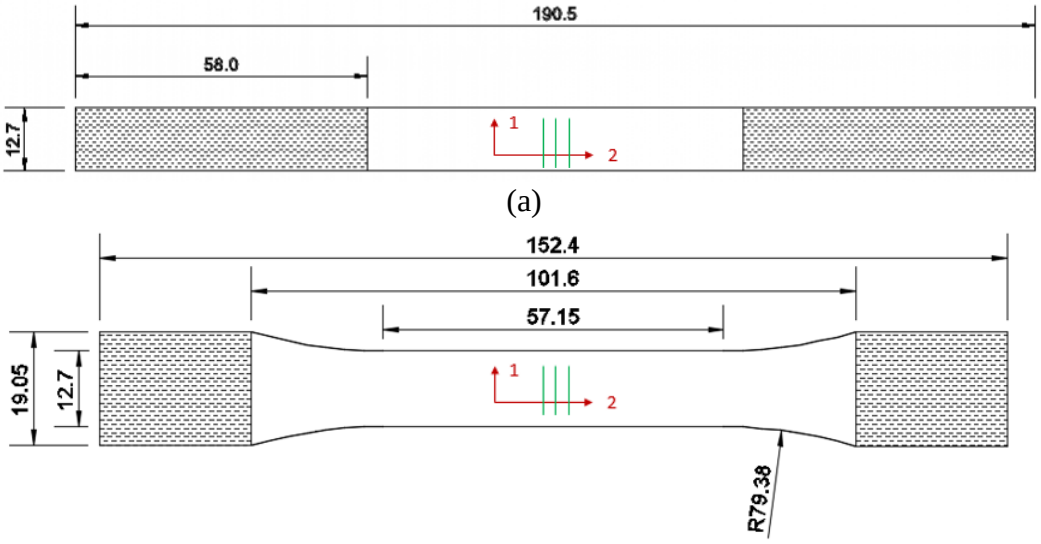

Fig. 14. Nominal 2-direction Tension Specimen Dimensions and Layout (a) Standard Specimen and (b) Dog Bone Specimen (All Dimensions in mm)

3-direction Tension Test: As with other through-thickness tests, this experiment is challenging since the available specimen length is very limited – in this instance, the maximum length was 18.3 mm (96 plies). A specimen geometry (Fig. 15) was created so that either the 1-3 or the 2-3 plane could be used for gathering strain data. Experiments using both specimen orientations were performed to see if any differences in the strain data could be discerned.

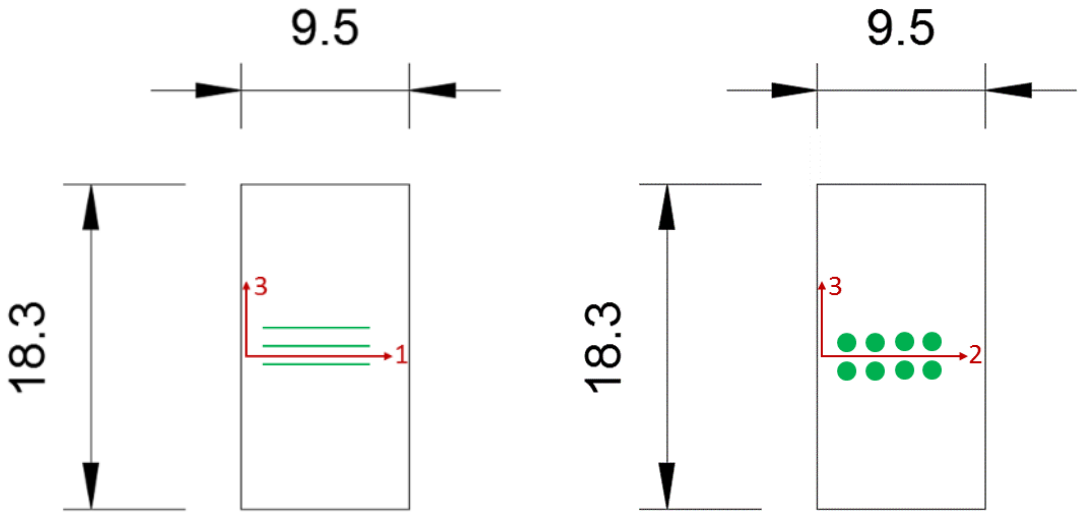

Fig. 15. Nominal 3-direction Tension Specimen Dimensions and Layout (a) 1-3 Plane Speckled and (b) 2-3 Plane Speckled (All Dimensions in mm)

The specimens had a nominal thickness of 1.5 mm (i.e. in the 2-direction of the specimen shown in Fig. 15a and in the 1-direction of the specimen shown in Fig. 15b). To ensure that the test coupon could be properly inserted into the hydraulic grips, a special sandwich specimen gripping assembly was constructed. The gripping assembly, comprised of G10 fiberglass, was used to transfer the load from the hydraulic grips into the specimen. The schematic of the gripping system is shown in Fig. 16.

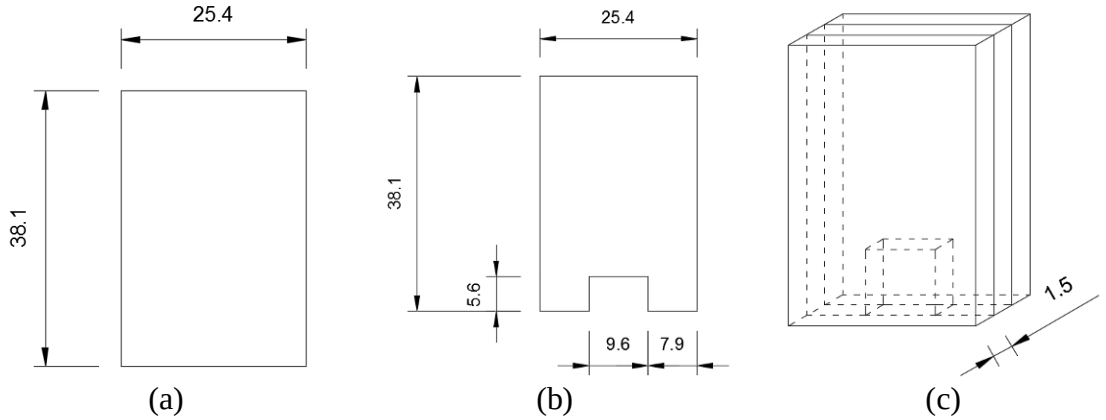

Fig. 16. Fiberglass Tab Layup Geometry (a) Outer Layers (b) Center Layer (c) Overall Layup (Dimensions in mm)

The fiberglass tabs were bonded together using Loctite liquid super glue[6]. Both ends of the specimen were bonded to the inside of the pocket formed by the fiberglass tabs, Fig. 16c, using 3M DP460 two-part toughened epoxy. The entire surface of the specimen that was inside the tabs was coated with the epoxy to ensure maximum load transfer capacity.

In-Plane Compression Test: Two in-plane compression experiments were performed. Both the 1-direction and 2-direction compression tests utilized flat specimens with geometries that are recommended by ASTM D3410/D3410M-16 (D30 Committee 2016), shown in Fig. 17.

[6] http://www.loctiteproducts.com/p/4/2/sg_bottle/overview/Loctite-Super-Glue-Longneck-Bottle.htm

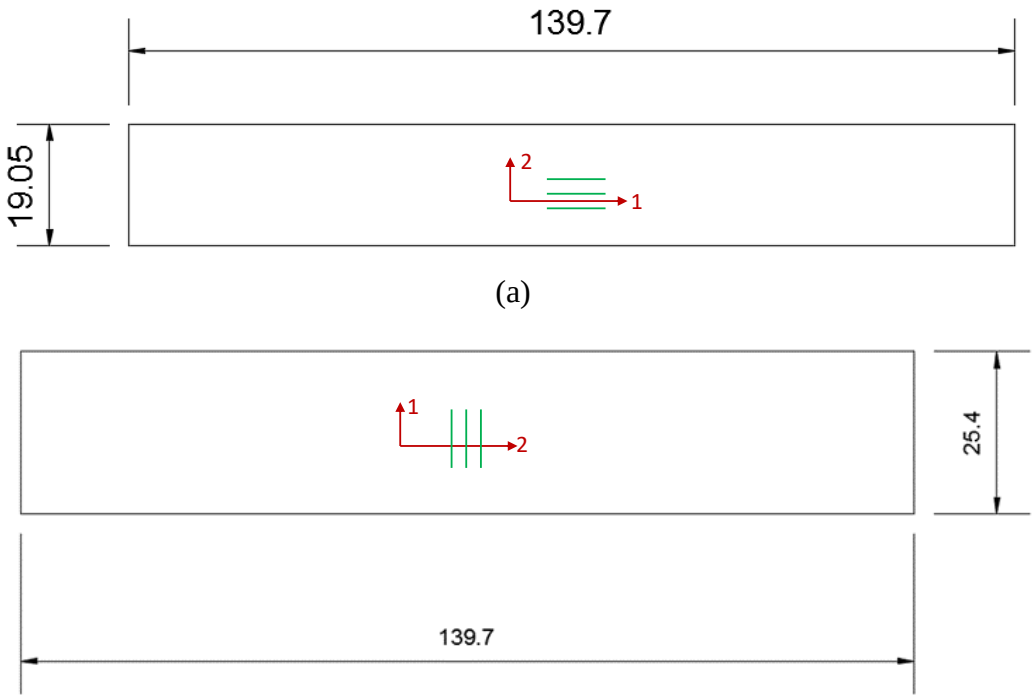

Fig. 17. Nominal Specimen Dimensions and Layout (a) 1-direction Compression Specimen and (b) 2-direction Compression Specimen (All Dimensions in mm)

The CLC fixture (Fig. 10g and Fig. 10h) was used in testing both specimens. A gage section of 12.7 mm (0.5 in) was used. A torque of 1700 N-mm (15 in-lb) was applied to each of the eight bolts in the CLC fixture. The torque was applied in multiple stages to each bolt, ensuring even gripping of the specimen.

Through-thickness Compression Test: Three through-thickness compression experiments were performed. The first is the 3-direction compression test using a parallel sided cube geometry (Fig. 18a,b). Similar to the 3-direction tension test, both the 1-3 and 2-3 planes were used for gathering strain data in separate experiments to determine if there was any discernable pattern in the deformation-related responses on the two surfaces. Additionally,

1-3 plane and 2-3 plane 45° off-axis compression tests were performed. The off-axis specimens were also parallel sided cubes with the thickness of the available composite panel dictating the dimensions (Fig. 18c,d). Currently, the underlying theory in the constitutive model uses either off-axis compression or off-axis tension data. Compression tests were chosen because of ease of testing, specimen preparation, and specimen machining.

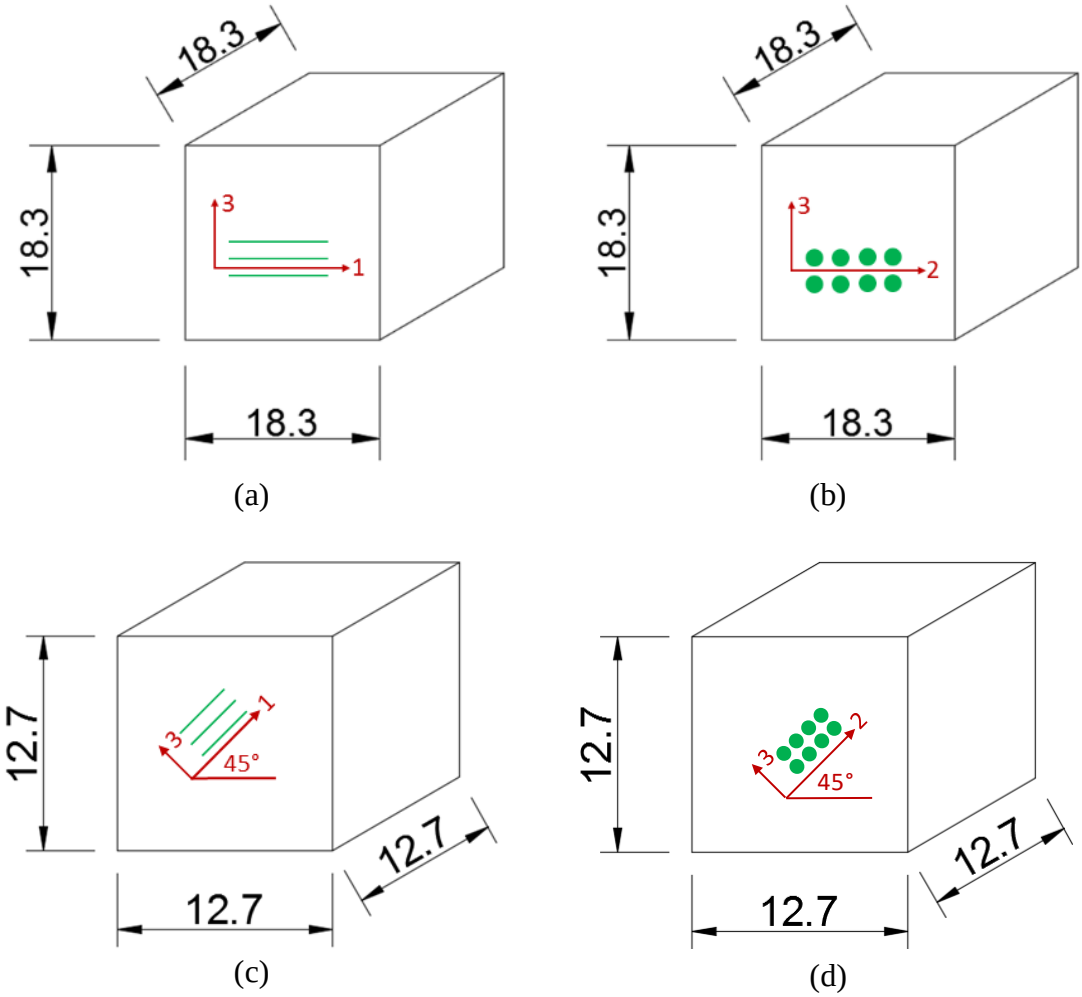

Fig. 18. Nominal Specimen Dimensions and Layout (a) 3- Direction Compression with 1-3 Plane Speckled and (b) 3-direction Compression with 2-3 Plane Speckled (c) 1-3 Plane 45° Off-axis Compression and (d) 2-3 Plane 45° Off-axis Compression (All Dimensions in mm)

The compression tests were performed using custom made A2 tool steel platens (Fig. 10e and Fig. 10f). The platens have square notches etched out of the face to ensure that the specimen is properly aligned within the test frame. The straight-sided specimens do not have the same level of sensitivity to eccentric loading as the waisted specimens and proper

alignment ensured that the stress state was nearly uniaxial and uniform as discerned from the digital images.

In-plane Shear Test: The Iosipescu shear test setup was used to perform the 1-2 plane shear experiments. During investigative testing, the specimen and tab geometry used to conduct the experiments were taken from ASTM D5379/D5379M-12 (D30 Committee 2012), as shown in Fig. 19. The specimens had a nominal thickness of 4.7 mm. The shaded regions indicate the area where G10 fiberglass tabs were used.

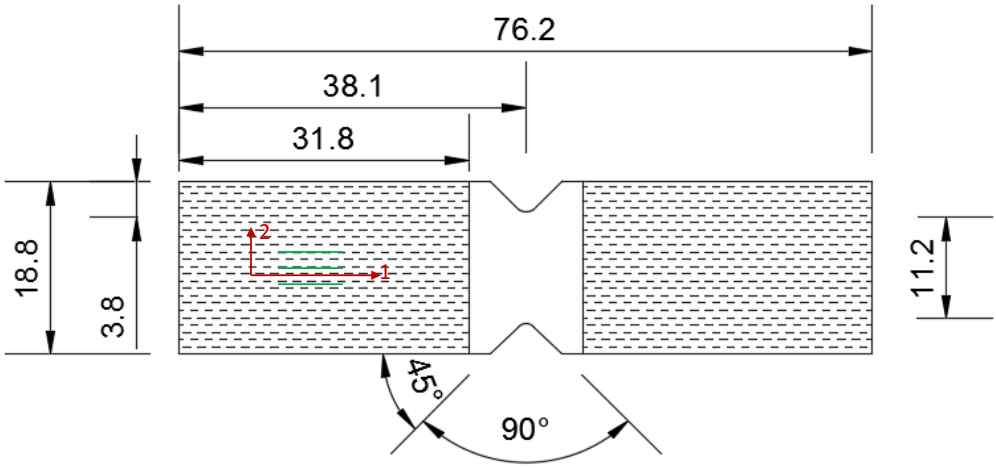

Fig. 19. ASTM D5379 Recommended Iosipescu Shear Specimen Nominal Dimensions and Layout (All Dimensions in mm)

As the test progressed, analysis of the test results showed that the specimen is not in a state of pure shear and the load-carrying capacity of the specimen does not diminish to zero. Rather, the specimen continues to excessively deform and the gage section twists to a point where the fibers bridging the cracks are effectively put into a state of tension. Finally, the

bottom right corner of the specimen rests on the fixture and the specimen can no longer deform. Since the objective is to obtain the complete stress-strain curve, the specimen geometry was modified. A deeper notch was used to reduce the cross-sectional area of the gage section and hence require a smaller force to induce failure. Since a deeper notch also causes a reduction in the structural stiffness of the specimen leaving it more susceptible to excess bending, the tabs were moved closer to each other to stiffen the gage section. The modified specimen is shown in Fig. 20. The shaded regions indicate the area where G10 fiberglass tabs were used.

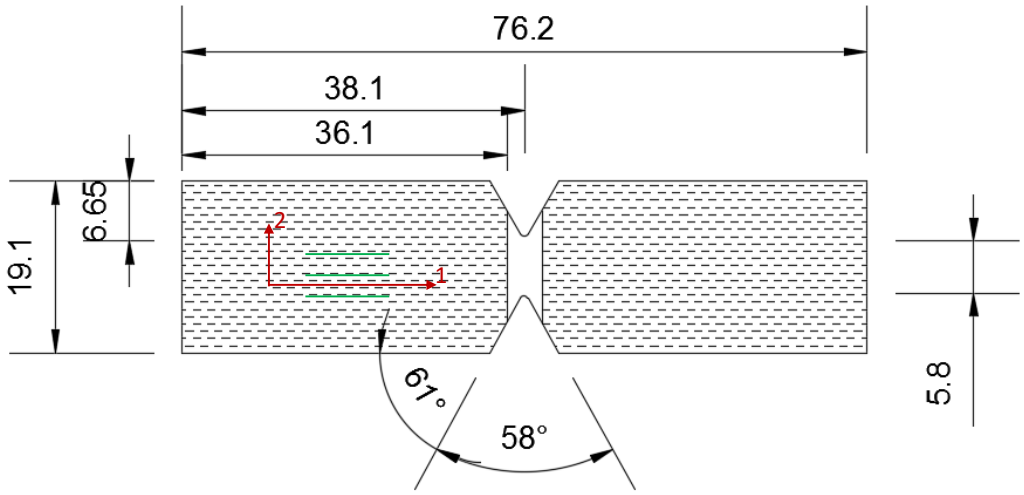

Fig. 20. Modified Iosipescu Shear Specimen Nominal Dimensions and Layout (All Dimensions in mm)

The modified specimen geometry allowed for much higher shear stress and strain values to be obtained.

Through-thickness Shear Test: Two through-thickness shear experiments were performed. Both 1-3 plane and 2-3 plane shear tests were performed with geometries that are recommended by ASTM D5379/D5379M-12 (D30 Committee 2012), and are shown in Fig. 21. The shaded regions indicate the area where G10 fiberglass tabs were used.

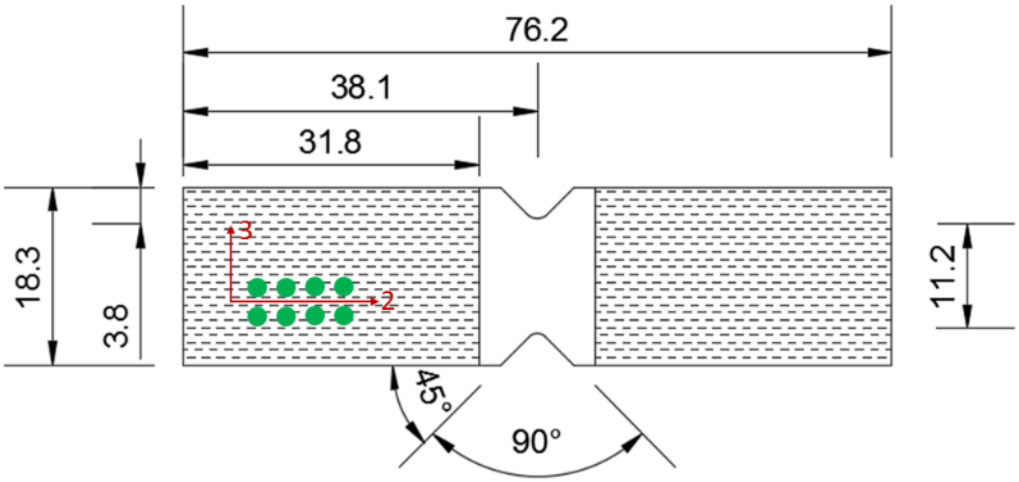

(a)

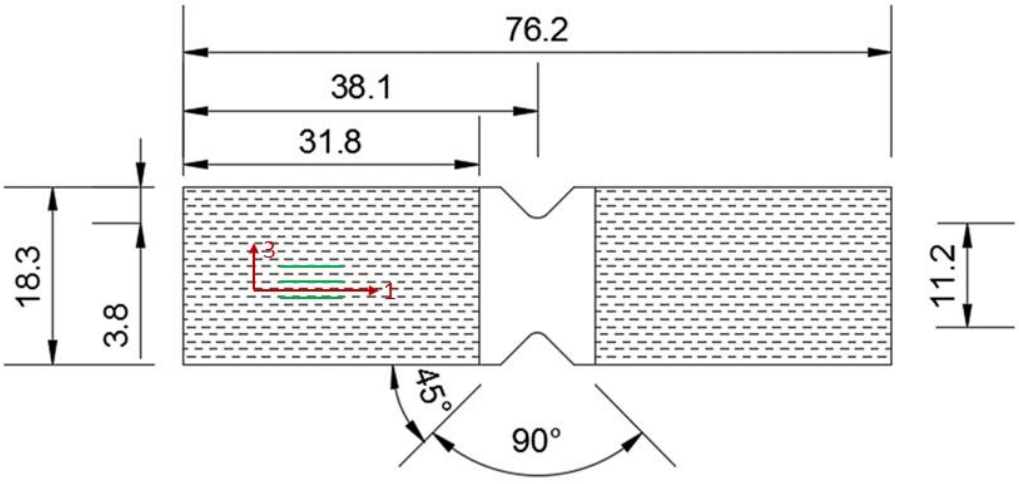

(b)

Fig. 21. Nominal Specimen Dimensions and Layout (a) 2-3 Plane Shear Specimen and (b) 1-3 Plane Shear Specimen (All Dimensions in mm)

The specimens had a nominal thickness of 0.122 in (3.1 mm). The height of the specimens (in the 3-direction) were limited by the thickness of the available composite panel. As such, the geometries deviate from the recommendations made by ASTM D5379.

In-plane Off-axis Tension Test: Four in-plane off-axis tension tests were performed. The results of the tests performed with a fiber angle (θ) of 45° to the loading axis is used directly as input while the remaining test results (fiber angles of 10°, 15°, and 30°) aid in computing the flow rule coefficients. The specimens were machined with dimensions commensurate with the recommendations provided by ASTM D3039/D3039M-17 (D30 Committee 2017a). Fig. 22 provides schematics of the specimens, where the shaded regions indicate the area where G10 fiberglass tabs were used.

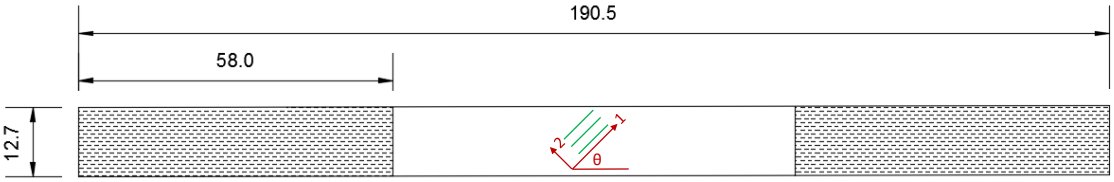

Fig. 22. Nominal Specimen Dimensions 1-2 Plane Off-axis Tension Tests (All Dimensions in mm)

In addition to the specimen geometry shown in Fig. 22, the 45° tests were performed with an alternative specimen geometry, shown in Fig. 23. The purpose was to determine if the length of the gage section had an influence on the observed response.

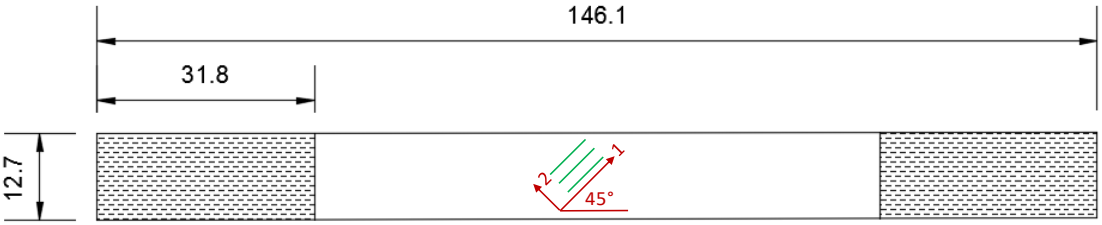

Fig. 23. Nominal Specimen Dimensions of Alternative 1-2 Plane Off-axis 45° Tension Test (All Dimensions in mm)

All specimens had a nominal thickness of 0.122 in (3.1 mm).

2.3 Experimental Results

This section presents the results of the twelve tests shown in

Table 2. The resulting stress-total strain curves are shown as well as various point properties of the material.

2.3.1 Principal Material Directions Tension Tests

The stress-strain curves from the PMD tension tests are shown in Fig. 24 and the results are summarized in Table 6. Note the enormous differences in the stiffness and the strengths that is typical of most unidirectional composites when comparing the fiber-direction (1-direction) to the transverse and through-thickness directions.

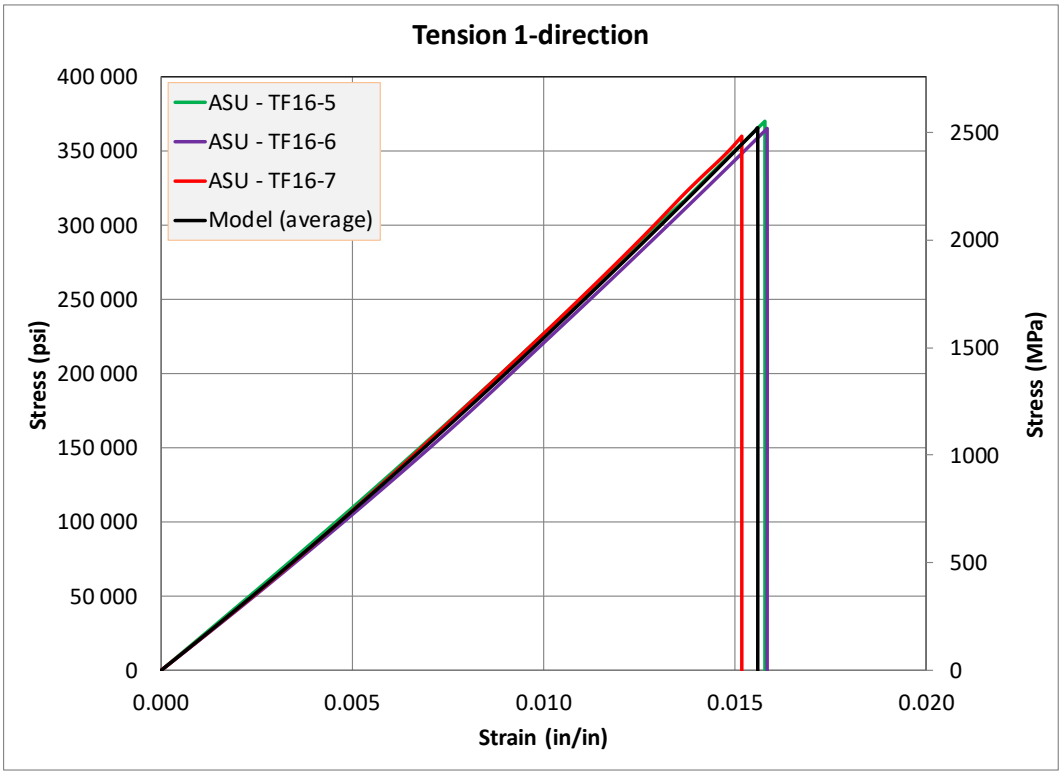

(a)

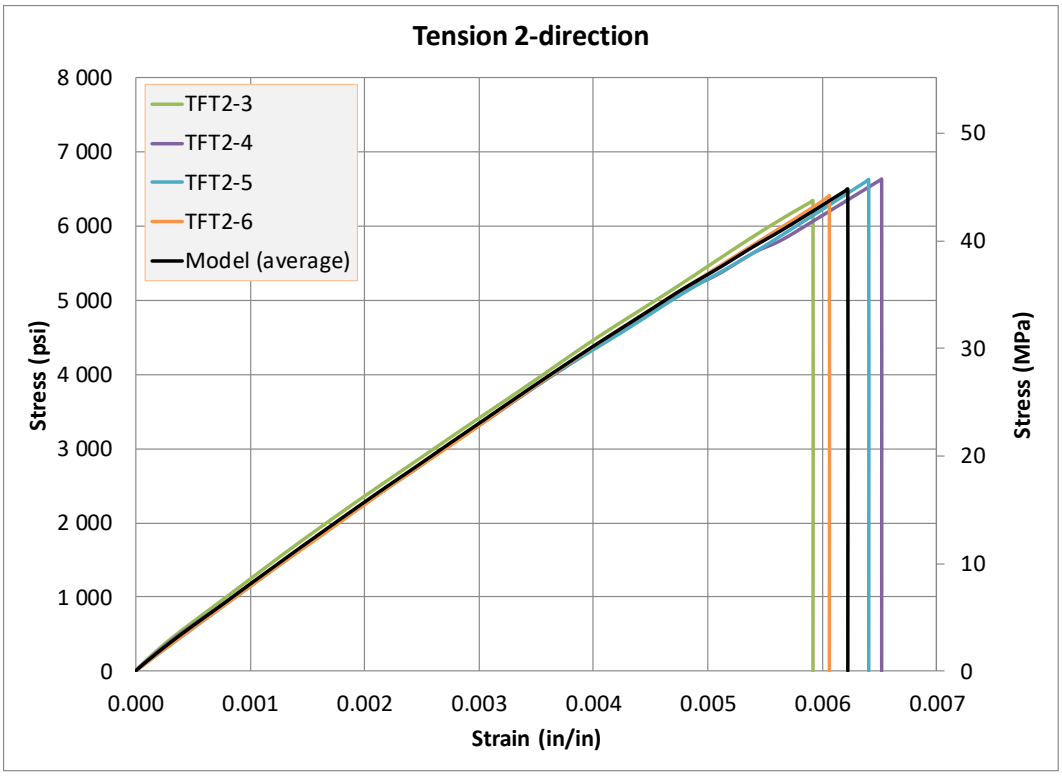

(b)

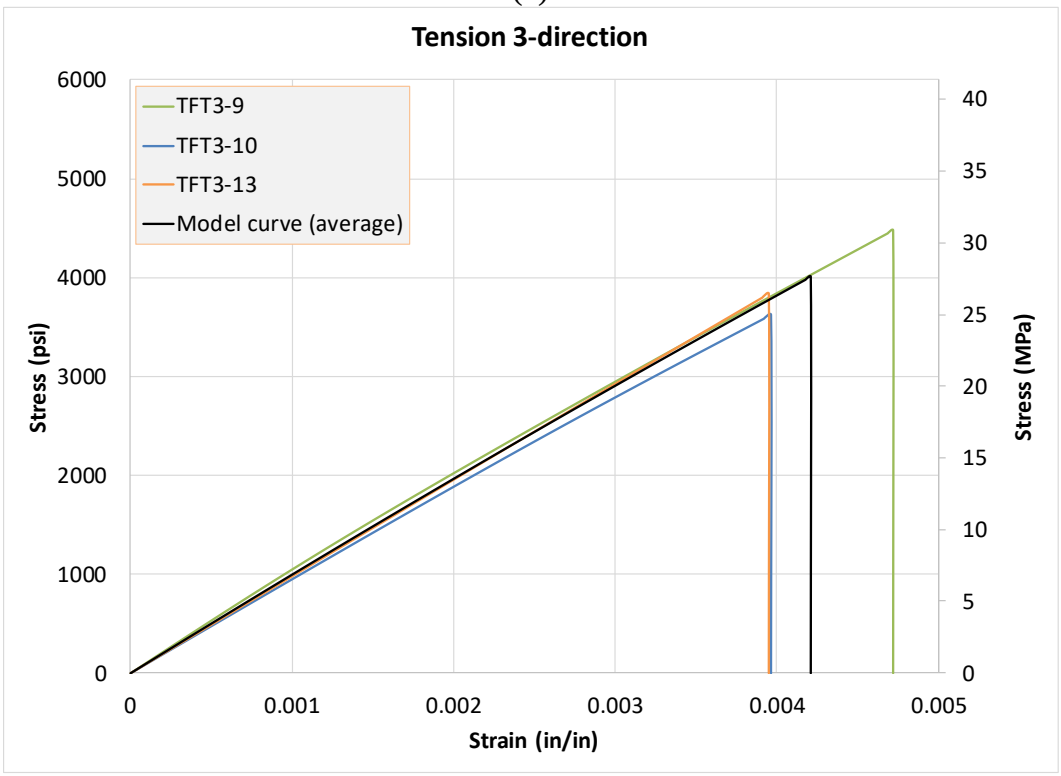

(c)

Fig. 24. Tension Stress-Strain Curves (a) 1-direction, (b) 2-direction, and (c) 3-direction

Table 6. Summary of Results for the PMD Tension Tests (Average Values [Coefficient of Variation, %])

	1-direction	**2-Direction**	**3-Direction**
Youngs's Modulus, GPa psi	161.7 23 457 871 [1.6%]	7.4 1 066 413 [1.3%]	6.7 966 505 [4.5%]
Poisson's Ratio	ν_{12}: 0.317 [1.6%]	ν_{21}: 0.017 [9.0%]	ν_{31}: 0.027 [1.9%] ν_{32}: 0.439 [0.0%]
Failure/Ultimate Strain	0.01560 [2.3%]	0.00622 [4.6%]	0.00421 [8.5%]
Peak Stress, MPa psi	2519.0 365 372 [2.0%]	44.8 6 502 [2.6%]	27.4 3 977 [9.0%]

Fig. 25 shows the tested specimens after failure is induced in the test specimen.

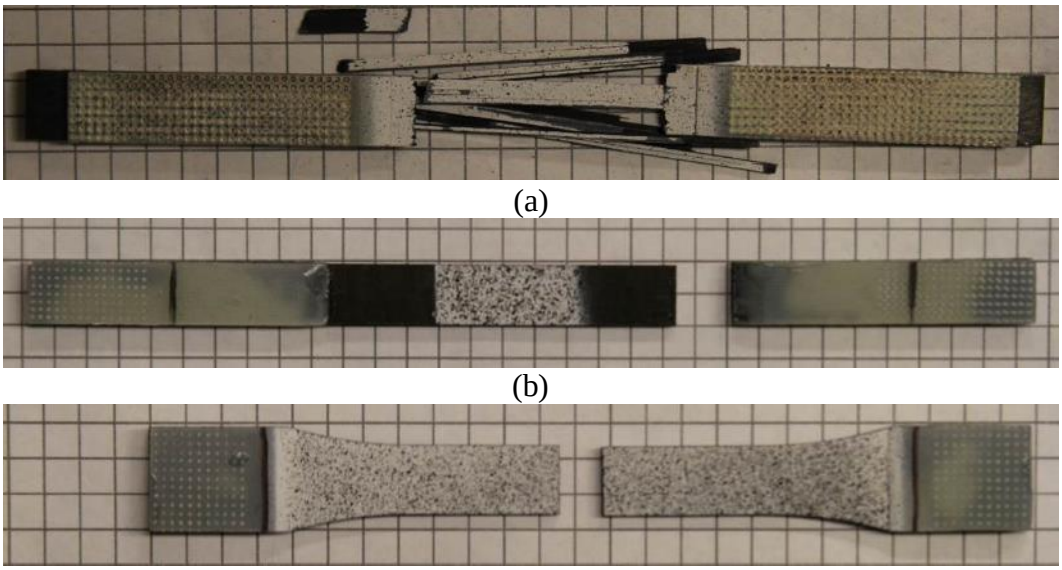

(a)

(b)

(c)

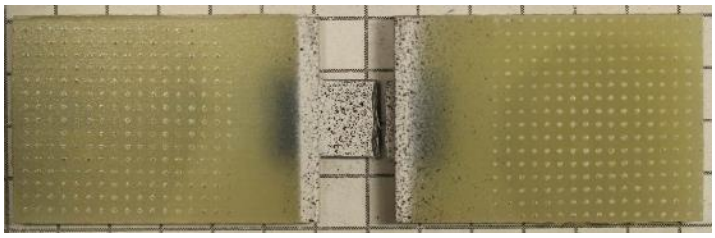

(d)

Fig. 25. Typical Specimen after Testing (a) 1-direction Tension (b) 2-direction Tension Using ASTM Standard Specimen (c) 2-direction Tension Using Modified Dog Bone Specimen (d) 3-direction Tension

All three of the PMD's exhibit mostly linear elastic behavior in tension. The 2-direction exhibits a slight nonlinearity near the point of failure. While the failure in all three directions was brittle, the failure mode in each of the PMD's was different.

In the 1-direction, two clear failure modes were observed as shown in Fig. 25a. The first was a failure of the matrix, parallel to the fibers. The second was a tensile failure of the fibers which appear to have initiated where the tapered section of the specimen starts. The fiber failure was likely due to a large strain concentration which was present due to the geometry of the specimen. The average cross-sectional area of the gage section was used to compute the stress value. Additionally, as shown in Fig. 24a, the 1-direction tension curves exhibited a slight stiffening behavior as the experiment progressed. The stiffening is most likely due to the straightening of the fibers, thus increasing the apparent stiffness of the composite. The average slope of the curves throughout the entire experiment was used to obtain an average modulus value.

Fig. 25b and Fig. 25c show the typical failure of a standard specimen and a dog bone specimen respectively in the 2-direction tests. Both specimen geometries exhibited inter-fiber failure. The dog bone shaped coupons consistently failed in the gage section of the specimen. Interestingly, though the failure locations were typically different when comparing the standard geometry and the dog bone geometry, the stress-strain curves of the respective specimen geometries were similar.

The failure of the 3-direction specimens was consistently interlaminar. This behavior was likely due to the ply boundary effect that is caused by the manufacturing process of laminated composites. The model curve was generated using specimens which had the 1-3 and 2-3 planes speckled for image analysis respectively (Fig. 15). The 3-direction tension and 2-direction tension tests show similar results as expected due to the relative transverse isotropy of the composite. However, the 3-direction curves exhibited a slightly lower modulus, a lower ultimate strain, and a lower ultimate stress as compared to the 2-direction curves. This behavior can be attributed to the effect of the ply boundaries on the 3-direction results. The difference in the 3-direction and 2-direction at the mesoscale can be clearly discerned from the micrograph of the T800S/F3900 composite system shown in Fig. 2. The different thickness and irregular ply boundaries can be readily identified and strictly speaking, transverse isotropy assumptions are not valid at this scale.

2.3.2 Principal Material Directions Compression Tests

The stress-strain curves from the PMD compression tests are shown in Fig. 26 and the results are summarized in

Table 7.

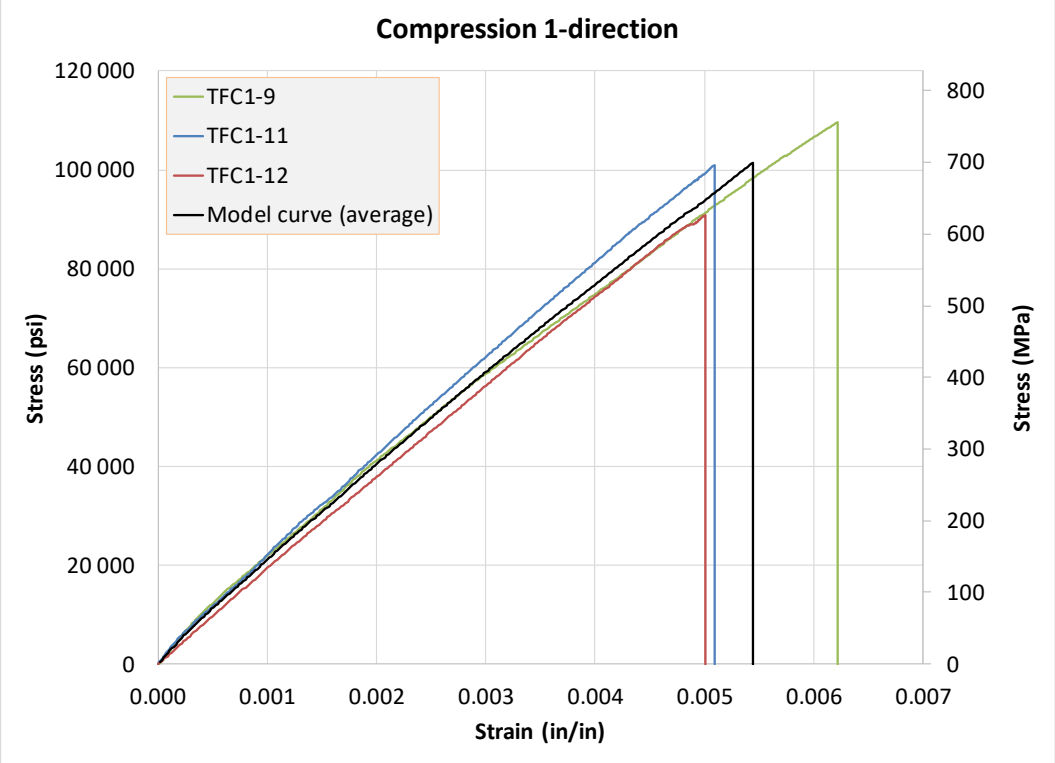
Compression 1-direction
TFC1-9
TFC1-11
TFC1-12
Model curve (average)
Stress (psi)
Stress (MPa)
Strain (in/in)
120 000
100 000
80 000
60 000
40 000
20 000
0
800
700
600
500
400
300
200
100
0
0.000
0.001
0.002
0.003
0.004
0.005
0.006
0.007

(a)

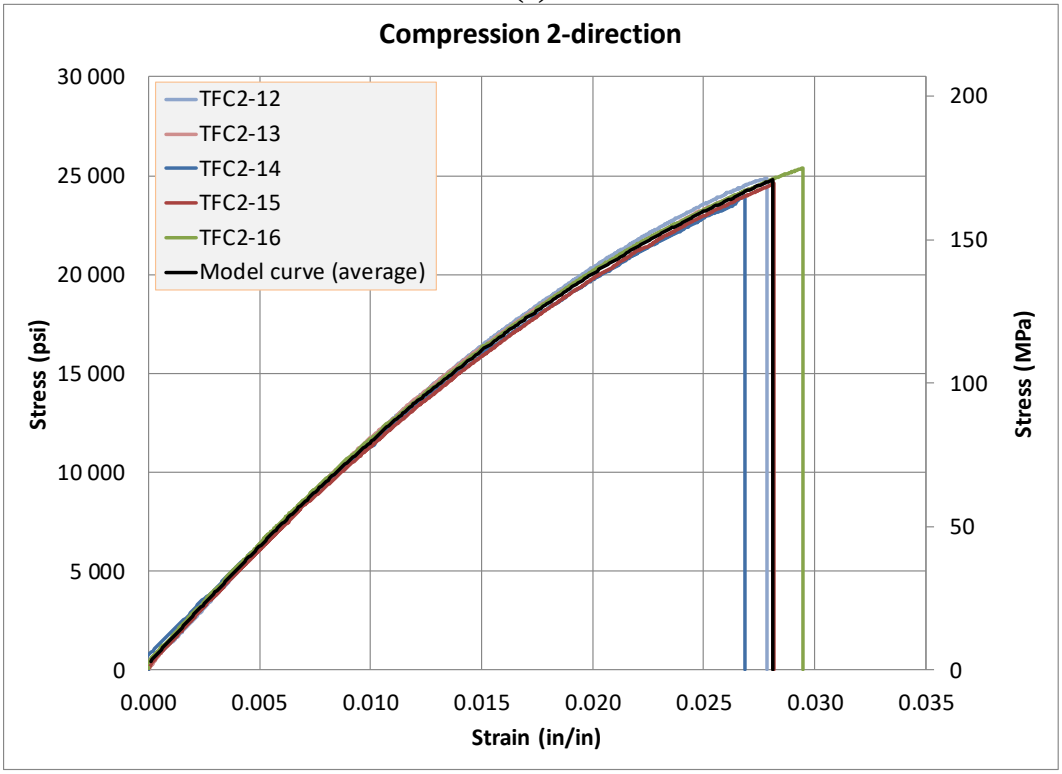
Compression 2-direction
TFC2-12
TFC2-13
TFC2-14
TFC2-15
TFC2-16
Model curve (average)
Stress (psi)
Stress (MPa)
Strain (in/in)
30 000
25 000
20 000
15 000
10 000
5 000
0
200
150
100
50
0
0.000
0.005
0.010
0.015
0.020
0.025
0.030
0.035

(b)

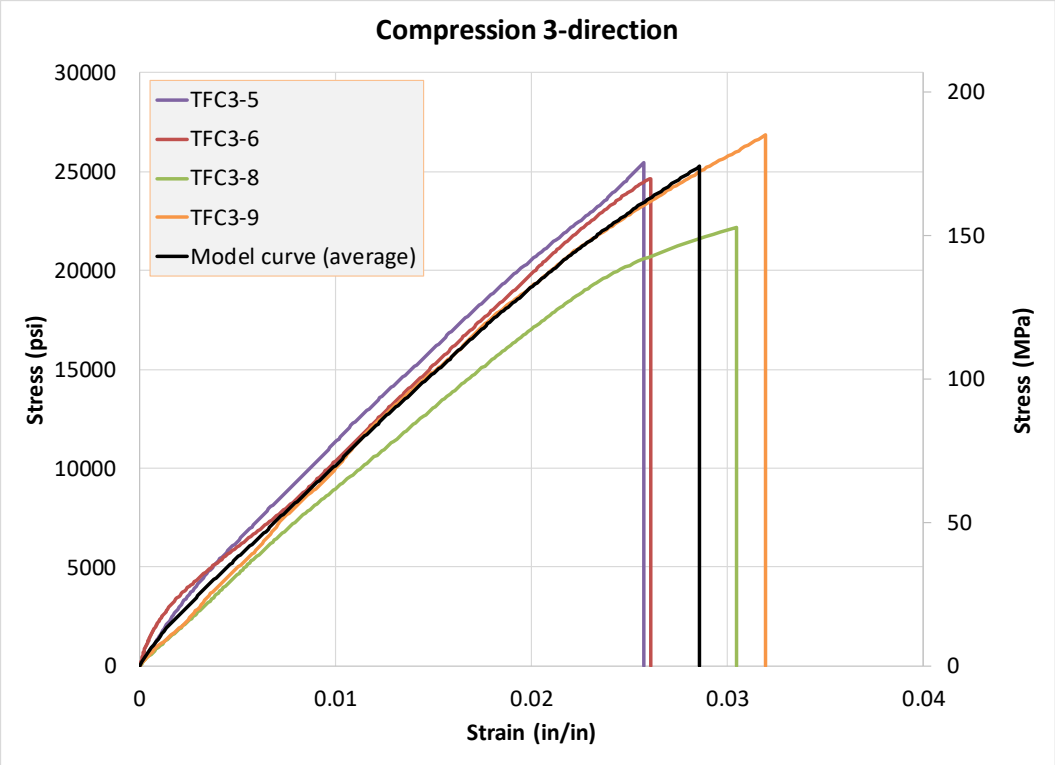

(c)

Fig. 26. Compression Stress-Strain Curves (a) 1-direction, (b) 2-direction, and (c) 3-direction

Table 7. Summary of Results for the Compression Tests (Average Values [Coefficient of Variation, %])

	1-direction	**2-Direction**	**3-Direction**
Youngs's Modulus, GPa psi	 129.4 18 775 652 [5.8%]	 7.7 1 119 123 [3.2%]	 7.2 1 038 690 [10.6%]
Poisson's Ratio	ν_{12}: 0.342 [8.4%]	ν_{21}: 0.021 [6.0%]	ν_{31}: 0.032 [17.1%] ν_{32}: 0.676 [4.9%] ν_{32}^{p}: 0.776 [0.9%]
Failure/Ultimate Strain	0.00629 [9.9%]	0.04127 [2.7%]	0.02856 [10.9%]
Peak Stress, MPa psi	727.5 105 513 [9.7%]	175.9 25 513 [2.5%]	170.9 24 784 [7.9%]

Fig. 27 shows the in-plane compression specimens after testing.

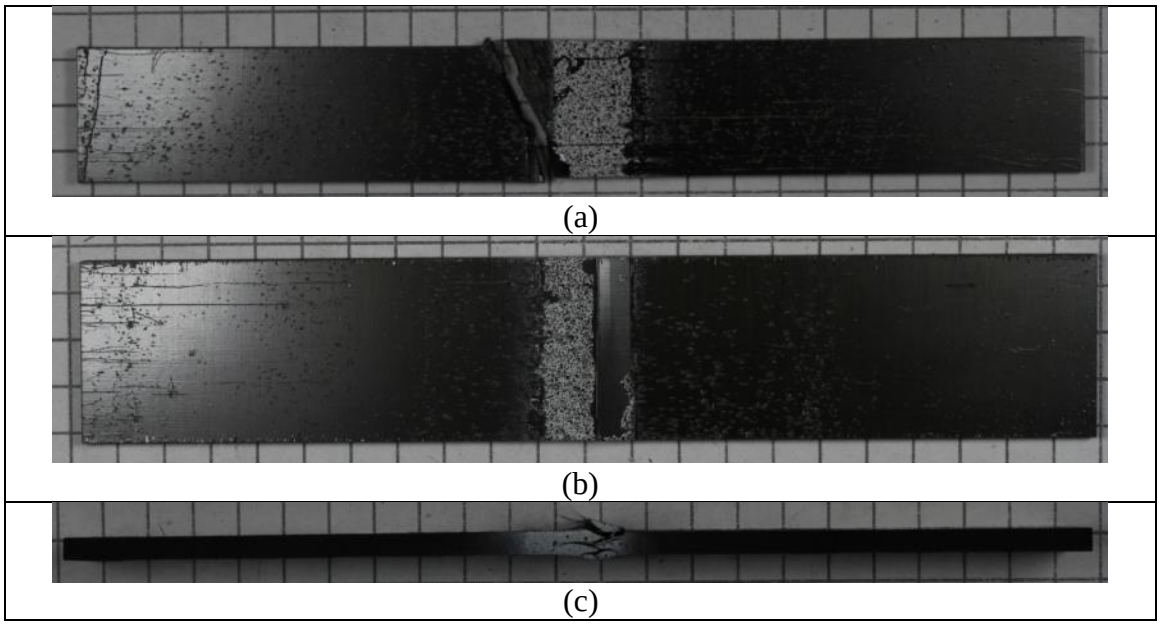

Fig. 27. Typical Specimen after Testing (a) 1-direction Compression, (b) 2-direction Compression In-plane View, and (c) 2-direction Compression Side View

A clear asymmetry in the tension and compression response of the T800/F3900 composite was observed. While the tension behavior was mostly linear, the material exhibited nonlinear behavior in compression – both the 2-direction and 3-direction specimens also failed at higher stresses and strains, while the 1-direction failed at a lower stress and strain. Though the overall behavior of the PMD's was comparatively different in tension and compression, the behavior in the initial regimes were nearly identical.

The 1-direction compression curves exhibited contrasting behavior compared to the 1-direction tension tests in that the stress-strain curve shown in Fig. 26a shows softening behavior with increasing stress/strain value. The failure of the 1-direction compression specimens was different from the tension specimens. The tension specimens exhibited

matrix failure, parallel to the fibers. However, as shown in Fig. 27a, the compression specimens failed across the fibers. The nonlinearity in the compression response is likely caused by microbuckling and fiber-kinking as the experiment progressed. The 2-direction compression specimens exhibit considerable nonlinear behavior. The nonlinearity can be attributed to the plastic behavior of the polymeric matrix. The failure observed was consistent with the 3-direction failure in the 2-3 plane. Cracks formed between and parallel to the plane of the fibers. A typical failed specimen is shown in Fig. 27b and Fig. 27c.

All of the through-thickness compression tests experienced brittle failure. The 3-direction compression specimens exhibited inter-fiber failure in the 2-3 plane which is typical of unidirectional composites under compression in the 2-3 plane. This failure is due to matrix cracking that requires less energy than fiber breakage. The cracks that are initiated in the specimen will propagate through the matrix more easily than cutting across the fibers. The off-axis compression specimens exhibited interlaminar failure. Typical failed specimens are shown in Fig. 28.

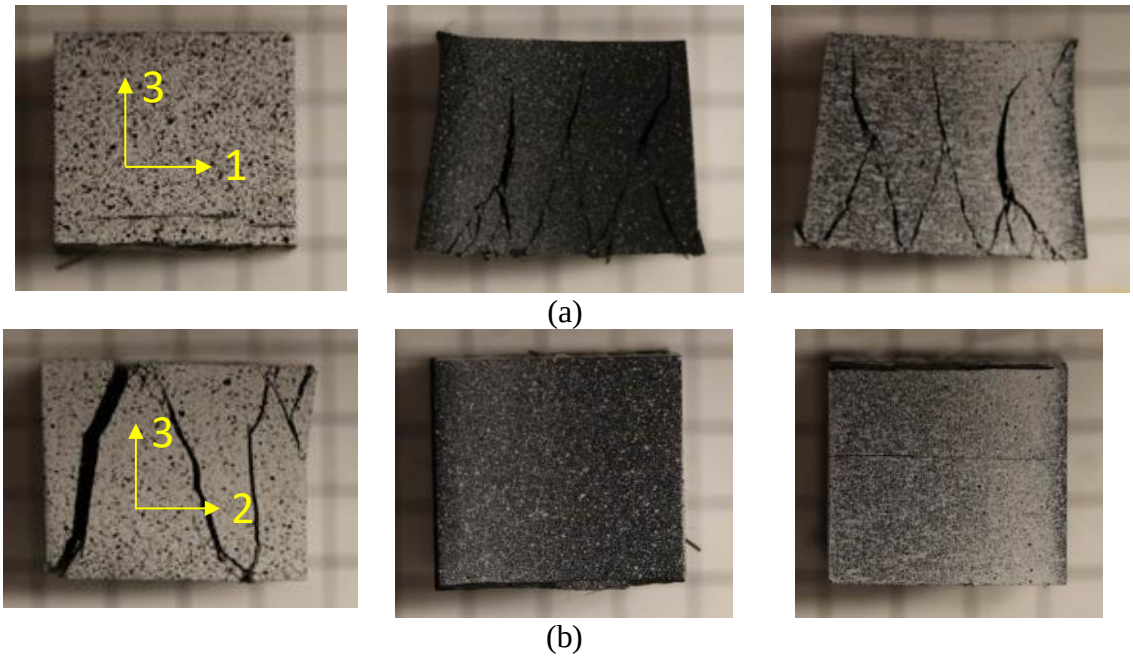

Fig. 28. Typical Failure of (a) 3-direction Compression with 1-3 Plane Speckled and (b) 3-direction Compression with 2-3 Plane Speckled (from Left to Right: Speckled (Front) Face of the Specimen, Left Face of the Specimen, Right Face of the Specimen)

Each of the through-thickness compression specimens formed large cracks on the speckled surface, except for 3-direction compression with the 1-3 plane speckled. The 3-direction specimens exhibited similar nonlinearity to the 2-direction experiments and the nonlinearity can be attributed to the plastic behavior of the matrix. Similar to the tension behavior, the 3-direction and 2-direction compression behavior is similar but not identical because of the ply boundary effects.

The value of the plastic Poisson's ratio in the 3-2 plane, ν_{32}^{p} in

Table 7, is computed for each replicate of the 3-direction compression test and averaged. An example of how the value is obtained is shown below for one of the replicates. Fig. 29 shows the specimen used for the computations.

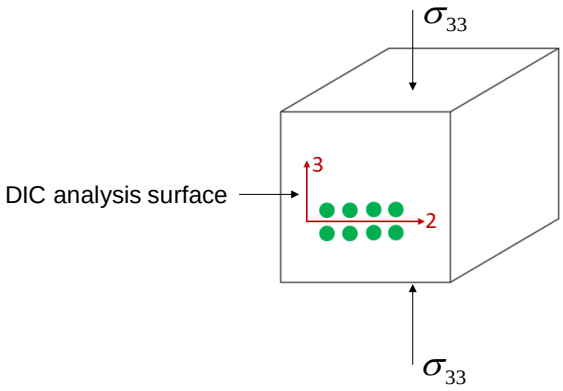

3-direction is referred to as *longitudinal* while 2-direction is referred to as *transverse*.

Fig. 29. Specimen Type Used to Compute ν_{32}^{p}

1. From longitudinal stress-total strain curve, determine the yield strain as the location on the curve where the behavior is no longer linear (Fig. 30).

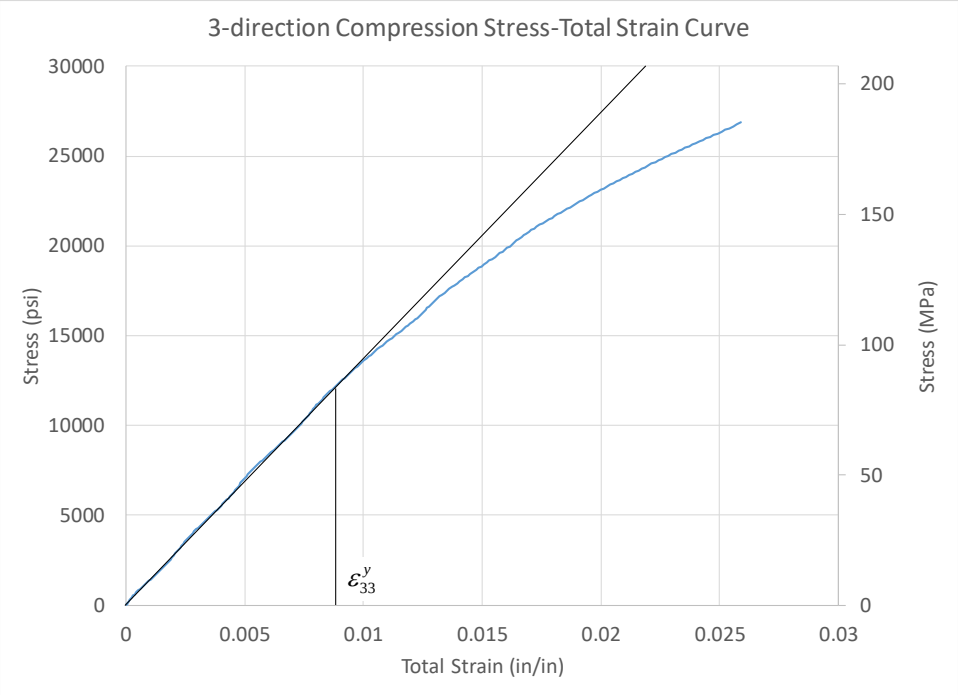

Fig. 30. Yield Strain Value for Single Replicate of 3-direction Compression Test

2. All longitudinal and transverse strains which occur prior to the longitudinal yield strain are assumed to be completely elastic. The "elastic" Poisson's ratio is computed by first plotting the negative of the transverse strain and the longitudinal strain then performing a linear regression (Fig. 31).

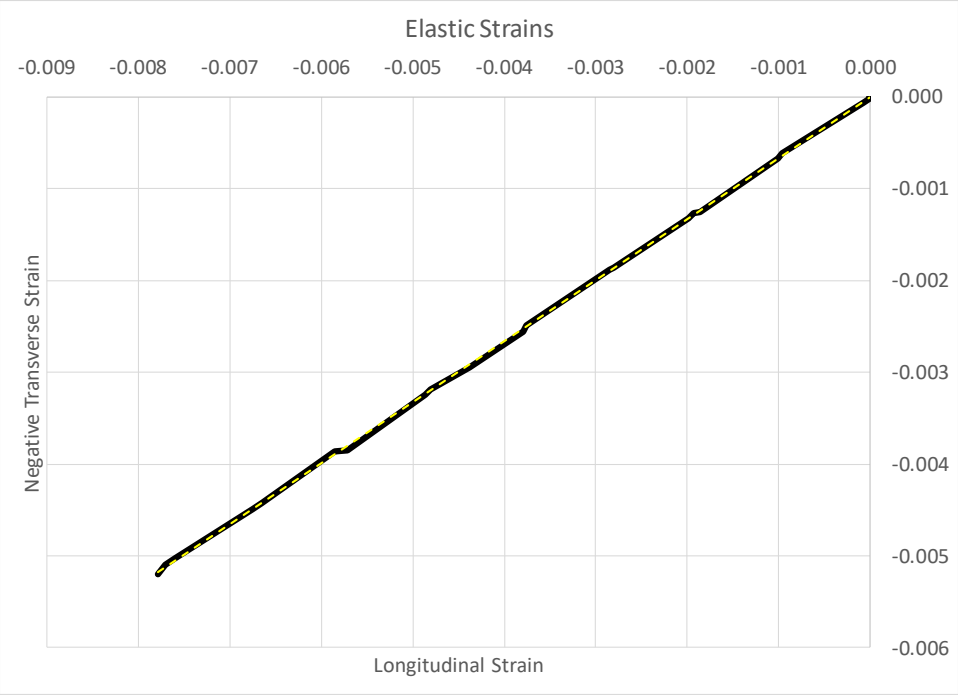

Fig. 31. Example of Linear Regression Performed to Compute ν_{32}

The value of ν_{32} is the slope of the regression line through the data.

$$\nu_{32} = -\frac{d\varepsilon_{22}^{e}}{d\varepsilon_{33}^{e}} \tag{2.52}$$

3. The longitudinal and transverse plastic strains are computed for all values of longitudinal stress, after the longitudinal yield strain, using the following equations which assume a linear decomposition of the total strain into additive elastic and plastic components.

$$\varepsilon_{33}^{p} = \varepsilon_{33}^{t} - \varepsilon_{33}^{e} = \varepsilon_{33}^{t} - \frac{\sigma_{33}}{E_{33}} \tag{2.53}$$

$$\varepsilon_{22}^{p} = \varepsilon_{22}^{t} - \varepsilon_{22}^{e} = \varepsilon_{22}^{t} - \nu_{32}\frac{\sigma_{33}}{E_{33}} \qquad 2.54$$

4. Similar to the elastic Poisson's ratio, the plastic Poisson's ratio is computed by first plotting the negative of the transverse plastic strain and the longitudinal plastic strain (Fig. 32)

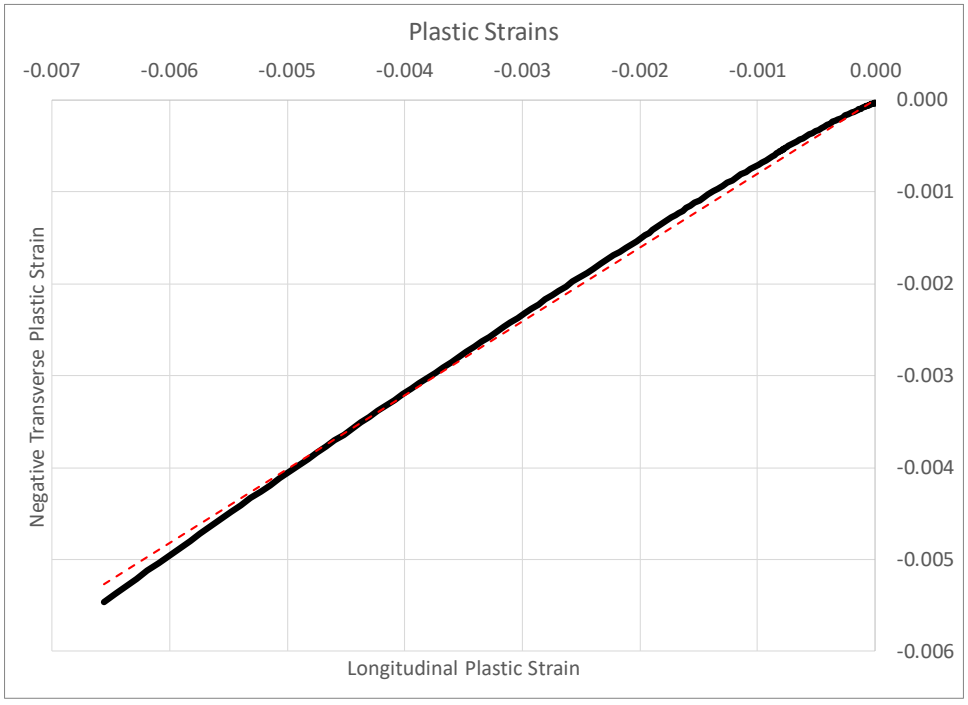

Fig. 32. Example of Linear Regression Performed to Compute ν_{32}^{p}

The slope of the linear regression line through the data is taken as the value of ν_{32}^{p}. Note that the slope of the data in Fig. 32 is not constant. However, the assumption in the current implementation is that the flow rule coefficients remain constant which is why a linear regression is performed.

2.3.3 Principal Material Plane Shear Test Results

The (model) stress-strain curves from the principal plane shear tests are shown in Fig. 33 and the results are summarized in Table 8. The 1-2 plane results were obtained from the modified Iosipescu specimen geometry (Fig. 20) whereas the 1-3 and 2-3 plane results were obtained using the ASTM recommended geometry (Fig. 21).

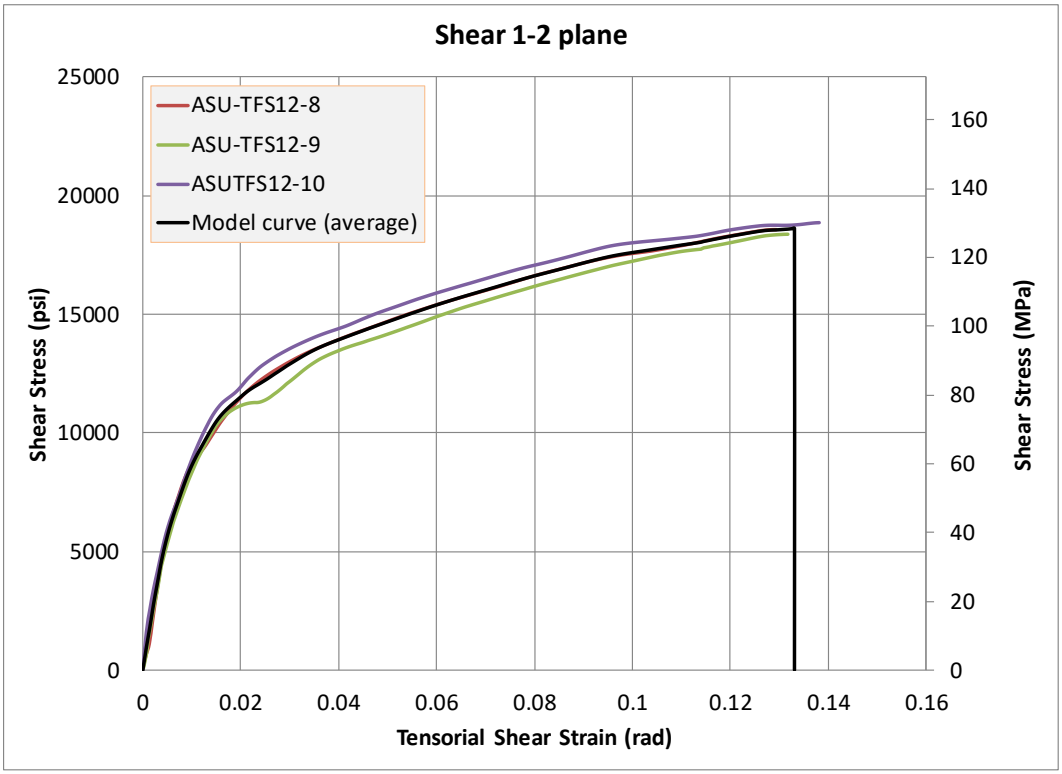

(a)

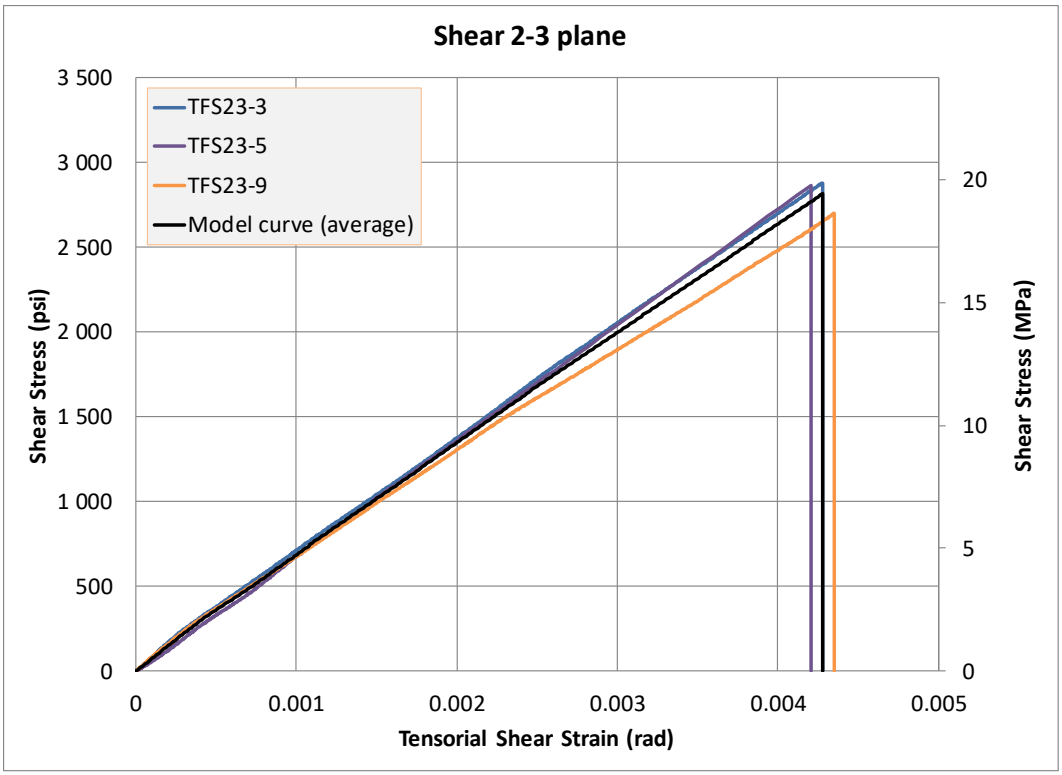

(b)

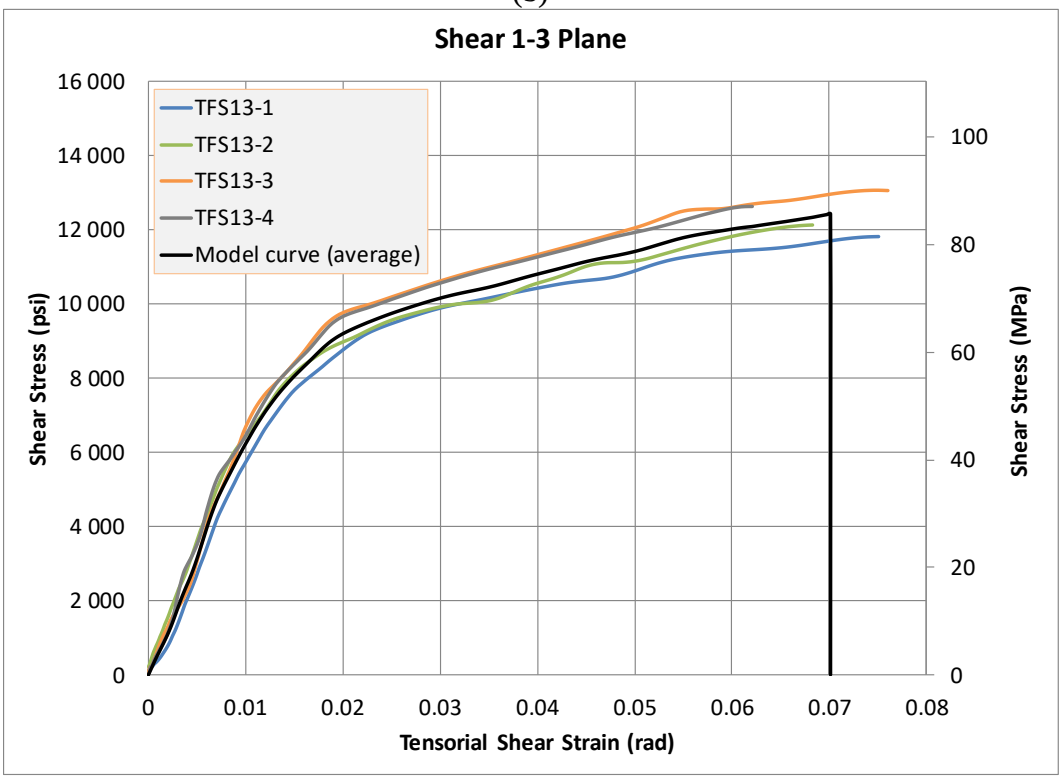

(c)

Fig. 33. Shear Stress-Strain Curves (a) 1-2 Plane, (b) 2-3 Plane, and (c) 1-3 Plane

Table 8. Summary of Results for the Shear Tests (Average Values [Coefficient of Variation, %])

	1-2 Plane	**2-3 Plane**	**1-3 Plane**
Shear Modulus, GPa	4.0	2.3	2.4
psi	579 489 [7.0%]	335 594 [3.3%]	347 738 [2.2%]
Failure/Ultimate Strain (tensorial)	0.13400 [3.3%]	0.00428 [1.7%]	0.07040 [9.3%]
Peak Stress, MPa	128.7	19.4	85.6
psi	18 670 [1.0%]	2 816 [3.5%]	12 419 [4.4%]

The 2-3 plane shear specimens failed in a similar manner to the compression tests in the same plane, parallel to and between the fiber planes. A typical failed 2-3 plane specimen is shown in Fig. 34.

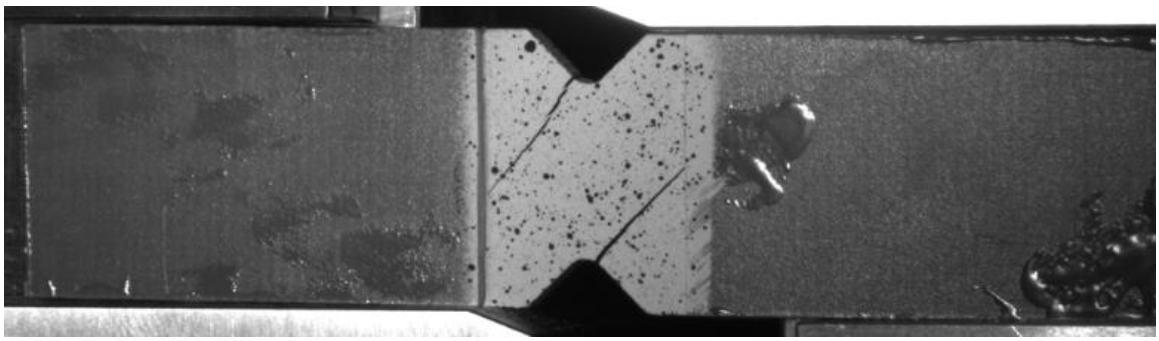

Fig. 34. Typical Failure Pattern of 2-3 Plane Shear Specimen

The failure pattern exhibited by the standard 1-2 plane and 1-3 plane specimens was consistent with the results reported in previous research (Broughton et al. 1990; Odegard and Kumosa 2000; Swanson et al. 1985). There were matrix cracks in the gage section,

between the notches, with two major cracks that emanate from the roots of the notches. A typical failed specimen is shown in Fig. 35.

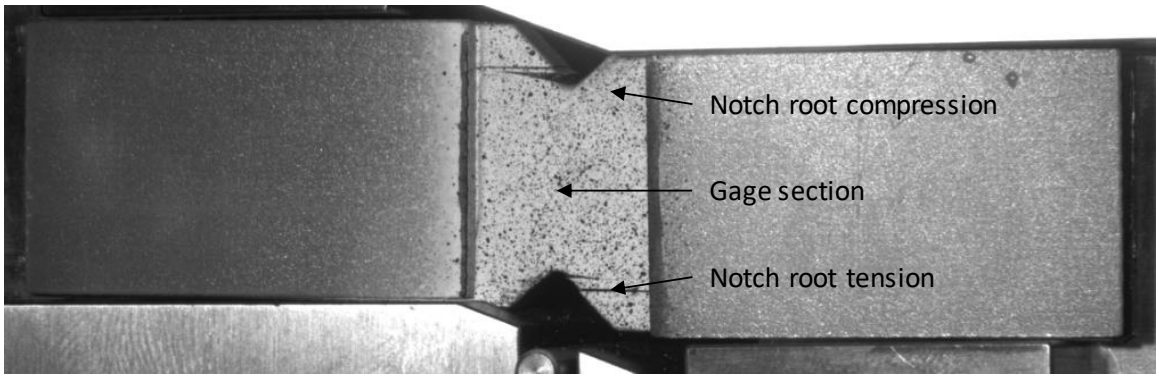

Fig. 35. Typical Failure Pattern of ASTM D5379 Recommended In-plane Shear Specimen

The cracks emanating from the notch roots, shown in Fig. 35, are caused by excessive transverse strains. The failure is not a true shear failure but rather it is failure caused by exceeding the tensile strength of the composite in the 2-direction. The formation of the cracks also coincides with the onset of nonlinearity in the stress-strain curve. After the cracks form at the notch roots, the gage section of the specimen remains in a state of pure shear for a short period, however, the specimen began to experience large deformations, excessively rotating the principal material axes, leading to a multiaxial loading state. For the specimen to be in a state of pure shear, the transverse and longitudinal components of strain would both have to be negligible. A comparison of the different strain components, obtained through DIC measurements, is shown in Fig. 36.

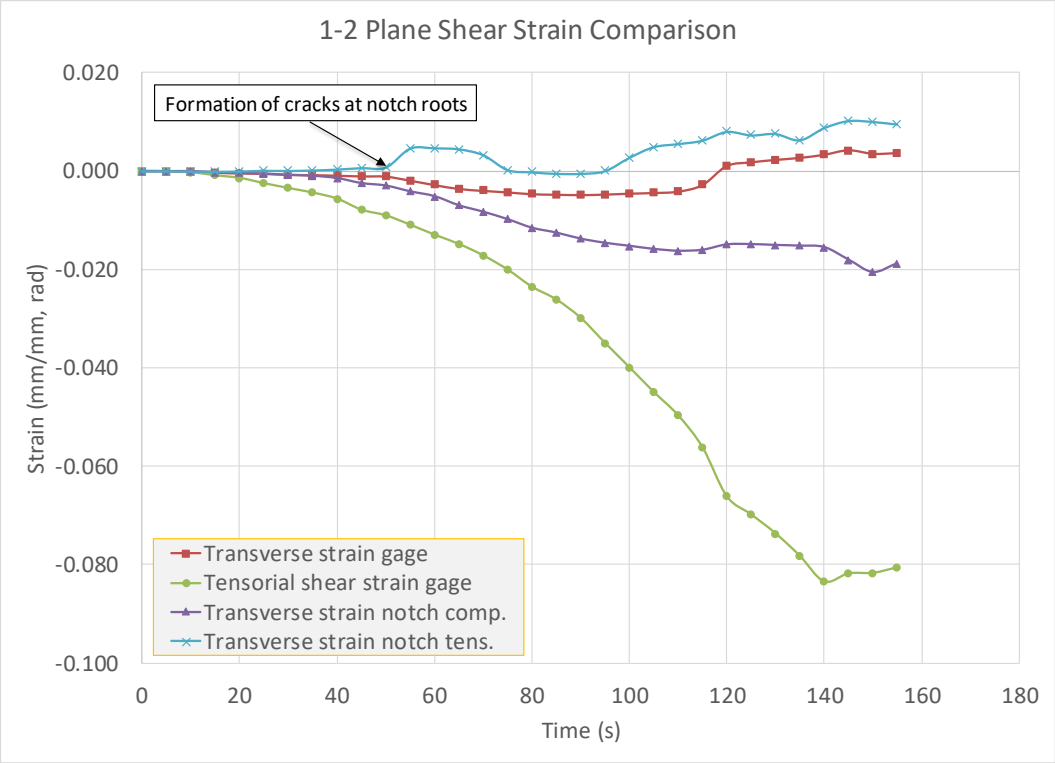

Fig. 36. Comparison of Strain Components for Typical 1-2 Plane Shear Test Using ASTM Recommended Geometry

Fig. 36 shows that the shear strain in the gage section of the specimen still dominates the state. However, near the notch tips, outside of the gage section, the transverse strains become large and will influence the apparent response of the specimen.

The stress-strain curve for the same specimen used for the strain comparison is shown in Fig. 37.

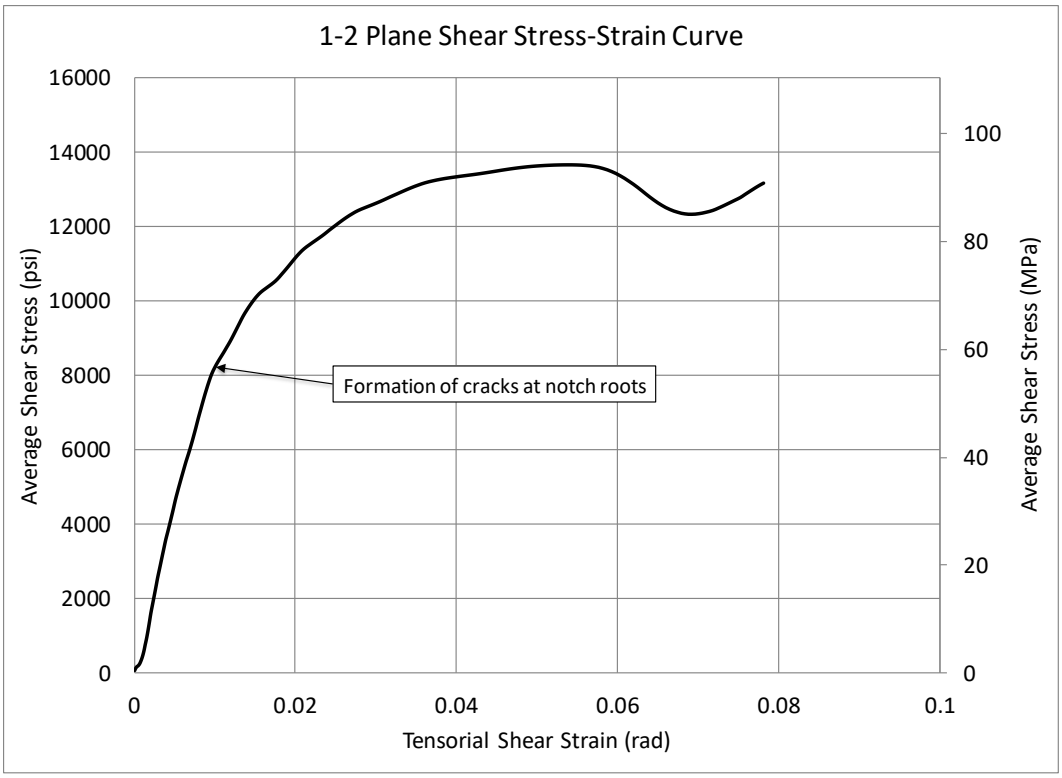

Fig. 37. Typical Stress-strain Curve for 1-2 Plane Shear Test Using ASTM Recommended Geometry

The failure pattern of the modified specimen was similar to that of the standard specimen. A typical failed specimen using the modified geometry is shown in Fig. 38.

Fig. 38. Typical Failure Pattern of the Modified 1-2 Plane Shear Test Iosipescu Specimen

The modified specimens exhibited nonlinear stress-strain behavior similar to the standard specimen. The onset of nonlinearity still coincided with the formation of the crack at the notch roots and the initial failure was still influenced by the transverse strain component. However, the modified specimens were consistently able to reach average shear stress and strain values larger than those of the standard specimens. The elastic behavior of both type of specimens was similar. A comparison of the stress-strain curves for both the ASTM recommended specimens and the modified specimens is shown in Fig. 39.

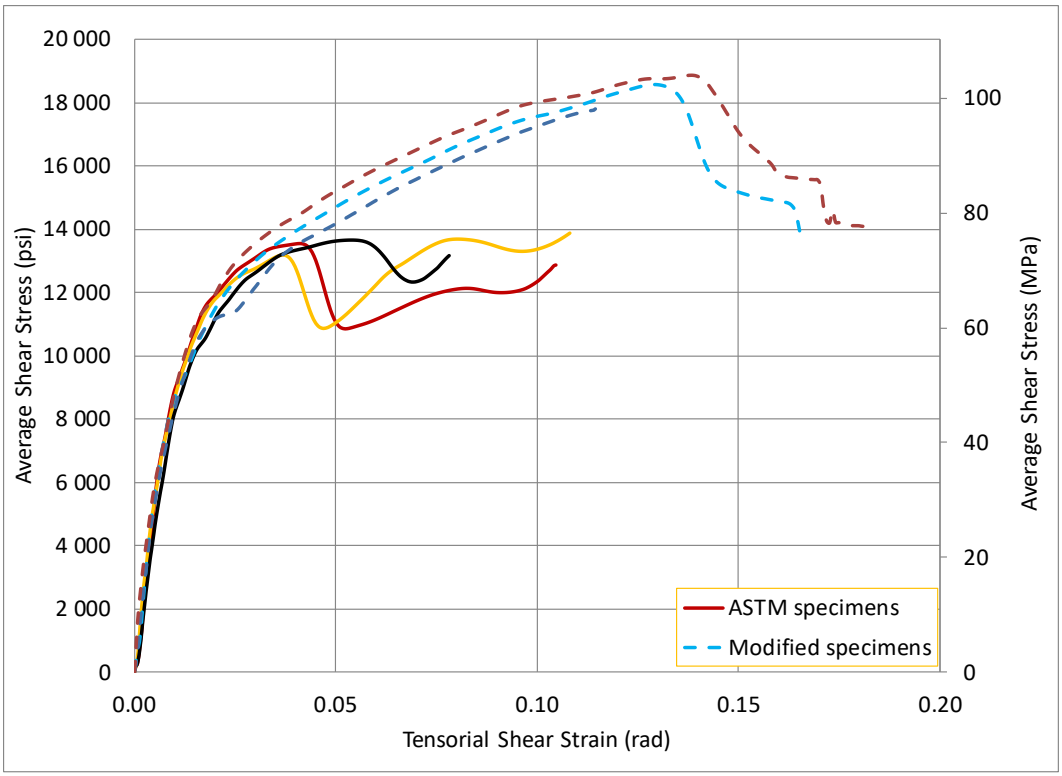

Fig. 39. Comparison of Stress-Strain Response of ASTM Recommended 1-2 Plane Shear Specimens and Modified 1-2 Plane Shear Specimens

In addition to the 1-2 shear test (S12), the 2-1 shear tests (S21) were also performed. The 2-1 shear test rotates the axes of the Iosipescu specimen by 90°. The ASTM D5379, Fig. 19, recommended specimen geometry was used to conduct these experiments. The problems inherent with the 1-2 shear specimens are not present when performing the 2-1 shear tests since the failure takes place much earlier in the test. Typically, the failure is well defined between the notches, parallel to the plane of the fibers, in the matrix. A typical failed specimen is shown in Fig. 40.

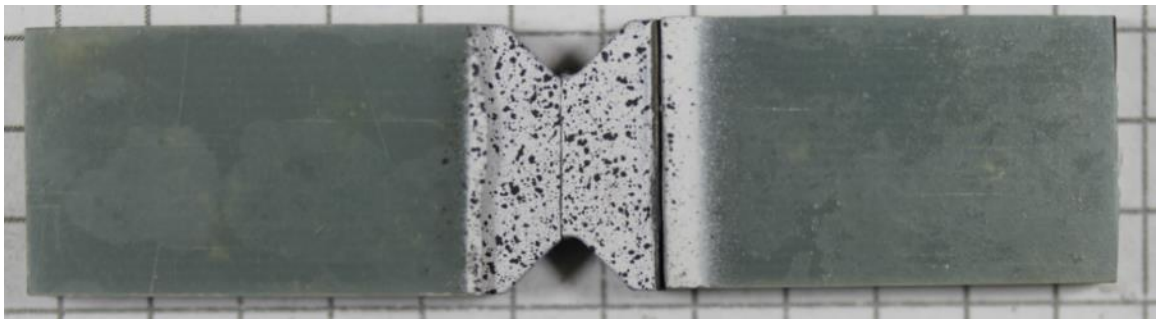

Fig. 40. Typical Failure Pattern of the 2-1 Plane Shear Specimen

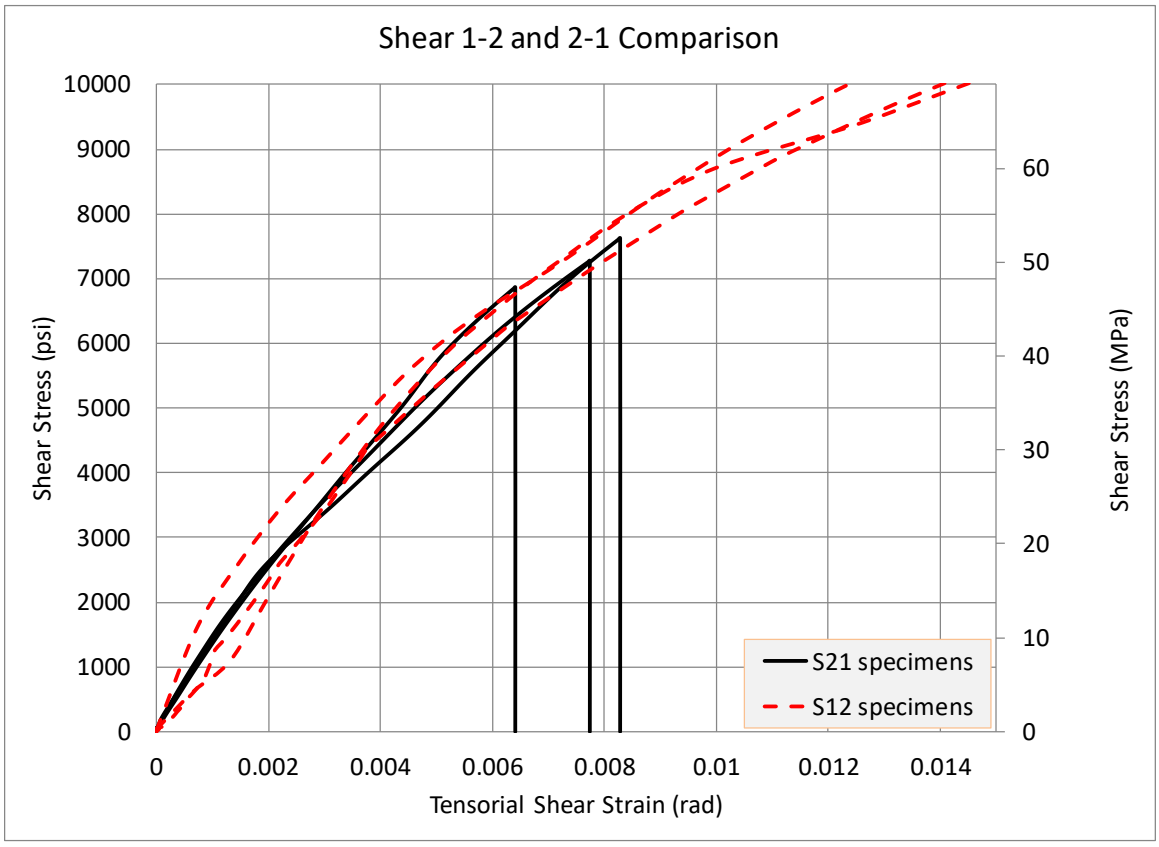

Fig. 41. Comparison of 1-2 and 2-1 Shear Tests

Fig. 41 shows that the initial behavior of the S12 experiments is similar to the S21 experiments, meaning G_{12} and G_{21} are the same which is what has been typically been assumed in other material models. The failure mode of the S21 experiments is consistent

with the manner in which the cracks form at the notch roots of the S12 experiments. The strain values at which the failure of the S21 specimens take place and the formation of the crack at notch roots in the S12 experiments are coincident. Though the overall behavior of the S12 and S21 specimens is different, a typical orthotropic material model is not designed to handle the differences. However, the S21 results provide insight into the shear strength of the composite. The 1-3 plane shear results show a high amount of nonlinearity similar to the 1-2 plane shear tests. As with the 2-direction and 3-direction tension/compression comparison, the 1-3 plane shear exhibits a lower modulus and lower ultimate stress and strain values even when compared to the ASTM recommended 1-2 plane shear geometry. 3-1 shear tests were not performed as the available panel was not thick enough to machine proper specimens.

2.3.4 45° Off-Axis Test Results

The model stress-strain curves from the 45° off-axis tests are shown in Fig. 42 and the results are summarized in Table 9.

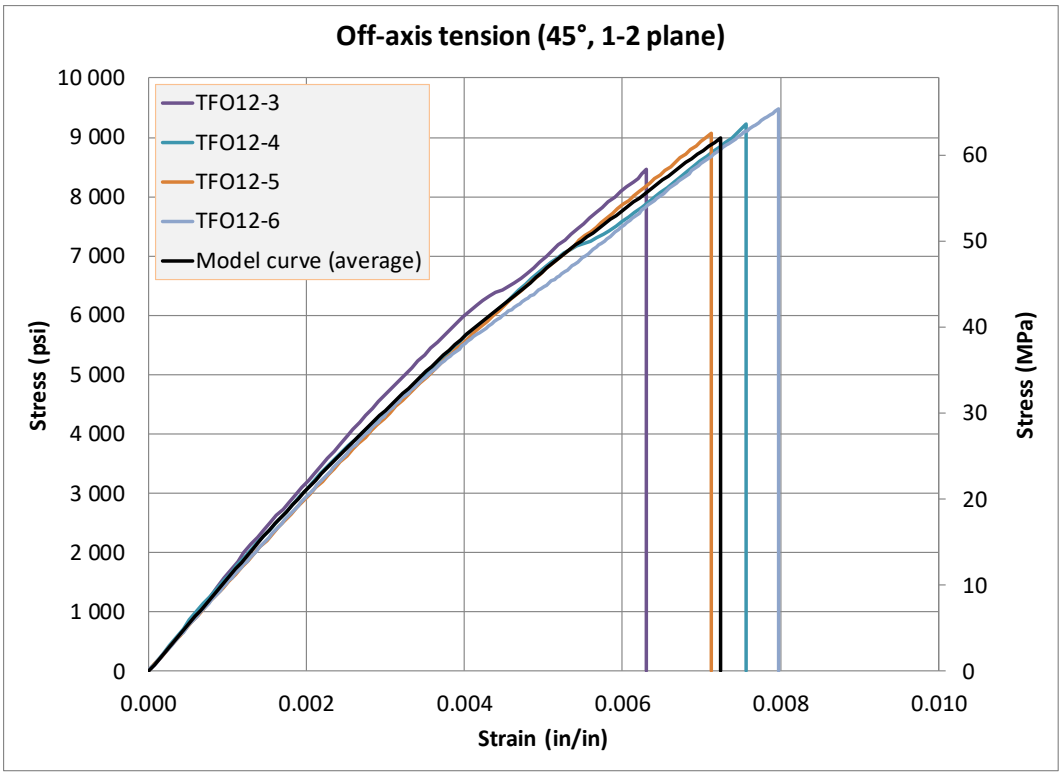
Off-axis tension (45°, 1-2 plane)
TFO12-3
TFO12-4
TFO12-5
TFO12-6
Model curve (average)
Stress (psi)
Stress (MPa)
Strain (in/in)
10 000
9 000
8 000
7 000
6 000
5 000
4 000
3 000
2 000
1 000
0
60
50
40
30
20
10
0
0.000
0.002
0.004
0.006
0.008
0.010

(a)

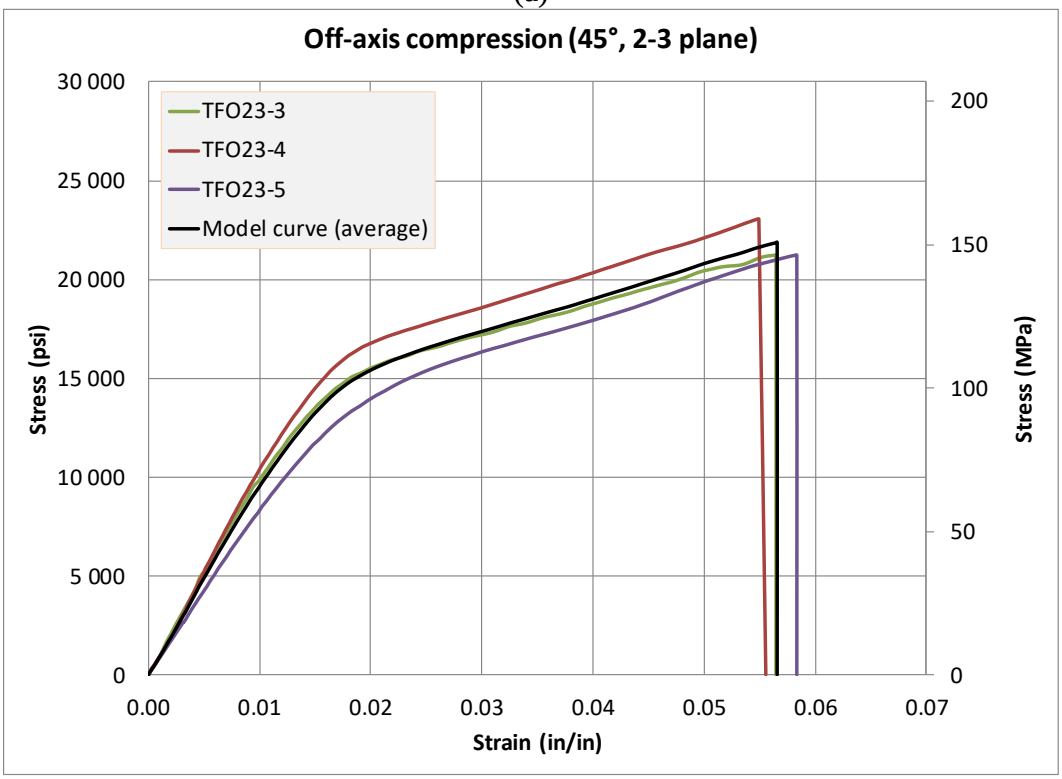
Off-axis compression (45°, 2-3 plane)
TFO23-3
TFO23-4
TFO23-5
Model curve (average)
Stress (psi)
Stress (MPa)
Strain (in/in)
30 000
25 000
20 000
15 000
10 000
5 000
0
200
150
100
50
0
0.00
0.01
0.02
0.03
0.04
0.05
0.06
0.07

(b)

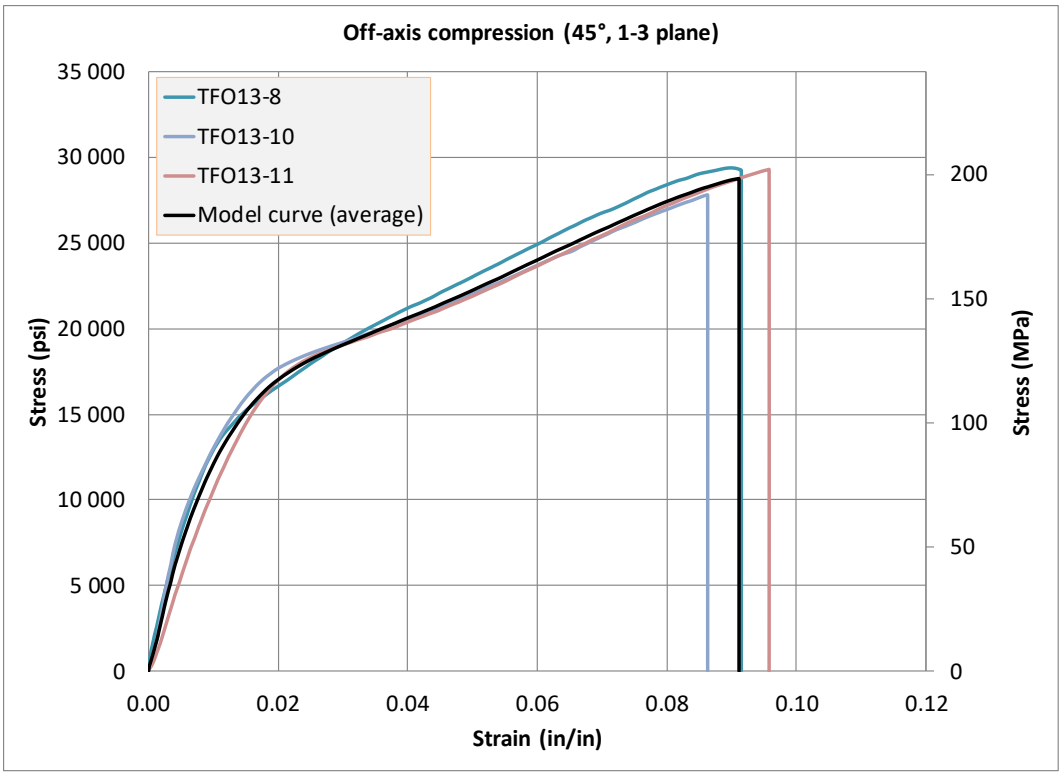

(c)

Fig. 42. 45° Off-axis Stress-Strain Curves (a) 1-2 Plane Tension, (b) 2-3 Plane Compression, and (c) 1-3 Plane Compression

Table 9. Summary of Results for the 45° Off-Axis Tests (Average Values [Coefficient of Variation, %])

	1-2 Plane (Tension)	**2-3 Plane (Compression)**	**1-3 Plane (Compression)**
Modulus, GPa psi	10.4 1 515 042 [3.2%]	6.5 947 991 [10.4%]	8.5 1 237 767 [12.1%]
Failure/Ultimate Strain	0.00724 [9.8%]	0.05661 [3.0%]	0.09120 [4.3%]
Peak Stress, MPa psi	62.4 9 054 [4.8%]	157.4 22 829 [4.9%]	198.4 28 775 [2.4%]

It should be noted that the 1-2 plane 45° off-axis tension test has contributions from the 1-2 plane shear, 1-direction tension, and 2-direction tension responses. The 2-3 and 1-3 plane 45° off-axis compression test also have contributions from their respective material axes. The failure of the specimens was also due to the combined loading state as none of the components of strain were negligible. Typical failed specimens are shown in Fig. 43.

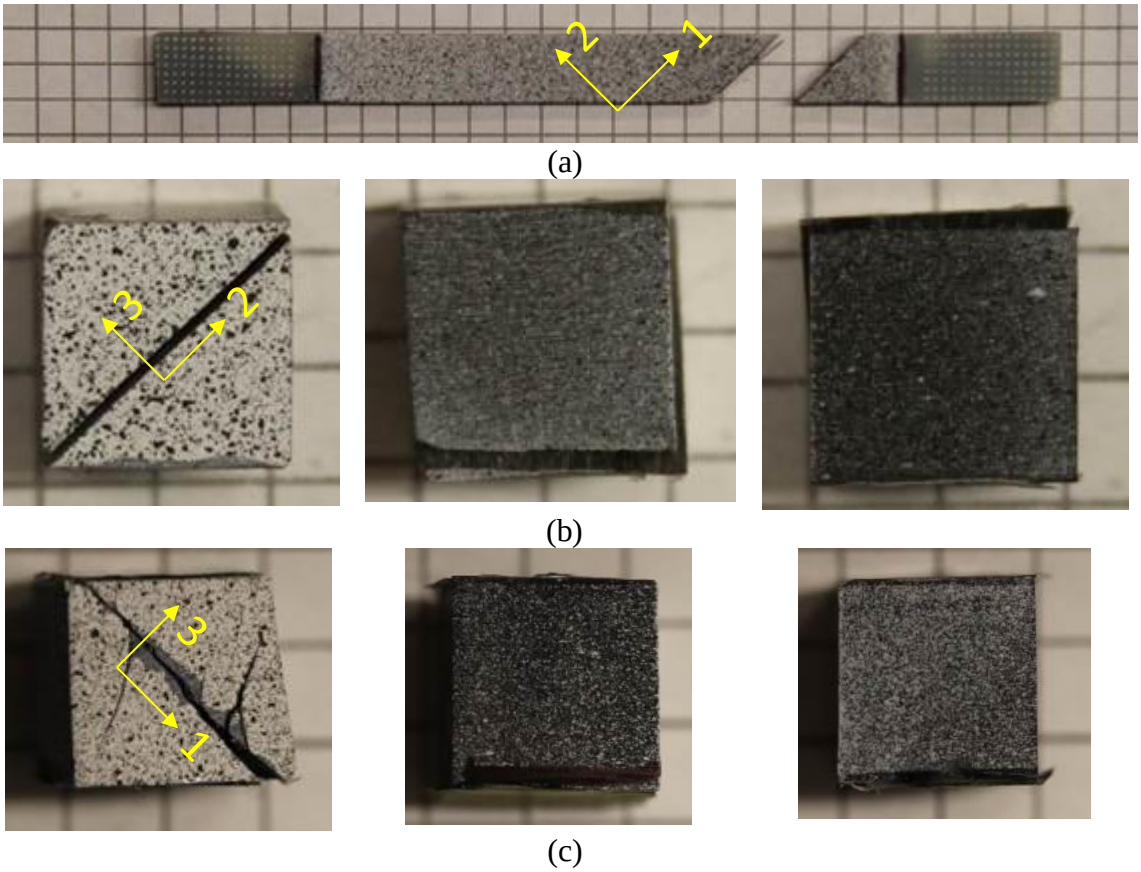

Fig. 43. Typical Failure of the (a) 1-2 Plane 45° Off-axis Tension Specimen (b) 2-3 Plane 45° Off-axis Compression Specimen (c) 1-3 Plane 45° Off-axis Compression Specimen

None of the off-axis tests resulted in failure along the loading direction. Rather each of the respective tests exhibited failure in the weakest direction being loaded. In the case of the

1-2 plane 45° off-axis tension test, the failure was consistently interfiber within the plane (Fig. 43a). For both the 2-3 and 1-3 plane 45° off-axis compression tests, the failure was consistently interlaminar (Fig. 43b,c).

2.3.5 Additional 1-2 Plane Off-Axis Tension Tests

The model curves of the additional off-axis tension tests are presented in Fig. 44. Table 10 provides a summary of the test results.

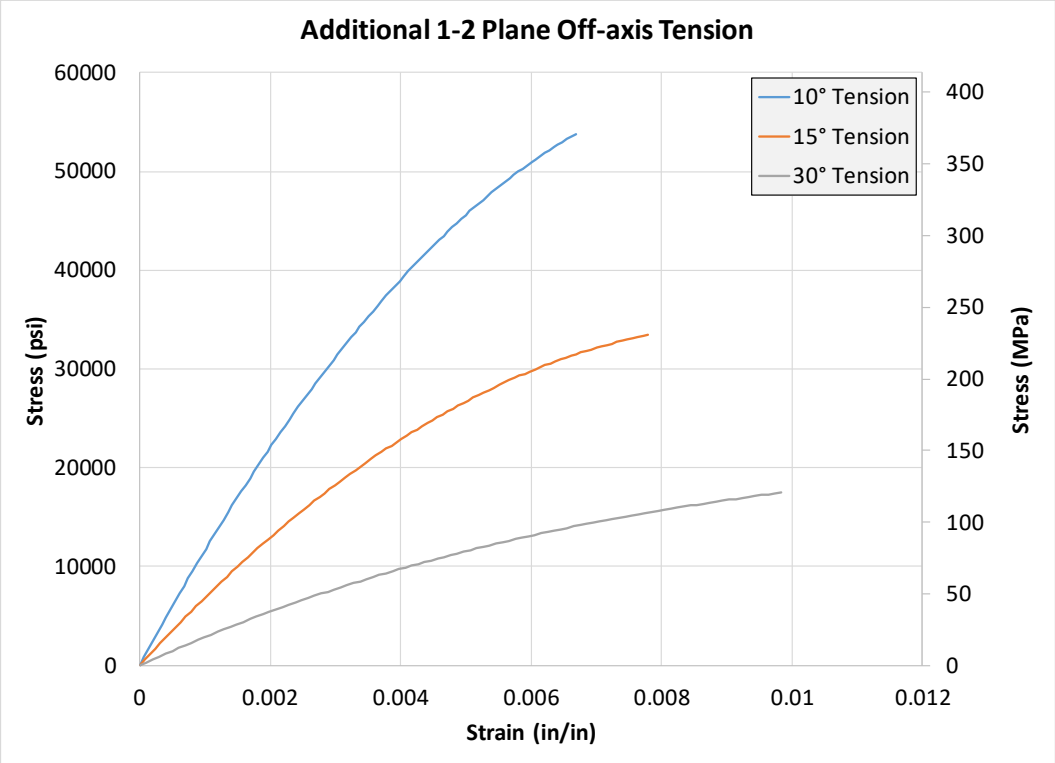

Fig. 44. 1-2 Plane 10°, 15°, and 30° Off-axis Tension Stress-Strain Curves

Table 10. Summary of Results for the Additional 1-2 Plane Off-Axis Tension Tests

(Average Values [Coefficient of Variation, %])

	10° Tension	**15° Tension**	**30° Tension**
Modulus, GPa psi	80.4 11 422 075 [1.79%]	47.1 6 959 172 [2.63%]	19.6 2 831 961 [3.55%]
Failure/Ultimate Strain	0.00668 [1.85%]	0.00779 [3.41%]	0.00983 [4.16%]
Peak Stress, MPa psi	370.8 53 495 [0.75%]	230.6 33 626 [0.25%]	120.5 17 471 [5.45%]

Similarly to the other off-axis tests (Fig. 43), the additional 1-2 plane off-axis tension tests failed along constituent boundaries. All three tests exhibited interfiber failure within the plane. Fig. 45 shows the typical failure modes of each specimen.

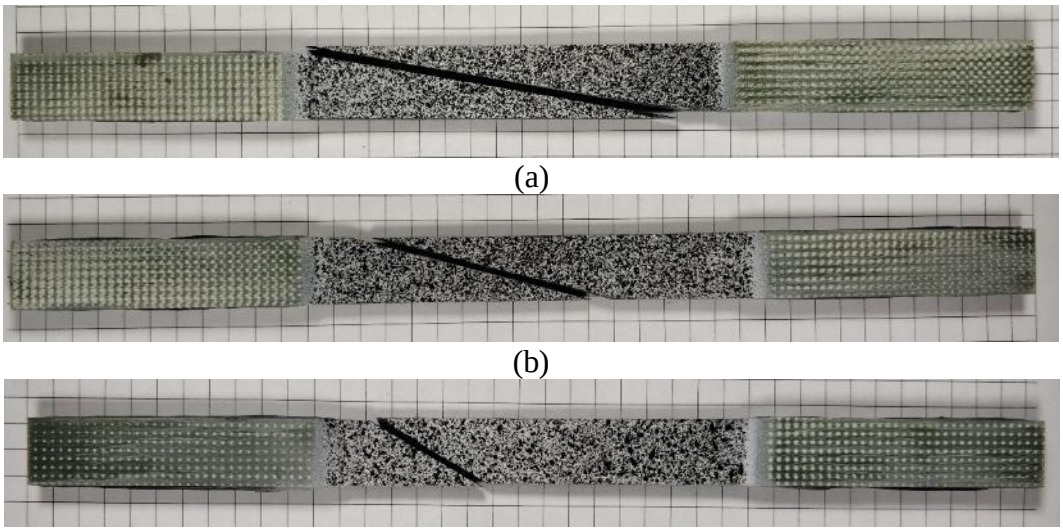

(a)

(b)

(c)

Fig. 45. Typical Failure of the 1-2 Plane Off-axis Tension Specimens (a) 10°, (b) 15°, and (c) 30°

2.3.6 Additional Observations

The experimental results show that many of the traditional (simplifying) assumptions made about UD composite behavior are not always satisfied, e.g. transverse isotropy and symmetric behavior of the material in tension and compression. A comparison of the 2-direction and 3-direction behavior in tension, compression and shear is shown in Fig. 46.

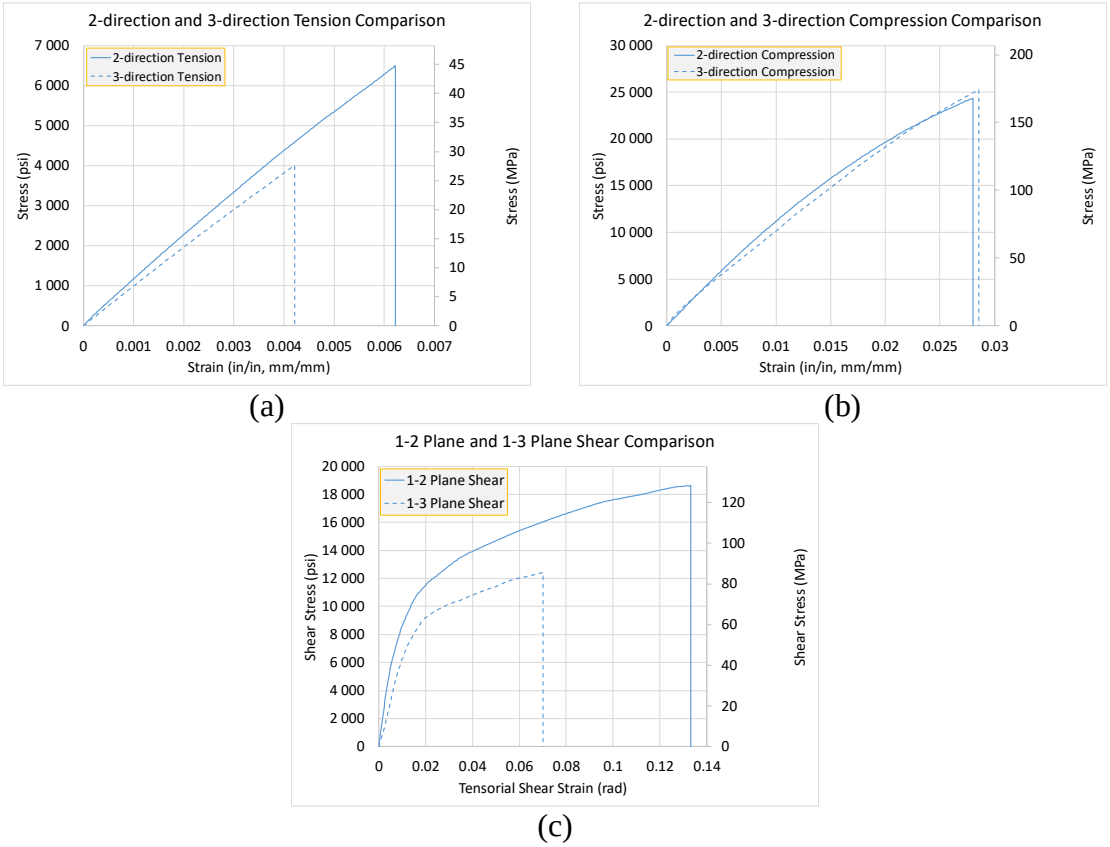

Fig. 46. Comparison of the Behavior of the 2-direction and 3-direction (a) Tension Behavior, (b) Compression Behavior, and (c) Shear Behavior

The 3-direction consistently exhibited lower ultimate strain values as well as lower stiffness than the 2-direction. The discrepancies in the 2-direction and 3-direction results can be explained by both the boundary between the plies and the extra epoxy resin shown

in Fig. 2. When looking at the laminate level, the extra resin and ply boundaries in the 3-direction yield more compliant behavior and the ply boundaries also reduce the apparent strength of the composite in the 3-direction. When looking at the lamina level, the 2-direction and 3-direction are visually identical. Typically, transverse isotropy assumptions are used because the weaknesses caused by the lamination process are ignored. However, this may not always be the proper way to handle the through-thickness properties in the context of finite element models. Determining whether or not to use through-thickness properties, determined from experiments, depends on how the model is built. For instance, if fewer elements are used to model the 3-direction than there are plies in the laminate, and no cohesive zone elements or tiebreak nodes are used to model the interlaminar interface behavior, then through-thickness properties may be required for accurate results. However, if cohesive zone elements or tiebreak nodes are used to model the ply boundaries, inclusion of through-thickness properties in the model may be overly conservative since the response of laminate testing in the 3-direction inherently includes the effects of the lamina boundaries and 2-direction would be preferable. The 1-2 plane off-axis tension and the 1-3 plane off-axis compression cannot be properly compared because the loading direction for the tests were different and there was clear asymmetric behavior between tension and compression. The asymmetric behavior is seen in the plastic behavior of the material. Typically, when the material was loaded in compression, the plasticity of the matrix dominated the overall composite behavior. The failure mechanisms in tension and compression are different for each respective material direction meaning a different combined state of stress and strain are required to induce failure. The tension/compression asymmetry exhibited by the data is handled by MAT 213 as both curves for each respective

PMD is required as input. However, the plastic potential function used in the flow rule implemented in MAT 213 is quadratic and inherently cannot differentiate between tensile and compressive stresses. The inability to differentiate between tension and compression in the plastic potential function becomes problematic when only either tension or compression in a given PMD exhibits significant nonlinearity, as the evolution of the yield surface is directly dependent on the flow rule. A comparison of the tension and compression behavior, for each principal material direction, is presented in Fig. 47.

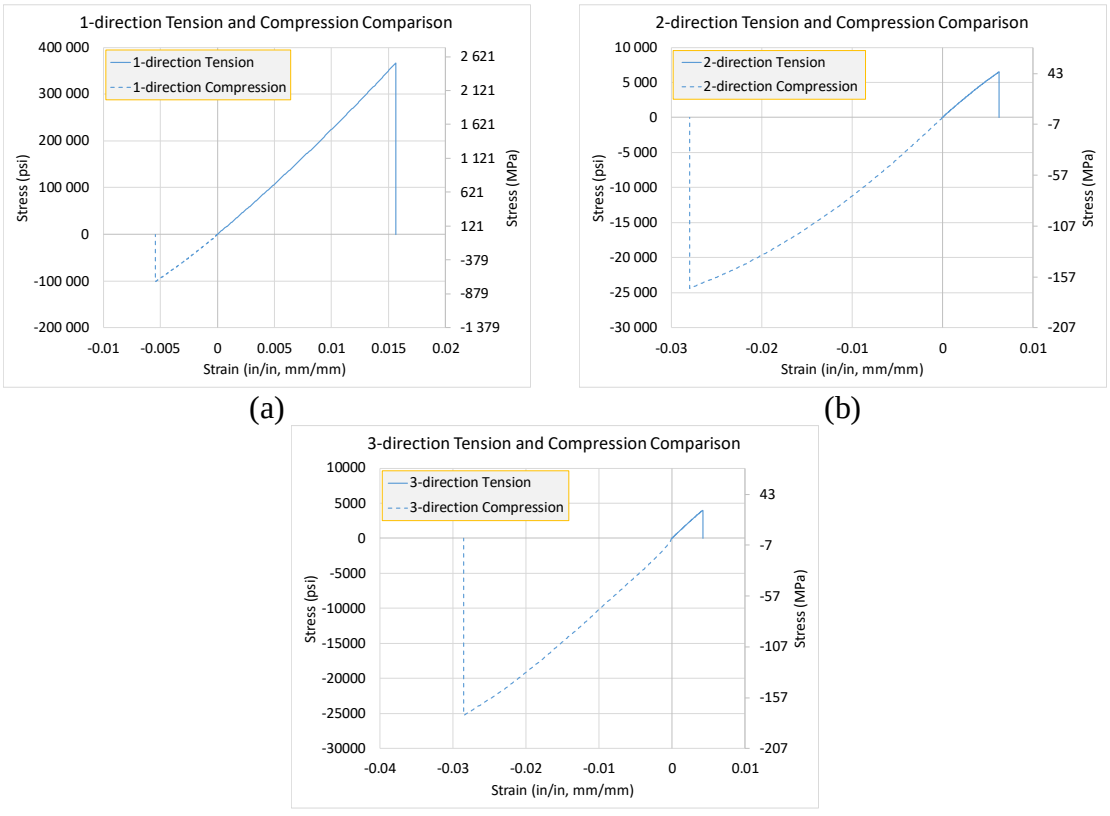

Fig. 47. Comparison of Tension and Compression Behavior (a) 1-direction, (b) 2-direction, and (c) 3-direction

2.3.7 Specific Gravity Testing

The mass density of the material is found in accordance with ASTM D792-13 (D20 Committee 2013a). First, the mass of the specimens in air is found using a scale. Second, a beaker is filled with water and the specimens are immersed in the liquid using a wire to suspend the specimen in the liquid and to prevent the specimen from contacting the beaker. The apparent mass of the specimen and the submerged portion of the wire in water are recorded. Third, the wire is submerged up to the same point as in the second step and its apparent mass in water is recorded. Using all three measurements, the specific gravity of the material is determined using Eq. 2.55. The samples used in the experiment were taken from the edge of the panels. The process was calibrated and verified by first using aluminum. The specific gravity obtained using aluminum is 2.61, which is within the reported range.

$$S_g = \frac{a}{a + w - b} \tag{2.55}$$

where S_g is the specific gravity, a is the apparent mass of specimen in air, b is the apparent mass of completely immersed specimen and partially immersed wire in liquid, and w is the apparent mass of partially immersed wire in liquid. Mass measurements are made using an AWS AL201S Analytical Balance[7] which has a resolution of 0.1 mg. The stand and beaker shown in Fig. 48 are part of a specific gravity kit obtained from Mineralab[8].

[7] http://www.awscales.com/analytical-balances/166-al-201s-analytical-balance
[8] http://www.mineralab.com/SGK-B/

(a) (b) (c)

Fig. 48. Specific Gravity Test Showing (a) Overall Test Setup, (b) Specimen and Wire Submerged in Water, and (c) Wire Submerged in Water

The results of the tests using multiple samples from the three different panel types (16-ply, 24-ply, and 96-ply) are reported in Table 11. In Table 11, ‘CV’ refers to the coefficient of variation.

Table 11. Specific Gravity Test Results

Sample	Mass: Specimen in Air (g)	Mass: Wire + Specimen Submerged (g)	Mass: Wire Submerged (g)	Specific Gravity
16-Ply_1	1.3496	0.8113	0.3258	1.5615
	1.3502	0.8115	0.3273	
	1.3498	0.8110	0.3245	
	Average: 1.3499	Average: 0.8113	Average: 0.3259	
	Std Dev: 0.00031	Std Dev: 0.00025	Std Dev: 0.00140	
	CV (%): 0.023	CV (%): 0.031	CV (%): 0.430	
16-Ply_2	0.6993	0.5786	0.3258	1.5661
	0.6990	0.5773	0.3246	
	0.6996	0.5784	0.3256	
	Average: 0.6993	Average: 0.5781	Average: 0.3253	
	Std Dev: 0.00030	Std Dev: 0.00070	Std Dev: 0.00064	
	CV (%): 0.043	CV (%): 0.121	CV (%): 0.198	
16-Ply_3	0.6867	0.5690	0.3257	1.5514
	0.6865	0.5707	0.3266	
	0.6854	0.5685	0.3242	
	Average: 0.6862	Average: 0.5694	Average: 0.3255	
	Std Dev: 0.00070	Std Dev: 0.00115	Std Dev: 0.00121	
	CV (%): 0.102	CV (%): 0.203	CV (%): 0.372	
24-Ply_1	0.5534	0.5783	0.3845	1.5513
	0.5548	0.5845	0.3841	
	0.5536	0.5804	0.384	
	Average: 0.5539	Average: 0.5811	Average: 0.3842	
	Std Dev: 0.00076	Std Dev: 0.00315	Std Dev: 0.00026	
	CV (%): 0.137	CV (%): 0.543	CV (%): 0.069	
24-Ply_2	0.567	0.5864	0.3846	1.5488
	0.5684	0.5839	0.3841	
	0.5678	0.5851	0.3832	
	Average: 0.5677	Average: 0.5851	Average: 0.3840	
	Std Dev: 0.00070	Std Dev: 0.00125	Std Dev: 0.00071	
	CV (%): 0.124	CV (%): 0.214	CV (%): 0.185	
96-Ply_1	11.4349	5.1205	1.0709	1.5514
	11.4348	5.1365	1.0614	
	11.4355	5.1405	1.0722	
	Average: 11.4351	Average: 5.1325	Average: 1.0682	
	Std Dev: 0.00038	Std Dev: 0.01058	Std Dev: 0.00590	
	CV (%): 0.003	CV (%): 0.206	CV (%): 0.552	

96-Ply_2	11.3898	5.1416	1.0659	1.5559
	11.3892	5.1441	1.0671	
	11.3902	5.1221	1.0673	
	Average: 11.3897	Average: 5.1359	Average: 1.0668	
	Std Dev: 0.00050	Std Dev: 0.01205	Std Dev: 0.00076	
	CV (%): 0.004	CV (%): 0.235	CV (%): 0.071	

The results in Table 11 are compiled in Table 12 with the average value in Table 12 being used as input to the material model.

Table 12. Specific Gravity Summary and Statistics

Sample	**Specific Gravity**
16-Ply_1	1.5615
16-Ply_2	1.5661
16-Ply_3	1.5514
24-Ply_1	1.5513
24-Ply_2	1.5488
96-Ply_1	1.5514
96-Ply_2	1.5559
Average	1.5552
Standard Deviation	0.0059
Coefficient of Variation (%)	0.38

2.3.8 Computation of Flow Rule Coefficients

As discussed in Section 2.1, when relating flow rule coefficients to the plastic Poisson's ratios (Eq. 2.30), the resulting system of equations is rank deficient. To overcome this problem, typically, one of the coefficients is set to a value of one, typically one of the values corresponding to the response in PMD (i.e. H_{11}, H_{22}, or H_{33}). For unidirectional composites, the value of H_{22} is often assumed as one (see Section 2.1). This leads to the 2-direction tension or compression stress-plastic strain response being the representative

effective stress-effective plastic strain response of the material. However, the choice of the master curve may not be obvious for some composite materials. This section provides details of how the coefficient values can be determined without first assuming a value of one of the coefficients. The reasoning used to reduce the plastic potential function (Eq. 2.13) for a unidirectional composite are provided by Eq. 2.31 through Eq. 2.33. The T800S/F3900 composite exhibited behavior which is consistent with the aforementioned assumptions (i.e. linear elastic in the fiber direction, isotropy in the 2-3 plane) thus the reduced form of the plastic potential function is written as

$$h^2 = H_{22}\left(\sigma_{22}^2 + \sigma_{33}^2\right) + 2H_{23}\sigma_{22}\sigma_{33} + H_{44}\left(\sigma_{12}^2 + \sigma_{13}^2\right) + H_{55}\sigma_{23}^2 \qquad 2.56$$

Under plane stress in the 1-2 plane, the plastic potential function is further reduced to

$$h^2 = H_{22}\sigma_{22}^2 + H_{44}\sigma_{12}^2 \qquad 2.57$$

Under arbitrary loading in the 1-2 plane (Fig. 4 and Eq. 2.5), the plastic potential function (effective stress) is written as follows

$$h = \sigma_x g(\theta) \qquad 2.58$$

The plastic multiplier increment (Eq. 2.19, effective plastic strain increment) is given by

$$d\lambda = \frac{d\varepsilon_{xx}^{p}}{g(\theta)} \tag{2.59}$$

where the value of $g(\theta)$ is dependent on the flow rule coefficient values and the rotation of the PMD with respect to the loading axis

$$g(\theta) = \left[H_{22} \sin^4(\theta) + H_{44} \sin^2(\theta) \cos^2(\theta) \right]^{\frac{1}{2}} \tag{2.60}$$

The plastic strain in the loading direction is computed as

$$\varepsilon_{xx}^{p} = \varepsilon_{xx}^{t} - \frac{\sigma_{xx}}{E_{xx}} \tag{2.61}$$

The results of tension or compression tests in the 1-2 plane can be used to determine the values of H_{22} and H_{44}. In this alternate procedure, the results of θ = 10°, 15°, 30°, 45°, and 90° tension tests are utilized. These curves are referred to as *fitting curves*. The average stress-total strain response from each of the curves is compiled in Fig. 49.

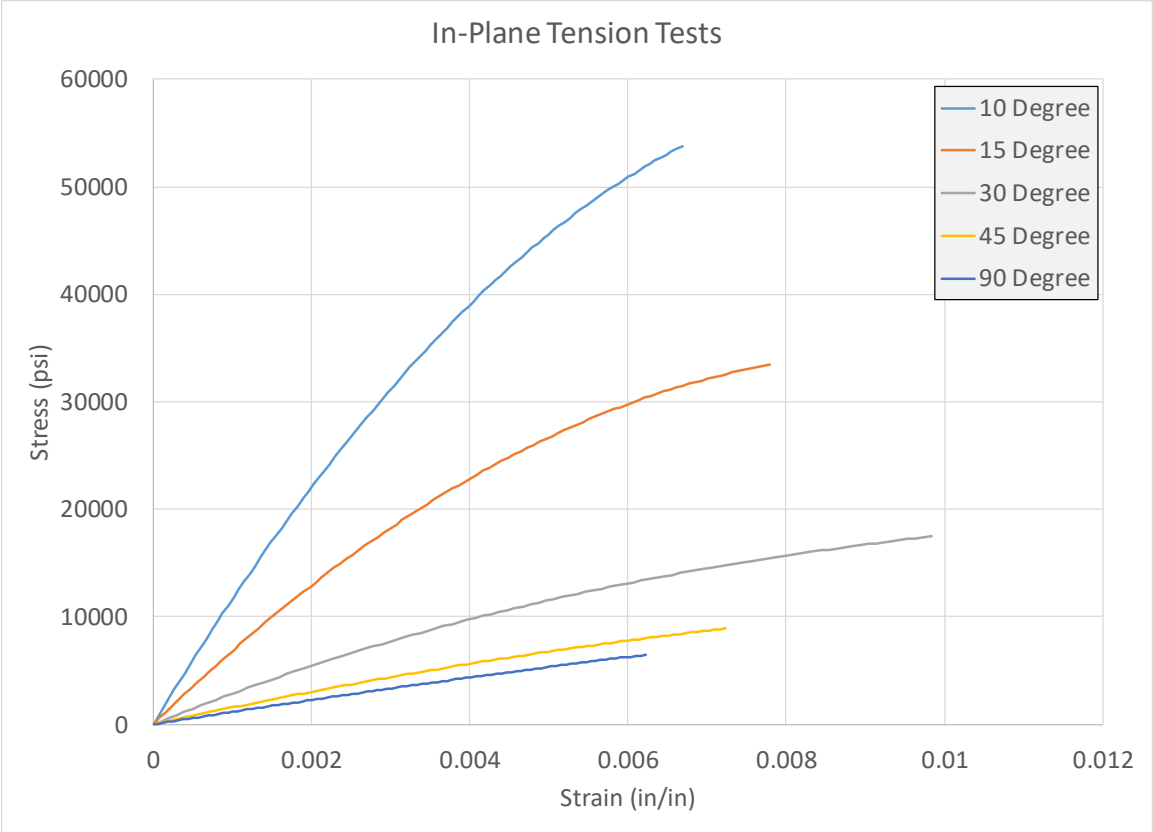

Fig. 49. Compilation of 1-2 Plane Tension Stress-total Strain Curves at Off-axis Angles of θ = 10°, 15°, 30°, 45°, and 90°

The first step in deriving the values of H_{22} and H_{44}, is converting each of the fitting curves from stress-total strain into stress-plastic strain using Eq. 2.61. The resulting curves are shown in Fig. 50.

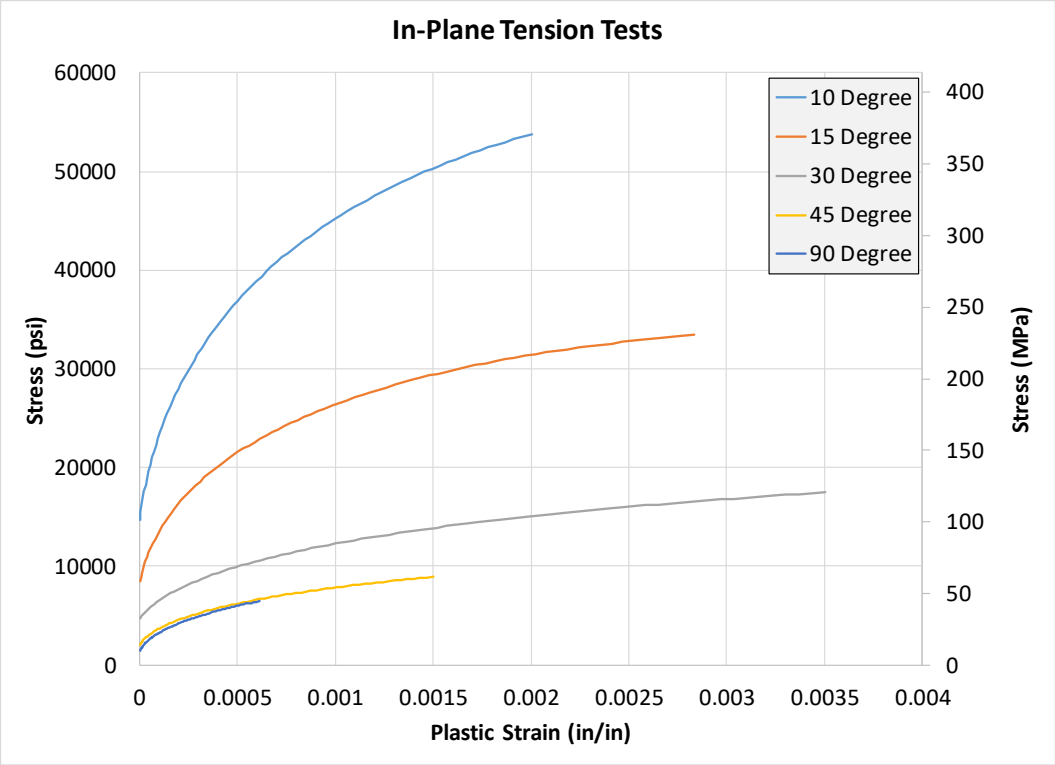

Fig. 50. 1-2 Plane Tension Stress-plastic Strain Curves at Off-axis Angles of θ = 10°, 15°, 30°, 45°, and 90°

With the assumption that the effective stress (h)-effective plastic strain (λ) curve is analogous to a composite property, the optimal values of H_{22} and H_{44} will result in the fitting curves collapsing onto a single unique curve in the effective stress-effective plastic strain space. Since there are currently only two degrees of freedom in the equation, H_{22} and H_{44}, an optimization technique can be used to find the optimal values with the only constraint being $H_{ii} \geq 0$ (Eq. 2.15). Using the current combination of H_{22} and H_{44}, each of the fitting curves is converted into h-λ space using Eq. 2.58 and Eq. 2.59 respectively. From the resulting fitting curves, the average response is computed, $\bar{h}$-λ, for the current

values of H_{22} and H_{44}. At each value of effective plastic strain, λ_j, the average effective stress, $\bar{h}_j$, is computed as

$$\bar{h}_j = \frac{1}{N}\sum_{i=1}^{N} h_i\left(\lambda_j\right) \tag{2.62}$$

where N is the number of fitting curves. To determine how far away the current combination of H_{22} and H_{44} are from optimal, the normalized root mean square error (NRMSE) is computed between the fitting curves and the average response as

$$NRMSE = \frac{\sqrt{\frac{1}{N}\sum_{j=1}^{M}\sum_{i=1}^{N}\left[h_i\left(\lambda_j\right) - \bar{h}\left(\lambda_j\right)\right]^2}}{\bar{h}_{\max} - \bar{h}_{\min}} \tag{2.63}$$

where M is the number of points along the curves where the computation is performed. The range of effective stress in the average curve is used as the normalizing parameter to provide a consistent frame of reference since the magnitude of the effective stress varies greatly depending on the values of H_{22} and H_{44}. The combination of H_{22} and H_{44} which minimizes the NRMSE is considered the optimal solution. Fig. 51 shows a comparison of the fitting curves in h-λ space for a non-optimal combination and an optimal combination.

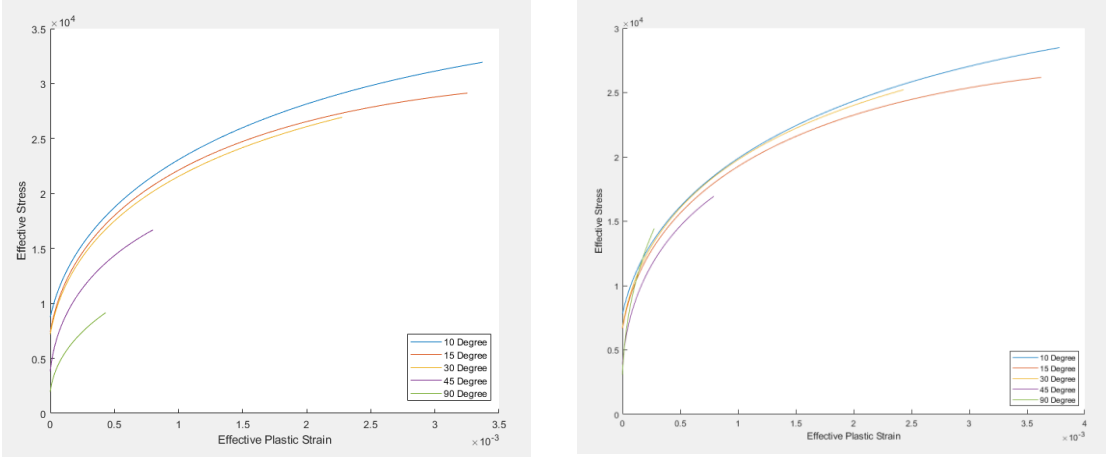

(a) (b)

Fig. 51. Fitting Curves in h-λ Space (a) Non-optimal $H_{22}=2$, $H_{44}=12$ and (b) Optimal $H_{22}=4.97$, $H_{44}=9.44$

The optimal combination of H_{22} and H_{44} in Fig. 51b may not be unique since the NRMSE function is not convex. Fig. 52 shows the NRMSE surface as a function of H_{22} and H_{44} with the computed optimal value denoted by a red circle.

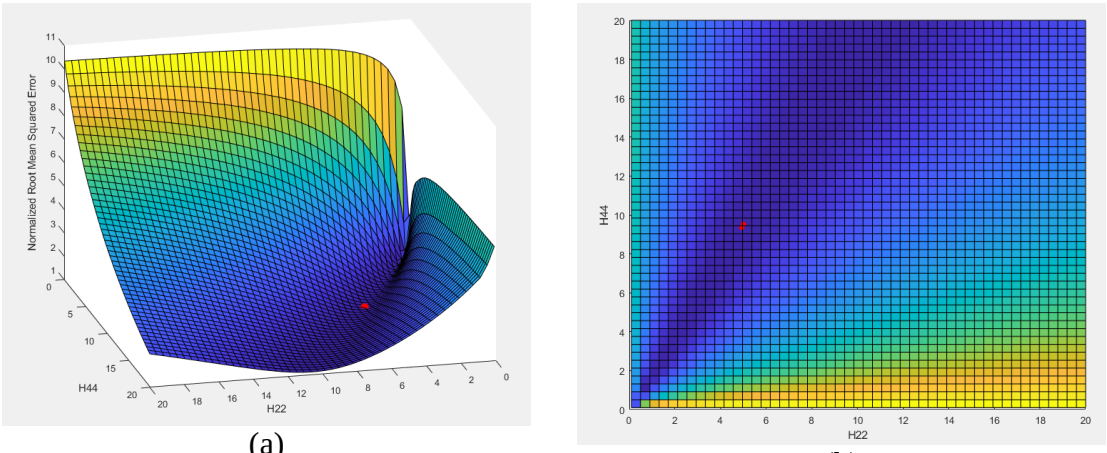

(a) (b)

Fig. 52. NRMSE Surface (a) Three-dimensional View and (b) Plan-view

The dark blue region in Fig. 52 is a *valley* where the values of NRMSE are approximately equal to the value reported in Fig. 51. In fact, all combinations of H_{22} and H_{44} within this region have a nearly constant ratio illustrated by the linear relationship in Fig. 53.

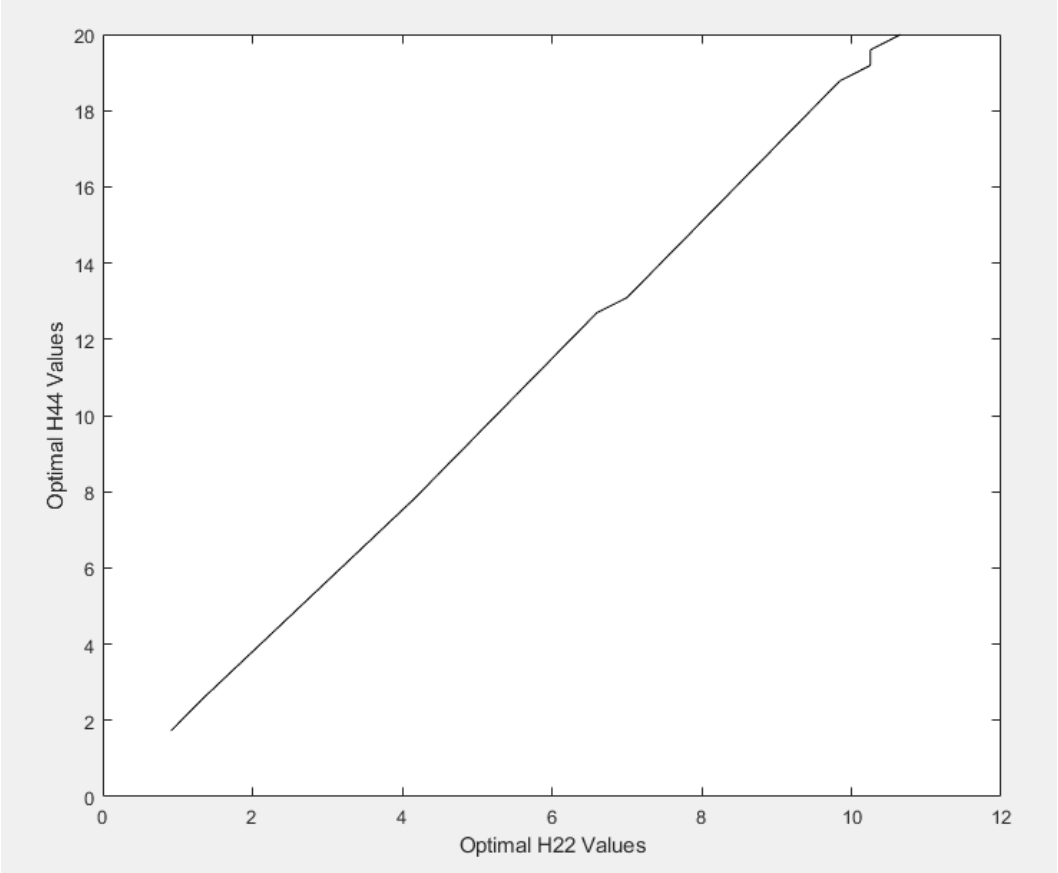

Fig. 53. Linear Relationship Between H_{22} and H_{44} in Minimum NRMSE Region

The relationship between H_{22} and H_{44} is approximately $\frac{H_{44}}{H_{22}} \cong 1.90$. This result is consistent with the assumption that other researchers have made by taking $H_{22} = 1$, effectively making the 2-direction tension or compression stress-plastic strain curve the master h-λ curve of the material indicating the proposed methodology offers a fairly

generalized method of initially computing a subset of the unknown flow rule coefficients. After computing H_{22} and H_{44}, H_{23} is computed using Eq. 2.30.

$$H_{23} = -\nu_{23}^{p} H_{22} = -\nu_{32}^{p} H_{33} = -\nu_{32}^{p} H_{22} \qquad 2.64$$

The value of ν_{32}^{p}, computed from 3-direction compression tests, is given in

Table 7 as -0.776 . The remaining unknown from Eq. 2.56 is H_{55} which can be computed using the same optimization procedure outlined in this section using the 2-direction tension curve as the master curve and the result from the 2-3 plane 45° off-axis compression test (Fig. 42b) as the fitting curve. The value of $g(\theta)$, given by Eq. 2.60, changes to

$$g(\theta)=\left[H_{22}\left(\cos^4(\theta)+\sin^4(\theta)\right)+\left(2H_{23}+H_{55}\right)\cos^2(\theta)\sin^2(\theta)\right]^{\frac{1}{2}} \qquad 2.65$$

The optimal flow rule coefficient values are presented in

Table 13.

Table 13. Optimal Flow Rule Coefficient Values for the T800S/F3900 Composite

Coefficient	**Optimal Value**
H_{11}	0.00
H_{22}	1.00
H_{33}	1.00
H_{44}	1.90
H_{55}	0.82
H_{66}	1.90
H_{12}	0.00
H_{23}	-0.776
H_{13}	0.00

The flow rule coefficients shown in

Table 13 are used in all finite element simulations presented in this dissertation.

The methodology discussed can be used to solve for the flow rule coefficients of any composite architecture. The only assumption made was related to the observed linear elastic behavior of the material in the 1-direction, $H_{11} = H_{12} = H_{13} = 0$. This assumption was necessary to preserve the physical admissibility of the resulting coefficients. For other composite architectures, there may be more degrees of freedom during the optimization, however, the process remains identical. Additionally, the choice of utilizing in-plane off-axis tension curves for the initial fitting process is for convenience only. Strictly speaking, the 2-3 plane 45° off-axis compression data could have been used alongside the in-plane curves during the optimization process to solve for H_{55} instead of in a serialized fashion. The proposed technique shows promise but may need to be refined further to streamline the process of deriving the flow rule coefficients.

3 DAMAGE SUB-MODEL

Within OEPDMM, the damage sub-model handles the degradation of elastic stiffness prior to the onset of failure. The behavior is captured through the introduction of a stress space titled the *effective stress space*. This stress space estimates the stress that would be carried by the material had it not been subjected to damage and is not to be confused with the effective stress, *h*, introduced in the previous chapter. The behavior is captured through a set of uncoupled and coupled damage experiments accounting for damage from all possible sources of loading. In this chapter the theoretical and implementation details of the damage sub-model, the experimental techniques used to derive the required input, and the results

of a case study using the T800S/F3900 carbon fiber/epoxy resin unidirectional composite system manufactured by Toray are presented.

3.1 Theoretical Details

In continuum damage mechanics (CDM) formulations utilized to model damage growth in materials such as concrete, isotropic damage formulations are often used (Kurumatani et al. 2016; Lemaitre 1985). Isotropic formulations attribute damage growth (elastic stiffness reduction) in a material to a single internal damage parameter, *d*. The general form of the constitutive relationship is written as

$$\boldsymbol{\sigma} = (1-d)\mathbf{C} : \left(\boldsymbol{\varepsilon}^{t} - \boldsymbol{\varepsilon}^{p}\right) \qquad 0 \le d \le 1 \tag{3.1}$$

Eq. 3.1 shows that all components in the stiffness tensor, **C**, are reduced by the same amount. These types of formulations have been shown to overestimate the growth of damage in fiber reinforced composites leading to a conservative prediction of the load carrying capacity of the material. Anisotropic damage growth models have been proposed to better represent the growth of damage in composites. Matzenmiller, Lubliner, and Taylor (1995) proposed a widely used model (MLT model) wherein anisotropic damage is utilized, e.g. LS-DYNA's MAT162 uses a form of the MLT model in its CDM methodology (Yen 2012). The proposed form of the compliance tensor for a plane stress case is shown below

$$\mathbf{H}(\boldsymbol{\omega}) = \begin{bmatrix} \dfrac{1}{\left(1-\omega_{11_{T,C}}\right)E_{11}} & -\dfrac{\nu_{21}}{E_{11}} & 0 \\ -\dfrac{\nu_{12}}{E_{22}} & \dfrac{1}{\left(1-\omega_{22_{T,C}}\right)E_{22}} & 0 \\ 0 & 0 & \dfrac{1}{(1-\omega_{12})G} \end{bmatrix} \qquad 0 \le \omega_{ij} \le 1 \qquad 3.2$$

where the variables ω_{ij} represent independent damage variables. The subscripts *T* and *C* indicate tension and compression respectively. The choice of whether a tension or compression damage variable is used in the computations depends on the sign of stress during the analysis. The MLT model offers attractive features such as handling damage growth due to tension and compression separately and reducing elastic stiffness components individually. One main disadvantage is that the growth of ω_{ij} depends only on σ_{ij}. For example, stresses induced in the 2-direction will not influence the growth of ω_{11}. This type of damage is referred to as uncoupled damage. The MLT model does allow for a quasi-coupling effect as the values of ω_{22} and ω_{12} increase proportionally to each other since these are both considered as representing matrix damage modes. However, this formulation is still restrictive as explained next.

A damage sub-model is necessary since the nonlinear behavior exhibited by fiber reinforced composite materials is likely due to a combination of both plastic flow, handled by the deformation sub-model, and microscopic damage, reflected in varying unloading moduli. The damage sub-model of OEPDMM utilizes experimentally derived damage

parameter-total strain curves to dictate the manner in which damage grows in the material. The underlying idea is to be consistent with the deformation sub-model and no assumptions are made regarding the architecture or behavior of the material. The damage model is based on the effective stress concept proposed by Kachanov (1958). The effective stress is related to the true stress through a fourth order damage tensor, **M**.

$$\boldsymbol{\sigma} = \mathbf{M} : \boldsymbol{\sigma}^{eff} \tag{3.3}$$

where $\boldsymbol{\sigma}$ is the Cauchy stress in the true space and $\boldsymbol{\sigma}^{eff}$ represents stresses in the effective stress space. The true stress space refers to the stress that would be measured directly from an experiment whereas the effective stress space is in reference to the equivalent undamaged material. In general **M** is full tensor, shown in Voigt notation below.

$$\begin{pmatrix} \sigma_{11} \\ \sigma_{22} \\ \sigma_{33} \\ \sigma_{12} \\ \sigma_{23} \\ \sigma_{13} \end{pmatrix} = \begin{bmatrix} M_{11} & M_{12} & M_{13} & M_{14} & M_{15} & M_{16} \\ M_{21} & M_{22} & M_{23} & M_{24} & M_{25} & M_{26} \\ M_{31} & M_{32} & M_{33} & M_{34} & M_{35} & M_{36} \\ M_{41} & M_{42} & M_{43} & M_{44} & M_{45} & M_{46} \\ M_{51} & M_{52} & M_{53} & M_{54} & M_{55} & M_{56} \\ M_{61} & M_{62} & M_{63} & M_{64} & M_{65} & M_{66} \end{bmatrix} \begin{pmatrix} \sigma_{11}^{eff} \\ \sigma_{22}^{eff} \\ \sigma_{33}^{eff} \\ \sigma_{12}^{eff} \\ \sigma_{23}^{eff} \\ \sigma_{13}^{eff} \end{pmatrix} \tag{3.4}$$

where the stress subscripts refer to the PMDs. The full damage tensor in Eq. 3.4 poses a problem since a multiaxial stress state in the effective space may be predicted by a uniaxial stress state in the true space, which is non-physical. Therefore, a semi-coupled directionally dependent tensor is used in the current implementation as

$$\begin{pmatrix}\sigma_{11}\\ \sigma_{22}\\ \sigma_{33}\\ \sigma_{12}\\ \sigma_{23}\\ \sigma_{13}\end{pmatrix}=\begin{bmatrix}M_{11} & 0 & 0 & 0 & 0 & 0\\ 0 & M_{22} & 0 & 0 & 0 & 0\\ 0 & 0 & M_{33} & 0 & 0 & 0\\ 0 & 0 & 0 & M_{44} & 0 & 0\\ 0 & 0 & 0 & 0 & M_{55} & 0\\ 0 & 0 & 0 & 0 & 0 & M_{66}\end{bmatrix}\begin{pmatrix}\sigma_{11}^{eff}\\ \sigma_{22}^{eff}\\ \sigma_{33}^{eff}\\ \sigma_{12}^{eff}\\ \sigma_{23}^{eff}\\ \sigma_{13}^{eff}\end{pmatrix} \quad 3.5$$

The semi-coupled nature of **M** stems from each of the diagonal elements being a function of all effective stresses induced in the material, e.g. $M_{kk}=M_{kk}\left(d_{11}^{kk},d_{22}^{kk},d_{33}^{kk},d_{12}^{kk},d_{23}^{kk},d_{13}^{kk}\right)$ where the repeating index does not imply a summation and the damage parameters are defined as d_{ij}^{kl} indicating damage has been induced in direction *ij* and the reduction of stiffness has manifested in direction *kl*. For full generalization, both normal and shear damage are attributed to all normal and shear terms. The contribution of damage terms to the overall stiffness reduction is handled through a path independent multiplicative series derived through a superposition principle. For example, consider a volume of undamaged material (State 0, Fig. 54a) being loaded first in the 2-direction with all other stress components being zero. The damage, in the form of cracks and voids, induced in the 2-direction caused by a stress applied in the 2-direction is labeled d_{22}^{22} (State 1, Fig. 54b). The new apparent 2-direction elastic stiffness of the material is given by

$$E_{22}^{1}=\left(1-d_{22}^{22}\right)E_{22}^{0} \quad 3.6$$

where E_{22}^{0} is the elastic stiffness of the undamaged material and E_{22}^{1} is the apparent elastic stiffness after loading to State 1 has ceased. From State 1, the material is unloaded to a stress-free state, State 2 (Fig. 54c). Under the hypothesis that damage is an irreversible thermodynamic process (Lemaître and Desmorat 2005), the damage induced by loading from State 0 to State 1 remains present in the material. The apparent elastic stiffness in the 2-direction at the end of State 2 is given by

$$E_{22}^{2} = E_{22}^{1} = \left(1 - d_{22}^{22}\right) E_{22}^{0} \tag{3.7}$$

From State 2, a uniaxial stress in the 3-direction is now applied, State 3 (Fig. 54d). The damage induced by loading in the 3-direction is assumed to result in further reduction of the apparent 2-direction elastic stiffness. This damage is labeled, d_{33}^{22}, a coupled damage parameter. The apparent elastic stiffness in the 2-direction at the end of State 3 is given by

$$E_{22}^{3} = \left(1 - d_{33}^{22}\right) E_{22}^{2} = \left(1 - d_{33}^{22}\right) E_{22}^{1} = \left(1 - d_{33}^{22}\right)\left(1 - d_{22}^{22}\right) E_{22}^{0} \tag{3.8}$$

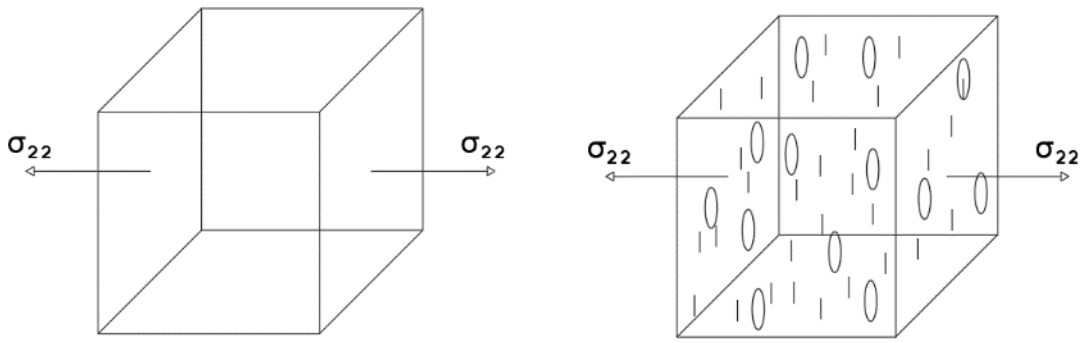

(a) (b)

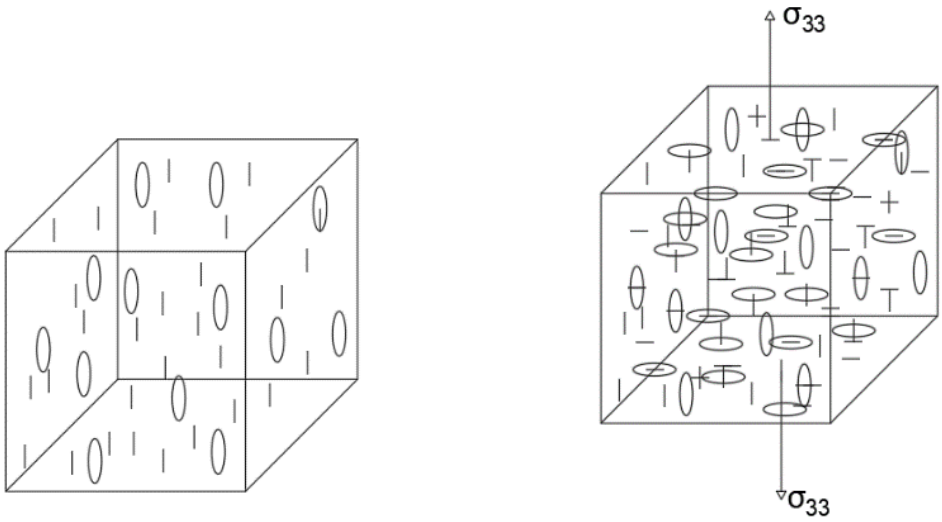

(c) (d)

Fig. 54. Assumed Damage Process (a) Undamaged Material (State 0), (b) Damaged Caused by 2-direction Stress (State 1), (c) Stress Free Material after Sustaining Damage (State 2), and (d) Additional Damage Caused by 3-direction Loading (State 3)

The same assumptions are used to obtain the contribution of all possible stresses on all apparent elastic stiffness values in the PMD and PMP. Additionally, no assumption is made regarding the symmetry of the material, meaning damage induced due to compression or tension loading in a given PMD are treated independently. The sign of the effective stress is the metric used to differentiate between tension and compression regimes. Eq. 3.5 is expanded and shown by Eq. 3.9.

$$
\begin{aligned}
\sigma_{11} &= \begin{cases} if\ \sigma_{11}^{eff} \geq 0 \rightarrow \left(1-d_{11_T}^{11_T}\right)\left(1-d_{11_C}^{11_T}\right)\left(1-d_{22_T}^{11_T}\right)\left(1-d_{22_C}^{11_T}\right)\left(1-d_{33_T}^{11_T}\right) \\ \quad \left(1-d_{33_C}^{11_T}\right)\left(1-d_{12}^{11_T}\right)\left(1-d_{23}^{11_T}\right)\left(1-d_{13}^{11_T}\right)\sigma_{11}^{eff} \\ if\ \sigma_{11}^{eff} < 0 \rightarrow \left(1-d_{11_T}^{11_C}\right)\left(1-d_{11_C}^{11_C}\right)\left(1-d_{22_T}^{11_C}\right)\left(1-d_{22_C}^{11_C}\right)\left(1-d_{33_T}^{11_C}\right) \\ \quad \left(1-d_{33_C}^{11_C}\right)\left(1-d_{12}^{11_C}\right)\left(1-d_{23}^{11_C}\right)\left(1-d_{13}^{11_C}\right)\sigma_{11}^{eff} \end{cases} \\
\sigma_{22} &= \begin{cases} if\ \sigma_{22}^{eff} \geq 0 \rightarrow \left(1-d_{11_T}^{22_T}\right)\left(1-d_{11_C}^{22_T}\right)\left(1-d_{22_T}^{22_T}\right)\left(1-d_{22_C}^{22_T}\right)\left(1-d_{33_T}^{22_T}\right) \\ \quad \left(1-d_{33_C}^{22_T}\right)\left(1-d_{12}^{22_T}\right)\left(1-d_{23}^{22_T}\right)\left(1-d_{13}^{22_T}\right)\sigma_{22}^{eff} \\ if\ \sigma_{22}^{eff} < 0 \rightarrow \left(1-d_{11_T}^{22_C}\right)\left(1-d_{11_C}^{22_C}\right)\left(1-d_{22_T}^{22_C}\right)\left(1-d_{22_C}^{22_C}\right)\left(1-d_{33_T}^{22_C}\right) \\ \quad \left(1-d_{33_C}^{22_C}\right)\left(1-d_{12}^{22_C}\right)\left(1-d_{23}^{22_C}\right)\left(1-d_{13}^{22_C}\right)\sigma_{22}^{eff} \end{cases} \\
\sigma_{33} &= \begin{cases} if\ \sigma_{33}^{eff} \geq 0 \rightarrow \left(1-d_{11_T}^{33_T}\right)\left(1-d_{11_C}^{33_T}\right)\left(1-d_{22_T}^{33_T}\right)\left(1-d_{22_C}^{33_T}\right)\left(1-d_{33_T}^{33_T}\right) \\ \quad \left(1-d_{33_C}^{33_T}\right)\left(1-d_{12}^{33_T}\right)\left(1-d_{23}^{33_T}\right)\left(1-d_{13}^{33_T}\right)\sigma_{33}^{eff} \\ if\ \sigma_{33}^{eff} < 0 \rightarrow \left(1-d_{11_T}^{33_C}\right)\left(1-d_{11_C}^{33_C}\right)\left(1-d_{22_T}^{33_C}\right)\left(1-d_{22_C}^{33_C}\right)\left(1-d_{33_T}^{33_C}\right) \\ \quad \left(1-d_{33_C}^{33_C}\right)\left(1-d_{12}^{33_C}\right)\left(1-d_{23}^{33_C}\right)\left(1-d_{13}^{33_C}\right)\sigma_{33}^{eff} \end{cases} \\
\sigma_{12} &= \left(1-d_{11_T}^{12}\right)\left(1-d_{11_C}^{12}\right)\left(1-d_{22_T}^{12}\right)\left(1-d_{22_C}^{12}\right)\left(1-d_{33_T}^{12}\right) \\
&\quad \left(1-d_{33_C}^{12}\right)\left(1-d_{12}^{12}\right)\left(1-d_{23}^{12}\right)\left(1-d_{13}^{12}\right)\sigma_{12}^{eff} \\
\sigma_{23} &= \left(1-d_{11_T}^{23}\right)\left(1-d_{11_C}^{23}\right)\left(1-d_{22_T}^{23}\right)\left(1-d_{22_C}^{23}\right)\left(1-d_{33_T}^{23}\right) \\
&\quad \left(1-d_{33_C}^{23}\right)\left(1-d_{12}^{23}\right)\left(1-d_{23}^{23}\right)\left(1-d_{13}^{23}\right)\sigma_{23}^{eff} \\
\sigma_{13} &= \left(1-d_{11_T}^{13}\right)\left(1-d_{11_C}^{13}\right)\left(1-d_{22_T}^{13}\right)\left(1-d_{22_C}^{13}\right)\left(1-d_{33_T}^{13}\right) \\
&\quad \left(1-d_{33_C}^{13}\right)\left(1-d_{12}^{13}\right)\left(1-d_{23}^{13}\right)\left(1-d_{13}^{13}\right)\sigma_{13}^{eff}
\end{aligned}
\qquad 3.9
$$

Eq. 3.9 shows 81 possible independent parameters used to describe the damaged state of the material. There are three additional parameters corresponding to uncoupled off-axis tests, $d_{12_{45°}}^{12_{45°}}$, $d_{23_{45°}}^{23_{45°}}$, and $d_{13_{45°}}^{13_{45°}}$, that are used to ensure convexity of the yield surface, for a total of 84 possible parameters. While the number of damage parameters appears to be large, it is unlikely that more than a handful of these parameters are significant for a given composite.

In the original formulation of the sub-model, the damage parameters were defined with respect to the effective plastic strain, λ, i.e. $d_{ij}^{kl}(\lambda)$. This is the strategy typically used when modeling isotropic materials as there is usually only a single damage parameter and the hardening behavior of the material is typically isotropic. The value of the effective plastic strain is a single scalar variable at a given integration point in the finite element model, meaning all of the damage parameters would grow irrespective of the PMD or PMP components contributing to the effective plastic strain. This leads to a conservative estimate of the damage induced in the model under the given loading conditions. In the next iteration, herein referred to as the *strain-based implementation*, the directional plastic strains were used as the internal state variable for tracking damage growth, i.e. $d_{ij}^{kl}\left(\varepsilon_{ij}^{p}\right)$ (Hoffarth 2016; Khaled et al. 2019b). While this provided a better physical representation of how the damage grows in the composite, the formulation lead to conservative results once again. The problem stems from the plastic strain interaction allowed by the plastic potential function, Eq. 2.13, through the H_{ij} values. In this case, stress-free plastic strains may excite damage parameters erroneously. Measuring the contribution of a directional plastic strain component to damage becomes difficult to perform experimentally. This is discussed in the experimental methods and results section of this chapter.

In the current implementation, herein referred to as the *stress-based implementation*, the effective stress is used as the internal state variable for tracking growth of the damage parameters, i.e. $d_{ij}^{kl}\left(\sigma_{ij}^{eff}\right)$. This strategy more easily suppresses stress-free strains from exciting damage parameters and still allows for anisotropic growth of damage. However,

one of the shortcomings is that under a state of constant stress with increasing plastic strain, damage will not increase, and all nonlinearity will be handled by the deformation sub-model. In the next section, implementation details are provided, including preprocessing of the experimental data and incorporation of damage into the plasticity algorithm.

3.2 Implementation Details

The implementation of the damage sub-model is separated into two parts: pre-processing, how input data is converted into a suitable form for the material model, and interaction with the deformation sub-model, how the concept of effective stress is used in the plasticity algorithm. The first assumption made in deriving the damage is that of strain equivalence (Lemaitre and Chaboche 1978). The hypothesis states that the strain behavior of the damaged material is represented by the constitutive relationship of the undamaged material where the stress is replaced by the effective stress. The effective stress rate can then be written as

$$\dot{\boldsymbol{\sigma}}^{eff} = \mathbf{C} : \left(\dot{\boldsymbol{\varepsilon}} - \dot{\boldsymbol{\varepsilon}}^{p} \right) \tag{3.10}$$

This assumption allows for all plasticity computations to be performed in the effective stress space, essentially decoupling the deformation and damage sub-models. The conversion of the input stress-total strain curves, described in Section 2.1, is affected as the curves are now converted and stored as effective stress-effective plastic strain, i.e. $\sigma_{ij}^{eff} - \lambda$. An outline of the conversion of the stress-total strain curves to effective stress-effective

plastic strain curves is as follows. First, input curves are converted from stress-total strain to effective stress-total strain to effective stress-plastic strain to effective stress-effective plastic strain, shown schematically as

$$\left(\sigma_{ij} - \varepsilon_{ij}^{t}\right) \rightarrow \left(\sigma_{ij}^{eff} - \varepsilon_{ij}^{t}\right) \rightarrow \left(\sigma_{ij}^{eff} - \varepsilon_{ij}^{p}\right) \rightarrow \left(\sigma_{ij}^{eff} - \lambda\right) \tag{3.11}$$

In this step, $\left(\sigma_{ij} - \varepsilon_{ij}^{t}\right) \rightarrow \left(\sigma_{ij}^{eff} - \varepsilon_{ij}^{t}\right)$, the input damage parameter-total strain curves are used.

$$\sigma_{ij}^{eff}\left(\varepsilon_{ij}^{t}\right) = \frac{\sigma_{ij}\left(\varepsilon_{ij}^{t}\right)}{1 - d_{ij}^{ij}\left(\varepsilon_{ij}^{t}\right)} \tag{3.12}$$

Eq. 3.12 shows that only uncoupled damage terms are used in the conversion. This is done since during the monotonic test, it is assumed that only uncoupled damage has manifested itself in the true stress-total strain response. This is consistent with the underlying reason for utilizing the effective stress as the independent internal state variable for damage growth. Second, using the assumption of strain equivalence, the plastic strains can then be computed as

$$\varepsilon_{ij}^{p}\left(\varepsilon_{ij}^{t}\right) = \varepsilon_{ij}^{t} - \frac{\sigma_{ij}\left(\varepsilon_{ij}^{t}\right)}{\left(1 - d_{ij}^{ij}\left(\varepsilon_{ij}^{t}\right)\right)E_{ij}} = \varepsilon_{ij}^{t} - \frac{\sigma_{ij}^{eff}\left(\varepsilon_{ij}^{t}\right)}{E_{ij}} \tag{3.13}$$

where E_{ij} is the Young's modulus in direction *ij*. In the case of shear curves, E_{ij} is replaced with $2G_{ij}$ since the input is assumed to be in terms of tensorial shear strain. Third, using the plastic work equivalence assumption, discussed in Section 2.1, the effective plastic strain is computed as

$$\lambda = \int \frac{\sigma_{ij}^{eff} \, d\varepsilon_{ij}^{P}}{h\left(\sigma_{ij}^{eff}\right)} \tag{3.14}$$

where the value of the plastic potential function in Eq. 3.14 is a function of the effective stresses. The resulting $\sigma_{ij}^{eff} - \lambda$ curves are used to track the evolution of flow stresses during the simulation. At this point, all uncoupled and coupled damage parameter-total strain curves are replaced with damage parameter-effective stress curves, i.e. $d_{kl}^{ij}\left(\varepsilon_{kl}^{t}\right) \rightarrow d_{kl}^{ij}\left(\sigma_{kl}^{eff}\right)$. Fig. 55 shows the pre-processed results from transforming the user data from the total stress-total strain curve to effective stress-effective plastic strain for two cases - with and without damage.

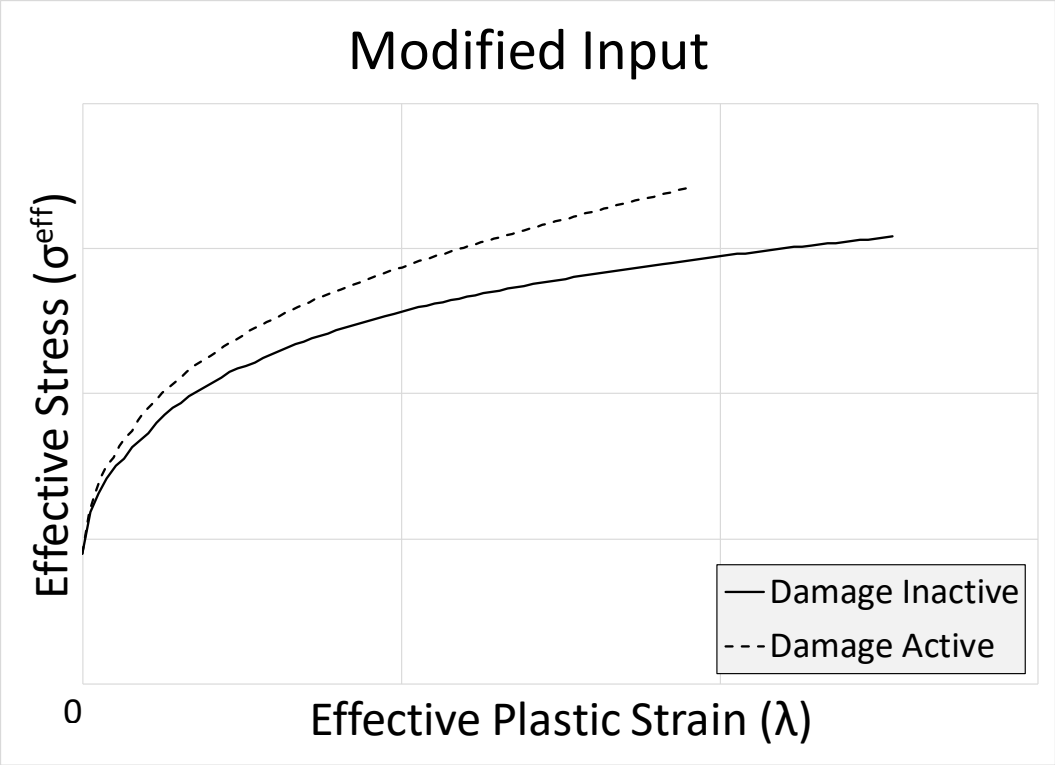

Fig. 55. Example Effective Stress-effective Plastic Strain Curves Constructed Using the Same Total Stress-strain Data and Subsequently Used to Track Yield Stress During Simulation for Two Different Cases – One Involving Deformation Only and the Other Involving Deformation and Damage

Fig. 55 shows that, since damage has been assumed to account for a portion of nonlinearity, the degree of plasticity in the given direction has decreased, as evidenced by the lower ultimate value of effective plastic strain. The verification tests presented in a later section show that this does not influence the nonlinear response of the material under monotonic loading and that the strain equivalence hypothesis is satisfied.

The damage model is seamlessly incorporated into the incremental plasticity algorithm. All plasticity computations are performed in the effective stress space since the unknown variable being solved for is the effective plastic strain, λ, and, through the assumption of strain equivalence, is the same in the true stress space and effective stress space. Denoting subscripts *t* as the previous instance of time and *t+1* as the current instance of time (for the unknown in the computations), the incremental algorithm is as follows.

1. The effective stress from the end of the previous time step, $\boldsymbol{\sigma}_t^{eff}$, is obtained from history and is used to compute the trial stress for the current time step.

$$\left(\boldsymbol{\sigma}_{t+1}^{eff}\right)^{trial} = \boldsymbol{\sigma}_t^{eff} + \mathbf{C} : \dot{\boldsymbol{\varepsilon}}_{t+1}^{total} \Delta t \tag{3.15}$$

   The undamaged stiffness tensor, $\mathbf{C}$, is used as it is consistent with the effective stress. All subsequent plasticity computations are performed using the effective trial stress. The yield function (Eq. 2.3) as well as the equation for the plastic multiplier increment (Eq. 2.24) are computed in terms of the effective stress. Additionally, the yield function coefficients, F_{ii} and F_i (Eq. 2.4), are computed using the yield stress curves which were converted using the damage parameters, Fig. 55. The radial return algorithm used to solve the nonlinear system of equations for $\Delta\lambda_{t+1}$ can be found in an earlier work (Hoffarth et al. 2016).

2. After converging to a value of the plastic multiplier increment, $\Delta\lambda_{t+1}$, the final stress state is computed using the flow rule, Eq. 2.14, and by using a linear decomposition of the total strain into elastic and plastic components.

$$\boldsymbol{\sigma}_{t+1}^{eff} = \left(\boldsymbol{\sigma}_{t+1}^{eff}\right)^{trial} - \Delta\lambda_{t+1}\mathbf{C} : \frac{\partial g}{\partial\left(\boldsymbol{\sigma}_{t+1}^{eff}\right)^{trial}} \tag{3.16}$$

The value of $\boldsymbol{\sigma}_{t+1}^{eff}$ is stored in history to be used at the beginning of the next time step in computing the elastic trial stress.

3. All damage parameters shown in Eq. 3.9 are then obtained for both $\boldsymbol{\sigma}_{t}^{eff}$ and $\boldsymbol{\sigma}_{t+1}^{eff}$. For each independent damage term, the larger of the two values is chosen to preserve the irreversibility condition.

$$\left(d_{kl}^{ij}\right)_{t+1} = \max\left(d_{kl}^{ij}\left(\left(\sigma_{kl}^{eff}\right)_{t}\right), d_{kl}^{ij}\left(\left(\sigma_{kl}^{eff}\right)_{t+1}\right)\right) \tag{3.17}$$

4. Finally, the stresses are converted from the effective stress space into the true stress space and passed back to LS-DYNA using the updated damage tensor.

$$\boldsymbol{\sigma}_{t+1} = \mathbf{M}\left(\left(d_{kl}^{ij}\right)_{t+1}\right)\boldsymbol{\sigma}_{t+1}^{eff} \tag{3.18}$$

The next section provides the methodology for deriving the damage parameters introduced in this section. The process and results of a case study using the T800S/F3900 composite are illustrated and presented.

3.3 Experimental Methods

The input data required to drive the damage model is in the form of damage parameter-total strain curves. The data is used to describe the damage that the specimen incurs under monotonic loading. However, the data is obtained from a series of cyclic loading curves. The assumption is that no additional damage is induced in the specimen during the elastic unloading/reloading cycles. The experimental methods are presented for obtaining both uncoupled and coupled damage parameters.

DIC was used to obtain strain field data during the experiments. The damage parameters are obtained through a series of cyclic loading procedures. In general, the procedures involve loading a given specimen in a certain direction into the nonlinear regime, the onset of which is determined from monotonic testing conducted earlier. After loading the specimen into the nonlinear regime (i.e. initial state to point 1 in Fig. 56a and Fig. 56b), it is unloaded to a stress-free state (i.e. point 1 to point 2 in Fig. 56a and Fig. 56b), and subsequently loaded elastically in the direction of interest. During the elastic loading cycle, three additional conditioning cycles are performed, for example, from point 2 to point 1a in Fig. 56a and Fig. 56c. The conditioning cycles yield multiple measurements of the elastic stiffness at the same level of damage and thus allow for discerning between reduction in

stiffness and experimental error. Fig. 56 shows how the uncoupled and coupled experimental procedures work.

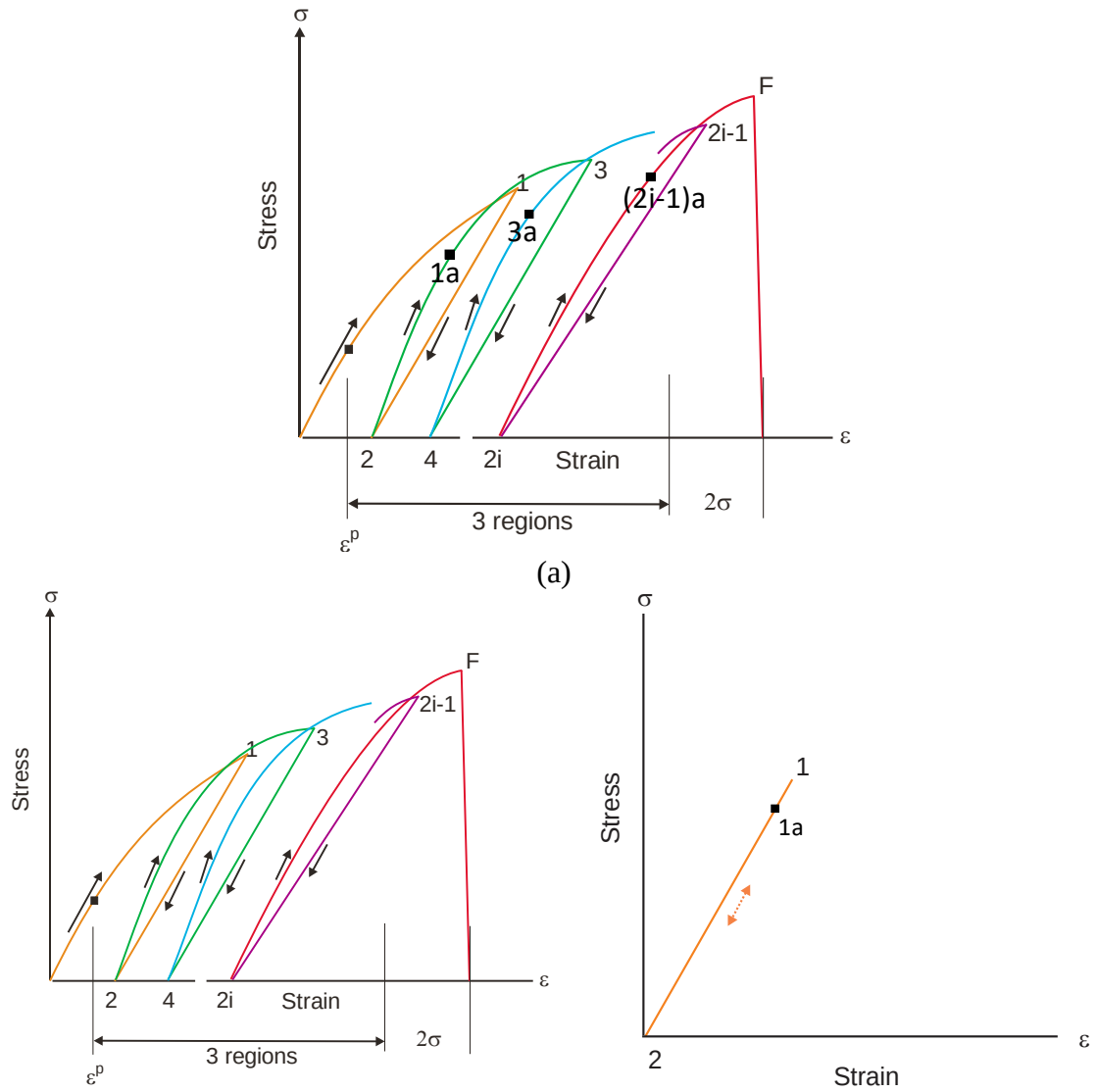

Fig. 56. Illustration of Experimental Procedure for (a) Uncoupled Damage Tests and (b), (c) Coupled Damage Tests

In this study, three cycles were performed on each specimen since three data points is the minimum required to discern any nonlinear behavior. However, any number of cycles could potentially be performed, and the number could be determined by observations made during investigative testing or by visual observations of crack growth during monotonic testing. As shown in Fig. 56(a-b), the final point of unload was chosen to be two standard deviations below the failure strain in the given direction. This was done to ensure that there was not a complete loss of load carrying capacity in the specimen before the desired number of cycles was performed, thereby accounting for potential specimen differences and experimental errors. The failure strain was obtained from monotonic testing to failure in the direction of interest. Additionally, Fig. 56 shows that the maximum stress point for the conditioning cycles, denoted 1a, 3a, etc. in Fig. 56, was approximately 80% of the stress induced when unloading was initiated. This was done to ensure no additional damage was accidently induced during the conditioning.

Prior to performing the cyclic procedure, the specimen is loaded elastically in the direction of interest to obtain the initial undamaged modulus. After performing the cyclic loading experiments, the damaged modulus must be computed corresponding to the value of strain at each point of unload, e.g. points 1 and 3 in Fig. 56a and Fig. 56b. The modulus can be computed using a variety of methods, two of which were used in the current research. The first is to perform a linear regression on the loading or unloading path during the interrogation cycles, illustrated by the dashed lines in Fig. 57b. The slope of the regression model is taken as the modulus and the values for all load and unload conditioning cycles, at the current value of strain, are averaged. The average slope is taken as the modulus

corresponding to the current level of damage. The second technique is used when the hysteresis loops become large and the load/unload path is highly nonlinear making it difficult to choose the region to perform the linear regression. In this case, an average slope is used which corresponds to the line between the point where unloading is initiated and the point corresponding to the stress-free state. An alternative method may be used to characterize damage for specimens exhibiting large hysteretic loops which involves computing the energy dissipated during loading/unloading which is a function of the size of the hysteretic loops. However, since the dissipated energy is likely due to both crack formation and heat dissipation caused by plastic flow, decoupling the two responses is necessary. This procedure would require characterizing the thermal properties of the composite which is part of the planned future work. Fig. 57 and Fig. 58 illustrate how both the methods are used.

(a)

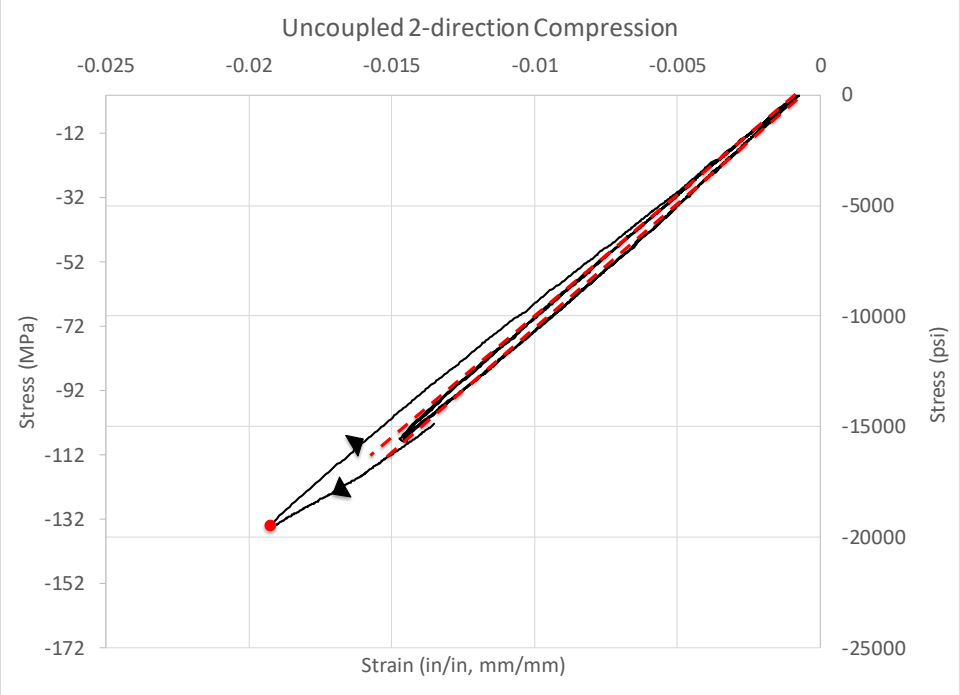

(b)

Fig. 57. General Procedure Used to Determine Reduced Modulus with Mostly Linear Load/Unload Behavior (a) Full Experimental Curve and (b) One Cycle Isolated

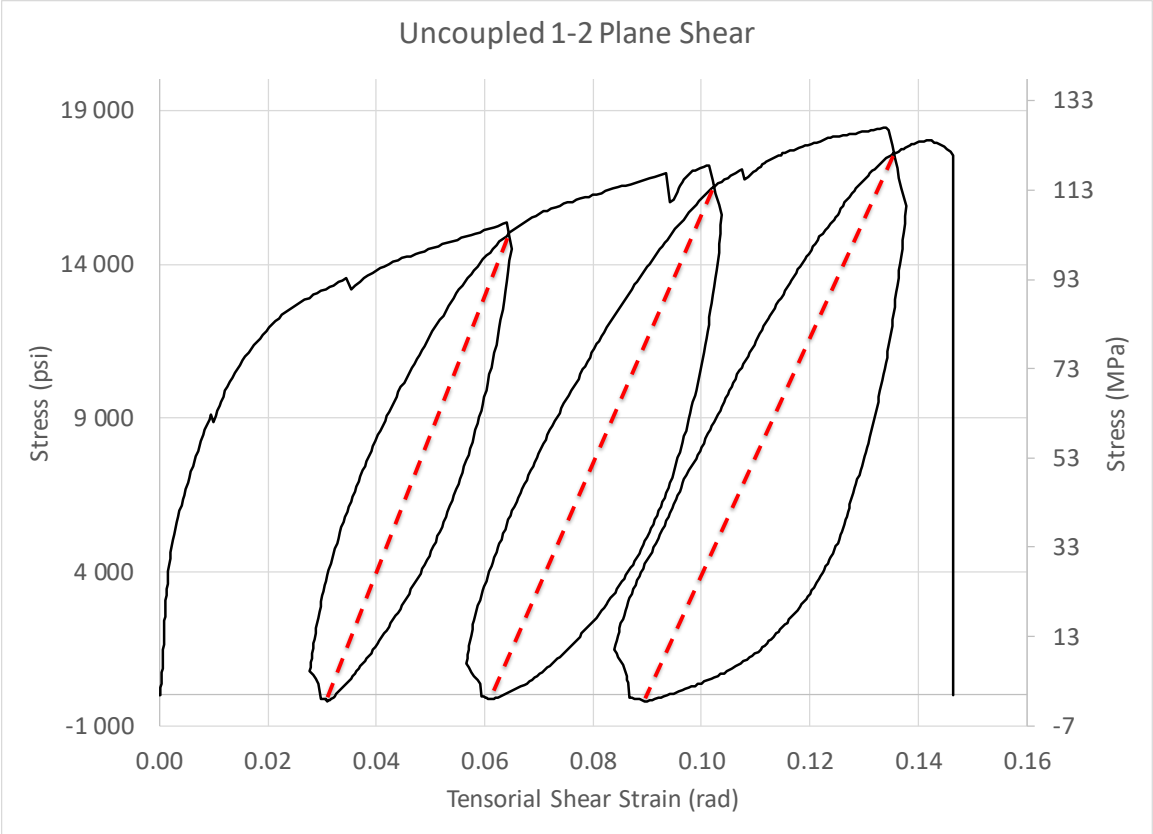

Fig. 58. General Procedure Used to Determine Reduced Modulus with Large Hysteretic Loops

The hysteretic behavior shown in Fig. 58 is not captured in the constitutive model as only linear elastic unloading behavior is considered. The damage parameters can now be computed as

$$d\left(\varepsilon_i^t\right) = 1 - \frac{E\left(\varepsilon_i^t\right)}{E\left(\varepsilon_0^t\right)} \qquad 3.19$$

where $d\left(\varepsilon_i^t\right)$ is the damage parameter corresponding to the total strain at unload point *i*, $E\left(\varepsilon_i^t\right)$ is the elastic stiffness corresponding to unload point *i*, and $E\left(\varepsilon_0^t\right)$ is the elastic stiffness corresponding to the undamaged specimen. After computing the damage parameter corresponding to all unload points, a damage-total strain curve is generated. The damage values begin at the initial plastic strain value corresponding to the direction in which damage is induced and ends at the final strain value of the corresponding monotonic curve of the direction in which damage is induced. Data can be extrapolated to the initial plastic strain value and final strain value using curve fitting techniques.

3.4 Experimental Results

While there are 84 possible damage parameters, obtaining all of them is unnecessary (and would most likely be impractical) for most composites. The damage-related experiments in the current study focus on characterizing the in-plane damage behavior of the T800-F3900 carbon fiber/epoxy resin unidirectional composite. The subset of parameters was chosen based on observations made during testing of the composite for the deformation sub-model. Only those in-plane directions or planes which exhibited significant nonlinearity were deemed to contribute significantly to the damaged state of the composite. Table 14 summarizes the damage parameters that have been obtained experimentally. In Table 14, the term *interrogate* means to perform cyclic loading in the elastic regime so as to measure the elastic stiffness at the current strain value in the loading direction, i.e. the direction in which damage is being induced.

Table 14. Damage Parameters Characterized in This Study for the T800S/F3900 Composite

Test name and parameter	Description
Uncoupled 2-direction compression $\left(d_{22_C}^{22_C}\right)$	Load specimen in 2-direction in compression, then interrogate specimen in elastic regime in 2-direction in compression
Uncoupled 1-2 plane shear $\left(d_{12}^{12}\right)$	Load specimen in 1-2 plane in shear, then interrogate specimen in elastic regime in 1-2 plane in shear
Coupled 2-direction compression 2-direction tension $\left(d_{22_C}^{22_T}\right)$	Load specimen in 2-direction in compression, then interrogate specimen in elastic regime in 2-direction in tension
Coupled 2-direction compression 1-2 plane shear $\left(d_{22_C}^{12}\right)$	Load specimen in 2-direction in compression, then interrogate specimen in elastic regime in 1-2 plane in shear

3.4.1 Uncoupled 2-direction Compression Test

The uncoupled 2-direction compression test is used to quantify the reduction in the 2-direction compression elastic stiffness as a result of damage induced by loading in the 2-direction in compression $\left(d_{22_C}^{22_C}\right)$. This test was performed because, when performing QS-

RT monotonic tests, the 2-direction compression stress-strain curve exhibited significant nonlinearity. It was concluded that the response was dominated by the plastic response of the matrix, cracking of the matrix, and interfacial debonding between the fiber and matrix, thus indicating that a portion of the inelastic response was due to damage. The specimen used to perform this test is shown in Fig. 17b.

Three representative stress-strain curves are shown in Fig. 59. Additionally, the model curve from the monotonic loading QS-RT experiments is also shown. The cyclic QS-RT curves are mostly enveloped by the monotonic QS-RT curves and the failure points are within the statistical distribution observed in the monotonic tests (Fig. 26b). From the cyclic loading tests (Fig. 59), the damage-total strain curves are generated (Fig. 60).

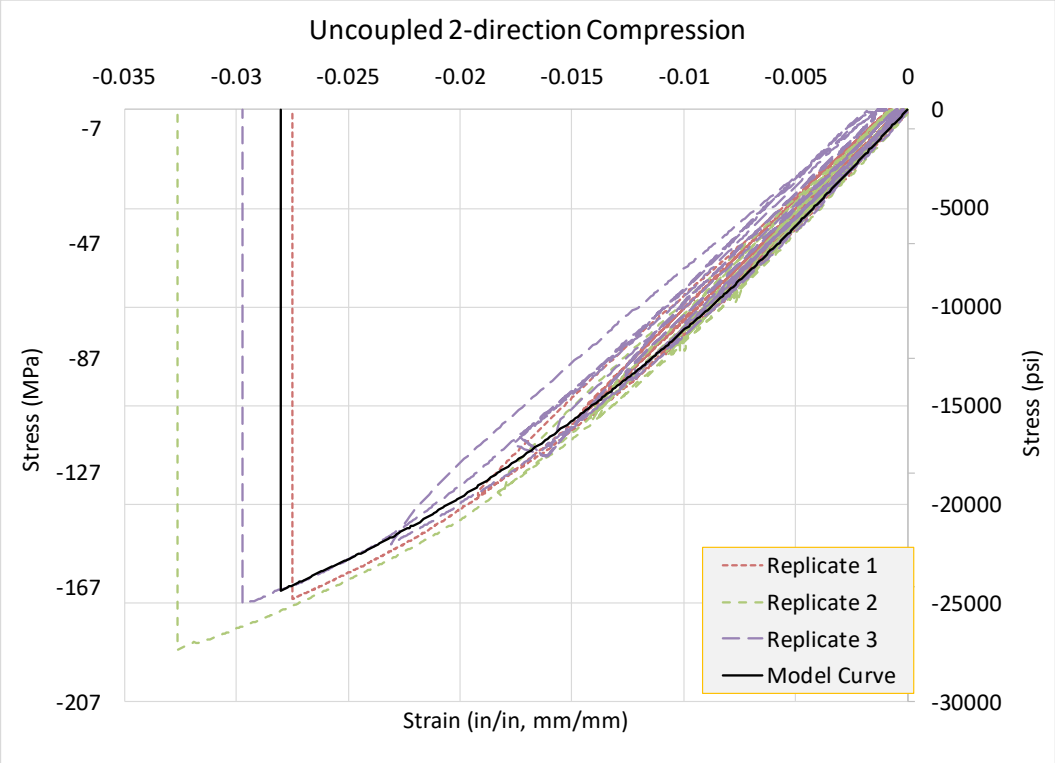

Fig. 59. Representative Stress-strain Curves for Uncoupled 2-direction Compression Tests

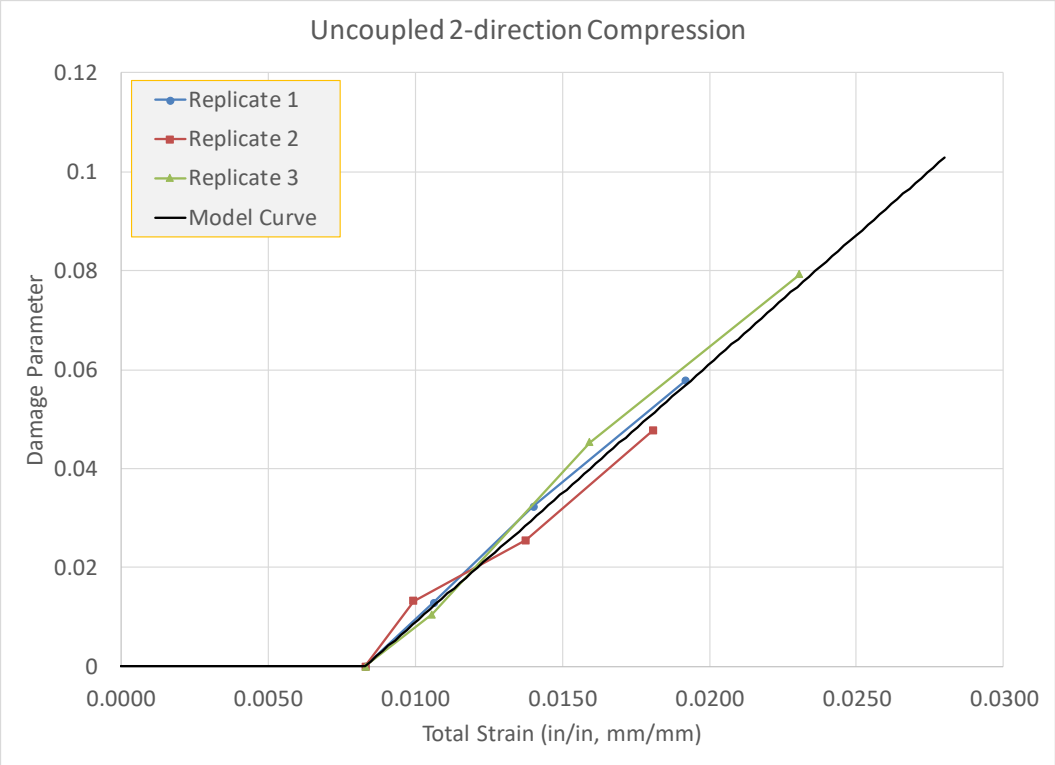

Fig. 60. Damage Parameter $\left(d_{22_c}^{22_c}\right)$-Total Strain $\left(\varepsilon_{22}\right)$ Curves for Uncoupled 2-direction Compression Tests

Note that the damage parameter has a value of zero where the onset of nonlinearity is deemed to begin and ends at the failure strain corresponding to the QS-RT model curve shown in Fig. 59. The model curve in Fig. 60 was generated by performing linear regressions on each individual replicate, extrapolating the data to the start and end points, and finally using an unweighted point-by-point average to generate the model data. Since the damage does not show an asymptotic behavior (Replicates 1-3 in Fig. 60), the damage was assumed to keep increasing after the final experimental damage data point since it is likely that cracks and other forms of damage in the material will continue growing until complete failure. Fig. 61 shows a typical specimen after testing.

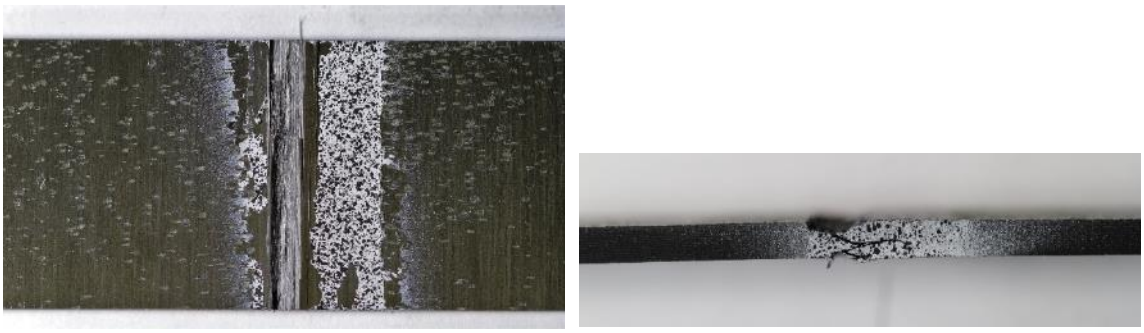

(a) (b)

Fig. 61. Uncoupled 2-direction Compression Specimen after Testing (a) Plan-view and (b) Side-view

Though testing the specimens to failure is not required, it was done with the uncoupled 2-direction compression to determine if the additional cyclic loading would have an impact on the failure when compared to the monotonically loaded specimens. Fig. 59 and Fig. 61 show that the failure stress/strain and the failure mode are generally unaffected by cyclic loading.

3.4.2 Uncoupled 1-2 Plane Shear Damage Test

The uncoupled 1-2 plane shear test is used to quantify the reduction in the 1-2 plane shear elastic stiffness as a result of damage induced by loading the 1-2 plane in shear $\left(d_{12}^{12}\right)$. This test was performed because, when performing QS-RT monotonic tests, the 1-2 plane shear stress-strain curve exhibited significant nonlinearity. The response was caused by plastic deformation of the matrix and intralaminar delamination, thus indicating that a portion of the inelastic response was due to damage. The specimen used to perform this test is shown in Fig. 20.

Four representative stress-strain curves are shown in Fig. 62. Additionally, the model curve from the monotonic loading QS-RT experiments is also shown. Fig. 63 shows the resulting damage parameter $\left(d_{12}^{12}\right)$-total strain $\left(\varepsilon_{12}\right)$curve.

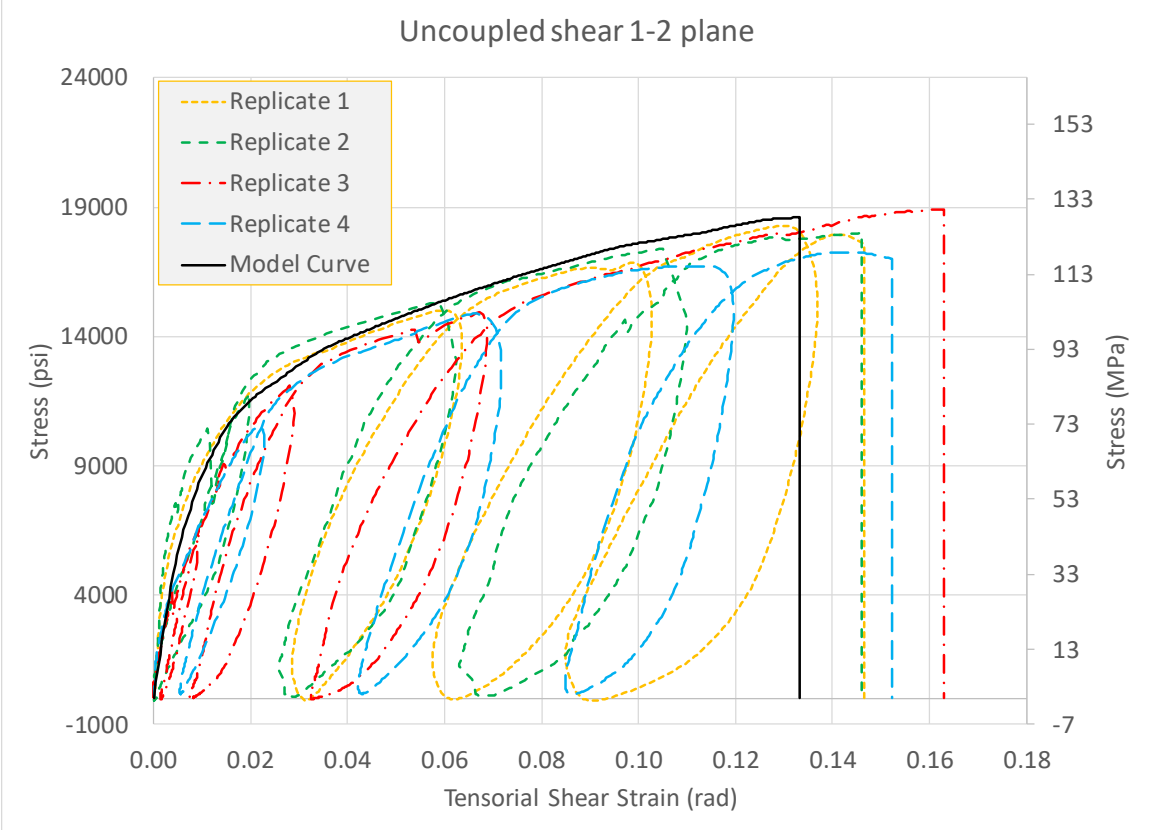

Fig. 62. Representative Stress-Strain Curves for Uncoupled 1-2 Plane Shear Tests

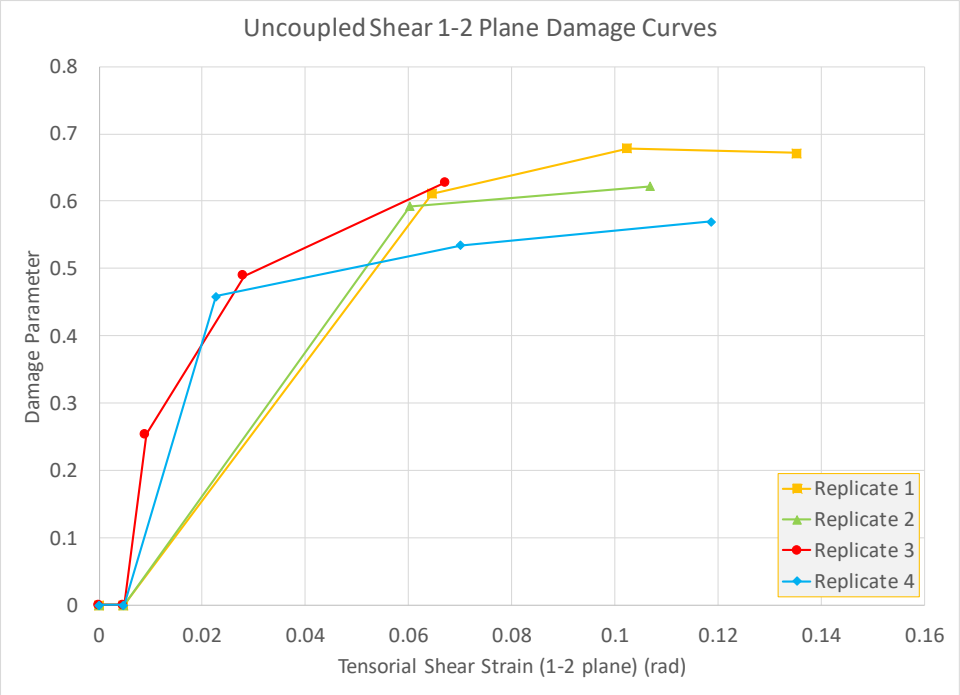

(a)

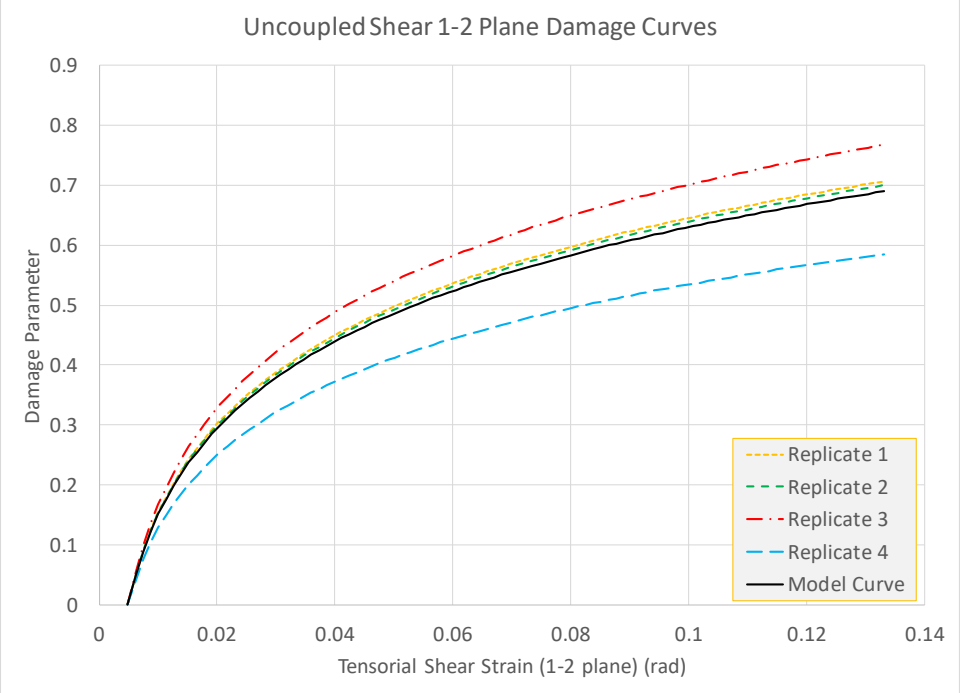

(b)

Fig. 63. Damage Parameter-Total Strain Curves for Uncoupled 1-2 Plane Shear Tests (a) Raw Data and (b) Processed Data With *Model* Curve

Fig. 63 shows that there is significant damage induced in the material at relatively low strains and the damage parameter asymptotically approaches the final value. This is supported by the observations made during the monotonic loading experiments where the size and number of cracks after a certain level of strain, plateaued as well as large cracks forming at the root of the notch, consistent with observations made in other research (Odegard and Kumosa 2000; Pierron and Vautrin 1998). The cracks present in the material influence the load transfer mechanisms of the structure and manifest themselves as a large reduction in the apparent elastic stiffness. None of the specimens from other damage tests show macro cracks prior to failure and hence show significantly lower values of damage than the uncoupled 1-2 plane shear tests. Fig. 64 shows a typical specimen after testing.

Fig. 64. Uncoupled 1-2 Plane Shear Specimen after Testing

The shear specimens were not taken to a point where there was a complete loss of load carrying capacity as (i) it was not necessary for the purpose of this research since extrapolation techniques are used to obtain damage parameters for all values of strain, and (ii) the issues with inducing shear failure in a unidirectional composite have been well documented by various other researchers (Odegard and Kumosa 2000; Pierron and Vautrin 1998).

3.4.3 Coupled 2-direction Compression 2-direction Tension Damage Test

The coupled 2-direction compression 2-direction tension test is used to quantify the reduction in the 2-direction tension elastic stiffness as a result of damage induced by loading the 2-direction in compression $\left(d_{22_C}^{22_T}\right)$. This test was performed because, when performing QS-RT monotonic tests, the 2-direction compression stress-strain curve exhibited significant nonlinearity, partially due to damage as previously mentioned. The damage present in material should hypothetically have an effect on the elastic stiffness in multiple coordinate directions as the load transfer mechanisms are altered due to loss of connectivity in the material's microstructure. The specimen used for this experiment is the same as the one shown in Fig. 17b. Fig. 65 shows all cycles, both the compression and tension loading phases, performed on a single specimen.

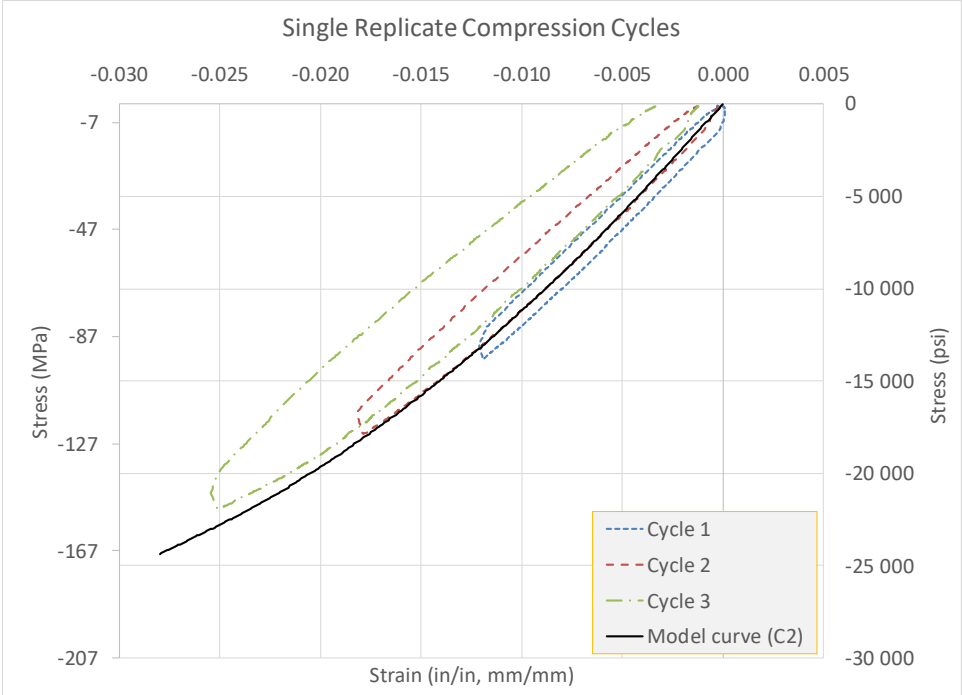

(a)

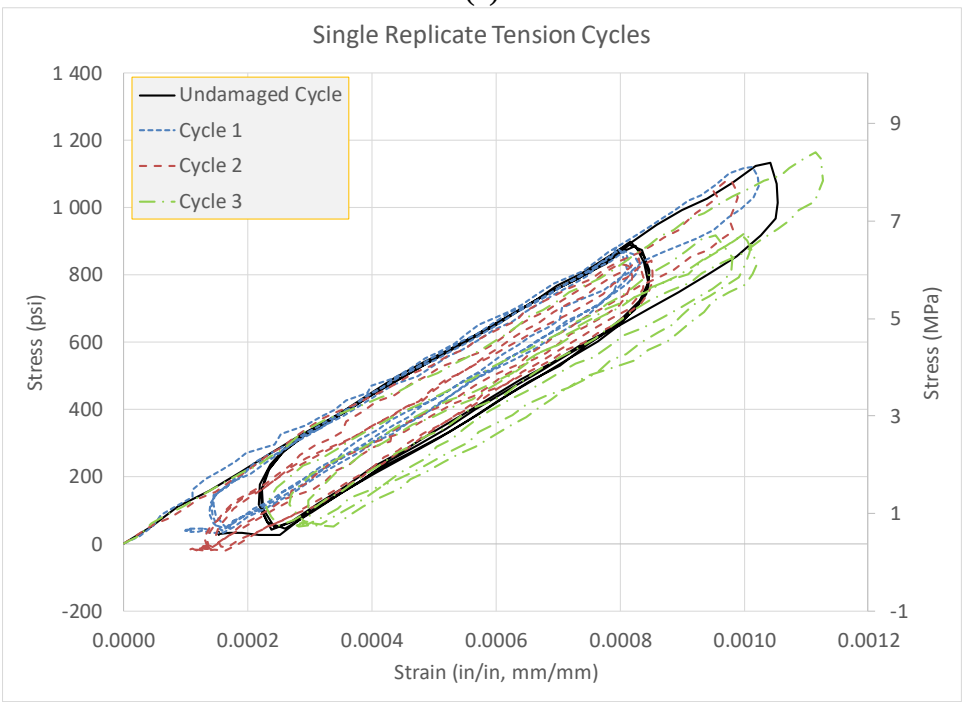

(b)

Fig. 65. Representative Stress-strain Curves for a Single Replicate of the Coupled 2-direction Compression 2-direction Tension Test (a) Compression Cycles and (b) Tension Cycles

Fig. 66 shows the resulting damage parameter $\left(d_{22_C}^{22_T}\right)$-total strain $\left(\varepsilon_{22}\right)$ curves for the three replicates.

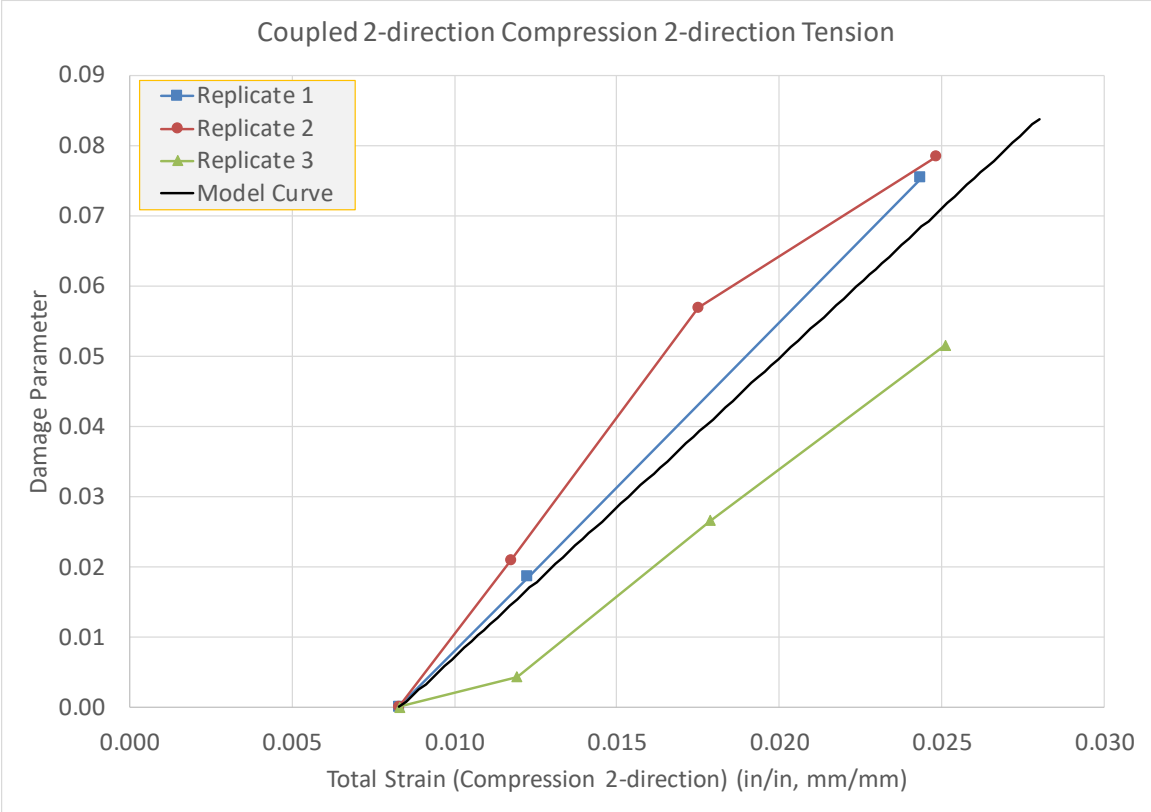

Fig. 66. Damage Parameter-Total Strain Curves for Coupled 2-direction Compression 2-direction Tension Tests

Comparing the damage parameters obtained in Fig. 60$\left(d_{22_C}^{22_C}\right)$ and Fig. 66$\left(d_{22_C}^{22_T}\right)$, show that the values of damage parameters are comparable. This indicates that, while the damage parameters are independent and were obtained from distinct experiments, for the T800S/F3900 composite, the mechanisms causing damage are likely the same and the parameters can be treated as being identical. This coupling between tension and

compression is often ignored in other damage models but is captured in the proposed damage formulation within OEPDMM.

3.4.4 Coupled 2-direction Compression 1-2 Plane Shear Damage Test

The coupled 2-direction compression 2-1 plane shear test quantifies the reduction in the 2-1 plane shear elastic stiffness as a result of damage induced by loading the 2-direction in compression $\left(d_{22_C}^{12}\right)$. This test was performed because, when performing QS-RT monotonic tests, the 2-direction compression stress-strain curve exhibited significant nonlinearity, partially due to damage, as previously mentioned. A schematic of the specimen used for this experiment is shown in Fig. 67.

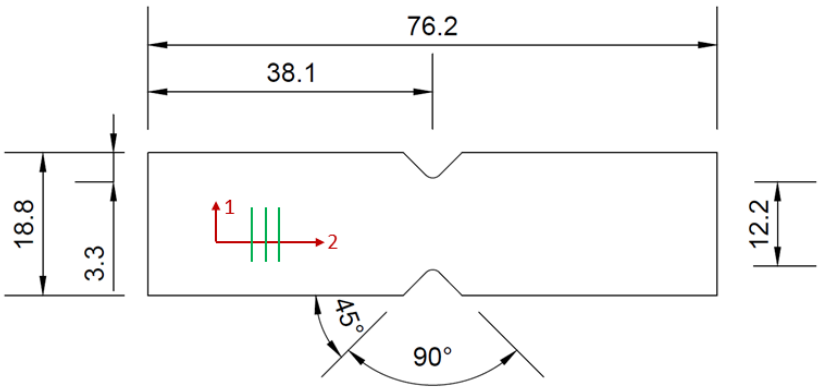

Fig. 67. Specimen Geometry Used for Coupled 2-direction Compression 2-1 Plane Shear Tests (Dimensions in mm)

The specimen uses the standard Iosipescu shear test geometry and leads to a non-constant gage section. This causes only a small region between the notches to be in a state of uniform compression. The measured stiffness comes from the 2-1 shear test (Fig. 67) rather than

the 1-2 shear test (Fig. 19) since the compression loading is in the 2-direction. The results of the QS-RT experiments show that while the overall though the stress-strain curve is different between the two experiments, the initial elastic regimes are essentially the same (Fig. 41). Hence the assumption is that the damage induced in the specimen will have the same effect when loading the material using either orientation. The tested specimen is shown in Fig. 68. The observed failure pattern is similar to that observed in the 2-direction compression tests using straight sided test coupons (Fig. 27b).

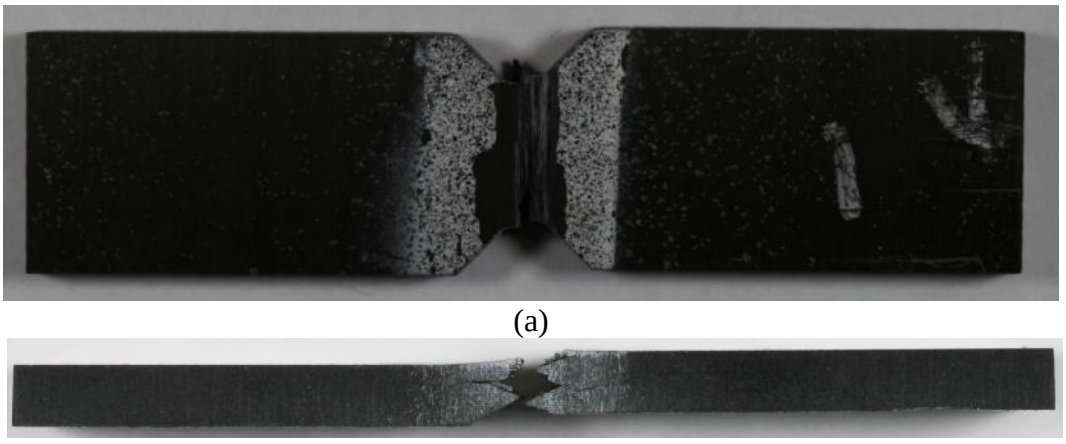

(a)

(b)

Fig. 68. Coupled 2-direction Compression 2-1 Plane Shear Investigative Specimen after Testing (a) Plan View and (b) Top Edge View

Fig. 69 shows all cycles (both the compression and shear loading phases), performed on a single specimen.

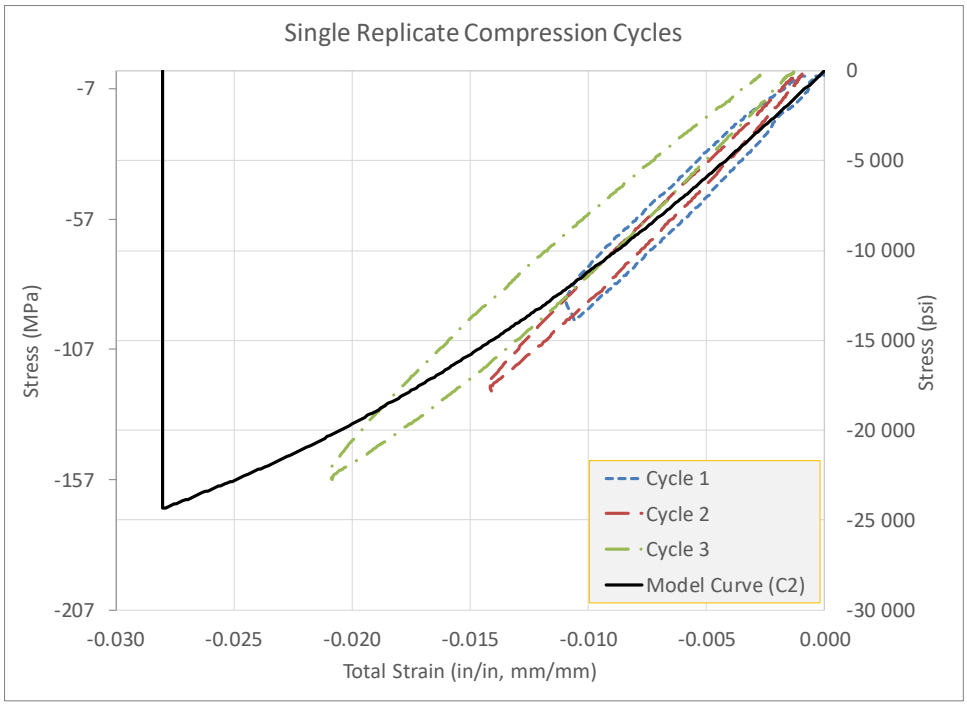

(a)

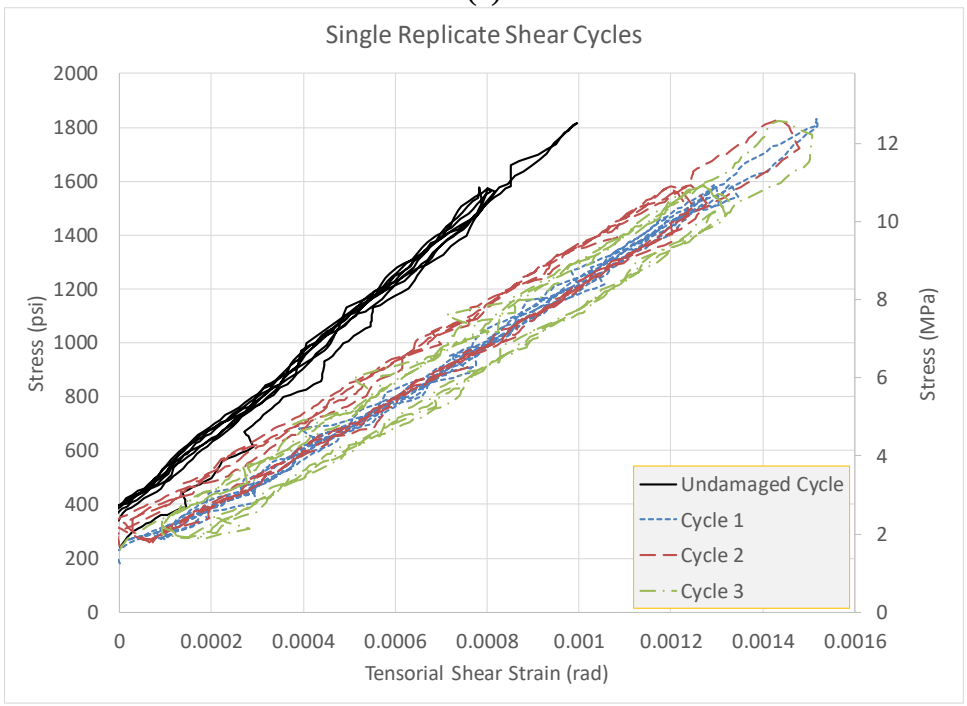

(b)

Fig. 69. Representative Stress-strain Curves for a Single Replicate of the Coupled 2-direction Compression 2-1 Plane Shear Test (a) Compression Cycles and (b) Shear Cycles

Compression cycles shown in Fig. 69a were performed using a modified CLC fixture (Fig. 10g,h) to allow for the smaller specimen size. The shear cycles were performed with a standard Iosipescu shear test fixture (Fig. 10d). Fig. 70 shows the resulting damage parameter $\left(d_{22_C}^{12}\right)$-total strain $\left(\varepsilon_{22}^{C}\right)$ curves for three replicates.

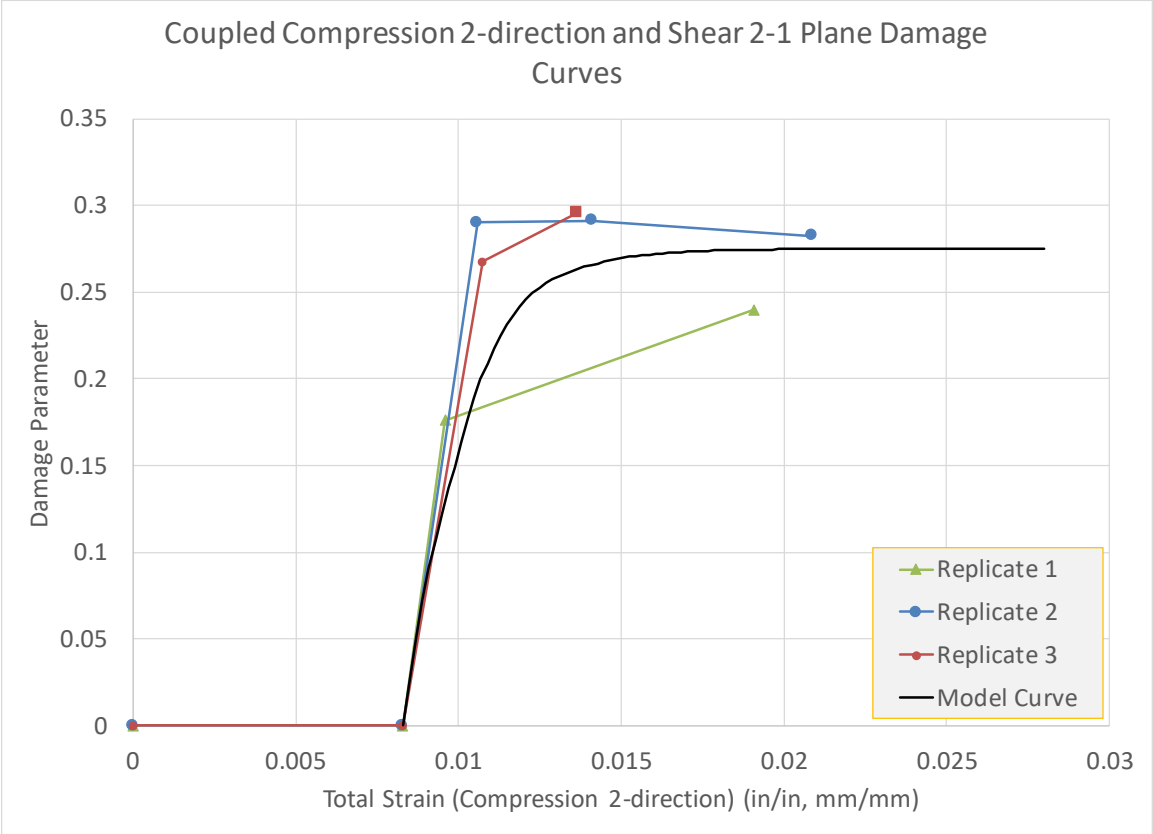

Fig. 70. Damage Parameter-Total Strain Curves for Coupled 2-direction Compression 2-1 Plane Shear Test

The curves shown in Fig. 70 suggest that there is a high amount of damage initially, but the damage curves asymptotically approach the final value. Additionally, replicate 2 shows that there is a small decrease in damage as the strain increases. This behavior is nonphysical

and is likely due to dispersion in the results caused by experimental variabilities. The procedure used to obtain these parameters called for moving the specimen between two separate test fixtures. This was probably a large contributor to the experimental error and variation in the results. Additionally, the specimen used for this experiment, Fig. 68, is likely not conducive to a proper compression test. A significant amount of specimen misalignment was observed after compression loading which is likely another contributor to the erroneous damage parameter values. The testing method is being investigated to better understand the damage modes and obtain reproducible and reliable data.

Finally, it should be noted that due to experimental limitations (brought about by required specimen geometries and available composite panel thicknesses), damage experiments could not be conducted to find the through-thickness damage curves. As shown in the validation simulations, their effects may be gaged by numerical experimentation.

3.5 Numerical Verification

Prior to using the implemented theory in impact test simulations, single element (SE) verification tests are used to ensure that the damage model is implemented correctly in the computer program and yield acceptable results. The simulations include both monotonic and cyclic loading. The former tests are used to illustrate that, even with the inclusion of damage, the nonlinear response remains unaffected. The latter tests illustrate that during unloading the stiffness reduction takes place according to the input curves. Examples of both an uncoupled and a coupled simulation are presented for the monotonic and cyclic

loading test cases. Fig. 71 shows a schematic of the unit volume cube finite element model used for both verification tests.

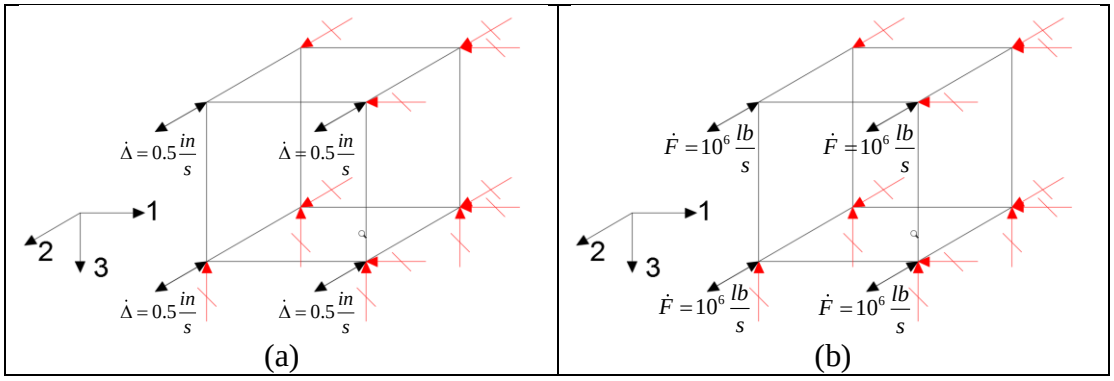

Fig. 71. SE Verification Test Finite Element Model Schematic with Boundary Conditions (a) Displacement-controlled Simulations and (b) Load-controlled Simulations (Arrows Which Have Been Crossed Out Represent Restrained Degrees of Freedom)

All simulations were successfully run using LS-DYNA solid element formulations 1 (reduced integration) and 2 (full integration). However, only the reduced integration simulations results are presented. Unless otherwise stated, the stress-based damage formulation is used.

3.5.1 Uncoupled 2-direction Compression Damage Test

The uncoupled 2-direction compression verification simulation uses the damage data presented in Fig. 60 (i.e. only using $d_{22_C}^{22_C}$). The simulations were performed under displacement control. The results of the verification tests for both the monotonic and cyclic loading cases as well as with deformation and damage (labeled *Def+Dam*) and without damage (labeled *Def*) included in the input are shown in Fig. 72.

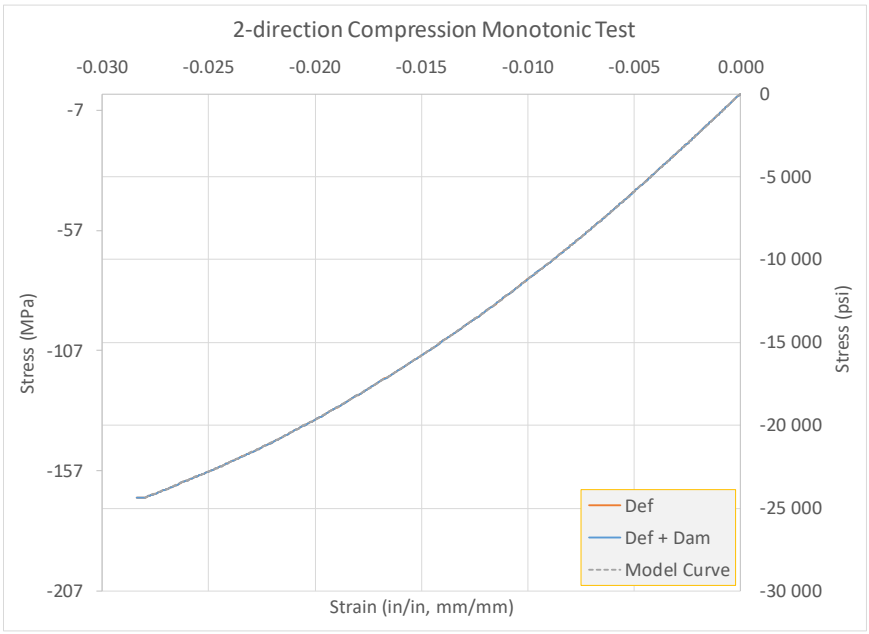

(a)

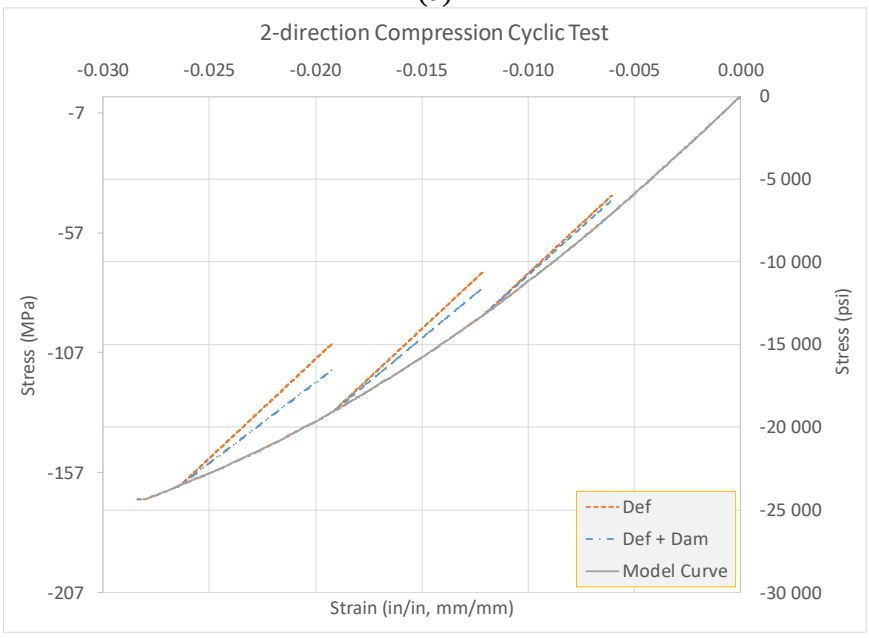

(b)

Fig. 72. Uncoupled Damage SE Verification Test Results (a) Monotonic Loading and (b) Cyclic Loading

Fig. 72a shows that the effects of the uncoupled damage do not manifest under monotonic loading. This is the expected result since plasticity computations are performed in the effective stress space and the uncoupled damage parameter has been used to modify the 2-direction compression input stress-total strain curve, illustrated by Fig. 55. However, the role of the damage model is clear when performing loading and unloading cycles, shown in Fig. 72b. The cyclic loading curve, with the uncoupled 2-direction compression damage parameter included in the model, exhibits a more compliant elastic unloading path which is consistent with the input damage parameter-total strain curve. Additionally, Fig. 72b shows that the cyclic loading curves are enveloped by the corresponding input 2-direction compression stress-strain curve that is consistent with the theory as well as the experimental results presented in the previous section.

3.5.2 Coupled 2-direction Compression 2-direction Tension

The coupled 2-direction compression 2-direction tension verification test uses the damage data presented in Fig. 66 (i.e. only using $d_{22_C}^{22_T}$). The simulations were performed under load control in order to avoid accidently entering the plastic regime when the stress reversal occurs. Damage is induced by loading the model in compression and interrogating the elastic tension regime. The unload path in the compression regime (i.e. negative stress) follows the undamaged modulus while the elastic regime in the tension regime (i.e. positive stress) follows the damaged modulus. The results of the SE verification test for both the monotonic and cyclic loading cases as well as with deformation and damage and without damage included in the input are shown in Fig. 73.

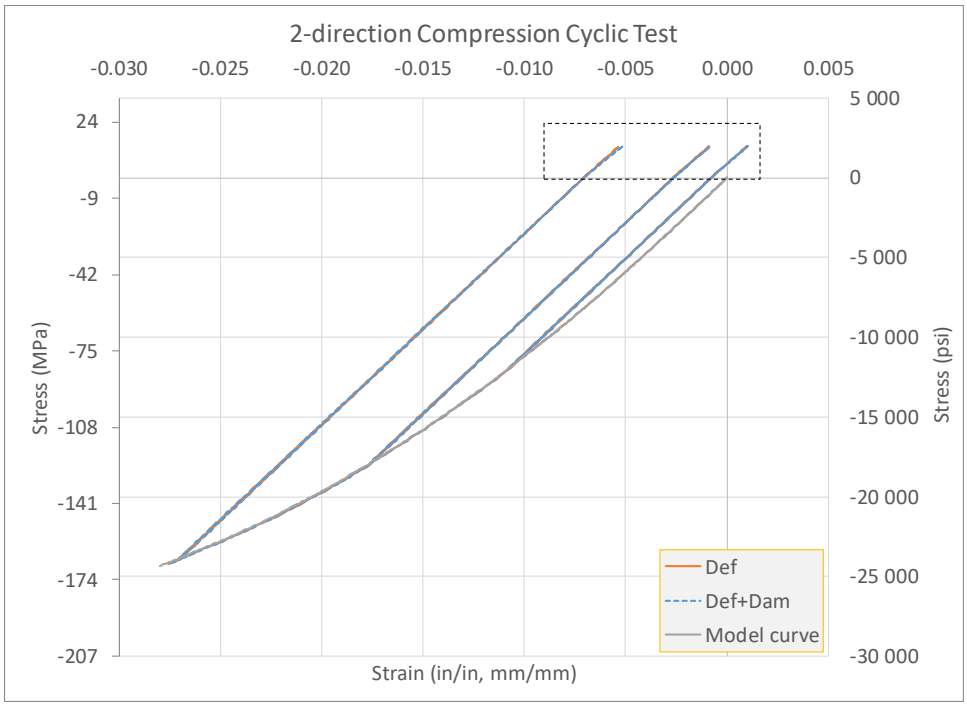

(a)

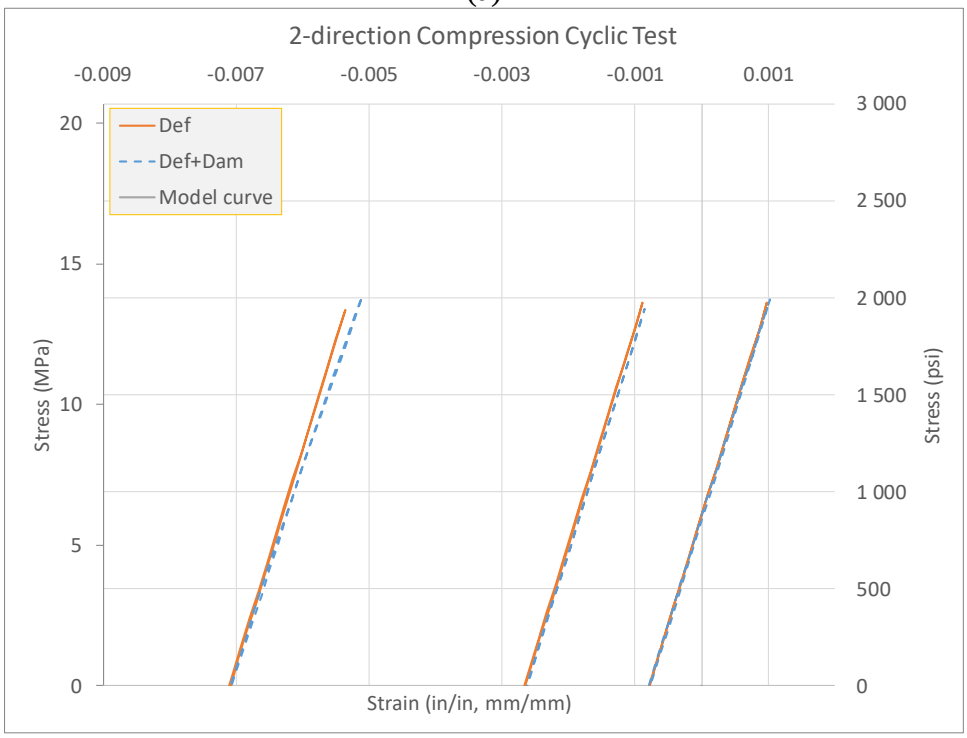

(b)

Fig. 73. Coupled Damage SE Verification Test Results (a) Full Stress-Strain Response with Dashed Lines Around Close-up Regime and (b) Close-up Tension Regime

Fig. 73 shows a clear reduction in the elastic tension stiffness as the plastic strain in compression increases. The difference in the elastic stiffness is small but consistent with the input data shown in Fig. 66. A second verification test was performed under displacement control to illustrate how coupled damage affects the yield surface. While the compression yield stress remains unchanged between the two simulations, the tension yield stress is expected to show softening when the coupled damage term is included. Fig. 74 shows the results of the verification tests with Fig. 75 showing a close-up of the tension regime.

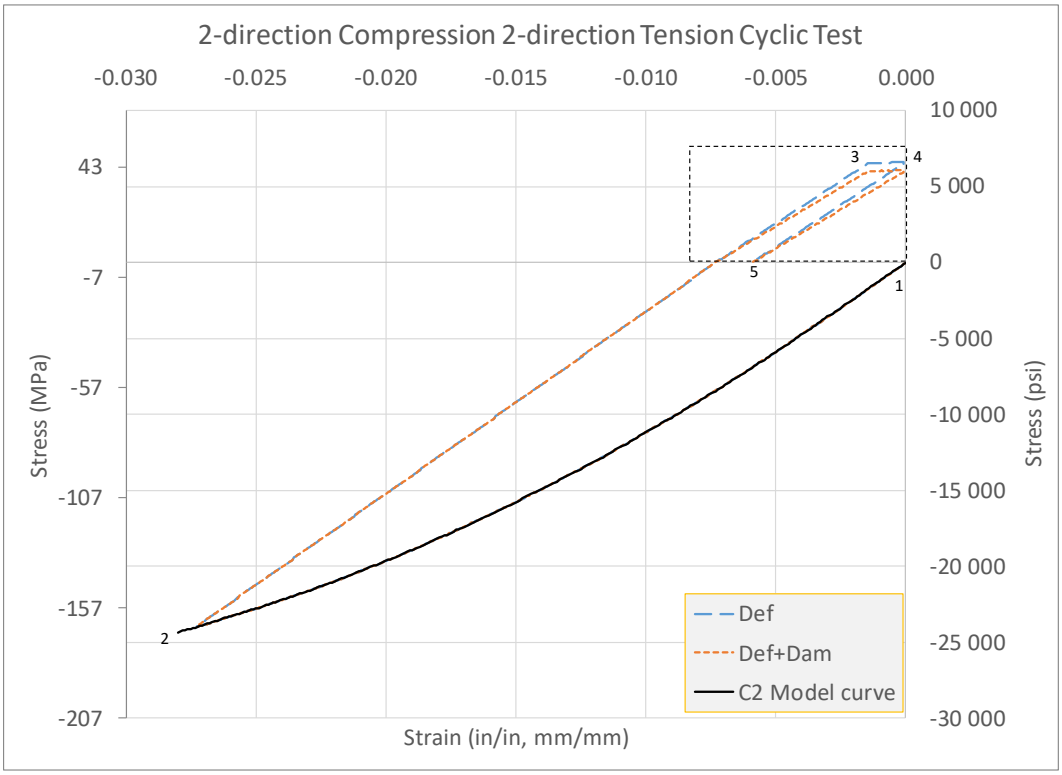

Fig. 74. Stress-Strain Responses of the Simulations. Loading Goes in the Following Order 1 → 2 → 3 → 4 → 5

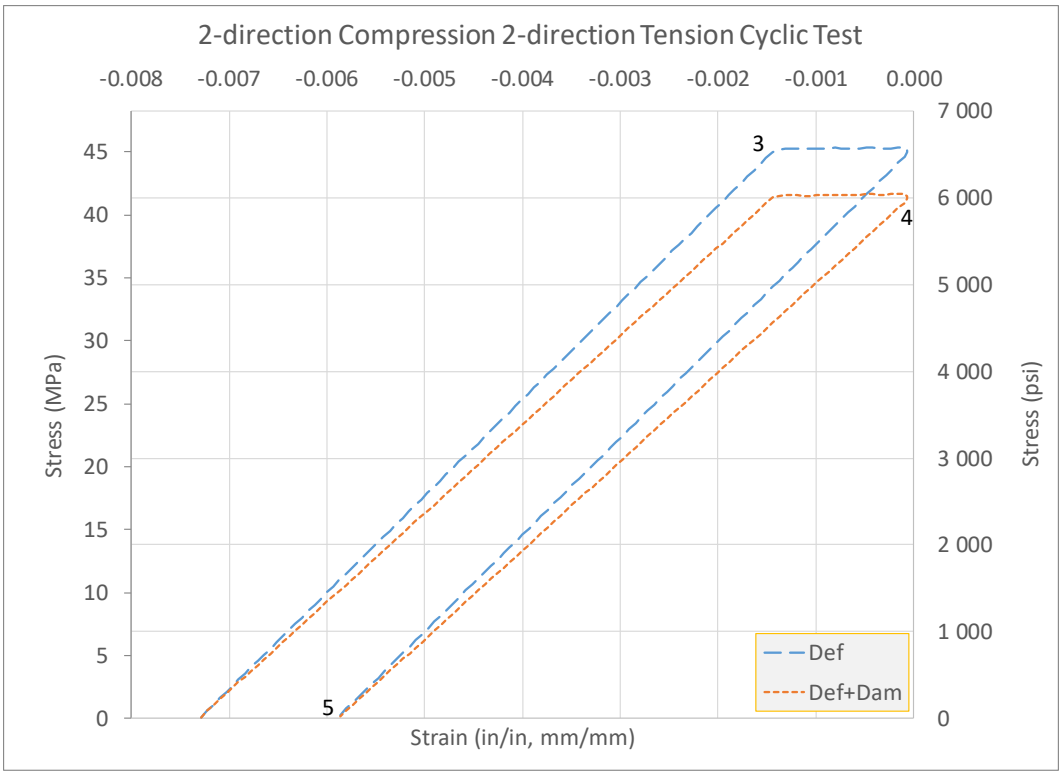

Fig. 75. Close-up of tension regime of the full stress-strain curve shown in Fig. 74

The results shown in Fig. 74 and Fig. 75 indicate that there is inherent softening of the material when coupled damage is included. The percent reduction in the yield value is equivalent to the percent reduction in the stiffness. This is to be expected since the 2-direction tension input curve does not account for coupled damage during the preprocessing step where the curves are converted from true stress to effective stress space. Only uncoupled damage terms are used in the initial conversion since, during the actual monotonic loading experiment, only uncoupled damage is being induced in the specimen. Thus, the 2-direction tension yield surfaces for the deformation only simulation and the deformation and coupled damage simulation are effectively the same. However, during the when the stress is converted from effective stress space to true stress space at the end of

the plasticity algorithm, the coupled damage parameter is used resulting in a reduction of the observed yield stress. Finally, during the unloading from point 4 to 5 in Fig. 75, the paths converge to the same strain value indicating that the strain equivalence assumption holds true.

3.5.3 Comparison of Stress-Based Implementation with Strain-Based Implementation

As mentioned in the introductory portion of this chapter, damage implementation, in the course of the research work has gone through multiple evolutions. The motivating factor is the desire to appropriately capture the damage evolution within the material without being over-conservative. During verification testing of the implementation using directional plastic strain $\left(\varepsilon_{ij}^{p}\right)$ as the tracking variable, the results when coupled damage parameters were included were conservative. Fig. 76 shows a test case wherein the effect of including $d_{33_r}^{22_C}\left(\varepsilon_{33_T}^{t}\right)$ on a monotonic 2-direction compression curve is illustrated using the directional plastic strain implementation. The SE finite element model used for the investigative simulation is shown in Fig. 71a.

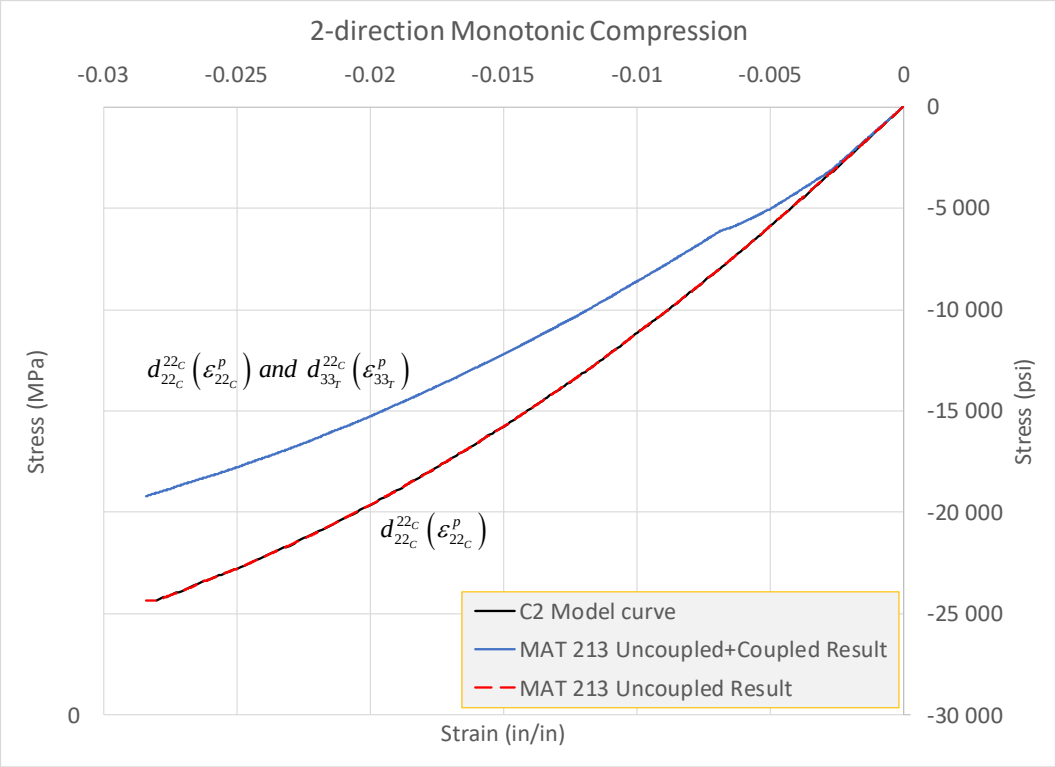

Fig. 76. Effect of Coupled Damage Parameters on Monotonic Loading Using Strain-based Damage Implementation

Fig. 76 shows that when only $d_{22_C}^{22_C}\left(\varepsilon_{22_C}^{t}\right)$ is used as input, the result from the simulation lies directly on top of the 2-direction compression input curve. However, when $d_{33_T}^{22_C}\left(\varepsilon_{33_T}^{t}\right)$ is also included, simulation under predicts the stress in the material. This occurs since the plastic potential function allows for growth of ε_{33}^{p} even when σ_{33} is zero. The coupled damage parameter, $d_{33_T}^{22_C}\left(\varepsilon_{33_T}^{t}\right)$, is then erroneously excited. As shown in Section 3.4, all the experiments were performed under uniaxial stress (not uniaxial strain) conditions. Thus all damage in an uncoupled test, should be attributed directly to stresses in the direction of

loading. The same simulation is performed using the implementation wherein directional effective stress $\left(\sigma_{ij}^{eff}\right)$ is the tracking variable and the results are presented in Fig. 77.

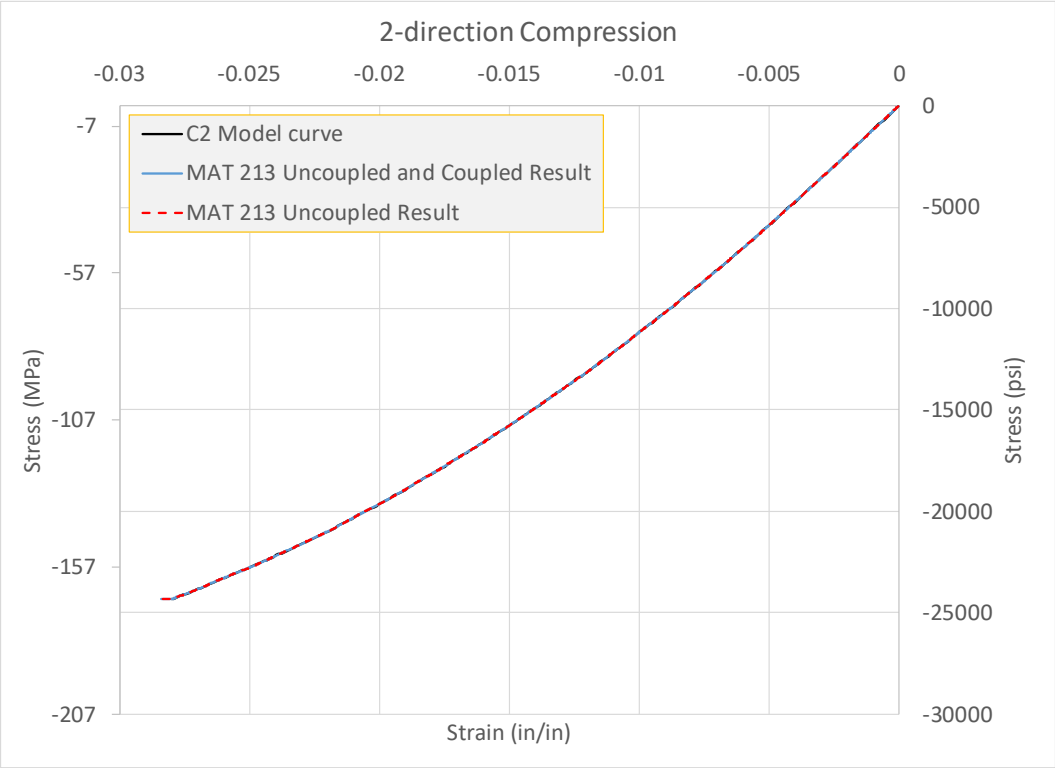

Fig. 77. Effect of Coupled Damage Parameters on Monotonic Loading Stress-based Damage Implementation

The results shown in Fig. 77 show that when both uncoupled and coupled damage are included in the simulation, the response lies on top of the input stress-strain curve, which is the expected outcome.

4 COHESIVE ZONE MODELING

Within OEPDMM, there are currently no provisions for handling interlaminar failure. This is by design since the OEPDMM is a material model for composite lamina and not for the interlaminar zone in a composite laminate. However, using MAT 213 in conjunction with cohesive zone modeling (CZM) helps in building the representative finite element models. The additional modeling comes in the form of using connective elements, called cohesive zone elements (CZE), between composite parts within the finite element model. The CZE essentially act as nonlinear springs. The properties of the CZE are in the form of traction separation laws (TSL) which describe the tractions that develop as a function of deformation in the element. Separate TSL are defined for both Mode I and Mode II fracture behavior with an analytical interaction law describing the mixed behavior. This section provides experimental details, including methodologies and results, used in deriving arbitrarily shaped TSL, using the T800S/F3900 carbon fiber/epoxy resin unidirectional composite system. Additionally, verification tests are performed showing how the derived TSL perform in a finite element environment.

4.1 Experimental Methods

Both Mode I (normal separation) and Mode II (axial shear) fracture behavior can be captured using cohesive zone models. The required fracture properties can be determined from the double cantilever beam (DCB) and end-notched flexure (ENF) tests since they have been shown to induce pure Mode I and Mode II states respectively (Gillespie Jr. et al. 1986b) and the data can be used to generate the two distinct traction-separation laws (TSL).

In the current work, the DCB and ENF experiments were performed in accordance with ASTM standards (D30 Committee 2013b, 2014), respectively. The test coupons were made from composite panels comprised of 24 unidirectional plies of the same fiber orientation. A Teflon film was inserted at the midplane of the panels during the curing process to generate an initial crack in the system. Fig. 78 shows one of the composite panels after the specimens were machined from it.

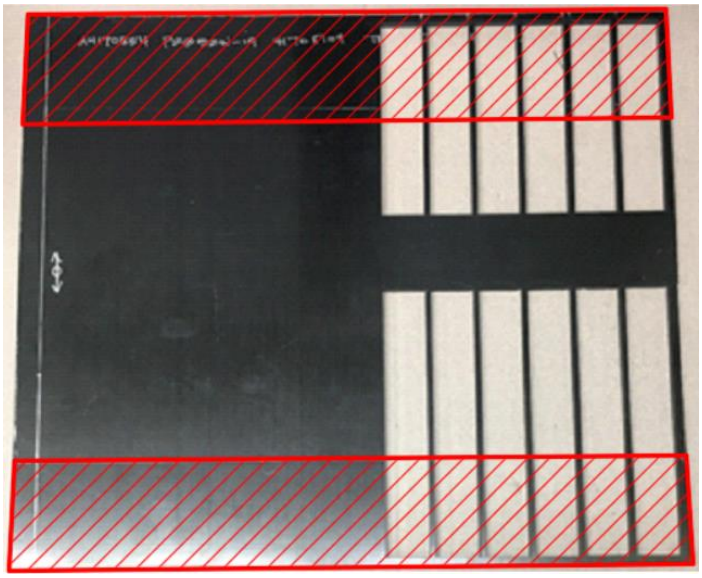

Fig. 78. T800/F3900 Composite Panel Used to Generate Test Coupons (Hatched Area Shows Where the Teflon Film Was Placed)

The experiments were performed under quasi-static displacement-controlled conditions. The test frame stroke rates were set to approximately 1.2 mm/min (0.05 in/min) and 0.6 mm/min (0.025 in/min) in the DCB and ENF experiments, respectively. The force values were recorded during the experiments using the test frame load cell. Two-dimensional

digital image correlation (DIC) was used to monitor full displacement fields of the specimens, including the region near the crack tip.

One camera was used to monitor the displacements in the locale of the crack tip and another monitored the entire specimen during the experiment to ensure that the experiment was being conducted correctly. Optical techniques, such as DIC, have been used by other researchers in monitoring crack behavior to characterize the fracture process, including TSL (Blaysat et al. 2015; Fernandes and Campilho 2017; Reiner et al. 2017; Shen and Paulino 2011; Yoneyama et al. 2006). Force data recorded from the load cell in conjunction with the displacement data recorded from DIC comprise the entirety of the data needed to generate the TSL.

In accordance with the relevant ASTM standards, a pre-cracking procedure was performed for both the DCB and ENF specimens. Pre-cracking is necessary since, during the manufacturing process, a resin rich zone develops near the edge of the Teflon insert which may lead to erroneous results. The DCB specimen was pre-cracked by loading the specimen in Mode I until the crack tip propagated approximately 5 mm (0.2 in). Similarly, the ENF specimens were loaded in Mode II until the crack tip propagated approximately 5 mm (0.2 in). Additionally, a compliance calibration, the details of which are presented later, was performed on the ENF specimens in accordance with ASTM D7905/D7905M–14 (D30 Committee 2014). This was done to determine the compliance of the specimen as a function of the initial crack length. This procedure was performed on both non-pre-

cracked and pre-cracked ENF specimens. Fig. 79 shows schematics of the DCB and ENF experiments.

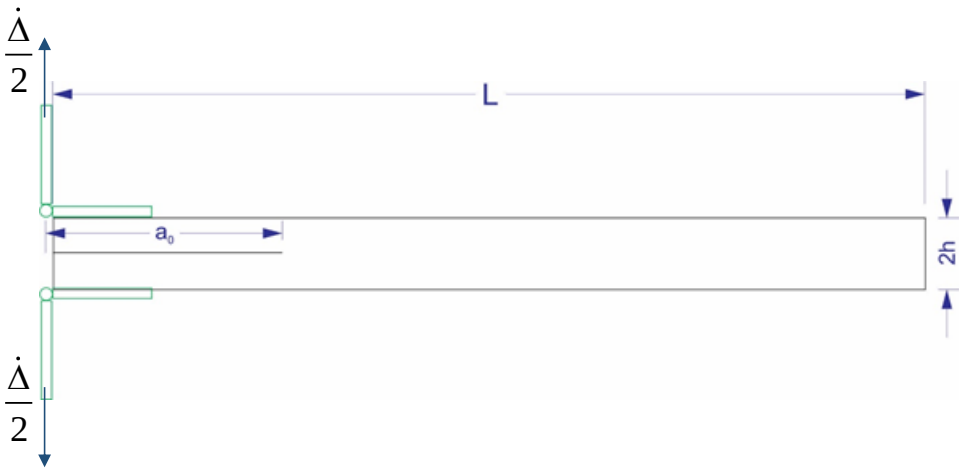

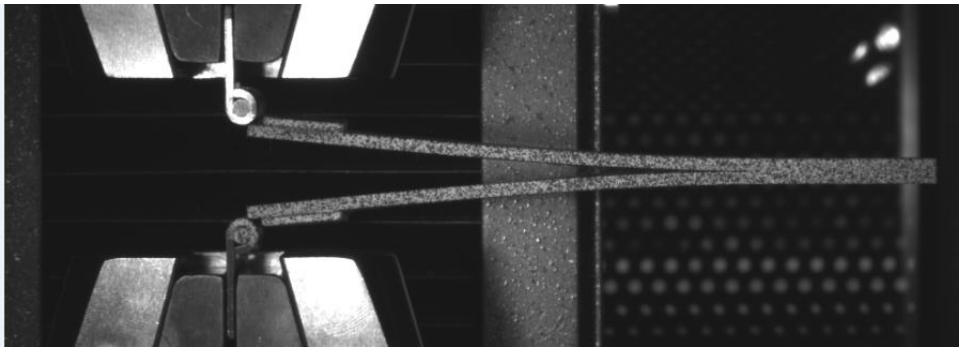

(a)

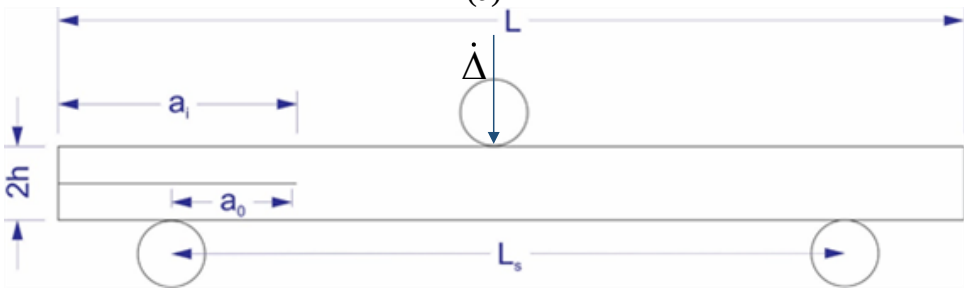

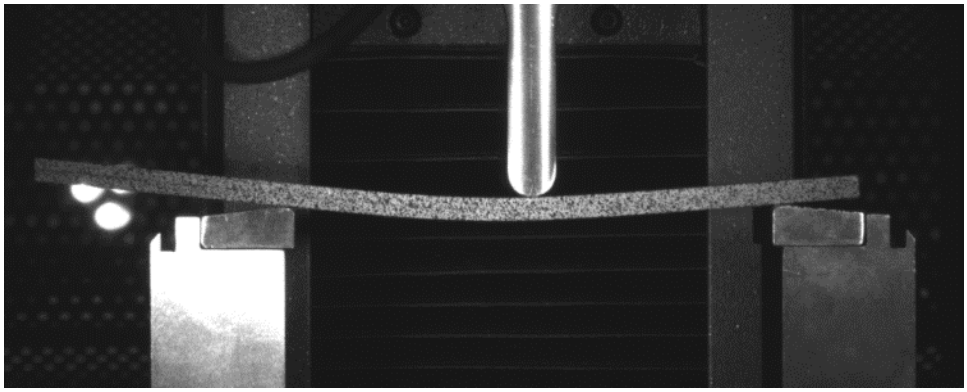

(b)

Fig. 79. Schematics of the (a) DCB and (b) ENF Experiments

Fig. 79a shows piano hinges that were used to induce Mode I loading in the DCB experiments and Fig. 79b shows a standard three-point bend fixture used to induce Mode II loading in the ENF experiments. The stainless-steel piano hinges were bonded to the composite test coupons using 3M-DP420 two-part toughened epoxy. Each surface was roughened with sand paper and cleaned with isopropyl alcohol to ensure a proper bond. In the DCB experiment, the crack length is defined as the perpendicular distance from where the load is being applied to the crack tip, while in the ENF experiment, the crack length is defined as the distance from the support to the crack tip, labeled as a_0 in Fig. 79b. In both the DCB and ENF experiments, the crack lengths were taken as recommended by the respective ASTM standards. During the compliance calibration for the ENF specimens, the free span of the specimen, L_s, was held constant. The effect of different crack lengths on the elastic compliance was measured by sliding the specimen along the supports rather than changing the position of the supporting fixture, i.e. the span was held constant to examine the change in compliance as a function of only the crack length. Since the distance from the edge of the specimen to the crack tip was different in the non-pre-cracked and pre-

cracked tests, the spans used in the two experiments were different. The location of the crack tips in the pre-cracked specimens were visually determined from DIC analysis.

4.2 Experimental Results

The results and data reduction techniques of both the DCB and ENF experiments are discussed in this section.

4.2.1 Double Cantilever Beam Tests

Table 15 shows the average dimensions of the pre-cracked DCB specimens (or, replicates). Note that *b* is the width of the specimen.

Table 15. Dimensions of Pre-cracked DCB Replicates

Replicate	**a_0 (mm, in)**	**h (mm, in)**	**b (mm, in)**	**L (mm, in)**
1	72.6, 2.86	2.39, 0.094	25.7, 1.01	126.7, 4.99
2	67.1, 2.64	2.39, 0.094	25.4, 1.00	127.0, 5.00
3	73.7, 2.90	2.36, 0.093	25.4, 1.00	126.7, 4.99

Fig. 80 shows the load-displacement results, measured at the load line (location where the load is applied), for three replicates of the pre-cracked DCB tests.

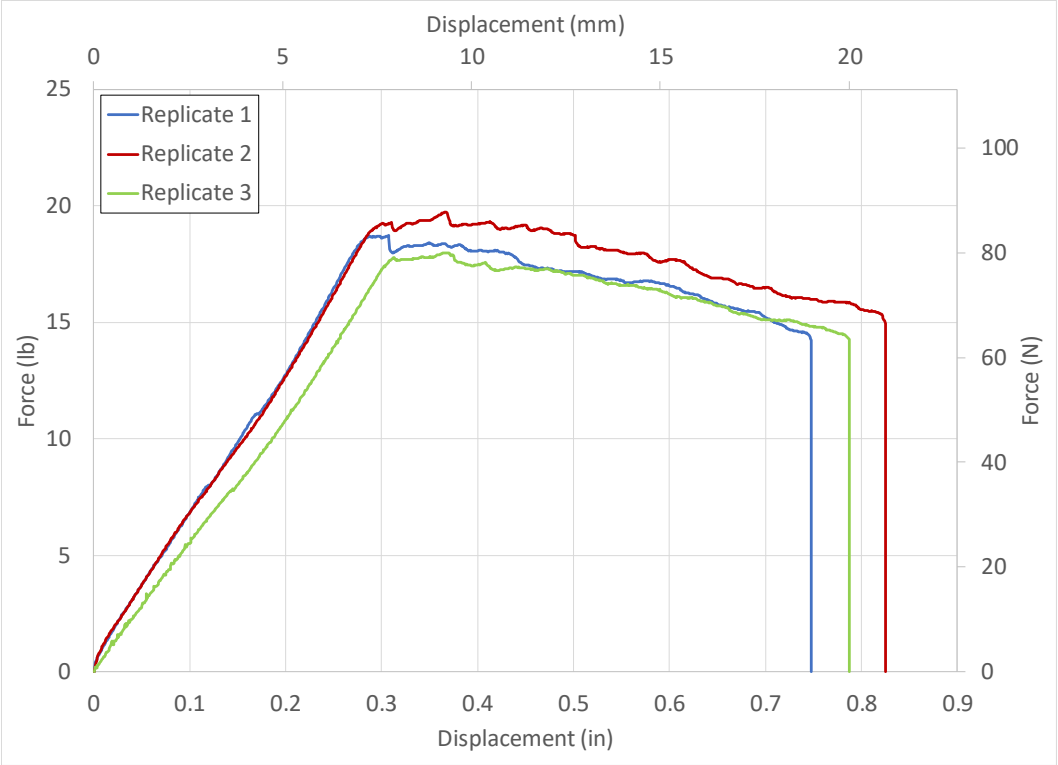

Fig. 80. Load-Displacement Curves from Three Replicates of the Pre-cracked DCB Experiment

DIC was used to compute the normal crack tip opening displacement. Fig. 81 shows the points above and below the crack tip used in computing the separation of the crack tip. The total separation is taken as the difference in the vertical displacement between two point-pairs at the same location along the length of the specimen, and multiple point pairs were used along the specimen length to track the opening as the crack propagated through the specimen. The additional point pairs were used as an aid in determining when the crack tip had reached that location by comparing the crack tip opening displacement (CTOD) at the points along the length with the CTOD of the initial crack at initiation of crack propagation.

Fiber-bridging can be observed in Fig. 81. As shown later, this manifests as an apparent toughening of the material as the crack length increases.

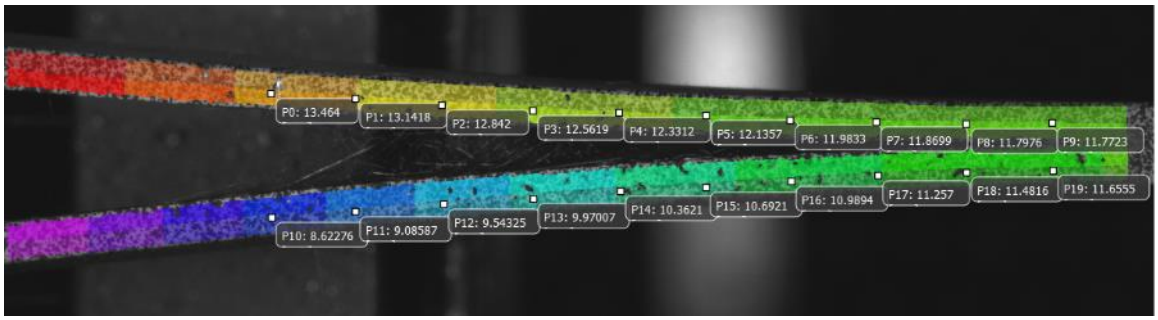

Fig. 81. Analysis Points Used for DIC Analysis of Crack Tip Separation in DCB Test

The Mode I energy release rate, G_I, can be computed using various methods. Based on the results of the testing required for the deformation sub-model, the composite exhibited linear elastic behavior when loading the material in tension through the thickness up until the peak load, and hence the material was assumed to conform to LEFM assumptions (Fig. 24c). Other authors (Andrews and Massabò 2007; Högberg et al. 2007; Rajan et al. 2018; Thouless 2018) have derived expressions for the *J* integral (Rice 1968) around the crack tip during a DCB experiment and used the results as the energy release rate when attempting to account for various aspects of the experiments (i.e. crack tip rotations, shear deformation, small scale yielding) that the ASTM standard does not include in subsequent analyses. The standard compliance method was used to compute the energy release rate as

$$G = \frac{P^2}{2b}\frac{\partial C(a)}{\partial a} \tag{4.1}$$

where $C(a)$ is the compliance of the specimen at a crack length a. The compliance method was compared with the method proposed by Högberg and co-workers (Högberg et al. 2007) and Thouless (2018), respectively, and the three methods showed little difference in the resulting energy values. Since no unloading cycles were performed, the compliance was taken as the ratio of displacement to load for a given time instance. An exponential function of the form shown in Eq. 4.2 was used to fit the experimental data to generate $C(a)$ as

$$C(a) = r_1 e^{r_2 a} + r_3 e^{r_4 a} \tag{4.2}$$

This method partially accounts for the rotation of the crack tip. Fig. 82 shows the plots of compliance against crack length along with the associated least squares regression equation.

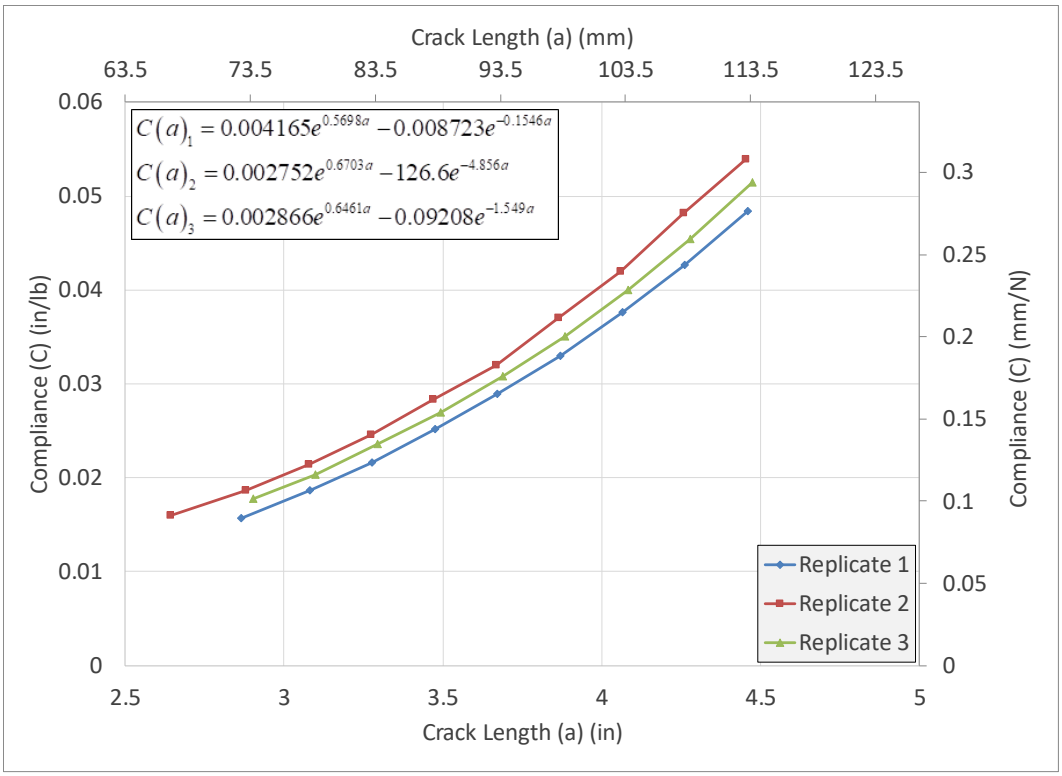

Fig. 82. Compliance vs Crack Length for Three Replicates of the DCB Experiment. Equations Shown Derived from Regression Analysis Using USCS Units

Using Eq. 4.1 along with the equations shown in Fig. 82 and the normal crack tip separation, δ_n obtained from DIC at the initial crack tip location, the $G-\delta_n$ plots were generated as shown in Fig. 83.

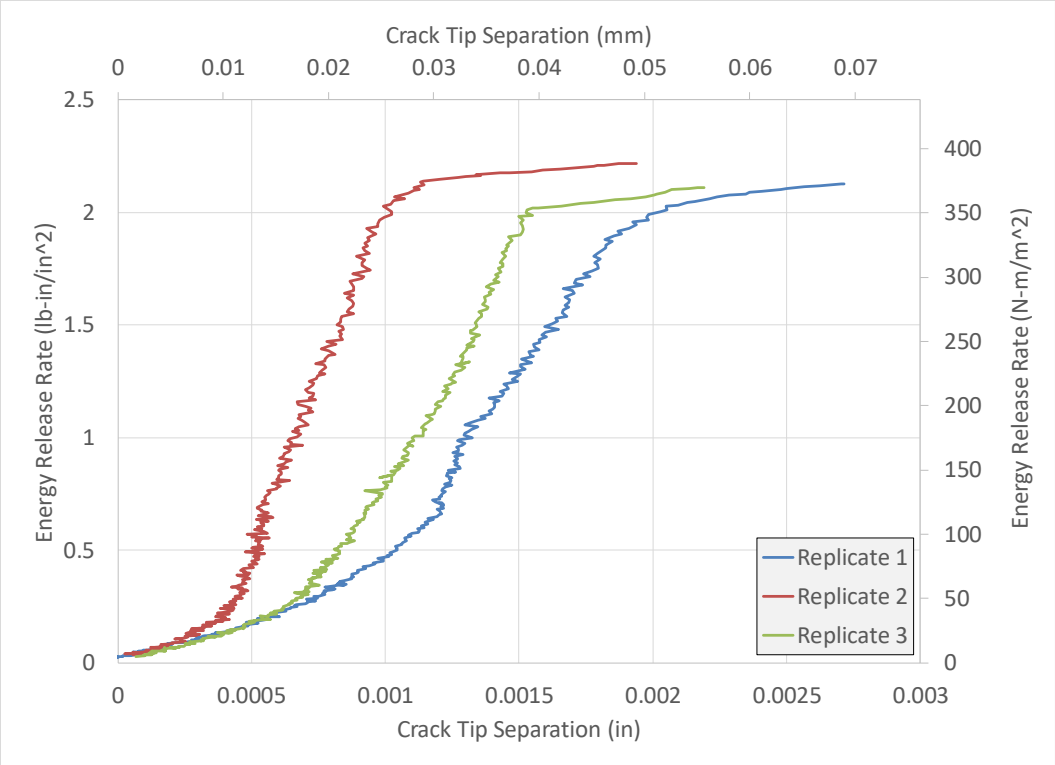

Fig. 83. $G-\delta_n$ Plots for Three Replicates of the DCB Experiment

The $G-\delta_n$ plots end when initiation of crack propagation takes place, determined to be when the softening in Fig. 80 begins. When making assumptions of linear elasticity under monotonic loading, the *J* integral is equivalent to the energy release rate, and can be written in terms of the work done by the tractions at the crack tip as

$$J_I = G_I = \int_0^{\delta} \sigma(\delta)\, d\delta \tag{4.3}$$

Differentiating Eq. 4.3 with respect to the crack tip separation, δ, gives rise to

$$\sigma(\delta) = \frac{\partial J}{\partial \delta} \tag{4.4}$$

Using the surface tractions estimated from Eq. 4.4 and the data shown in Fig. 83, the TSL curves were generated as shown in Fig. 84. As stated earlier, the term *model curve* is used to denote the curve used in the subsequent (deterministic) finite element simulations and is computed as the average response from the three replicates.

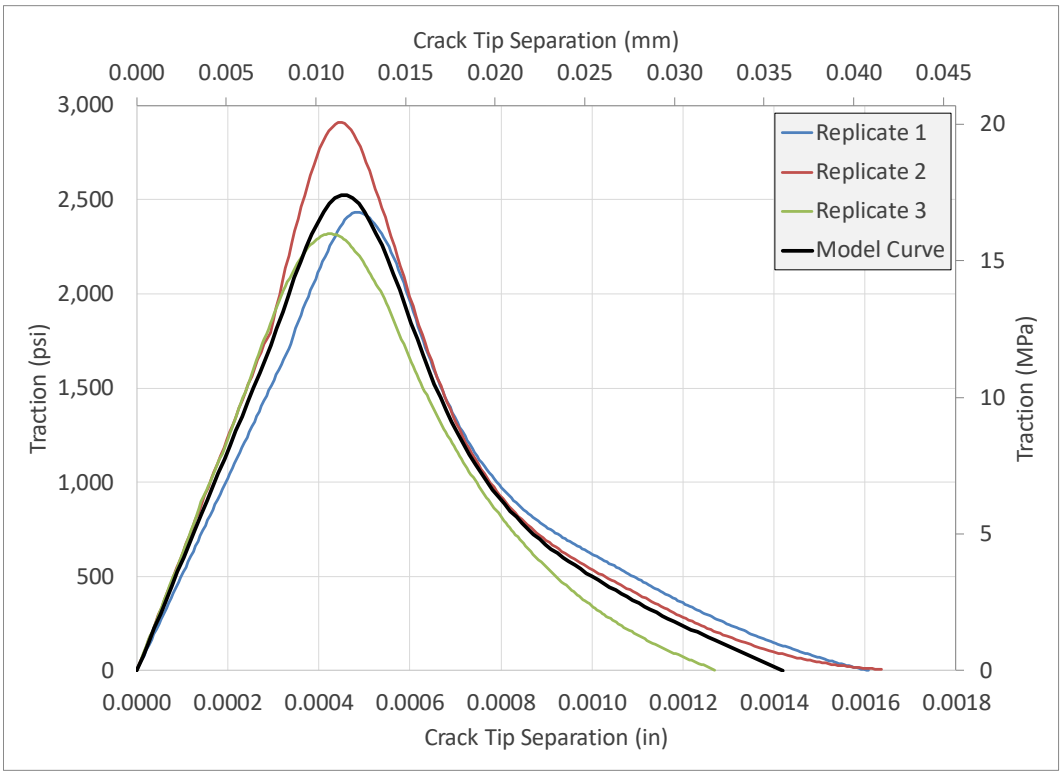

Fig. 84. Experimentally Obtained TSL from Three Replicates of the DCB Experiment

It should be noted that both the DIC and load data were smoothened using the robust locally estimated scatterplot smoothing (rloess) algorithm available in MATLAB (*MATLAB and Statistics Toolbox* 2018) prior to computing the derivative since the numerical derivative

of the curves shown in Fig. 83 was sensitive to the amount of noise in the experimental data.

4.2.2 End Notched Flexure Test

The process used to generate the TSL for the Mode II behavior was similar to that used for Mode I. Table 16 shows the specimen dimensions for multiple replicates of the pre-cracked ENF test.

Table 16. Dimensions of Pre-cracked ENF Replicates

Replicate	**a_0 (mm, in)**	**h (mm, in)**	**b (mm, in)**	**Ls (mm, in)**
1	30.0, 1.18	2.39, 0.094	25.7, 1.01	100.1, 3.94
2	30.0, 1.18	2.39, 0.094	25.7, 1.01	100.1, 3.94
3	30.0, 1.18	2.36, 0.093	25.7, 1.01	100.1, 3.94

All replicates had the same initial crack length of 30 mm (1.18 in). The analysis shown in subsequent sections utilizes this initial crack length as per the ASTM recommendation. Fig. 85 shows the load-displacement results of the pre-cracked ENF tests at the load line.

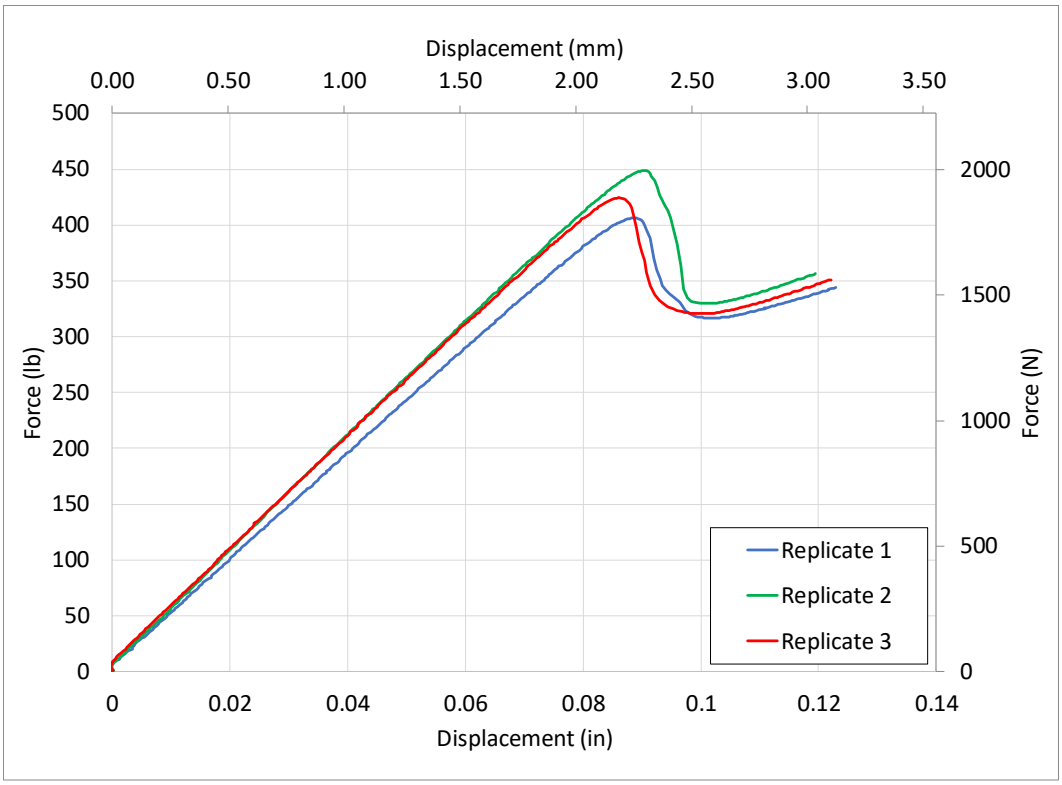

Fig. 85. Load Displacement Curves from Three Replicates of the Pre-cracked ENF Experiment

As with DCB experiments, DIC was used to compute the shear crack tip displacement throughout the experiment. Fig. 86 shows the points above and below the original crack tip used in computing the shear displacement of the crack tip. The total separation is taken as the difference in the horizontal displacement between the two points since the rotations computed by DIC were small, i.e. $\tan\theta \approx \theta$. The crack tip location in the pre-cracked experiment was determined from the compliance calibration performed on the non-pre-cracked specimens. The compliance calibration yielded a relationship between compliance and crack length for the given span. Upon unloading during the initial pre-cracking, the compliance was measured, and the relationship was used to determine where the initial

crack tip was located for the pre-cracked procedure. Fig. 86 shows one of the specimens near the end of the experiment.

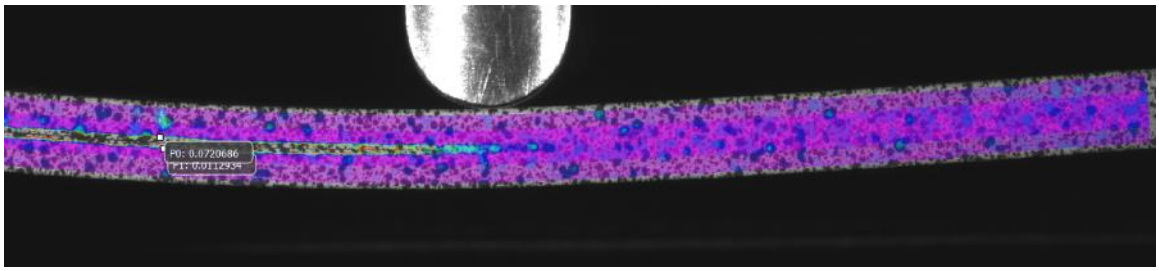

Fig. 86. The Two Analysis Points Used for DIC Analysis of Crack Tip Separation in ENF Test

The J-integral was computed using the closed form solution proposed by Leffler and co-workers (Leffler et al. 2007) as

$$J_{II} = \frac{9}{16}\frac{P^2 a^2}{Eb^2 h^3} + \frac{3}{8}\frac{P\delta_t}{bh} \tag{4.5}$$

where E is the Young's modulus of the material along the axis of bending and δ_t is the shear displacement at the crack tip. The J-integral expression shown in Eq. 4.5 was used to compute the crack driving force instead of the traditional compliance calibration method since during shear experiments in the 1-3 plane, nonlinear behavior was observed implying that the assumptions used in LEFM would likely not be applicable (Fig. 33c). The solution proposed by Leffler and co-workers is intended for adhesive joints with isotropic adherends. The values obtained from Eq. 4.5 were compared with the standard compliance

method recommended by the ASTM (D30 Committee 2014) and with a solution proposed by Zhao and co-workers (Zhao et al. 2016) specifically for composites. The energies predicted by Eq. 4.5 were higher than those predicted by the ASTM by approximately 20%. However, the results were consistent with the solution proposed by Zhao and co-workers. The *J*-integral was used along with the shear displacement measurements, at the initial crack tip location, from the DIC analysis to generate the Mode II TSL using Eq. 4.3 and Eq. 4.4. The plots of $J-\delta_t$ are shown in Fig. 87.

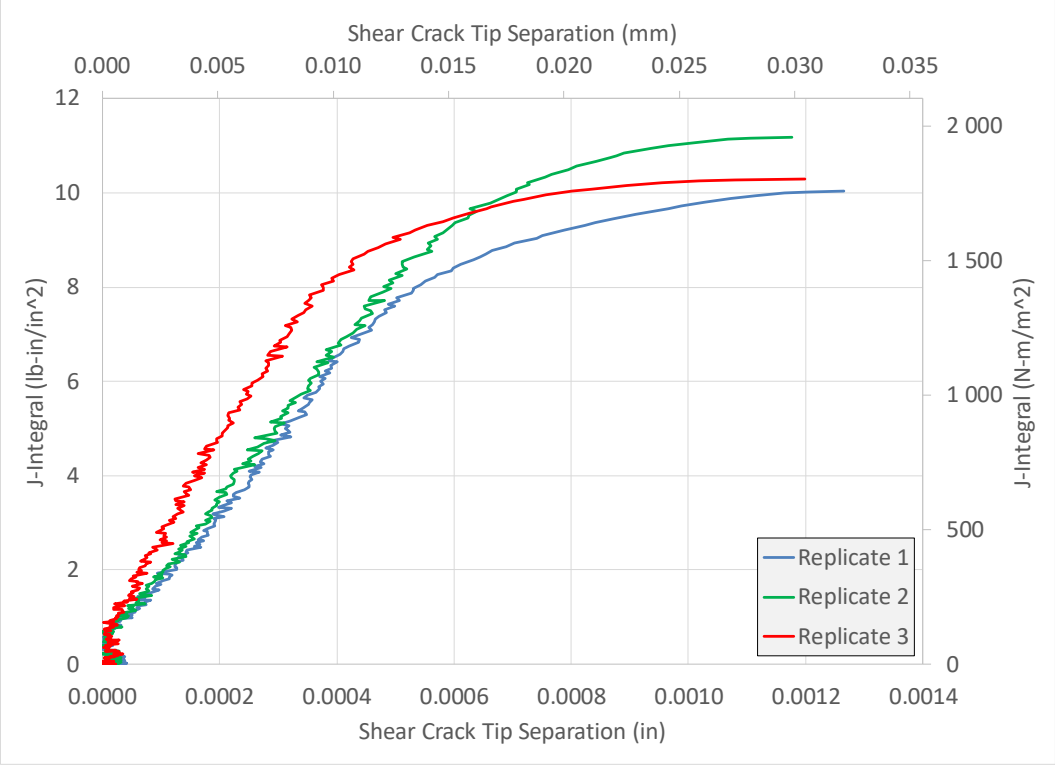

Fig. 87. $J-\delta_t$ Plots for Three Replicates of the ENF Experiment

The data in Fig. 85 shows that there is a small nonlinear regime after the peak load is reached. Thus, the peak load was not used to determine when the crack began to propagate.

Rather, the point where the load suddenly drops was taken instead and the maximum value of J_{II} in Fig. 88 corresponds to that point. The point where the load suddenly drops is approximately where the J-integral reaches its peak value and then plateaus indicating that the tractions have become zero. Eq. 4.4 was used with the data in Fig. 87 to estimate the tractions at the crack tip providing the TSL data (Fig. 88).

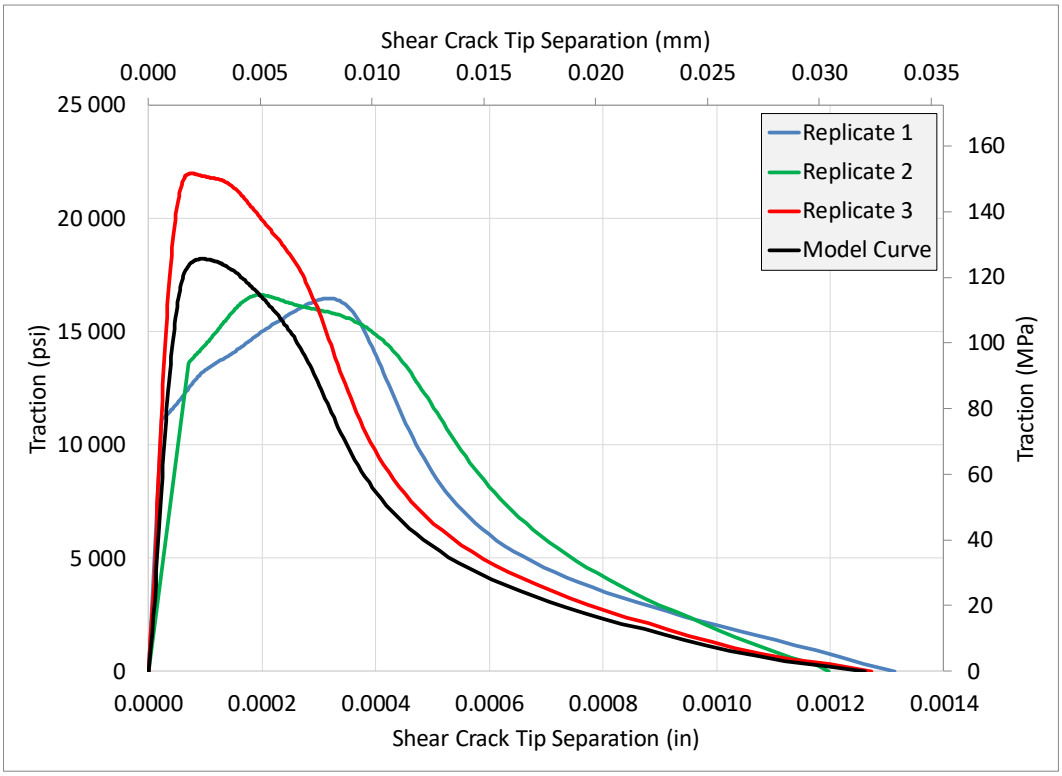

Fig. 88. Experimentally Obtained TSL from Three Replicates of the ENF Experiment

As before, the raw experimental data used to generate the TSL in Fig. 88 was smoothed to make it suitable for input into the FE simulation. The initial linear portion of each of the replicate TSL curves in Fig. 88 was estimated since, as the data in Fig. 87 shows, the value of the *J*-integral begins to increase without an increase in the crack tip separation. The

behavior may be attributed to a few sources with the most predominant factor being the inadequate spatial resolution in the DIC analysis. Each pixel represented approximately $2.54x10^{-4}$ mm (10^{-3} in) which may not have provided enough fidelity in the data to track the crack. The large (initial) slope may also be attributed to the effect of friction between the crack surfaces (Carlsson et al. 1986). The portion of the curves in Fig. 87 exhibiting extremely large slopes was ignored. A straight line was connected from the origin to the point in the TSL curves where the data began to appear to be reliable.

While the proposed approach of experimentally deriving the traction-separation shows promise, the proposed approach can be improved. Mixed-mode bending tests will yield parameters for the mixed mode fracture law yielding enhanced capabilities for modeling delamination. Using DIC to measure displacement and strain in the vicinity of discontinuities is a huge challenge. While there have been a few methods proposed to overcome the issue (Poissant and Barthelat 2010), the techniques haven't been thoroughly validated in the literature nor are they widely available in commercial software packages. Refining the techniques used in making measurements near discontinuities in a material will hopefully lead to higher fidelity data coming from tests like the DCB or ENF.

4.3 Numerical Verification

Both DCB and ENF models of the same dimensions as the experiments were built and analyzed using LS-DYNA to verify that the proposed TSL are appropriate. First, a convergence analysis and boundary condition study were performed to find the appropriate finite element (FE) model with a view to balancing compute time and accuracy. Three

element sizes were compared in both the DCB and ENF simulations: 2.54, 1.27, and 0.635 mm (0.1, 0.05, 0.025 in). The three DCB models had 1000 solid and 230 CZ elements, 8000 solid and 920 CZ elements, and 64000 solid and 3680 CZ elements, respectively. Similarly, the three ENF models had 1300 solid and 330 CZ elements, 10400 solid and 1320 CZ elements, and 83200 solid and 5280 CZ elements, respectively. The elements representing the composite material had an aspect ratio of unity while the cohesive zone elements had a thickness of approximately 2.54×10^{-4} mm (10^{-5} in). These element sizes were chosen since they are similar to the element sizes used in the impact validation simulation presented in Chapter 5 of this dissertation. The composite parts were modeled using LS-DYNA's MAT 213 with material properties presented in Chapter 2. A single layer of cohesive zone elements was used at the mid-plane of the model which spanned from the initial crack tip to the edge of the composite specimen. LS-DYNA's MAT 186 (LSTC 2017b) was used to model the cohesive zone elements using the TSL model curves shown in Fig. 84 and Fig. 88. MAT 186 allows for arbitrarily shaped normalized TSLs to be input and accounts for mixed-mode delamination using the Benzeggagh-Kenane law with mixed mode fracture law exponent set equal to 1.0 (Benzeggagh and Kenane 1996). Damping was utilized through the *DAMPING_GLOBAL keyword in LS-DYNA with *valdmp*, the system damping constant used as a multiplier on the force vector due to system damping, set equal to 638.5 (LSTC 2017a). The chosen value of *valdmp* is equivalent to twice the fundamental frequency of the structure which was obtained by performing a modal analysis in LS-DYNA on the final, converged FE models respectively. Both the DCB and ENF simulations used the same *valdmp* value. In all verification and validation simulations, the global energies – total energy ratio, sliding energy ratio, kinetic energy

ratio, internal energy ratio and damping energy ratio, were checked to ensure that the models were behaving properly (Deivanayagam et al. 2014). In the verification tests, the kinetic, damping, and sliding energies were significantly lower than the internal energy meaning the quasi-static behavior was being captured properly.

4.3.1 Double Cantilever Beam Test

In the DCB experiment, the FE model used 8-node fully integrated hexahedral solid elements where the initial direction of the fibers in all the elements was oriented in the global x-direction. An initial crack length of approximately 71.1 mm (2.8 in) was used since that was the average initial crack length of the pre-cracked DCB specimens in the experiments (Table 15). Additionally, the stainless-steel tabs were modeled using standard steel elastic material properties. Fig. 89 shows the finite element model with boundary conditions.

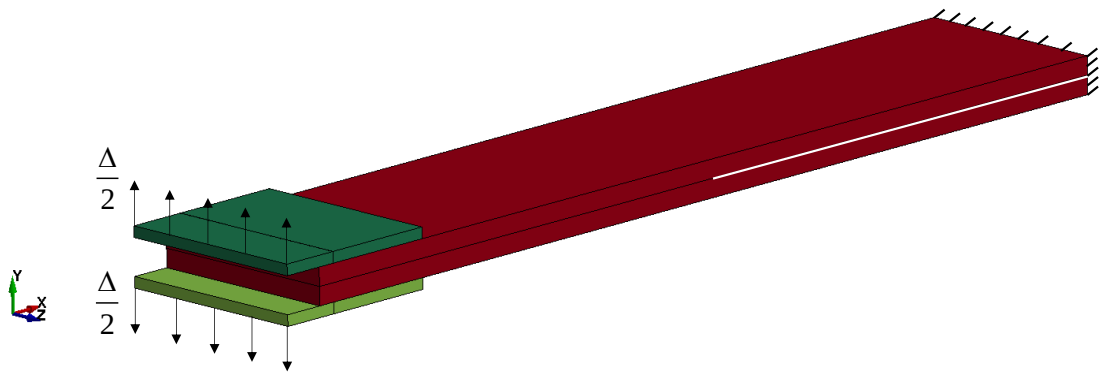

Fig. 89. FE Model of the DCB Specimen Showing Nodes on Steel Piano Hinges Where Displacement Is Prescribed in the Y-direction, Nodes on the Back Face Where All Translational Degrees of Freedom Are Restrained, and Highlighted Initial Location of Cohesive Zone Elements Across Entire Width of Specimen

Fig. 90 shows the results of the simulations compared with the experimental data.

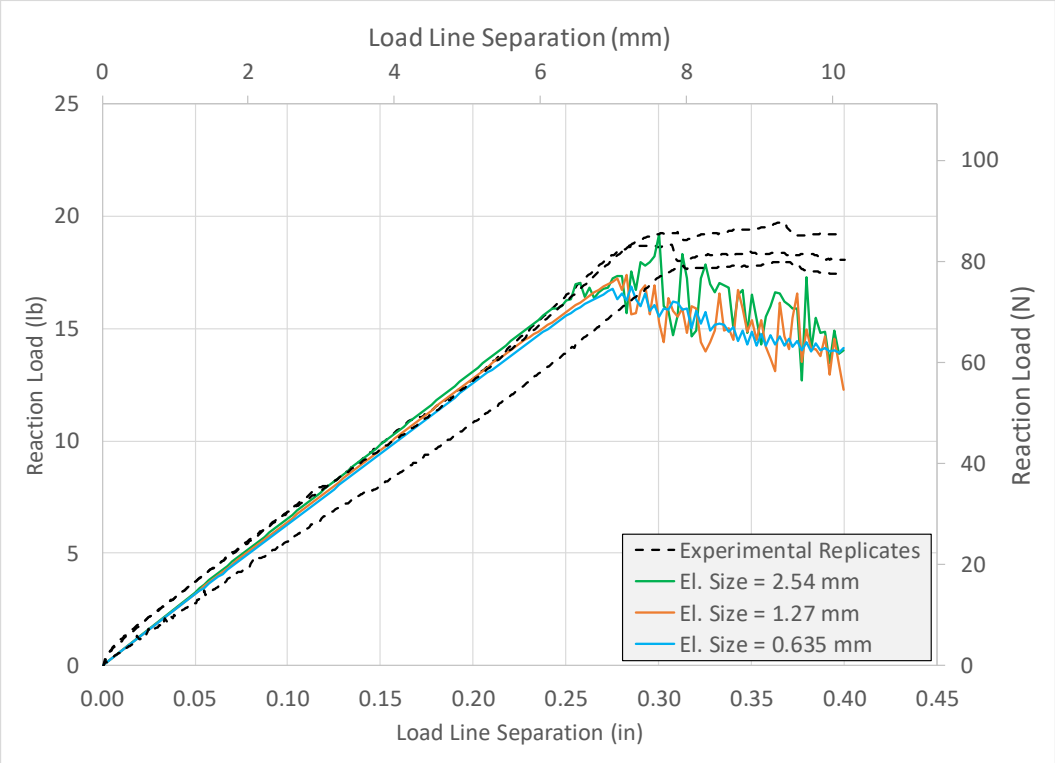

Fig. 90. DCB Simulation Results

The reaction load shown for the simulation was taken as the sum of the nodal reaction forces through the width of the top arm of the model (Fig. 89). Fig. 90 shows that the element size had a minor effect on the peak load predicted by the simulation. The differences between the FE simulation and experimental results can possibly be explained as follows. The peak load is under predicted by approximately 5%-10% across all three simulations. During a sensitivity analysis, the peak load was dictated by the peak traction and the critical energy release rate value used in the simulation. Fig. 84 shows a peak traction of approximately 17.2 MPa (2500 psi). Since the traction is computed directly from the data shown in Fig. 83, the method used in computing the energy release rate, the crack

tip separation, or a combination of both may have contributed to the difference. The source of error in the crack tip separation computations may be caused by various sources. First, the spatial resolution in the DIC analysis may not have been good enough causing improper computations of the displacement fields. Second, it has been shown experimentally and predicted by simulation that the crack front in a DCB specimen is not straight through the width where delamination begins (Jiang et al. 2014). Since the pre-cracking procedure propagates the initially straight manufactured crack by a small increment, the crack front is likely no longer straight and choosing where to measure the crack tip separation becomes difficult as the results are sensitive to even a small change (±0.012 in, ±0.5 mm) in the sampling location. Fig. 91 shows the delamination front over time predicted by the FE simulation suggesting that delamination does not take place evenly across the width, i.e. the pre-cracked DCB specimen's initial state was probably not modeled correctly.

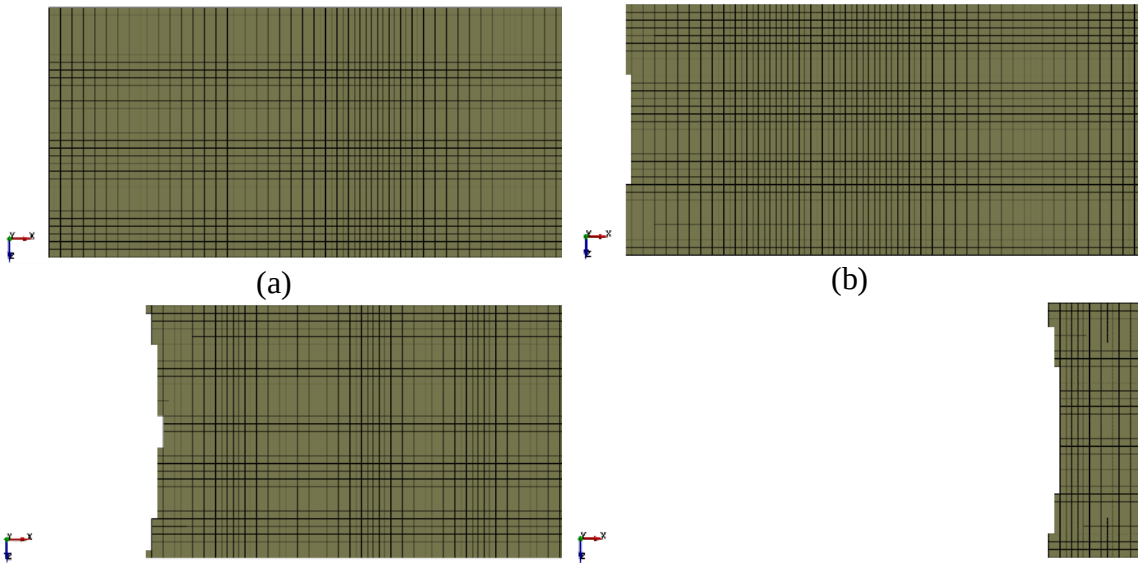

Fig. 91. Delamination Front Predicted by the Two Finer FE Models of DCB Experiment (a) t=0.0s, (b) t=0.055s (Onset of Delamination), (c) t=0.07s, and (d) t=0.15s (Termination of Simulation)

More advanced techniques, such as x-ray tomography, may need to be used to determine where the crack tip is located since visual observation through DIC leads to a high amount of subjectivity which may cause errors to propagate through the entire analysis.

In addition to the peak load being under predicted, post peak slope of the simulation also under predicts the experimental results. This was likely caused by fiber bridging (Fig. 81) causing an apparent increase in the critical energy release rate as the crack front propagated through the specimen. The cohesive zone modeling approach is the ideal way to handle such toughening behavior given that it is intended for nonlinear fracture processes. As previously mentioned, other researchers have employed techniques to overcome toughening behavior exhibited by fiber reinforced composites (Heidari-Rarani et al. 2013;

Li et al. 2005). However, the methodologies proposed by those researchers have deficiencies such as relying on numerical calibration or relying on superposition of assumed responses to account for the contribution of the composite constituents to the overall response. Part of the difficulty in deriving the traction-separation law, solely from experimental data, is in measuring the size fracture process zone using DIC since the technique assumes the material is a continuum and discontinuities may lead to erroneous strain measurements. The extent to which the bridging fibers away from the crack tip contribute to the apparent material toughness is a part of future work and should aid in refining the proposed technique. Using Eq. 4.1 and the compliance equations shown in Fig. 82, crack growth resistance curves (R-curves) were generated for each of the three replicates showing a rising trend (Fig. 92).

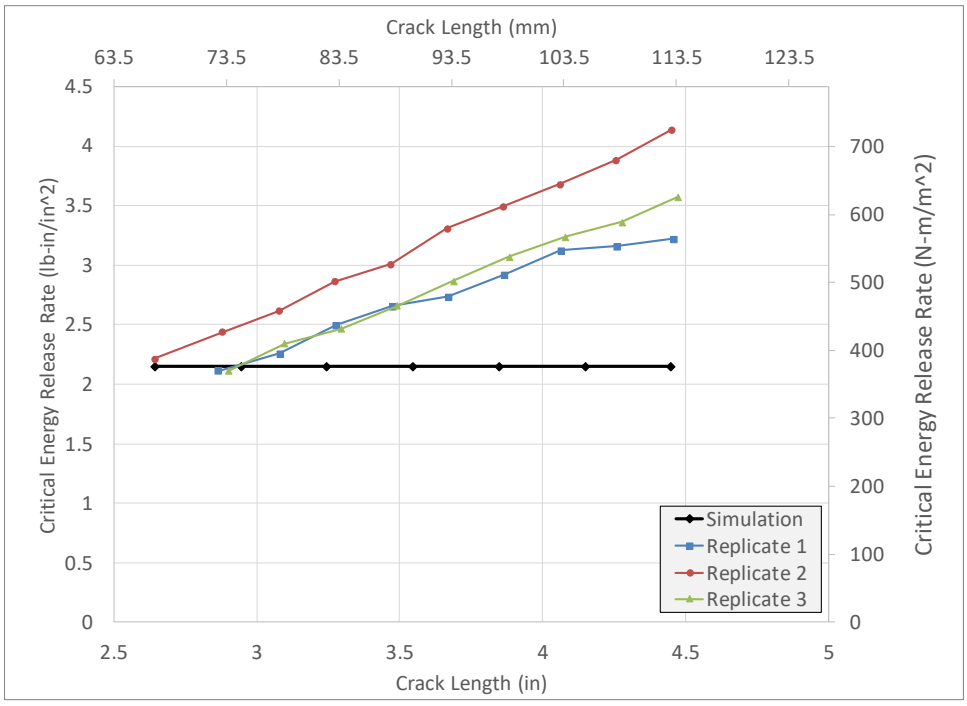

Fig. 92. R-curves for Three Replicates of the DCB Experiment Showing Rising Trend

The increase in crack growth resistance was not captured in the finite element simulation as all the cohesive zone elements along the length of the specimen were modeled using the same TSL shown in Fig. 84 thus underestimating the overall load carrying capacity of the specimen.

4.3.2 End-Notched Flexure Test

In the ENF experiment, the FE model used 8-node fully integrated hexahedral solid elements were used to model the composite parts where the initial direction of the fibers in all elements were oriented parallel to the free span of composite specimen. An initial crack length of approximately 30 mm (1.18 in) was used since that was the estimated initial crack length of the all pre-cracked ENF specimens in the experiments (Table 16). Fig. 93 shows the finite element model with support and loading fixtures that were modeled as rigid bodies with standard elastic properties of steel.

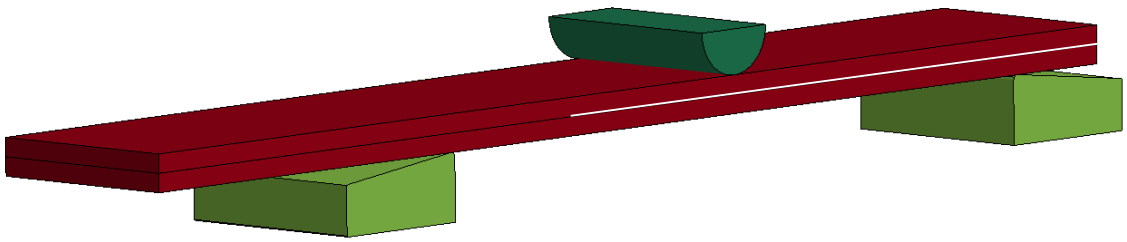

Fig. 93. FE Model of the ENF Specimen Including Support and Loading Fixtures and Highlighted Location of Cohesive Zone Elements

The two supporting fixtures were completely fixed from translation while the loading cylinder was fixed completely except a prescribed displacement rate in the vertical

direction. The *CONTACT_AUTOMATIC_SURFACE_TO_SURFACE definition was used to handle contact between the composite specimen and the support/loading components. A static and dynamic coefficient of friction of 0.1 was used between the composite and steel components (Naik et al. 2009). Fig. 94 shows the results of the simulations compared with the experimental data and shows the FE simulations under predict the average peak load observed in the experiments by approximately 2%-5%. Fig. 94 shows that the element size had a minor effect on the peak load predicted by the simulations. The general shape of the load-displacement curve is predicted well by the simulations including the nonlinear region after the peak load.

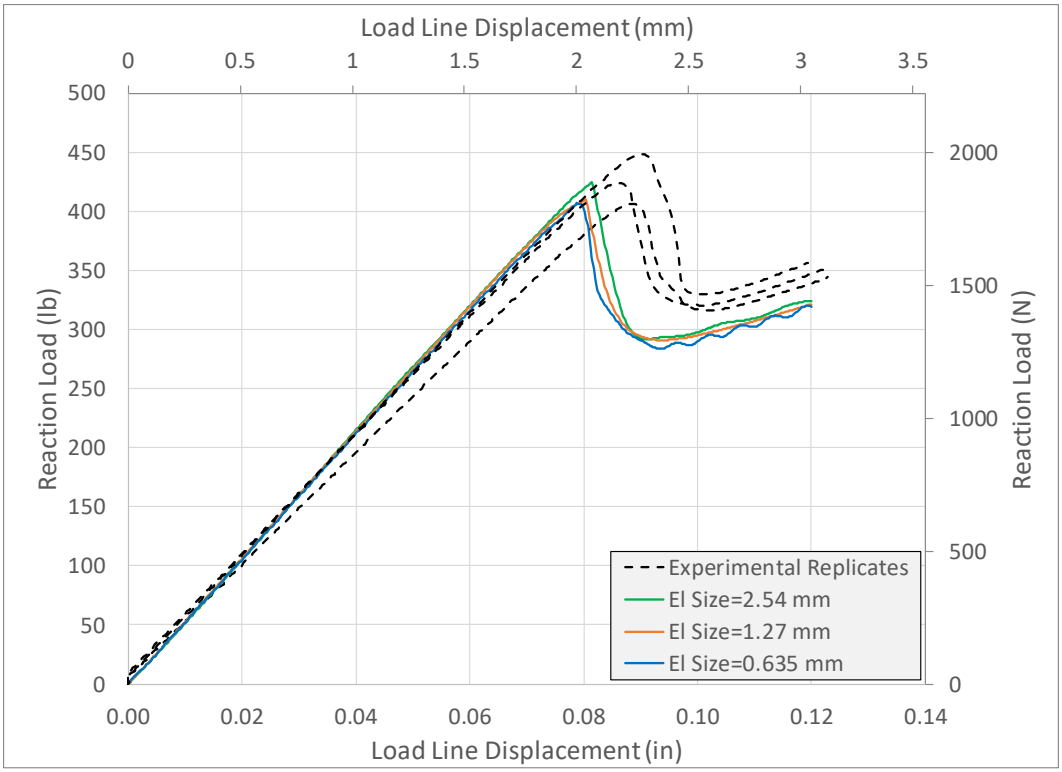

Fig. 94. ENF Simulation Results Using Experimentally Obtained TSL

It should be noted that typically, calibration the TSL would be performed to achieve a better match in the verification simulations and subsequently use the resulting values in the validation simulation. However, one of the goals of this research is to determine whether the original, experimental TSL can be used confidently in validation testing. Because of this, the unaltered *model curve* from Fig. 84 and Fig. 88 are used in impact validation simulations presented in the next chapter.

5 OEPDMM VALIDATION STUDY

Several impact validation simulations were performed with various combinations of the data derived in Chapters 2, 3, and 4. The first objective is to provide a study showing how the various input parameters in OEPDMM influence the simulation results. Several combinations of deformation, damage, and cohesive zone input were used and compared. The second objective is to highlight the efficacy of the developed tabulated plasticity-damage approach. The simulation results are compared with experimental data provided by NASA Glenn Research Center (NASA-GRC). Several comparison metrics were utilized including nodal displacements, principal strains, and delamination patterns to compare the finite element simulation results with experimentally obtained results. Both quantitative and qualitative comparisons are made.

5.1 Experimental Methods

Dynamic impact tests were performed at NASA-GRC (Pereira 2017) in accordance with ASTM D8101/D8101M-17 (D30 Committee 2017b). An aluminum (AL 2024) projectile (Fig. 97d) with a mass of 50 g was used to strike a T800S/F3900 composite plate at different velocities. The composite plates (305 x 305 x 3.1 mm) had a total of 16 unidirectional plies. The projectile was fired using a single stage gas gun. A total of 14 impact tests were conducted with the projectile velocity varying between 119 ft/s (36.27 m/s) and 530 ft/s (161.54 m/s) corresponding to impact energies of 24.25 lb-ft (32.88 J) and 481.16 lb-ft (652.37 J) respectively. One of the tests, identified as LVG 1064 (236 ft/s,

71.93 m/s), was selected to validate the deformation and damage sub-models as well as the cohesive zone model. Fig. 95 shows the LVG 1064 panel after the experiment.

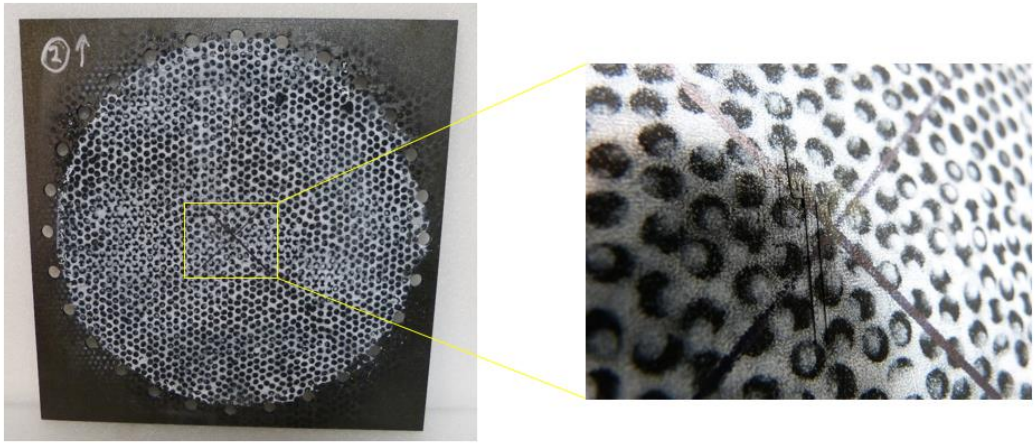

Fig. 95. LVG 1064 Impact Panel after Testing

After testing, the LVG 1064 panel exhibited minor surface damage while containing the projectile. Ultrasound C-scan imaging of the panel (Fig. 96) showed localized damage near the point of impact indicating possible delamination. These characteristics make the test an ideal candidate to exercise the deformation and damage sub-models in MAT 213 as well as the cohesive zone model without utilizing a composite failure model. The lower velocity experiments showed little to no damage in the C-scan image meaning during the simulation, the damage sub-model likely would not have been exercised. The higher velocity experiments showed major failure or complete perforation of the panel meaning a failure model introducing element erosion would likely be necessary to accurately simulate the event. LVG 1064 provided a proper middle ground.

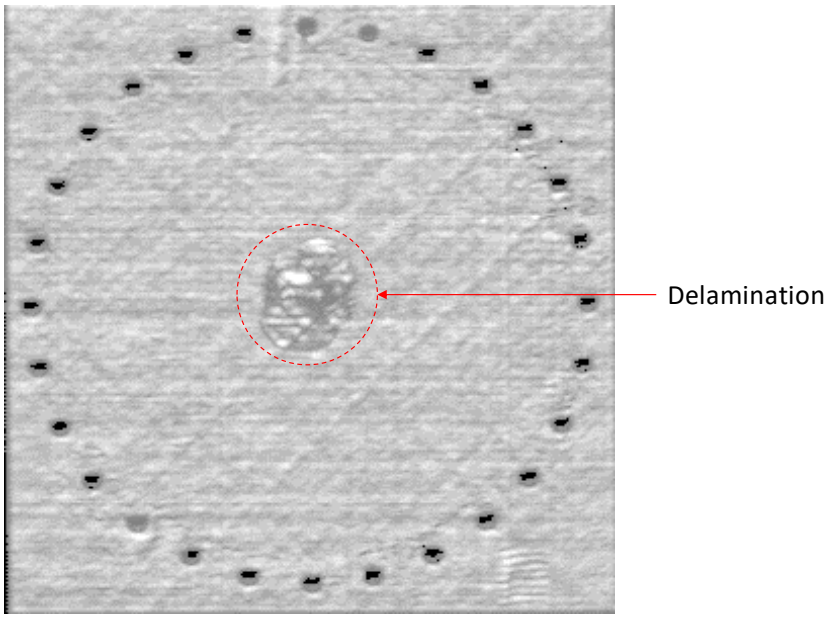

Fig. 96. Ultrasound C-scan Image of LVG 1064 after Testing.

The ultrasound C-scan technique provides a superimposed image of where delamination or damage has occurred through the thickness of the panel. However, the technique does not provide insight into where delamination has occurred or the extent of delamination between specific ply boundaries. More invasive techniques are likely required to obtain that information. Fig. 97 shows images of the experimental test setup.

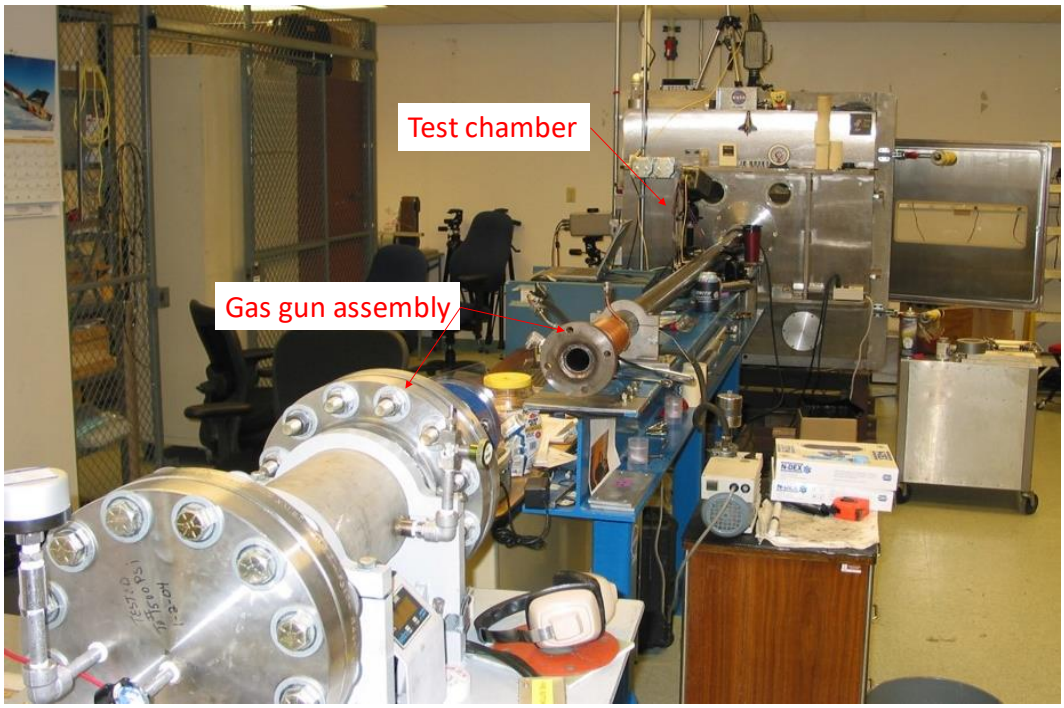
Test chamber
Gas gun assembly

(a)

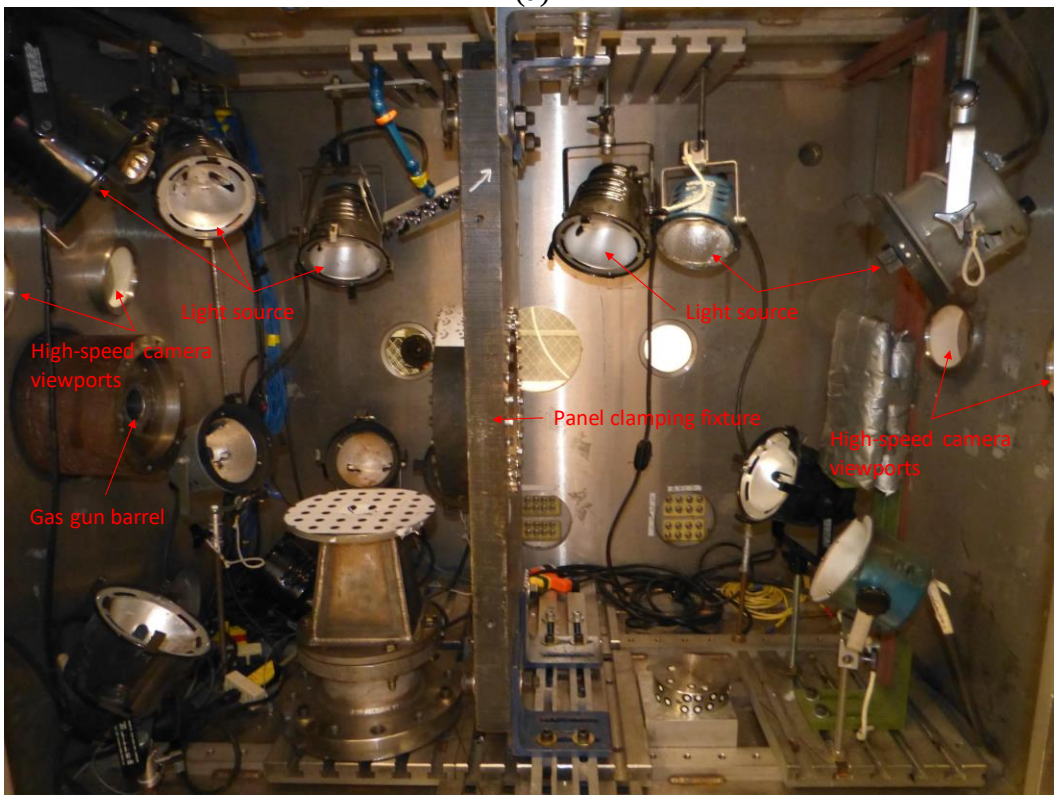
Light source
Light source
High-speed camera viewports
Panel clamping fixture
High-speed camera viewports
Gas gun barrel

(b)

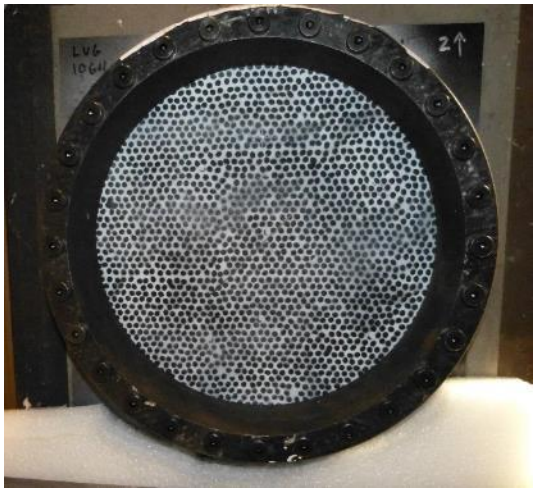

(c)

(d)

Fig. 97. Experimental Test Setup Used for Dynamic Impact Tests (a) Gas Gun Assembly and Test Chamber, (b) Internal View of Test Chamber, (c) Panel in Clamping Fixture, and (d) Hollow AL 2024 Projectile with Radiused Front Face

Full details of the test setup are provided by Melis and co-workers (Melis et al. 2018). DIC was used to generate full displacement fields during the impact event on both the front side (impact side) and back side (opposite to impact side) of the composite panel. DIC images of the front of the panel were captured using two Photron SA1.1[9] cameras capturing images at 40,000 fps. DIC images of the back of the panel were captured using two Photron SA-Z[10] cameras capturing images at 80,000 fps. Fig. 97b shows viewports in the test chamber for the high-speed cameras while Fig. 97c shows the typical speckle pattern present on both sides of the panel.

[9] https://photron.com/fastcam-sa1-1/
[10] https://photron.com/fastcam-sa-z/

5.2 Finite Element Modeling

A convergence analysis and boundary condition study were performed to find the optimal finite element mesh (balancing accuracy and computational cost) to carry out the simulations. Fig. 98 shows a schematic representation of one quarter of the FE model of the composite panel with the modeling details.

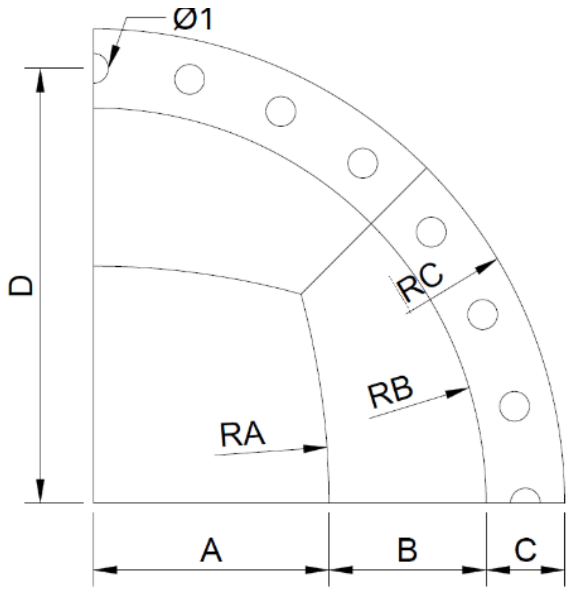

Zone A: Length of 3”, 49 elements along length, in-plane aspect ratio approximately 1.03:1, max in-plane element length of 0.063”

Zone B: Length of 2”, 25 elements along length, in-plane aspect ratio approximately 1.09:1, max in-plane element length of 0.08”

Zone C: Length of 1”, 10 elements along length, in-plane aspect ratio approximately 1.12:1, max in-plane element length of 0.11”

D = 5.5” (Distance from center of plate to center of bolt hole regions)

Ø1 = 0.378” (Bolt hole region diameter)

RA = 10”
RB = 5”
RC = 6”

Fig. 98. Impact Panel FE Model Characteristic Dimensions

Fig. 98 shows that only the region of the panel contained within the clamping fixture was modeled for the simulations. The regions outside of the fixture were assumed to have

negligible effect on the response of the system. Each ply in the layup was modeled using one element through the thickness (thickness of 0.0075”). Fig. 99a shows the nodes which were fixed from in-plane translation (restraint imposed by the bolts) while Fig. 99b shows nodes which were fixed from out-of-plane translations (restraints imposed by the clamping fixture). These restraints were obtained from a study performed to observe how sensitive the finite element model response is to changes in the boundary conditions under low and high velocity impact conditions. In Fig. 99, the 0° plies (Fig. 100) are initially oriented along the global x-axis.

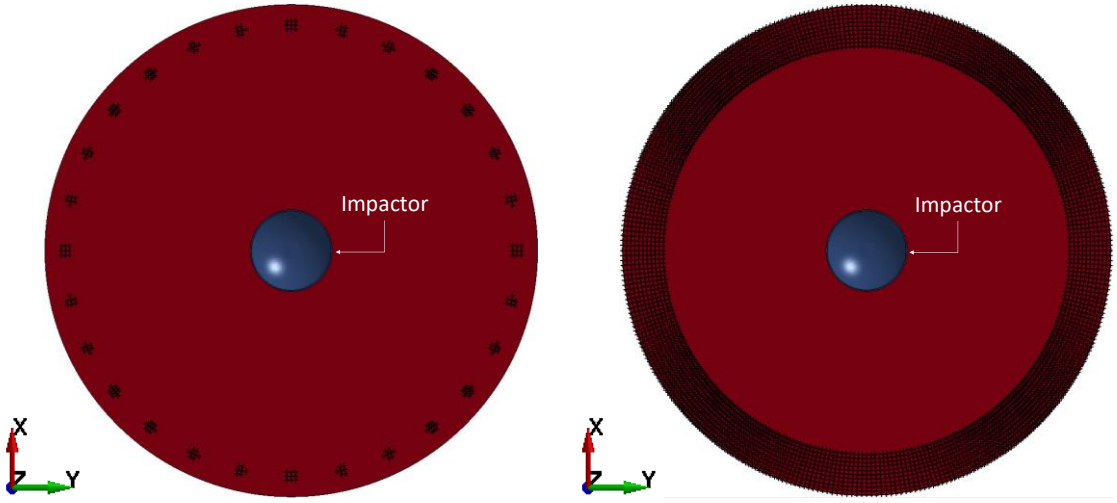

(a) (b)

Fig. 99. FE Model Used for Composite Plate Showing (a) Nodes Assigned Bolted Boundary Conditions and (b) Nodes Assigned Clamped Boundary Conditions

The *CONTACT_ERODING_ SURFACE_TO_SURFACE contact definition in LS-DYNA (LSTC 2017a) was used to handle contact between the aluminum impactor and composite panel while the *CONTACT_ERODING_SINGLE_ SURFACE contact definition was used to handle contact between the individual plies of the composite panel.

The eroding contact definitions ensure the contact remains active when new free surfaces are created after the cohesive zone elements are eroded at failure. Fig. 100 shows a cross-section schematic of the FE model including the location of the CZE layers.

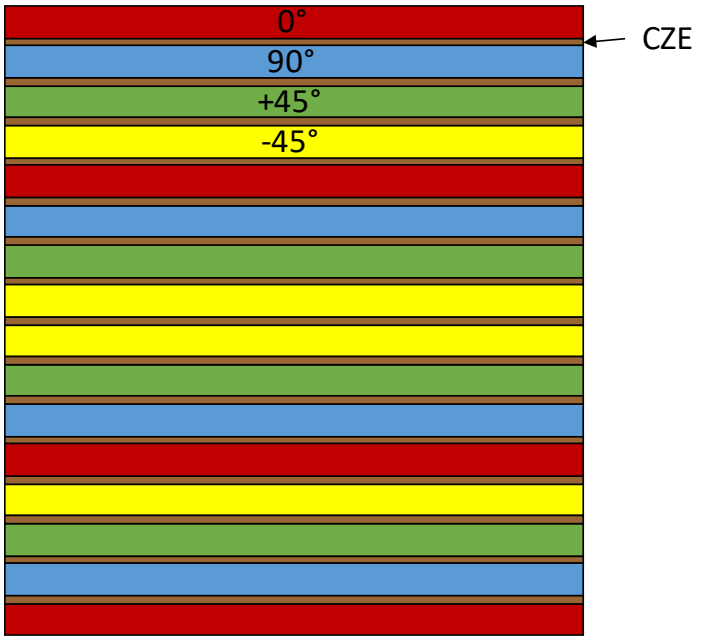

Fig. 100. Cross-section of FE Model of Composite Panel

LS-DYNA's MAT 24 (LSTC 2017b), a piecewise linear plasticity model with strain rate effects, was used to model the aluminum impactor. The strain-rate dependent information was taken from publicly available data (Nicholas 1980). Fig. 101 shows the FE model of the aluminum whose dimensions can be found in ASTM D8101/D8101M-17 (D30 Committee 2017b). Table 17 provides a summary of the FE model.

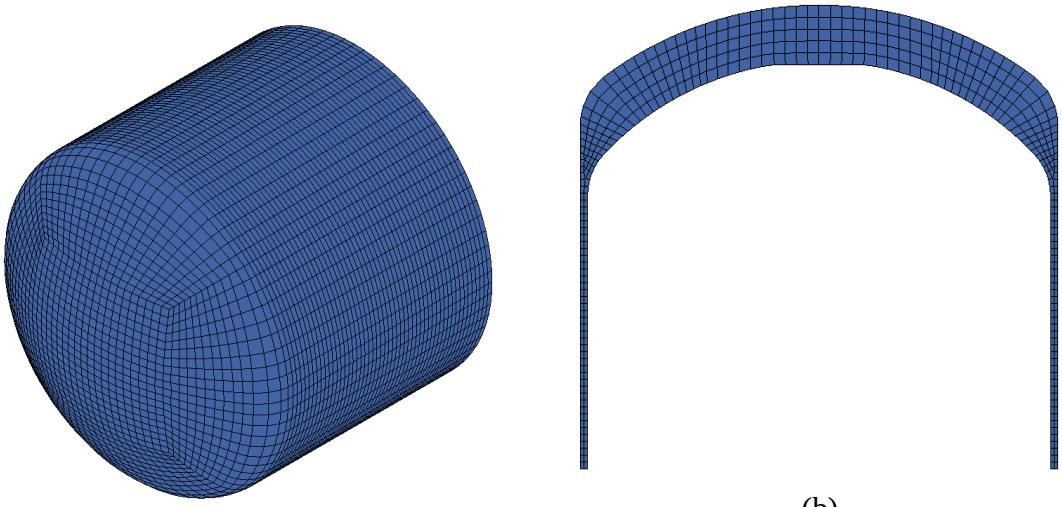

(a) (b)

Fig. 101. FE Model of Aluminum Projectile Used in Impact Simulations (a) Isometric View and (b) Cross-section

Table 17. Full FE Model Characteristics

Component	**Total Number of Elements**	**Total Number of Layers**	**Element Type (LS-DYNA Element Formulation)**
Composite parts	390 000	16	Hexahedral solid (integration scheme varies)
Aluminum impactor	17 000	15	Hexahedral solid (elform=1)
Cohesive zone elements	350 000	-	Non-zero thickness hexahedral element (elform=19)

5.3 Comparison Between OEPDMM Predictions and Experimental Results

A variety of runs were performed with different combinations of input parameters to gain insight into the sensitivity of the material model to the data. The runs include parametric studies using different combinations of deformation and damage related input, a parametric study illustrating how the element formulation used affects the predicted response, and finally a comparison of the strain-based and stress-based damage implementations.

5.3.1 Deformation and Damage Sub-Model Study

Several runs were performed to exercise the deformation and damage sub-models using different combinations of material data input. The quasi-static/room temperature data presented in Chapter 2 was used to drive the deformation sub-model. The damage parameter *model curves* presented in Chapter 3 were used as input to the damage sub-model.

Table 18 summarizes the five runs that were performed, each using a distinct combination of input parameters.

Table 18. Model Characteristics of the FE Simulations

Material Model ID	**Model Characteristics**	**Included Damage Parameters**
FOMND	Fully orthotropic model with no damage parameters	None
FOMID	Fully orthotropic model with in-plane damage parameters only	$d_{22_C}^{22_C}$, d_{12}^{12}, and $d_{22_C}^{22_T}$
TIMND	Transversely isotropic model with no damage parameters	None
TIMID	Transversely isotropic model with in-plane damage parameters only	$d_{22_C}^{22_C}$, d_{12}^{12}, and $d_{22_C}^{22_T}$
TIMIOD	Transversely isotropic with in-plane and out-of-plane damage parameters	$d_{22_C}^{22_C}$, d_{12}^{12}, $d_{22_C}^{22_T}$, $d_{33_C}^{33_C}$, d_{13}^{13}, and $d_{33_C}^{33_T}$

Nominally, one would expect the unidirectional composite to be transversely isotropic. However, micrograph images along with experimental data show that this is likely not the case for this particular composite at the laminate level. “Fully orthotropic” (

Table 18) indicates the input used for the model was taken directly from the results of the corresponding experiments. “Transversely isotropic” indicates that all 3-direction parameters were set to the 2-direction counterparts. Damage related data have been experimentally obtained for a subset of the in-plane damage parameters: $d_{22_C}^{22_C}$, d_{12}^{12}, $d_{22_C}^{22_T}$, and $d_{22_C}^{12}$. A model including in-plane damage only would use these parameters. Using the transverse isotropy assumption, $d_{33_C}^{33_C}$, d_{13}^{13}, $d_{33_C}^{33_T}$, and $d_{33_C}^{13}$ are also included in the simulation by setting them equal to their in-plane counterparts and a model including out-of-plane damage would use these parameters. The transversely isotropic simulations were run both with and without out-of-plane damage to determine which parameters had the most significant effect on the response.

LS-DYNA’s MAT 186 (LSTC 2017b) was used for the cohesive zone elements with the model curves in Fig. 84 and Fig. 88 as input. The size of the cohesive zone elements, near the point of impact, used in the validation simulation is approximately 1.5 mm (0.06 in) and is within the range of the element sizes used in the DCB and ENF simulations studies. The unaltered model curves from Fig. 84 and Fig. 88 were used as input to MAT 186. The Benzeggagh-Kenane mixed mode law (Benzeggagh and Kenane 1996) was used with the mixed-mode exponent (XMU) set to 1.0 in the simulation, corresponding to a linear relationship between mixed mode fracture toughness and the mode-mixity.

The first metric used for comparison is the out-of-plane displacement of the backside of the panel. Fig. 102 shows the out-of-plane displacement field captured from the experiment and the simulations at the instance of time when the peak displacement occurs.

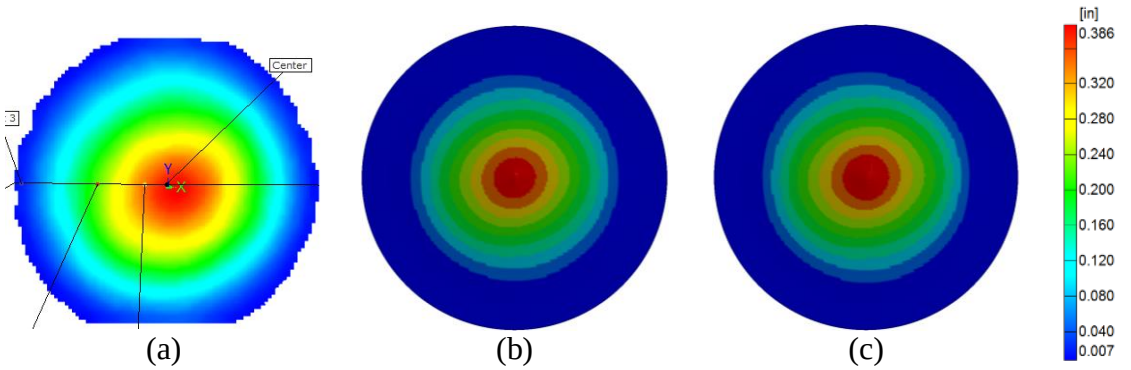

(a) (b) (c)

Fig. 102. Out-of-Plane Displacement Contour (a) Experiment, (b) TIMID Simulation, and (c) TIMIOD Simulation ($t=4.75(10)^{-4}$)

Qualitatively, the contours produced by the simulation are consistent with the experiment. Fig. 103 provides a quantitative comparison of the out-of-plane displacement of the center point of the panel in both the experiment and the simulations.

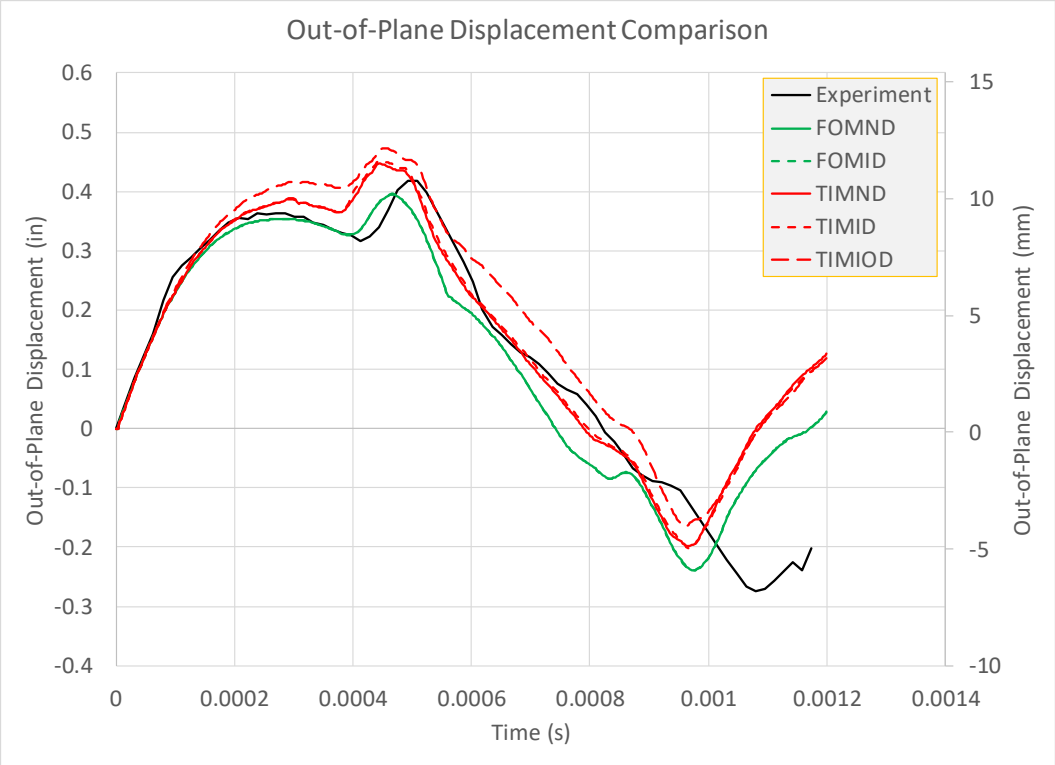

Fig. 103. Out-of-Plane Displacement Time History Comparison of the Center of the Composite Plate

The experimental data shown is choppy because the small surface cracks at the impact location caused DIC data to be lost. The simulations were all terminated before the composite panel stopped oscillating since most of the damage observed in the experiment happened near the time of impact. Models utilizing only in-plane damage parameters show little to no change when compared with deformation only runs. Inclusion of the 3-direction damage parameters has the largest effect on the response of the system as is evidenced by the difference in the response between TIMID and TIMIOD. TIMIOD yields a higher estimate of the peak displacement than TIMND. This is expected as the stiffness of the material has been reduced. Additionally, the out-of-plane displacement graphs of the

transverse isotropy models which include damage (TIMID, TIMIOD), match the experimental data better than the deformation only models. Both the impacted panel and the simulation showed permanent deformations that were too small to compare against each other.

The next metric used for comparison is the maximum principal strain of the backside of the panel. Fig. 104 shows the maximum principal strain field from the experiment and the simulations at the instance of time just before the peak value occurs.

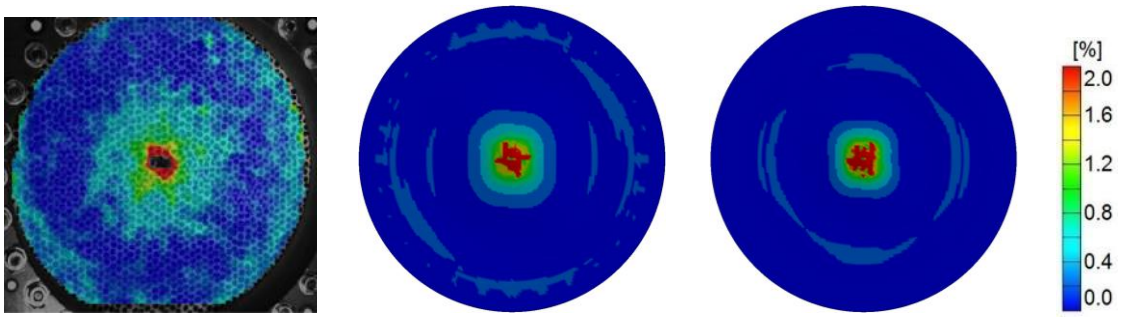

(a) (b) (c)

Fig. 104. Maximum Principal Strain Contour (a) Experiment, (b) TIMID Simulation, and (c) TIMIOD Simulation ($t=1.04(10)^{-4}$ s)

The maximum principal strain contour produced by the simulations compare favorably with the experimental results. Fig. 105 provides a quantitative comparison of the maximum principal strain of a point to the right of center in both the experiment and the simulations respectively.

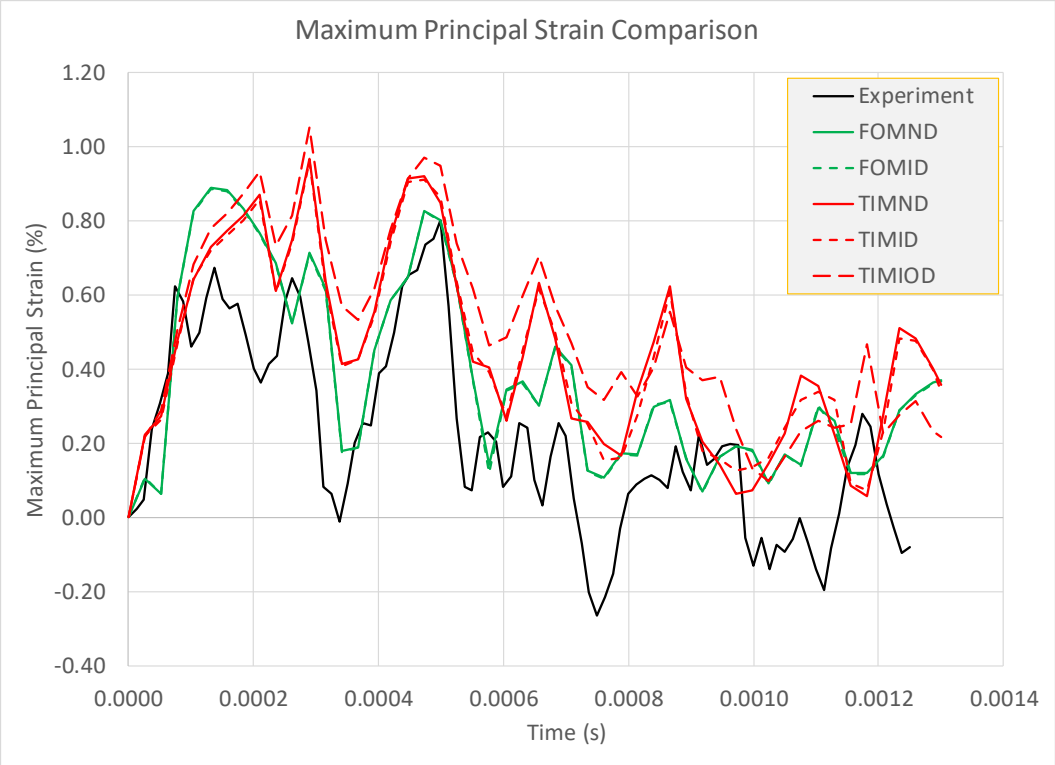

Fig. 105. Maximum Principal Strain Comparison Time History Comparison to the Right of Center of the Composite Plate

Fig. 105 shows that all of the models consistently overestimate the experimental response with the fully orthotropic models providing the closest match. The comparison of the principal strain at a single point may be misleading since it provides only a local comparison of the plate response and is subject to numerical error as strain is the gradient of displacement and any noise in the displacement will propagate during strain computations. The final metric used for comparison is the delamination and damage observed in the panel. Fig. 106 provides a comparison of the damage exhibited in the experiment, obtained through ultrasonic scan of the panel after the test, and the interlaminar delamination predicted by the finite element model.

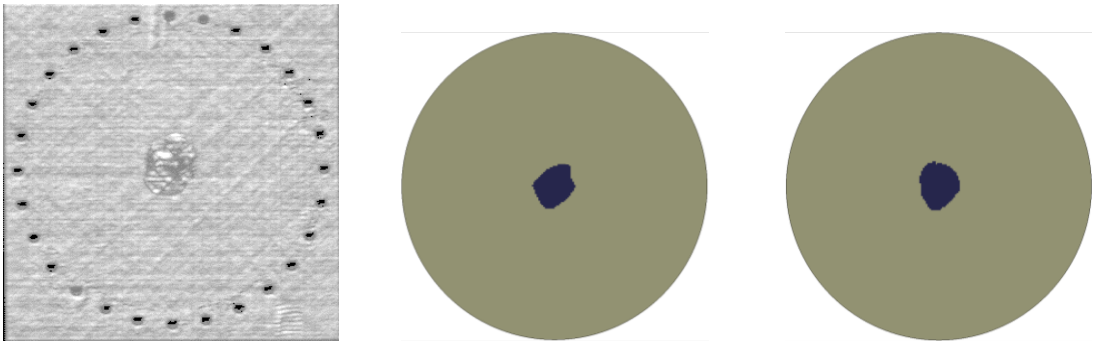

(a) (b) (c)

Fig. 106. Delamination Plot Comparison (a) Scanned Image from Ultrasound C-scan of the Tested Panel, (b) Simulation, and (c) TIMIOD Simulation

The dark region in the center of Fig. 106b and Fig. 106c correspond to failed cohesive zone elements - LS-Prepost (LSTC 2018b) was used with a transparency of 90% to show delamination through the thickness of the model. The location and overall shape and size of the experimental and simulation results are quite similar. Since the scanned image does not indicate between which layers delamination has occurred, the simulation results were processed to answer that question. Fig. 107 shows the failed cohesive zone elements between each ply starting from the side of the panel opposite the impact (Ply 16-15 boundary). The images show that visually observable delamination has occurred in 10 ply boundaries (15-14, 13-12, 12-11, 11-10, 10-9, 8-7, 7-6, 5-4, 4-3, 3-2).

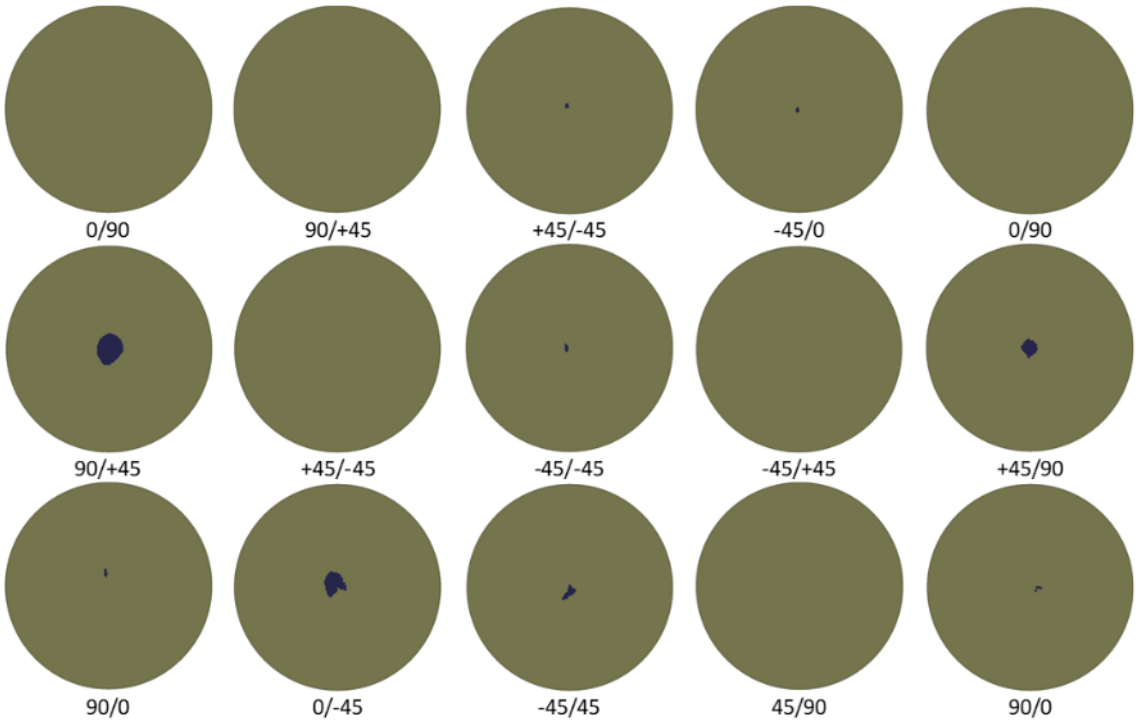

Fig. 107. Cohesive Zone Element Failure Between Adjacent Plies in the FE Model (TIMIOD Simulation)

Though failure of the cohesive zone was captured in the simulation, the surface cracks observed in the experiment were not captured by the finite element model since no failure/erosion criteria were used for the composite parts. However, Fig. 108 shows a comparison of the surface cracks from the experimental panel with the contour plots of two dominant damage parameters, $\left(d_{12}^{12}\right)$ and $\left(d_{33_C}^{33_C}\right)$ at the instance of time when the size of the damage zone has stabilized. Amongst the damage parameters included in the simulations (

Table 18), the dominant damage parameters are defined as those whose final values are the largest when compared to their peak damage values from the experiments.

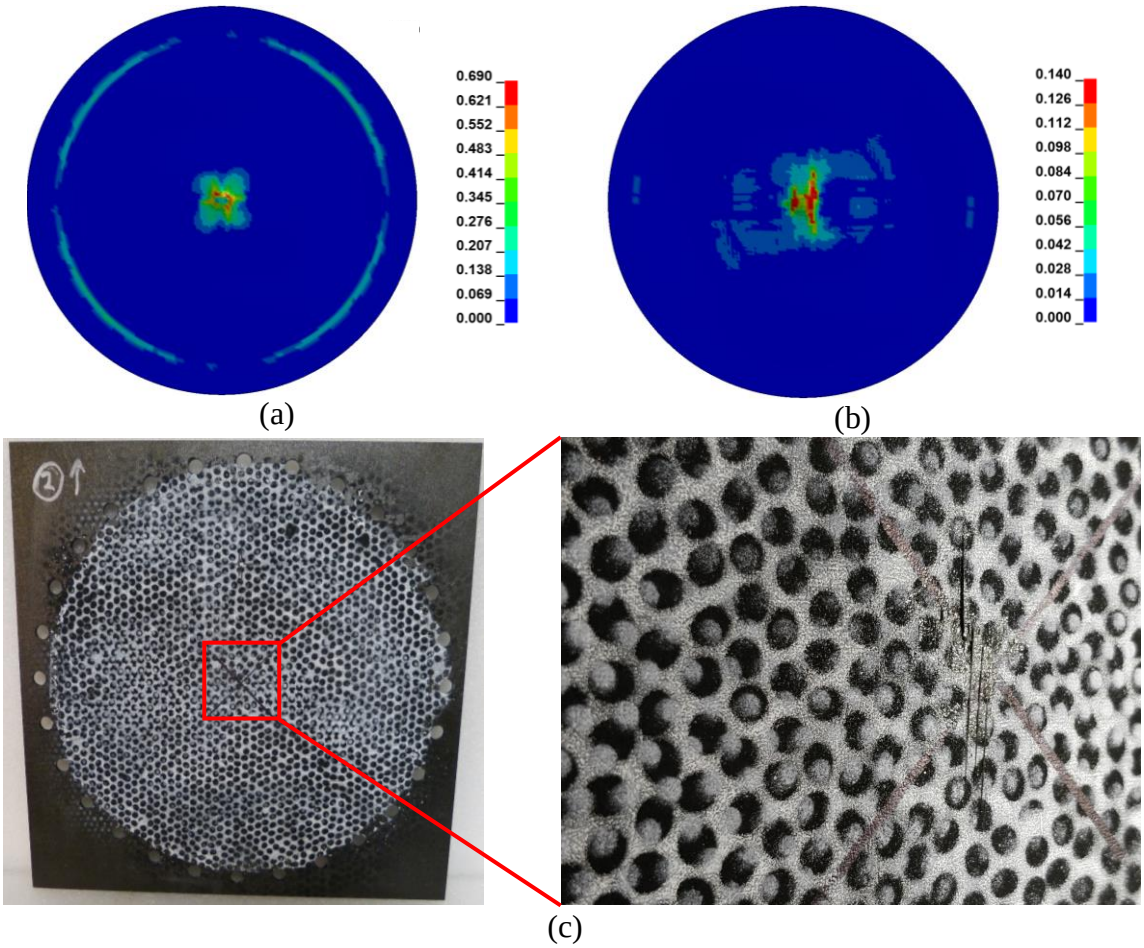

Fig. 108. Dominant Damage Parameter Observed in (a) TIMID Simulation $\left(d_{12}^{12}\right)$ and (b) TIMIOD Simulation $\left(d_{33_C}^{33_T}\right)$.

Each of the impact simulations presented thus far have been performed using solid elements with a reduced integration scheme to represent the composite parts. However, reduced integration elements are prone to *hourglassing*, spurious energy modes that may

lead to erroneous results. Fig. 109 shows a comparison of the global hourglass energy compared with the global internal energy computed during the TIMID simulation.

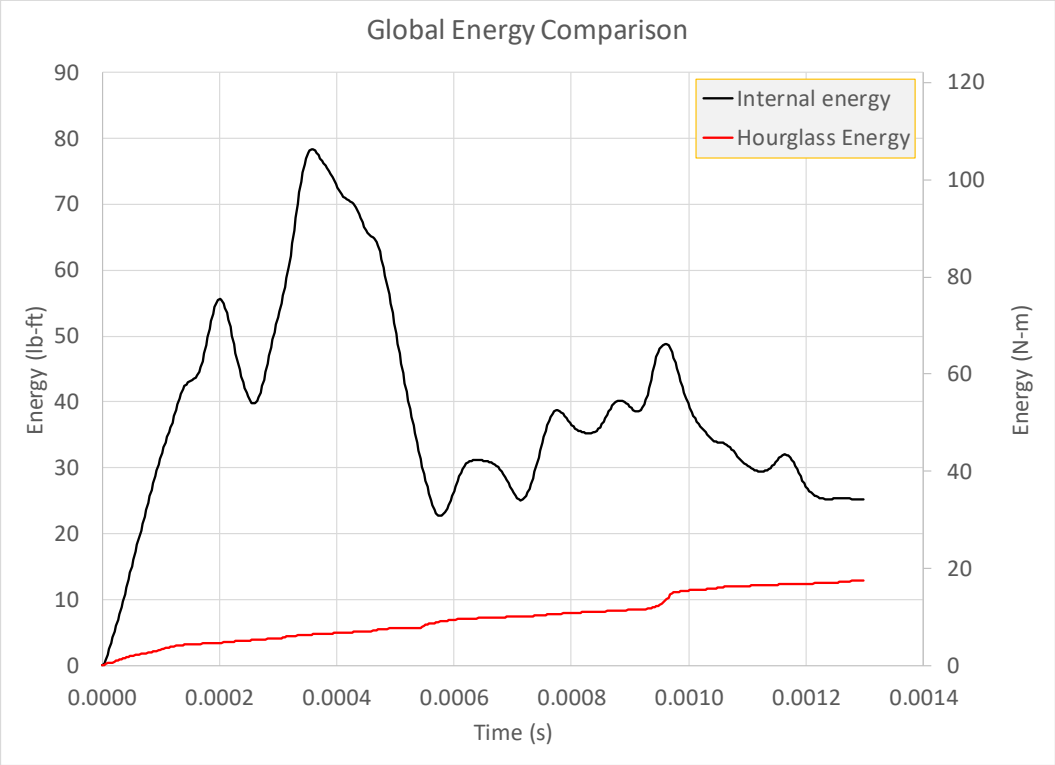

Fig. 109. Comparison of Global Energies for TIMID Simulation Using Reduced Integration Scheme

Fig. 109 shows that a significant portion of the total energy in the simulation is attributed to hourglassing. A study was performed using the TIMID simulation to gauge the effect of element formulation on the simulation response.

Table 19 outlines the solid element formulations used in the additional simulations.

Table 19. LS-DYNA Element Formulations Used in Impact Simulations

LS-DYNA Element Formulation	**Element Formulation Characteristics (LSTC 2017a)**
elform 1	Constant stress solid element.
elform 2	Fully integrated selective reduced (S/R) integration solid element
elform -1	Fully integrated S/R solid intended for elements with poor aspect ratio, efficient formulation
elform -2	Fully integrated S/R solid intended for elements with poor aspect ratio, accurate formulation

Fig. 110 shows a comparison of the out-of-plane displacement history from simulations using the different element formulations.

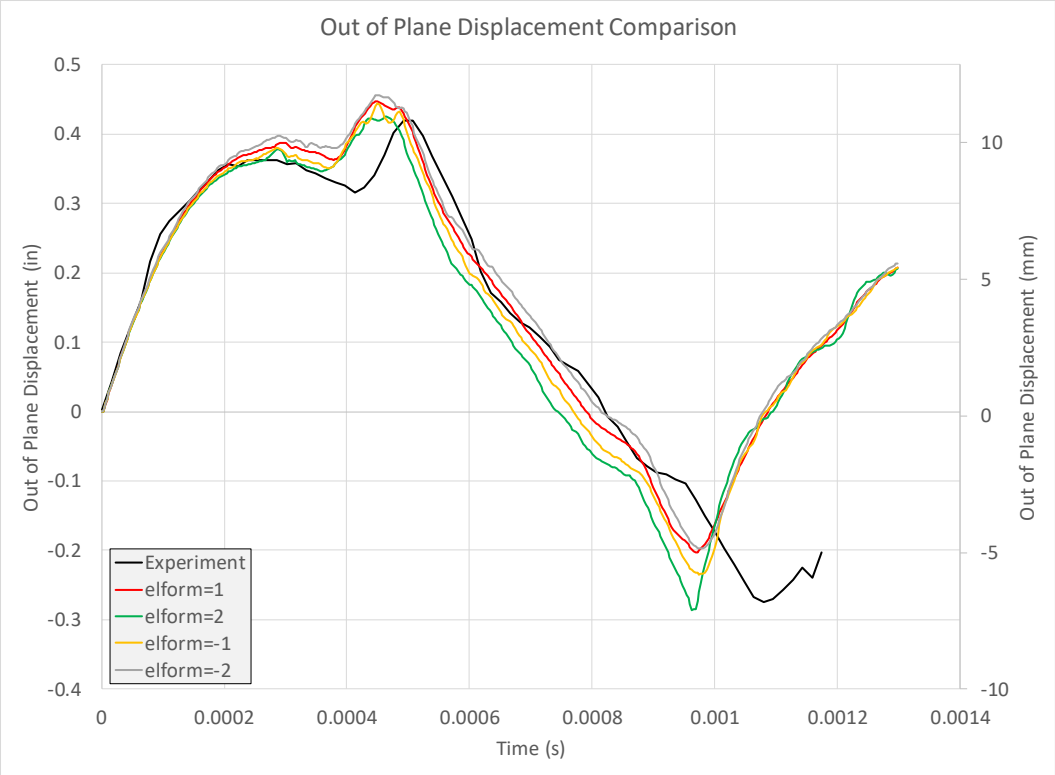

Fig. 110. Comparison of Predicted Out-of-plane Displacement Using Different Solid Element Formulations for Composite Parts

Fig. 110 shows that there are minor differences in the predicted response with element formulation 2 yielding the best match with the positive and negative peaks. However, while there is little difference in the displacement response, the predicted delamination was drastically different when comparing the different formulations. Fig. 111 shows the delamination predicted by the respective models.

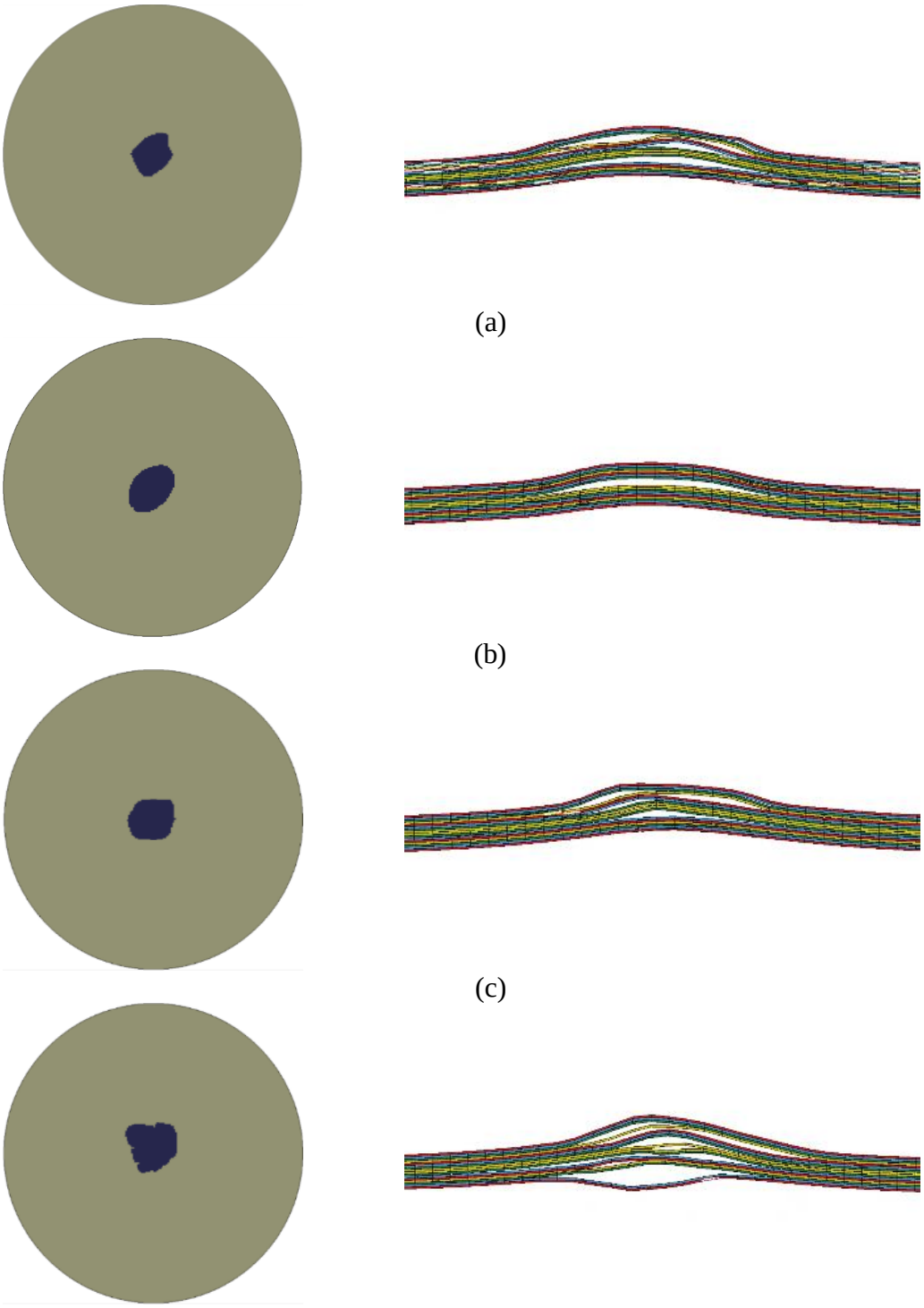

(a)

(b)

(c)

(d)

Fig. 111. Predicted Delamination Using Different Element Formulations Showing Total Delamination Predicted and Cross Section of Delaminated Area (a) Elform=1, (b) Elform=2, (c) Elform=-1, and (d) Elform=-2

Comments and Observations: Across all simulations, the predicted out-of-plane displacement compared well with the experimental data both qualitatively and quantitatively. While there are probably numerous reasons that may be used to explain the difference, the boundary conditions at the edge of the panel likely have the most impactful role. In the simulation, only the circular portion of the plate within the fixed region is modeled with the assumption that any stress waves imparted on the panel and fixture would be confined to that region. However, the bolt holes and clamping fixture likely do not completely restrain the plate. Similarly, a comparison of the principal strains shows the experimental and simulation values to be close both qualitatively and quantitatively. However, a similar difference in the phase is observed as the characteristic points in the plots all occur earlier in the simulation than in the experiment with the trend being mostly similar. To obtain a more accurate assessment of the roles played by the bolts, bolt pre-tensioning and the support fixture, would involve a very detailed study that currently is outside the scope the research work. Additionally, these simulations showed large strain rates in the elements near the impact region ($O(10^3 / s)$). However, no rate dependent data was used in the simulations. The T800S/F3900 composite has been shown to exhibit rate dependent behavior in both the uniaxial behavior (Deshpande 2018; Yang 2016) as well as the fracture behavior (Nandakumar 2010). Including rate effects in both the composite properties as well as the cohesive zone element properties is likely necessary for correctly representing the behavior of the material. The experimentally derived TSL used in the validation simulations proved to be able to accurately represent the delamination behavior observed in the experiment. However, while the TSL derived fully from experimental data was shown to be valid for the small range of element sizes used in the verification and

validation simulations, the results may change when using element sizes outside of this range. Techniques to perform mesh size regularization, making the response independent of cohesive zone element length, would help move the standard procedure away from numerical calibration of TSL to deriving them experimentally using some of the proposed methodology. Additionally, there was a clear dependence of the predicted delamination on the solid element formulation used in the simulations. While each of the element formulations predict similar size and location of delaminated area, which compares well with the UT scan of the experimental panel, Fig. 106, Fig. 111 shows that the distribution and total amount of delamination predicted by the models varies. Comparison of the layer-by-layer delamination from the experiment and simulation would be useful to further validate the TSL used in the simulation. However, that information is not currently available and hence the comparison cannot be made. The delamination predicted in the simulation was caused by mixed mode fracture events. The Benzeggagh-Kenane mixed-mode fracture law exponent needs to be properly determined through mixed mode bending experiments in order to accurately represent the traction-separation behavior.

5.3.2 Comparison of Strain-Based and Stress-Based Damage Formulations

Each of the impact simulations presented thus far have used the strain-based damage implementation. A comparison using the strain based $\left(d_{ij}^{kl}\left(\varepsilon_{ij}^{p}\right)\right)$ and stress based $\left(d_{ij}^{kl}\left(\sigma_{ij}^{eff}\right)\right)$ damage formulations presented in Chapter 3, was performed to illustrate how the choice of the internal state variable influences the response. The simulations included the following damage parameters: $d_{22_C}^{22_C}$, d_{12}^{12}, $d_{22_C}^{22_T}$, $d_{22_C}^{12}$, $d_{33_C}^{33_C}$, d_{13}^{13}, $d_{33_C}^{33_T}$, and $d_{33_C}^{13}$. The choice of damage parameters was made purely to illustrate the differences between the two

implementations. The parameters may not be physically appropriate for the given problem. Fig. 112 shows a comparison of the out-of-plane displacement predicted at the center of the panel for the two formulations.

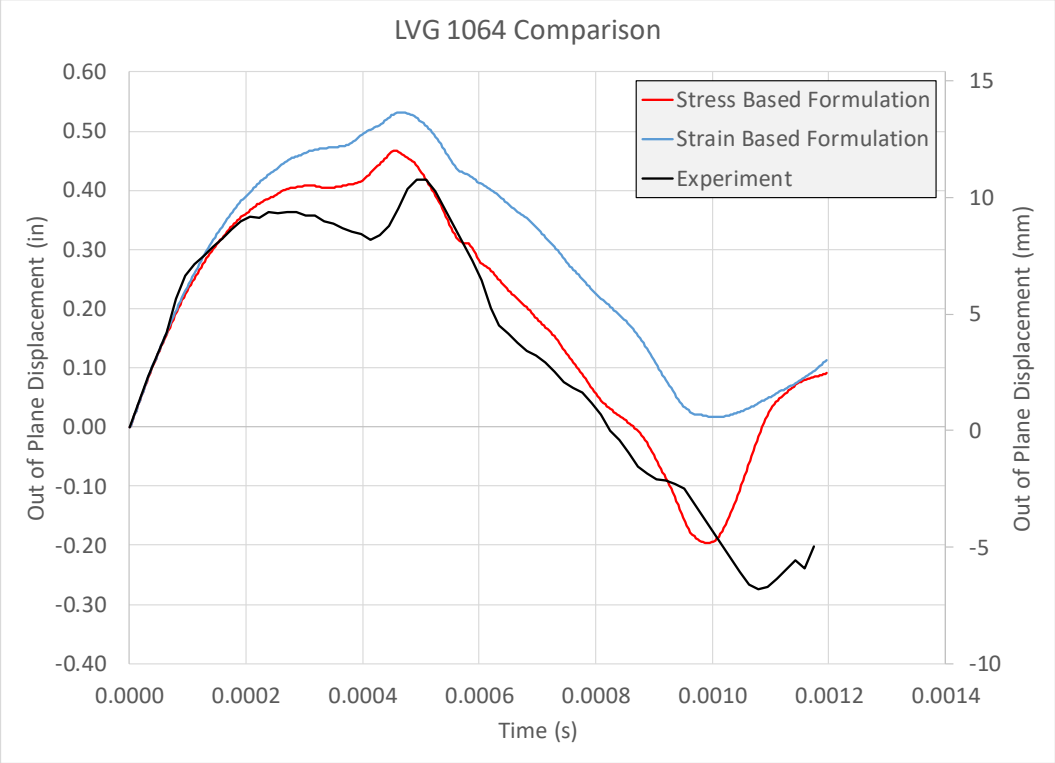

Fig. 112. Comparison of TIMIOD Simulation Using Strain-based and Stress-based Damage Formulation

Consistent with the simulations presented in Chapter 3 (Fig. 76), when coupled damage is included in the simulations, the strain-based formulation results in a more conservative estimate of the response of the system than the stress-based formulation. One of the concerns in using a stress-based damage formulation was due to the possibility of spurious stress oscillations that are often experienced in dynamic explicit finite element simulations due to numerical error. The development of spurious stresses may lead to damage

parameters being erroneously excited which in turn may cause element instabilities. However, during this simulation, no element instabilities were detected, and the simulation ran to completion without premature error termination. More rigorous testing of the proposed approach is necessary to ensure spurious stress oscillations do not adversely affect the solution and also the implementation is robust enough to handle a variety of load conditions.

6 CONCLUSIONS

Composite materials are becoming increasingly popular in the design of structural components with applications ranging from aerospace and automotive to civil and biomedical. With the increased ubiquity, the need for powerful, predictive numerical tools is necessary to accurately model the manner in which the structures deform, sustain damage, and ultimately fail. The behavior of composite materials has been shown to be dependent on strain rate and temperature. The nonlinear behavior has also been shown to have contributions from both plastic flow of the material as well as damage. In the past, proposed models have often ignored some of these contributing factors. Additionally, the previously proposed models have been developed for specific architectures, assuming the behavior of the composite material. As new composite architectures are being developed, these models may not be suitable for the required analyses. A new orthotropic elasto-plastic damage material model (OEPDMM) relying completely on tabulated experimental data has been developed and implemented as MAT 213 in LS-DYNA. The model utilizes a generalized approach wherein no assumption regarding the material behavior is made and tabulated data is used to drive the plasticity deformation sub-model, in the form of stress-strain curves at different rates and temperatures; the semi-coupled damage sub-model, in the form damage parameter-total strain curves; and the failure sub-model, in the form of a tabulated failure surface. MAT 213 has been developed with the intent of simulating impact and crush events, two critical loading conditions for aerospace structures, in order to shorten design time and move away from a high number of large scale physical experiments necessary for aircraft certification.

In this dissertation, the theoretical details governing the deformation sub-model have been provided. The hardening of the composite material is based on a form of the Tsai-Wu failure criteria with non-associative plastic flow utilizing a general quadratic plastic potential function. Driving the deformation model requires high fidelity experimental data to accurately assess the efficacy of the developed approach. The T800S/F3900 carbon fiber/epoxy resin unidirectional composite system was used to illustrate how the data required to drive the deformation sub-model is obtained under quasi-static and room temperature conditions. Twelve stress-strain curves in the respective principal material directions (PMD) and principal material planes were obtained, namely 1-direction, 2-direction, and 3-direction tension and compression tests, 1-2 plane, 2-3 plane, and 1-3 plane shear and off-axis tension/compression tests. The steps used in post processing the data and deriving the input parameters were provided.

The theoretical and implementation details of the damage sub-model were also provided. The formulation of the damage sub-model allows for the effects of damage coupling between all shear and normal components. The effective stress concept and the assumption of strain equivalence were used, which allowed for the damage and plasticity computations to be decoupled. The implemented model utilizes the directional effective stress as the internal state variable used to evolve damage. Through numerical simulations, it was shown that using the directional effective stress as opposed to the directional plastic strain or effective plastic strain resulted in a more accurate representation of the material behavior. The T800S/F3900 composite was again used to illustrate the experimental methods that may be used to gather the data required to drive the damage sub-model. The

data was derived from cyclic loading tests which provide the reduction in apparent elastic as a function of the total strain at unloading. Procedures for obtaining both uncoupled and coupled damage parameters were presented.

Since composites are typically used as stacked laminates to overcome intrinsic weaknesses in the material, accurately modeling the interfaces is important. This is often done by representing the interface as a separate entity through cohesive zone modeling. Typically, the traction-separation laws (TSL) used in driving cohesive zone models (CZM), are obtained through an iterative trial and error process by altering input in the simulation and attempting to match experimental results. However, this may lead to a non-unique combination of parameters that would have to be changed under new loading conditions. To enhance the predictive capabilities of MAT 213, test procedures were presented for deriving arbitrarily shaped TSL necessary for CZM. Both Mode I and Mode II relationships were derived for the T800S/F3900 composite from the double cantilever beam (DCB) and end-notched flexure tests respectively. The resulting TSL were used in verification simulations and accurately reproduced the experimental results. The TSL were also successfully utilized in the impact validation.

The high velocity impact validation simulation was used to highlight the efficacy of the proposed material model. The MAT 213 predictions compared well with the experimental results across all validation metrics: displacements fields, max principal strain fields, and delamination/damage. Numerous parametric studies were presenting illustrating the sensitivity of the predicted response to several material model and FE model parameters.

Table 20 outlines the current state of MAT 213 with respect to features that are desirable within a predictive material model as well as planned features part of the future work.

Table 20. Current and Future Features in MAT 213

Desirable Feature	**MAT 213**
Input parameters based on physically meaningful experimental data.	All sub-models within MAT 213 (deformation, damage, and failure) are driven completely by coupon level uniaxial testing in the various composite PMDs. Each of the sub-models account for asymmetric tension/compression behavior observed in composite materials.
Effects of strain rate need to be accounted for in a flexible, unified manner accounting for anisotropy of rate effects.	MAT 213 account for rate dependency by allowing stress-strain curves to be input as a function of various strain rates. A viscoelastic formulation is currently being developed to more appropriately account for the physical behavior of composites subjected to high strain-rates.
Effects of temperature need to be accounted for in a flexible, unified manner.	MAT 213 account for temperature dependency by allowing stress-strain curves to be input as a function of various temperatures. The temperature dependent formulation is currently being improved by accounting for the conversion of plastic work to heat (adiabatic heating conditions) common in impact and crush events.

Damage related capabilities.	MAT 213 includes a fully generalized effective stress-based semi-coupled damage model driven by experimental data.
Failure related capabilities.	The failure models being incorporated into MAT 213 include established analytical models, both strain and stress based, as well as the capability for the user to supply a general tabulated failure surface. A subset of the failure models include mesh regularization methods to adjust for localization effects during simulations.
Explicit modeling of interlaminar delamination via tiebreak contact and cohesive zone elements.	While MAT 213 does not have inbuilt provisions to handle interlaminar behavior, it has been shown that cohesive zone models work well in conjunction with MAT 213 to accurately predict composite behavior.
Capable of being used with several finite element formulations (thin shell, thick shell, solid).	All simulations shown in this dissertation were successfully performed using several solid element formulations available in LS-DYNA. Support for thin and thick shells is under development.
Computational efficiency.	A major focus of the future work is to identify the bottlenecks in the current numerical algorithm and improve the implementation to increase the computational speed.

While the developed approach shows promise, more work may be required to refine the experimental and data processing techniques outlined in this dissertation. The techniques were successful for the unidirectional composite presented but additional considerations may be necessary if a different material architecture is to be modeled. Additionally, further validation of the material model is necessary to ensure the accuracy of the developed approach. The impact test simulated compared favorably with the experiment, however, higher velocity impacts and energy absorbing crush tests will need to be simulated to investigate the behavior of the model under various loading conditions. These additional validation tests likely require the use strain rate and temperature dependent data as well as failure related data which were absent from the simulations presented in this research. In addition to the future work outlined in Table 20, the theoretical basis of the model may need to be altered based on the observations made from the experiments to better represent the material behavior. These steps will aid in maturing the developed model into a predictive tool.

REFERENCES

Aboudi, J., Arnold, S. M., and Bednarcyk, B. A. (2013). *Micromechanics of Composite Materials*. Elsevier, Waltham, MA.

Adams, D. F. (2013). "Thickness-tapered unidirectional composite specimens." *Composites World*.

Adams, D., Moriarty, J., Gellegos, A., and Adams, D. F. (2003). *Development of the V-notched rail shear test for composite laminates*. FAA Technical Report, Office of Aviation Research, Washington D.C.

Adams, D. O., and Adams, D. F. (2002). *Tabbing guide for composite specimens*. FAA Technical Report, Office of Aviation Research, Washington D.C.

Andrews, M. G., and Massabò, R. (2007). "The effects of shear and near tip deformations on energy release rate and mode mixity of edge-cracked orthotropic layers." *Engineering Fracture Mechanics*, 74(17), 2700–2720.

Arrese, A., Boyano, A., De Gracia, J., and Mujika, F. (2017). "A novel procedure to determine the cohesive law in DCB tests." *Composites Science and Technology*, 152, 76–84.

Azzi, V., and Tsai, S. (1965). "Anisotropic strength of composites." *Experimental Mechanics*, 5(9), 283–288.

Barenblatt, G. (1962). "The mathematical theory of equilibrium cracks in brittle fracture." *Advances in Applied Mechanics*, 7, 55–129.

Benzeggagh, M. L., and Kenane, M. (1996). "Measurement of mixed-mode delamination fracture toughness of unidirectional glass/epoxy composites with mixed-mode bending apparatus." *Composites Science and Technology*, 56(4), 439–449.

Berg, C. (1972). "A note on the construction of the equivalent plastic strain increment." *Journal of Reasearch of the National Bureau of Standards-C. Engineering and Instrumentation*, 76C(1–2), 53–54.

Bland, D. (1957). “The associated flow rule of plasticity.” *Journal of the Mechanics and Physics of Solids*, 6, 71–78.

Blaysat, B., Hoefnagels, J. P. M., Lubineau, G., Alfano, M., and Geers, M. G. D. (2015). “Interface debonding characterization by image correlation integrated with Double Cantilever Beam kinematics.” *International Journal of Solids and Structures*, 55, 79–91.

Borg, R., Nilsson, L., and Simonsson, K. (2004). “Simulating DCB, ENF and MMB experiments using shell elements and a cohesive zone model.” *Composites Science and Technology*, 64(2), 269–278.

Broughton, W. R., Kumosa, M., and Hull, D. (1990). “Analysis of the Iosipescu shear test as applied to unidirectional carbon-fibre reinforced composites.” *Composites Science and Technology*, 38(4), 299–325.

Broughton, W., and Sims, G. (1994). *An overview of through-thickness test methods for polymer matrix composites*. National Laboratory, UK.

Camanho, P. P., Davila, C. G., and de Moura, M. F. (2003). “Numerical Simulation of Mixed-Mode Progressive Delamination in Composite Materials.” *Journal of Composite Materials*, 37(16), 1415–1438.

Caner, F. C., Bažant, Z. P., Hoover, C. G., Waas, A. M., and Shahwan, K. W. (2011). “Microplane Model for Fracturing Damage of Triaxially Braided Fiber-Polymer Composites.” *Journal of Engineering Materials and Technology*, 133(2), 021024-1-021024–12.

Cantwell, W., and Morton, J. (1989). “Comparison of the low and high velocity mpact response of CFRP.” *Composites*, 20(6), 545551.

Cao, S., Wang, X., and Wu, Z. (2011). “Evaluation and prediction of temperature-dependent tensile strength of unidirectional carbon fiber-reinforced polymer composites.” *Journal of Reinforced Plastics and Composites*, 30(9), 799–807.

Carlsson, L. A., Gillespie, J. W., and Pipes, R. (1986). "On the Analysis and Design of the End Notched Flexure (ENF) Specimen for Mode II Testing." *Journal of Composite Materials*, 20, 594–604.

Chandra, N. (2002). "Evaluation of interfacial fracture toughness using cohesive zone model." *Composites Part A: Applied Science and Manufacturing*, 33(10), 1433–1447.

Chang, F.-K., and Chang, K.-Y. (1987a). "Post-Failure Analysis of Bolted Composite Joints in Tension or Shear-Out Mode Failure." *Journal of Composite Materials*, 21, 809–833.

Chang, F.-K., and Chang, K.-Y. (1987b). "A Progressive Damage Model for Laminated Composites Containing Stress Concentrations." *Journal of Composite Materials*, 21, 834–855.

Choi, H. Y., Downs, R. J., and Chang, F.-K. (1991). "A New Approach toward Understanding Damage Mechanisms and Mechanics of Laminated Composites Due to Low-Velocity Impact: Part I—Experiments." *Journal of Composite Materials*, 25(8), 992–1011.

Clark, B. (2015). "NASA Creates Partnership to Advance Composite Materials for Aircraft of the Future." *National Institute of Aerospace Press Releases*, Hampton, VA.

Clark, G. (1989). "Modelling of impact damage in composite laminates." *Composites*, 20(3), 209–214.

Correlated Solutions, Inc. (2009). "Digital Image Correlation: Overview of Principles and Software." University of South Carolina Columbia, South Carolina.

Correlated Solutions, Inc. (2018). *Speckle Pattern Fundamentals*. Application Note.

D20 Committee. (2015a). *ASTM D3846-08: Test Method for In-Plane Shear Strength of Reinforced Plastics*. ASTM International.

D20 Committee. (2013a). *ASTM D792-13: Test Methods for Density and Specific Gravity (Relative Density) of Plastics by Displacement*. ASTM International.

D30 Committee. (2015b). *ASTM D4255/D4255M-15a: Test Method for In-Plane Shear Properties of Polymer Matrix Composite Materials by the Rail Shear Method*. ASTM International.

D30 Committee. (2017a). *ASTM D3039/D3039M-17: Test Method for Tensile Properties of Polymer Matrix Composite Materials*. ASTM International.

D30 Committee. (2013b). *ASTM D5528-13: Test Method for Mode I Interlaminar Fracture Toughness of Unidirectional Fiber-Reinforced Polymer Matrix Composites*. ASTM International.

D30 Committee. (2017b). *ASTM D8101/D8101M-17: Standard Test Method for Measuring the Penetration Resistance of Composite Materials to Impact by a Blunt Projectile*. ASTM International.

D30 Committee. (2012). *ASTM D5379/D5379M-12: Test Method for Shear Properties of Composite Materials by the V-Notched Beam Method*. ASTM International.

D30 Committee. (2014). *ASTM D7905/7905M-14: Test Method for Determination of the Mode II Interlaminar Fracture Toughness of Unidirectional Fiber-Reinforced Polymer Matrix Composites*. ASTM International.

D30 Committee. (2016). *ASTM D3410/D3410M-16: Test Method for Compressive Properties of Polymer Matrix Composite Materials with Unsupported Gage Section by Shear Loading*. ASTM International.

Daniel, I., and Lee, J.-W. (1990). "Damage Development in Composite Laminates Under Monotonic Loading." *Journal of Composites Technology and Research*, 12(2), 98–102.

Deivanayagam, A., Vaidya, A., and Rajan, S. D. (2014). "Enhancements to Modeling Dry Fabrics for Impact Analysis." *Journal of Aerospace Engineering*, 27(3), 484–490.

Deshpande, Y. (2018). “Quasi-static and dynamic mechanical response of T800/F3900 composite in tension and shear.” Master’s, Ohio State University, Columbus, OH.

Donadon, M. V., Iannucci, L., Falzon, B. G., Hodgkinson, J. M., and de Almeida, S. F. M. (2008). “A progressive failure model for composite laminates subjected to low velocity impact damage.” *Computers & Structures*, 86(11–12), 1232–1252.

Drucker, D. (1956). “On uniquness in the theory of plasticity.” *Quarterly of Applied Mathematics*, 14(1), 35–42.

Dugdale, D. S. (1960). “Yielding of steel sheets containing slits.” *Journal of the Mechanics and Physics of Solids*, 8(2), 100–104.

Elices, M., Guinea, G. V., Gómez, J., and Planas, J. (2002). “The cohesive zone model: advantages, limitations and challenges.” *Engineering Fracture Mechanics*, 69(2), 137–163.

Elmarakbi, A. M., Hu, N., and Fukunaga, H. (2009). “Finite element simulation of delamination growth in composite materials using LS-DYNA.” *Composites Science and Technology*, 69(14), 2383–2391.

Ferguson, R. F., Hinton, M. J., and Hiley, M. J. (1998). “Determining the through-thickness properties of FRP materials.” *Composites Science and Technology*, 58(9), 1411–1420.

Fernandes, R. L., and Campilho, R. D. S. G. (2017). “Testing different cohesive law shapes to predict damage growth in bonded joints loaded in pure tension.” *The Journal of Adhesion*, 93(1–2), 57–76.

Finn, S. R., He, Y.-F., and Springer, G. S. (1993). “Delaminations in composite plates under transverse impact loads — Experimental results.” *Composite Structures*, 23(3), 191–204.

FLIR Integrated Imaging Solutions, Inc. (2019). “Grasshopper3 5.0 MP Mono USB3 Vision (Sony ICX625).”

Forghani, A., Zobeiry, N., Poursartip, A., and Vaziri, R. (2013). "A structural modelling framework for prediction of damage development and failure of composite laminates." *Journal of Composite Materials*, 47(20–21), 2553–2573.

Fuchs, P. F., and Major, Z. (2011). "Experimental Determination of Cohesive Zone Models for Epoxy Composites." *Experimental Mechanics*, 51(5), 779–786.

Gilat, A., Goldberg, R. K., and Roberts, G. D. (2002). "Experimental study of strain-rate-dependent behavior of carbon/epoxy composite." *Composites Science and Technology*, 62(10–11), 1469–1476.

Gillespie Jr., J. W., Carlsson, L. A., and Pipes, R. B. (1986b). "Finite Element Analysis of the End Notched Flexure Specimen for Measuring Mode II Fracture Toughness." *Composites Science and Technology*, 27, 177–197.

Gillespie Jr., J. W., Carlsson, L. A., Pipes, R. B., Rothschilds, R., Trethewey, B., and Smiley, A. (1986a). *Delamination growth in composite materials*. NASA Langley Research Center, Hampton, VA, 210.

Goldberg, R. K., Carney, K. S., DuBois, P., Hoffarth, C., Khaled, B., Shyamsunder, L., Rajan, S. D., and Blankenhorn, G. (2018). "Implementation of a tabulated failure model into a generalized composite material model." *Journal of Composite Materials*, 52(25), 3445–3460.

González, C., and LLorca, J. (2007). "Mechanical behavior of unidirectional fiber-reinforced polymers under transverse compression: Microscopic mechanisms and modeling." *Composites Science and Technology*, 67(13), 2795–2806.

Griffith, A. (1920). "The phenomena of rupture and flow in solids." *Philosohpical Transactions of the Royal Society of London*, 221, 163–198.

Ha, S. K., Jin, K. K., and Huang, Y. (2008). "Micro-Mechanics of Failure (MMF) for Continuous Fiber Reinforced Composites." *Journal of Composite Materials*, 42(18), 1873–1895.

Harrington, J., Hoffarth, C., Rajan, S. D., Goldberg, R. K., Carney, K. S., DuBois, P., and Blankenhorn, G. (2017). "Using Virtual Tests to Complete the Description of a Three-Dimensional Orthotropic Material." *Journal of Aerospace Engineering*, 30(5), 04017025-1-04017025–14.

Hashemi, S., Kinloch, A. J., and Williams, J. G. (1990). "The Analysis of Interlaminar Fracture in Uniaxial Fibre-Polymer Composites." *Proceedings of the Royal Society A: Mathematical, Physical and Engineering Sciences*, 427(1872), 173–199.

Hawong, J.-S., Shin, D.-C., and Baek, U.-C. (2004). "Validation of pure shear test device using finite element method and experimental methods." *Engineering Fracture Mechanics*, 71(2), 233–243.

Heidari-Rarani, M., Shokrieh, M. M., and Camanho, P. P. (2013). "Finite element modeling of mode I delamination growth in laminated DCB specimens with R-curve effects." *Composites Part B: Engineering*, 45(1), 897–903.

Hill, R. (1948). "A theory of the yielding and plastic flow of anisotropic metals." *Proceedings of the Royal Society of London. Series A. Mathematical and Physical Sciences*, 193, 281–297.

Hinton, M. J., Kaddour, A., and Soden, P. (2004). *Failure criteria in fibre reinforced polymer composites: the world-wide failure exercise*. Elsevier, The Boulevard, Langford Lane Kidlington, Oxford OX5 1GB UK.

Hinton, M., and Kaddour, A. (2012). "The background to the Second World-Wide Failure Exercise." *Journal of Composite Materials*, 46(19–20), 2283–2294.

Hoffarth, C. (2016). "A Generalized Orthotropic Elasto-Plastic Material Model for Impact Analysis." PHD Dissertation, Arizona State University, Tempe, AZ.

Hoffarth, C., Khaled, B., Shyamsunder, L., Rajan, S., Goldberg, R., Carney, K., DuBois, P., and Blankenhorn, G. (2017). "Verification and Validation of a Three-Dimensional Orthotropic Plasticity Constitutive Model Using a Unidirectional Composite." *Fibers*, 5(1), 12.

Hoffarth, C., Rajan, S. D., Goldberg, R. K., Revilock, D., Carney, K. S., DuBois, P., and Blankenhorn, G. (2016). "Implementation and validation of a three-dimensional plasticity-based deformation model for orthotropic composites." *Composites Part A: Applied Science and Manufacturing*, 91, 336–350.

Högberg, J. L., Sørensen, B. F., and Stigh, U. (2007). "Constitutive behaviour of mixed mode loaded adhesive layer." *International Journal of Solids and Structures*, 44(25–26), 8335–8354.

Hsiao, H. M., and Daniel, I. M. (1998). "Strain rate behavior of composite materials." *Composites Part B: Engineering*, 29(5), 521–533.

Hussain, A. K., and Adams, D. F. (2004). "Analytical evaluation of the two-rail shear test method for composite materials." *Composites Science and Technology*, 64(2), 221–238.

Ilyushin, A. (1961). "On the postulate of plasticity." *Prikl. Mat. Mekh*, 25, 503–507.

Irwin, G. (1957). "Analysis of stresses and strains near the end of a crack traversing a plante." *Journal of Applied Mechanics*, 24, 361–364.

Jacob, G. C., Starbuck, J. M., Fellers, J. F., Simunovic, S., and Boeman, R. G. (2004). "Strain rate effects on the mechanical properties of polymer composite materials." *Journal of Applied Polymer Science*, 94(1), 296–301.

Jelf, P. M., and Fleck, N. A. (1992). "Compression Failure Mechanisms in Unidirectional Composites." *Journal of Composite Materials*, 26(18), 2706–2726.

Jiang, Z., Wan, S., Zhong, Z., Li, M., and Shen, K. (2014). "Determination of mode-I fracture toughness and non-uniformity for GFRP double cantilever beam specimens with an adhesive layer." *Engineering Fracture Mechanics*, 128, 139–156.

Johnson, W., and Mangalgiri, P. (1987). "Investigation of Fiber Bridging in Double Cantilever Beam Specimens." *Journal of Composites Technology and Research*, 9(1), 10–13.

Johnston, J. P., Pereira, J. M., Ruggeri, C. R., and Roberts, G. D. (2017). "High Speed Thermal Imaging on Ballistic Impact of Triaxially Braided Composites." *32nd Annual Technical Conference of the American Society for Composites*, Purdue University; West Lafayette, IN, 1–14.

Jones, R., Paul, J., and Tay, T. E. (1988). "Assessment of the Effect of Impact Damage in Composites: Some Problems and Answers." *Composite Structures*, 10, 51–73.

Joshi, S. P., and Sun, C. T. (1987). "Impact-Induced Fracture in a Quasi-Isotropic Laminate." *Journal of Composites Technology & Research*, 9(2), 40–46.

Kachanov, L. (1958). "Time of the Rupture Process under Creep Conditions." *Izvestia Akademi Nauk SSSR, Old. Tekhn. Nauk,* 8, 26–31.

Kachanov, L. (1977). "Separation failure of composite materials." *Mechanics of Composite Materials*, 12(5), 812–815.

Kaddour, A., Hinton, M., Smith, P., and Li, S. (2013). "The background to the third world-wide failure exercise." *Journal of Composite Materials*, 47(20–21), 2417–2426.

Karayaka, M., and Kurath, P. (1994). "Deformation and Failure Behavior of Woven Composite Laminates." *Journal of Engineering Materials and Technology*, 116(2), 222–232.

Karush, W. (1939). "Minima of Functions of Several Variables with Inequalities as Side Constraints." M.Sc Dissertation, Dept. of Mathematics, University of Chicago, Chicago, IL.

Khaled, B. M., Shyamsunder, L., Holt, N., Hoover, C. G., Rajan, S. D., and Blankenhorn, G. (2019a). "Enhancing the predictive capabilities of a composite plasticity model using cohesive zone modeling." *Composites Part A: Applied Science and Manufacturing*, 121, 1–17.

Khaled, B., Shyamsunder, L., Hoffarth, C., Rajan, S. D., Goldberg, R. K., Carney, K. S., DuBois, P., and Blankenhorn, G. (2019b). "Damage characterization of composites to support an orthotropic plasticity material model." *Journal of Composite Materials*, 53(7), 941–967.

Kim, J.-K., MacKay, D. B., and Mai, Y.-W. (1993). "Drop-weight impact damage tolerance of CFRP with rubber-modified epoxy matrix." *Composites*, 24(6), 485–494.

Krueger, R., Shivakumar, K. N., and Raju, I. S. (2013). "Fracture Mechanics Analyses for Interface Crack Problems - A Review." *54th AIAA/ASME/ASCE/AHS/ASC Structures, Structural Dynamics, and Materials Conference*, American Institute of Aeronautics and Astronautics, Boston, Massachusetts.

Kuhn, H., and Tucker, A. (1951). "Nonlinear Programming." *Proceedings of 2nd Berkeley Symposium*, University of California Press, Berkeley, CA, 481–492.

Kurumatani, M., Terada, K., Kato, J., Kyoya, T., and Kashiyama, K. (2016). "An isotropic damage model based on fracture mechanics for concrete." *Engineering Fracture Mechanics*, 155, 49–66.

Lee, M. J., Cho, T. M., Kim, W. S., Lee, B. C., and Lee, J. J. (2010). "Determination of cohesive parameters for a mixed-mode cohesive zone model." *International Journal of Adhesion and Adhesives*, 30(5), 322–328.

Leffler, K., Alfredsson, K. S., and Stigh, U. (2007). "Shear behaviour of adhesive layers." *International Journal of Solids and Structures*, 44, 530–545.

Lemaitre, J. (1985). "A Continuous Damage Mechanics Model for Ductile Fracture." *Journal of Engineering Materials and Technology*, 107, 83–89.

Lemaitre, J., and Chaboche, J. L. (1978). "Aspects phenomelogiques de la rupture par endommagement." *Journal de Mecanique Appliquee*, 2(3).

Lemaître, J., and Desmorat, R. (2005). *Engineering damage mechanics: ductile, creep, fatigue and brittle failures*. Springer, Berlin ; New York.

Li, S., Thouless, M. D., Waas, A. M., Schroeder, J. A., and Zavattieri, P. D. (2005). "Use of mode-I cohesive-zone models to describe the fracture of an adhesively-bonded polymer-matrix composite." *Composites Science and Technology*, 65(2), 281–293.

Liu, P. F., and Zheng, J. Y. (2008). "Progressive failure analysis of carbon fiber/epoxy composite laminates using continuum damage mechanics." *Materials Science and Engineering: A*, 485(1–2), 711–717.

Lomov, S. V., Bogdanovich, A. E., Ivanov, D. S., Mungalov, D., Karahan, M., and Verpoest, I. (2009). "A comparative study of tensile properties of non-crimp 3D orthogonal weave and multi-layer plain weave E-glass composites. Part 1: Materials, methods and principal results." *Composites Part A: Applied Science and Manufacturing*, 40(8), 1134–1143.

LSTC. (2018a). *LS-DYNA*. Livermore Software Technology Corporation, Livermore, CA.

LSTC. (2017b). "LS-DYNA Keyword User's Manual, Volume II: Material Models, LS-DYNA R10.0."

LSTC. (2017a). "LS-DYNA Keyword User's Manual, Volume I: Keywords, LS-DYNA R10.0."

LSTC. (2018b). *LS-PrePost*. Livermore Softwrae Technology Corporation, Livermore, CA.

Lubarda, V., Mastilovic, S., and Knap, J. (1996). "Some comments on plasticity postulates and non-associative flow rules." *International Journal of Mechanical Sciences*, 38(3), 247–258.

Luo, Q., and Tong, L. (2009). "Energy release rates for interlaminar delamination in laminates considering transverse shear effects." *Composite Structures*, 89(2), 235–244.

Maimí, P., Camanho, P. P., Mayugo, J. A., and Dávila, C. G. (2007a). "A continuum damage model for composite laminates: Part I – Constitutive model." *Mechanics of Materials*, 39(10), 897–908.

Maimí, P., Camanho, P. P., Mayugo, J. A., and Dávila, C. G. (2007b). "A continuum damage model for composite laminates: Part II – Computational implementation and validation." *Mechanics of Materials*, 39(10), 909–919.

Maire, J. F., and Chaboche, J. L. (1997). "A new formulation of continuum damage mechanics (CDM) for composite materials." *Aerospace Science and Technology*, 1(4), 247–257.

Martin, R. H., and Murri, G. B. (1988). *Characterization of Mode I and Mode II delamination growth and thresholds in graphite/peek composites*. NASA Langley Research Center, Hampton, VA, 52.

Masters, J. (1987). "Characterization of Impact Damage Development in Graphite/Epoxy Laminates." *Fractography of Modern Engineering Materials: Composites and Metals*, J. Masters and J. Au, eds., ASTM International, 100 Barr Harbor Drive, PO Box C700, West Conshohocken, PA 19428-2959, 238-238–21.

MATLAB and Statistics Toolbox. (2018). The MathWorks, Inc., Natick, MA.

Matzenmiller, A., Lubliner, J., and Taylor, R. L. (1995). "A constitutive model for anisotropic damage in fiber-composites." *Mechanics of Materials*, 20(2), 125–152.

Medina, C., Canales, C., Arango, C., and Flores, P. (2014). "The influence of carbon fabric weave on the in-plane shear mechanical performance of epoxy fiber-reinforced laminates." *Journal of Composite Materials*, 48(23), 2871–2878.

Melin, L. N., and Neumeister, J. M. (2006). "Measuring constitutive shear behavior of orthotropic composites and evaluation of the modified Iosipescu test." *Composite Structures*, 76(1–2), 106–115.

Melis, M., Pereira, M., Goldberg, R. K., and Rassaian, M. (2018). "Dynamic Impact Testing and Model Development in Support of NASA's Advanced Composites Program." *2018 AIAA/ASCE/AHS/ASC Structures, Structural Dynamics, and Materials Conference*, American Institute of Aeronautics and Astronautics, Kissimmee, Florida.

Mirzaali, M. J., Buerki, A., Schwiedrzik, J., Zysset, P. K., and Wolfram, U. (2015). "Continuum damage interactions between tension and compression in osteonal bone." *Journal of the Mechanical Behavior of Biomedical Materials*, 49, 355–369.

Naik, D., Sankaran, S., Mobasher, B., Rajan, S. D., and Pereira, J. M. (2009). "Development of reliable modeling methodologies for fan blade out containment analysis – Part I: Experimental studies." *International Journal of Impact Engineering*, 36, 1–11.

Nandakumar, P. N. (2010). "Rate sensitivity of the interlaminar fracture toughness of laminated composites." Master's, Wichita State University, Wichita, KS.

Neumeister, J. M., and Melin, L. N. (2003). "A modified Iosipescu shear test for anisotropic composite panels." San Diego, CA.

Nicholas, T. (1980). *Dynamic Tensile Testing of Structural Materials Using a Split Hopkinson Bar Apparatus*. Air Force Wright Aeronautical Laboratories: Materials Laboratory, Wright-Patterson Air Force Base, OH.

Odegard, G., and Kumosa, M. (2000). "Determination of shear strength of unidirectional composite materials with the Iosipescu and 10 degree off-axis shear tests." *Composites Science and Technology*, 27.

Ogihara, S., and Reifsnider, K. L. (2002). "Characterization of Nonlinear Behavior in Woven Composite Laminates." *Applied Composite Materials*, 9, 249–263.

Ogin, S. L., Brøndsted, P., and Zangenberg, J. (2016). "Composite materials." *Modeling Damage, Fatigue and Failure of Composite Materials*, Elsevier, 3–23.

Oller, S., Oñate, E., Miquel, J., and Botello, S. (1996). "A plastic damage constitutive model for composite materials." *International Journal of Solids and Structures*, 33(17), 2501–2518.

Ortega, A., Maimí, P., González, E. V., and Trias, D. (2016). "Characterization of the translaminar fracture Cohesive Law." *Composites Part A: Applied Science and Manufacturing*, 91, 501–509.

Paley, M., and Aboudi, J. (1992). "Micromechanical analysis of composites by the generalized cells model." *Mechanics of Materials*, 14(2), 127–139.

Pereira, J. M. (2017). "Dynamic Impact Tests in Support of NASA Advcanced Composites Project."

Philippidis, T. P., and Vassilopoulos, A. P. (2001). "Stiffness Reduction of Composite Laminates under Combined Cyclic Stresses." *Advanced Composites Letters*, 10(3), 113–124.

Pierron, F., and Vautrin, A. (1998). "Measurement of the in-plane shear strengths of unidirectional composites with the Iosipescu test." *Composites Science and Technology*, 57(12), 1653–1660.

Pinho, S. T., Iannucci, L., and Robinson, P. (2006). "Physically based failure models and criteria for laminated fibre-reinforced composites with emphasis on fibre kinking. Part II: FE implementation." *Composites Part A: Applied Science and Manufacturing*, 37(5), 766–777.

Poissant, J., and Barthelat, F. (2010). "A Novel 'Subset Splitting' Procedure for Digital Image Correlation on Discontinuous Displacement Fields." *Experimental Mechanics*, 50, 353–364.

Prager, W. (1947). "An introduction to the mathermatical theory of plasticity." *Journal of Applied Physics*, 18, 375–383.

Prel, Y., Davies, P., Benzeggagh, M., and de Charentenay, F. (1989). "Mode I and Mode II Delamination of Thermosetting and Thermoplastic Composites." *Composite Materials: Fatigue and Fracture, Second Volume*, P. Lagace, ed., ASTM International, 100 Barr Harbor Drive, PO Box C700, West Conshohocken, PA 19428-2959, 251–269.

Rajan, S., Sutton, M. A., Fuerte, R., and Kidane, A. (2018). "Traction-separation relationship for polymer-modified bitumen under Mode I loading: Double cantilever beam experiment with stereo digital image correlation." *Engineering Fracture Mechanics*, 187, 404–421.

Raju, K., and Acosta, J. (2010). *Crashworthiness of composite fuselage structures-material dynamic properties, Phase I*. FAA Technical Report, National Institute for Aviation Research, Wichita State University, Wichita, KS, 303.

Reiner, J., Torres, J. P., and Veidt, M. (2017). "A novel Top Surface Analysis method for Mode I interface characterisation using Digital Image Correlation." *Engineering Fracture Mechanics*, 173, 107–117.

Rice, J. (1968). "A path independent integral and the approximate analysis of strain concentration by notches and cracks." *Journal of Applied Mechanics*, 35, 379–386.

Russell, A., and Street, K. (1985). "Moisture and Temperature Effects on the Mixed-Mode Delamination Fracture of Unidirectional Graphite/Epoxy." *Delamination and Debonding of Materials*, W. Johnson, ed., ASTM International, 100 Barr Harbor Drive, PO Box C700, West Conshohocken, PA 19428-2959, 349–370.

Schultheisz, C. R., and Waas, A. M. (1996). "Compressive failure of composites, part I: Testing and micromechanical theories." *Progress in Aerospace Sciences*, 32(1), 1–42.

Shen, B., and Paulino, G. H. (2011). "Direct Extraction of Cohesive Fracture Properties from Digital Image Correlation: A Hybrid Inverse Technique." *Experimental Mechanics*, 51, 143–163.

Shim, V. P. W., and Yang, L. M. (2005). "Characterization of the residual mechanical properties of woven fabric reinforced composites after low-velocity impact." *International Journal of Mechanical Sciences*, 47(4–5), 647–665.

Shokrieh, M. M., and Omidi, M. J. (2009). "Tension behavior of unidirectional glass/epoxy composites under different strain rates." *Composite Structures*, 88(4), 595–601.

Shyamsunder, L., Khaled, B. M., Rajan, S. D., Goldberg, R. K., Carney, K. S., DuBois, P., and Blankenhorn, G. (2019). "Implementing deformation, damage and failure in an orthotropic plastic material model." *Journal of Composite Materials*, Submitted, awaiting decision.

Simo, J., and Taylor, R. (1986). “A return mapping algorithm for plane stress elastoplasticity.” *International Journal of Numerical Methods in Engineering*, 22, 649–670.

Skourlis, T. P., and McCullough, R. L. (1993). “The effect of temperature on the behavior of the interphase in polymeric composites.” *Composites Science and Technology*, 49(4), 363–368.

Šmilauer, V., Hoover, C. G., Bažant, Z. P., Caner, F. C., Waas, A. M., and Shahwan, K. W. (2011). “Multiscale simulation of fracture of braided composites via repetitive unit cells.” *Engineering Fracture Mechanics*, 78(6), 901–918.

Sun, C. T., and Chen, J. L. (1989). “A Simple Flow Rule for Characterizing Nonlinear Behavior of Fiber Composites.” *Journal of Composite Materials*, 23(10), 1009–1020.

Sun, C. T., and Chen, J. L. (1991). “A micromechanical model for plastic behavior of fibrous composites.” *Composites Science and Technology*, 40(2), 115–129.

Sun, C. T., and Vaidya, R. S. (1996). “Prediction of composite properties from a representative volume element.” *Composites Science and Technology*, 56(2), 171–179.

Sun, X. C., and Hallett, S. R. (2017). “Barely visible impact damage in scaled composite laminates: Experiments and numerical simulations.” *International Journal of Impact Engineering*, 109, 178–195.

Sun, X. C., and Hallett, S. R. (2018). “Failure mechanisms and damage evolution of laminated composites under compression after impact (CAI): Experimental and numerical study.” *Composites Part A: Applied Science and Manufacturing*, 104, 41–59.

Sutton, M., Orteu, J.-J., and Schreier, H. W. (2009). *Image Correlation for Shape, Motion and Deformation Measurements. Basic Concepts, Theory and Applications*. Springer US.

Swanson, S., Messick, M., and Toombes, G. (1985). “Comparison of torsion tube and Iosipescu in-plane shear test results for a carbon fibre-reinforced epoxy composite.” *Composites*, 16(3), 220–224.

Thiruppukuzhi, S. V., and Sun, C. T. (1998). “Testing and modeling high strain rate behavior of polymeric composites.” *Composites Part B: Engineering*, 29(5), 535–546.

Thomason, J. L., and Yang, L. (2011). “Temperature dependence of the interfacial shear strength in glass–fibre polypropylene composites.” *Composites Science and Technology*, 71(13), 1600–1605.

Thouless, M. D. (2018). “Shear forces, root rotations, phase angles and delamination of layered materials.” *Engineering Fracture Mechanics*, 191, 153–167.

Tsai, S. W., and Wu, E. M. (1971). “A General Theory of Strength for Anisotropic Materials.” *Journal of Composite Materials*, 5, 58–80.

Tsouvalis, N. G., and Anyfantis, K. N. (2011). “Determination of the fracture process zone under Mode I fracture in glass fiber composites.” *Journal of Composite Materials*, 46(1), 27–41.

Uyaner, M., and Kara, M. (2007). “Dynamic Response of Laminated Composites Subjected to Low-velocity Impact.” *Journal of Composite Materials*, 41(24), 2877–2896.

Vaziri, R., Olson, M., and Anderson, D. (1991). “A Plasticity-Based Consitutitve Model for Fibre-Reinforced Composite Laminates.” *Journal of Composite Materials*, 25, 512–535.

Vic-3D. (2016). en, Correlated Solutions, Inc.

Vic-Snap. (2016). Correlated Solutions, Inc.

van der Vossen, B. C. W., and Makeev, A. (2018). “Characterization of Cohesive Zone Laws Using Digital Image Correlation.” Seattle, WA, 15.

Waas, A. M., and Schultheisz, C. R. (1996). “Compressive failure of composites, part II: Experimental studies.” *Progress in Aerospace Sciences*, 32(1), 43–78.

Walrath, D., and Adams, D. (1983). “The Iosipescu shear test as applied to composite materials.” *Experimental Mechanics*, 23, 105–110.

Walter, T. R., Subhash, G., Sankar, B. V., and Yen, C. F. (2010). “Monotonic and cyclic short beam shear response of 3D woven composites.” *Composites Science and Technology*, 70(15), 2190–2197.

Welsh, L. M., and Harding, J. (1985). “Effect of strain rate on the tensile failure of woven reinforced polyester resin composites.” *Le Journal de Physique Colloques*, 46(C5), C5-405-C5-414.

Wilkins, D., Eisenmann, J., Camin, R., Margolis, W., and Benson, R. (1982). “Characterizing Delamination Growth in Graphite-Epoxy.” *Damage in Composite Materials: Basic Mechanisms, Accumulation, Tolerance, and Characterization*, K. Reifsnider, ed., ASTM International, 100 Barr Harbor Drive, PO Box C700, West Conshohocken, PA 19428-2959, 168-168–16.

Wilkins, D. J. (1981). *A comparison of the delamination and environmental resistance of a graphite-epoxy and a graphite-bismaleimide*. Naval Air Systems Command Technical Report, Naval Air Systems Command, Washington D.C., 221.

Wu, H.-Y. T., and Springer, G. S. (1988). “Measurements of Matrix Cracking and Delamination Caused by Impact on Composite Plates.” *Journal of Composite Materials*, 22, 518–532.

Xie, M., and Adams, D. (1995). “A plasticity model for unidirectional composite materials and its applications in modeling composites testing.” *Composites Science and Technology*, 54, 11–21.

Yang, P. (2016). “Experimental techniques and mechanical behavior of T800/F3900 at various strain rates.” Master’s, Ohio State University, Columbus, OH.

Yashiro, S., Ogi, K., Nakamura, T., and Yoshimura, A. (2013). “Characterization of high-velocity impact damage in CFRP laminates: Part I – Experiment.” *Composites Part A: Applied Science and Manufacturing*, 48, 93–100.

Yen, C.-F. (2012). “A ballistic material model for continuous-fiber reinforced composites.” *International Journal of Impact Engineering*, 46, 11–22.

Yoneyama, S., Morimoto, Y., and Takashi, M. (2006). “Automatic Evaluation of Mixed-mode Stress Intensity Factors Utilizing Digital Image Correlation.” *Strain*, 42, 21–29.

Zhao, Y., Seah, L. K., and Chai, G. B. (2016). “Measurement of interlaminar fracture properties of composites using the J-integral method.” *Journal of Reinforced Plastics and Composites*, 35(14), 1143–1154.

Zhu, Y., Liechti, K. M., and Ravi-Chandar, K. (2009). “Direct extraction of rate-dependent traction–separation laws for polyurea/steel interfaces.” *International Journal of Solids and Structures*, 46(1), 31–51.